

**Impact of charge and solubility on nanoparticle uptake and transformations *in planta*
through spatially resolved chemical speciation**

Submitted in partial fulfillment of the requirements for

the degree of

Doctor of Philosophy

in

Civil and Environmental Engineering

Eleanor R. Spielman-Sun

B.A., Chemistry, Oberlin College

M.S., Civil and Environmental Engineering, Carnegie Mellon University

Carnegie Mellon University
Pittsburgh, PA

May, 2019

ACKNOWLEDGEMENTS

Funding for this thesis was provided by the following sources: the U.S. National Science Foundation (NSF) and the Environmental Protection Agency (EPA); Center for the Environmental Implications of NanoTechnology (CEINT; EF-1266252); Nano for Agriculturally Relevant Materials (NanoFARM; CBET-1530563); Materials Characterization Facility at Carnegie Mellon University (MCF-677785); NSF Integrated Graduate Education and Research Traineeship Nanotechnology Environmental Effects and Policy (IGERT-NEEP; DGE-0966227); and the Dowd Fellowship from the College of Engineering at Carnegie Mellon University. Synchrotron-related work was carried out at the following facilities: XFM and SRX Beamlines of the National Synchrotron Light Source II (NSLS-II), a U.S. Department of Energy (DOE) Office of Science User Facility operated for the DOE Office of Science by Brookhaven National Laboratory under Contract No. DE-SC0012704; Beamlines 11-2 and 4-1 at Stanford Synchrotron Radiation Lightsource (SSRL), a national user facility of the DOE Office of Basic Energy Sciences; and the XFM beamline (AS162/XFM/10714) at the Australian Synchrotron, Victoria, Australia.

The research presented in this dissertation and my journey through the Ph.D. program at Carnegie Mellon University would not have been possible without the support of a great many professors, colleagues, and friends. I am grateful for the time, energy, and care they have all extended to train me as a researcher, to create a positive working environment throughout my time here, and to prepare for the next stage in my career as a researcher in environmental engineering.

I sincerely thank my advisor, Dr. Greg Lowry. I am grateful for his willingness to prioritize the needs of his students among his busy work schedule and his frankness (most of the time). He also taught me to never yawn during your advisor's talk at a conference. I have no doubt that I have become a better scientist due to his mentoring. I also thank Dr. Enzo Lombi for hosting me

in his lab in the University of South Australia (UniSA) and serving on my committee. He has provided excellent advice and guidance regarding x-ray imaging of plants. While at UniSA, I am also grateful to Dr. Erica Donner, Dr. Anzhela Malysheva, Dr. Gianluca Brunetti, Susie Ritch, and Thea Read, also at UniSA, for their willingness to provide support and improve my research. My research in Australia would not have been successful without their support.

I thank my committee members, Dr. David Dzombak and Dr. Elizabeth Casman, for their interest in my research and the time and effort they have spent in providing comments to improve the quality of my work. Dave provided important advice on my research, particularly insights into the redox and water chemistry aspects. Liz, in particular, contributed a valuable perspective on the broader impacts on my work.

I also thank my wonderful synchrotron x-ray team. Dr. John Stegemeier was the first person to teach me X-ray absorption spectroscopy and how to operate a beamline; his patience and overall support at the start of my PhD was vital for my first paper. Dr. Astrid Avellan, in particular, has been both an awesome coffee drinking buddy and an incredible mentor and friend. Her enthusiasm and dedication is truly inspiring, and I hope we can continue collaborating together in the future. Garret Bland has also become a wonderful friend, and his support through my PhD has been invaluable. I leave the master synchrotron notebook in both his and Emma Clement's very capable hands.

Many collaborators and colleagues have provided helpful feedback and friendly encouragement. I thank Ron Ripper and Brian Belowich for their support in lab and cheerful presence in the lab/office. I am especially grateful to Dr. Stacey Louie who, as my Research Experiences for Undergraduates (REU) research mentor in the summer of 2013, shared a great deal of knowledge to help get me started and inspired me to join the research group and pursue a

PhD in environmental engineering. I am thankful to all of my current and former labmates who have helped me in numerous ways through the years: Dr. Aniela Burant, Dr. Clint Noack, Dr. Amy Dale, Dr. Lauren Bergman, Dr. Megan Leitch, Dr. Eric McGivney, Dr. Joe Moore, Dr. Alex Bertuccio, Dr. Nizette Consolazio, Dr. Ke Gai, Dr. Adam Cadwallader, Dr. Kelly Good, Dr. Jonathan Callura, Xiaoyu Gao, Stephanie Laughton, Rucha Vaidya, Jie Yun, Yilin Zhang, Brian Vencalek, Meng-Chen Lee. Each one of them has contributed something meaningful during my time at CMU, through knowledge and technical assistance, moral support, and friendship both inside and outside of the lab. A special thanks goes to Stephanie Laughton, one of my best friends in lab and who has provided invaluable scientific and personal support. She is already an incredibly dedicated teacher and I have no doubt she will become a successful professor.

I've had the fortune to work at several synchrotron facilities and am grateful to all the beamline scientists: Dr. Daryl Howard and Dr. Martin DeJonge at the Australian Synchrotron; Dr. Ryan Davis at SSRL; and Dr. Juergen Thieme and Dr. Ryan Tapper, at NSLS-II. This work would not have been possible without their support—particularly at 2 AM when the beam goes down.

Outside of CMU, I am grateful to my boyfriend and best friend, William Thomas, who has always supported me by editing numerous emails, listening to all my practice presentations, and commiserating about the struggles of graduate school. I am also grateful to my brother, Max, for his love and support. Most of all, I am grateful to my parents, Dan and Frances, who always emphasized the importance of hard work and fostered a love of science in me from a young age. In particular, I am grateful for all the hours my dad spent helping me with my math and science homework throughout the years; there are not many kids who can rely on their parents for help on their quantum mechanics homework. Both of them inspired me to follow in their footsteps and become (at least some sort of) a doctor.

ABSTRACT

Plant nanobiotechnology promises transformative solutions to the most vexing problems threatening global food security, e.g. drought, disease, and soil nutrient deficiencies. However, poor understanding of how NP physiochemical properties affect their fate in/on plants and the lack of effective methods to deliver the nanomaterials to where they are needed in a precise plant compartment impedes these technological innovations. This thesis evaluates how three specific NP properties, charge, solubility, and coating, influence plant uptake, metal distribution, and *in planta* NP transformation, which will provide insight into the design of efficient and safe nano-enabled agrochemicals.

The first objective of this work was to evaluate the influence of surface charge on NP uptake by roots, translocation, and distribution in plant tissue. Wheat was hydroponically exposed to CeO₂ NPs functionalized with positively-charged, negatively-charged, or neutral dextran coatings. While the positively-charged NPs adhered significantly more to the roots, the negatively-charged NPs translocated to the shoots most efficiently. Whereas Ce from negatively-charged NP exposed plant was found mostly in the leaf veins, Ce was in the nonvascular leaf tissue of the neutral NP exposed plant. These results demonstrate that different CeO₂ NP surface charges result in different Ce localization in leaves.

The second objective of this thesis was to compare the influence of charge on NP uptake and distribution between different types of plants. Experiments with these particles using two monocotyledons (corn and rice) and two dicotyledons (tomato and lettuce) indicated that while total Ce uptake was plant-species dependent, likely due to differences in transpiration rates, Ce distribution in the leaves was driven by NP surface charge and were generalizable across all four plants. Comparing leaf vasculature, Ce was able to move much further outside of the main

vasculature in the dicot plants than monocot plants, likely due to the larger airspace volume in dicot leaves compared to monocot leaves. This work clearly demonstrates that tuning NPs coating charge can achieve plant compartment targeting after root uptake.

The third objective of this work was to determine the influence of Cu-based NP 1-h solubility on metal uptake, distribution and speciation over time in wheat. Higher 1-h solubility $\text{Cu}(\text{OH})_2$ NPs provided more uptake of Cu after 1 h of exposure, but the lower 1-h solubility materials (CuO and CuS NPs) were more persistent on/in the roots and continued to slowly deliver Cu to plant leaves over 48 h. The initial NP composition significantly influenced the Cu speciation within the plant roots; the Cu in plants exposed to CuS NPs was mostly reduced and/or sulfidized while the Cu in the CuO NP exposed plants was oxidized and bound to organics. This work demonstrates that tuning initial NP speciation can allow for the delivery of different metal species, resulting in controllable delivery rates and bioavailabilities.

The fourth objective of this work was to determine how coating can be modified to increase NP adherence to plant leaf structures, specifically pathogen points of entry. Gold nanoparticles were coated with a biomolecule with affinity for a specific chemical moiety found on guard cells to target leaf stomata. After rinsing, NPs with this coating remained strongly adhered to the stomata on the leaf surface. These results demonstrate, for the first time, active, targeted delivery of NPs to a specific site on live plants via foliar application.

Overall, this thesis demonstrates that tuning NP physicochemical properties to achieve specific bioavailability, distribution, targeted delivery in plants is possible. These findings provide key information for the design of nano-enabled agrochemicals that are more targeted, more efficient, and less wasteful.

TABLE OF CONTENTS

Acknowledgements	ii
Abstract	v
List of Figures	x
List of Tables	xii
Chapter 1: Introduction	1
1.1 Motivation	2
1.2 Background	2
1.2.1 Potential for Nanotechnology in Agriculture	2
1.2.2 Influence of Surface Properties on Nanoparticle-Plant Interactions	3
1.2.2.1 Effect of Surface Charge on Metal Distribution and Uptake by Roots	3
1.2.2.2 Effect of NP Coating on Leaf Attachment	4
1.2.3 Influence of NP Transformations on Metal Interactions with Plants	5
1.2.3.1 Plant-Induced Oxidation and Reduction of NPs	5
1.2.3.2 Effect of NP Dissolution on Metal Distribution and Uptake by Roots	5
1.3 Objectives and Overview of this Thesis	7
1.3.1 Objective 1	7
1.3.2 Objective 2	8
1.3.3 Objective 3	8
1.3.4 Objective 4	9
1.4 References for Chapter 1	9
Chapter 2: Impact of Surface Charge on Cerium Oxide Nanoparticle Uptake and Translocation by Wheat (<i>Triticum aestivum</i>)	16
Abstract	17
2.1 Introduction	18
2.2 Materials and Methods	18
2.2.1 Cerium Dioxide Nanoparticles	18
2.2.2 Plant Growth	19
2.2.3 μ -XRF and Fluorescence XANES Imaging	20
2.3 Results and Discussion	21
2.3.1 Characterization of NPs	21
2.3.2 Total Ce Association/Uptake in Roots and Shoots	22
2.3.3 Ce Distribution and Speciation in Roots after 8 H of Exposure	25
2.3.4 Ce Distribution and Speciation in Roots after 34 H of Exposure	26
2.3.5 Ce Distribution and Speciation in Leaves after 34 H of Exposure	28
2.4 Environmental Implications	31
2.5 References for Chapter 2	32
Chapter 3: Nanoparticle Surface Charge Influences Uptake, Translocation, and Leaf Distribution in Vascular Plants with Contrasting Anatomy	37
Abstract	38
3.1 Introduction	39
3.2 Materials and Methods	40

3.2.1	Material Characterization	40
3.2.2	Plant Growth and Exposure	40
3.2.3	Plant Health Measurements	41
3.2.4	Total Ce Association and Uptake	42
3.2.5	X-Ray Absorption Spectroscopy	42
3.2.6	XRF and μ -XANES Collection and Analysis	43
3.3	Results and Discussion	44
3.3.1	NP Characterization	44
3.3.2	Total Ce Uptake	44
3.3.3	Plant Health	47
3.3.4	Ce Reduction in Roots	49
3.3.5	Ce Distribution in Leaves	51
3.4	Environmental Implications	57
3.5	References for Chapter 3	57
Chapter 4:	Temporal Evolution of Copper Distribution and Speciation in Roots of <i>Triticum aestivum</i> Exposed to CuO, Cu(OH)₂, and CuS Nanoparticles	62
	Abstract	63
4.1	Introduction	64
4.2	Materials and Methods	65
4.2.1	Chemicals	65
4.2.2	CuS NP Synthesis	66
4.2.3	Cu NP Characterization	66
4.2.4	Plant Exposure	67
4.2.5	μ -XRF and Fluorescence XANES Imaging	68
4.3	Results and Discussion	70
4.3.1	NP Characterization	70
4.3.2	Total Cu Association/Uptake in Roots and Shoots	70
4.3.3	Change in Cu Distribution over Time	73
4.3.4	Change in Cu Speciation over Time	74
4.4	Environmental Implications	78
4.5	References for Chapter 4.	79
Chapter 5:	Active Targeted Delivery of Nanoparticles to Stomatal Guard Cells	84
	Abstract	85
5.1	Introduction	86
5.2	Materials and Methods	88
5.2.1	Materials	88
5.2.2	Coating Attachment Protocol	88
5.2.3	Nanoparticle Characterization	88
5.2.4	Plant Growth and Exposure	88
5.2.5	Darkfield Hyperspectral Imaging	89
5.2.6	X-Ray Fluorescence Imaging	89
5.3	Results and Discussion	90
5.3.1	Materials Characterization	90
5.3.2	Microscope Images of AuNPs on Leaf Surface	91
5.3.3	X-Ray Fluorescence Maps	92
5.4	Future Work	93

5.5 References for Chapter 5	94
Chapter 6: Summary of Major Contributions and Perspectives for Future Work	97
6.1 Summary of Major Contributions	98
6.1.1 Major Contributions of Objective 1	98
6.1.2 Major Contributions of Objective 2	98
6.1.3 Major Contributions of Objective 3	99
6.1.4 Major Contributions of Objective 4	100
6.2 Perspectives for Future Research	101
6.2.1 Future Research for Objective 1	101
6.2.2 Future Research for Objective 2	102
6.2.3 Future Research for Objective 3	103
6.2.4 Future Research for Objective 4	104
6.3 References for Chapter 6	105
Appendix A: Supporting Information for Chapter 2	109
Appendix B: Supporting Information for Chapter 3	121
Appendix C: Supporting Information for Chapter 4	139
Appendix D: Supporting Information for Chapter 5	149
Appendix E: Effect of Silver Concentration and Chemical Transformations on Release and Antibacterial Efficacy in Silver-Containing Textiles	152
Abstract	153
E.1 Introduction	154
E.2 Materials and Methods	156
E.2.1 Ag-Enabled Textiles	156
E.2.2 Textile Exposure	157
E.2.3 Determination of Ag Transformations in Textiles	158
E.2.4 Antimicrobial Efficacy of Textiles	159
E.3 Results and Discussion	160
E.3.1 Ag Release from Textiles under “Use-Phase” Scenario	160
E.3.2 Ag Release from Textiles under “End-of-Life” Scenario	162
E.3.3 Ag Transformation in Ag ⁰ -Coated Textiles	164
E.3.4 Antimicrobial effectiveness of Textiles	166
E.4 Environmental Implications	172
E.5 References Appendix E	173

LIST OF FIGURES

Figure 2.1: Total Ce Uptake in Wheat Roots and Leaves	24
Figure 2.2: Ce Distribution in Wheat Roots after 1 h Exposure	24
Figure 2.3: Ce Distribution in Wheat Roots after 8 h Exposure	26
Figure 2.4: Ce Distribution in Wheat Roots after 34 h Exposure	28
Figure 2.5: Ce Distribution in Wheat Leaves after 34 h Exposure	30
Figure 3.1: Differences between Monocot and Dicot Plants	39
Figure 3.2: Total Ce Uptake and Translocation Efficiencies	46
Figure 3.3: Correlation between Root Surface Area and Ce Uptake	47
Figure 3.4: Measurements of Plant Health	49
Figure 3.5: Ce Reduction in Plant Roots	51
Figure 3.6: XRF Maps of Monocot Leaves	54
Figure 3.7: XRF Maps of Dicot Leaves from Negative and Neutral Exposures	55
Figure 3.8: XRF Maps of Dicot Leaves from Positive Exposure	56
Figure 4.1: NP Solubility Schematic	65
Figure 4.2: Total Cu Uptake in Wheat Roots and Shoots	71
Figure 4.3: Cu Distribution in Wheat Roots	74
Figure 4.4: Cu Speciation in Wheat Roots	75
Figure 4.5: Pixel-by-Pixel XANES Analysis of Cu in Wheat Roots	77
Figure 5.1: NP Targeting Strategies to Stomata	87
Figure 5.2: TEM and UV-Vis Spectra of NPs	90
Figure 5.3: Light Microscope Images of Control Leaves	91
Figure 5.4: Cytoviva Images of Leaves Exposed to Coated NPs	92
Figure 5.5: XRF Maps of Leaves Exposed to Coated NPs	93
Figure A.1: Ce LIII XANES of CeO ₂ NPs and model compounds	111
Figure A.2: Hydrodynamic Diameters of CeO ₂ NPs	113
Figure A.3: XANES Spectra for Ce in Wheat Roots after 8 h Exposure	114
Figure A.4: K Distribution in Wheat Roots after 8 h Exposure	115
Figure A.5: XANES Spectra for Ce in Wheat Roots after 34 h Exposure	116
Figure A.6: Traverse Ce Concentrations in Wheat Roots after 34 h Exposure	117
Figure A.7: XANES Spectra for Ce in Wheat Leaves after 34 h Exposure	118
Figure A.8: Traverse Ce and Zn Concentrations in Leaf after 34 h Exposure	119
Figure A.9: Ca Distribution in Wheat Leaf after 34 h Exposure	120
Figure B.1: Hydrodynamic Diameters of CeO ₂ NPs	122
Figure B.2: XFM Maps of Corn Leaf Exposed to CeO ₂ (-) NPs	126
Figure B.3: XFM Maps of Corn Leaf Exposed to CeO ₂ (0) NPs	127
Figure B.4: XFM Maps of Rice Leaf Exposed to CeO ₂ (-) NPs	128
Figure B.5: XFM Maps of Rice Leaf Exposed to CeO ₂ (0) NPs	129
Figure B.6: XFM Maps of Lettuce Leaf Exposed to CeO ₂ (-) NP s.	130
Figure B.7: XFM Maps of Lettuce Leaf Exposed to CeO ₂ (0) NPs	131
Figure B.8: XFM Maps of Tomato Leaf Exposed to CeO ₂ (-) NPs.	132

Figure B.9: Tri-Colored XFM Map of Tomato Leaf Exposed to CeO ₂ (–) NPs.	133
Figure B.10: XFM Maps of Tomato Leaf Exposed to CeO ₂ (0) NPs.	134
Figure B.11: XFM Maps of Lettuce Leaf Exposed to CeO ₂ (0) NPs.	135
Figure B.12: XFM Maps of Lettuce Leaf Exposed to CeO ₂ (0) NPs.	136
Figure B.13: XFM Maps of Tomato Leaf Exposed to CeO ₂ (0) NPs.	137
Figure B.14: XFM Map of Ce Accumulation in Trichomes	138
Figure C.1: Cu XANES Models	141
Figure C.2: TEM Images and XRD Spectra of Cu NPs	142
Figure C.3: Traverse Cu Concentration in Wheat Roots	144
Figure C.4: XANES Spectra for Cu in Wheat Roots after 1 h Exposure	145
Figure C.5: XANES Spectra for Cu in Wheat Roots after 12 h Depuration	146
Figure C.6: XANES Spectra for Cu in Wheat Roots after 48 h Depuration	147
Figure D.1: Microscope Images of Leaf Exposed to LM6M-NP Solution	151
Figure E.1: Ag Release under “Use-Phase” Scenarios	161
Figure E.2: Ag Release under “End-of-Life” Scenarios	163
Figure E.3: XANES Spectra for Ag ⁰ -Fabric	165
Figure E.4: Antimicrobial Efficacy of Fabrics	167

LIST OF TABLES

Table 4.1: CuO, CuS, and Cu(OH) ₂ NP Characterization	70
Table 5.1: AuNP Characterization	91
Table A.1: CeO ₂ NP Dissolution in Spent Hydroponic Medium	112
Table B.1: Dissolved Fraction of Ce Remaining in Solution	123
Table B.2: Root Ce Uptake/Association and Root Surface Area	124
Table B.3: XANES Fitting Statistics for Monocot and Dicot Roots	125
Table C.1: Total Cu Uptake in Roots and Shoots	143
Table C.2: XANES Fitting Statistics for Cu in Wheat Roots	148
Table D.1: Summary of Antibodies	150
Table E.1: Summary of Ag-Enabled Fabrics	157
Table E.2: XANES Fitting Statistics for Ag-Enabled Fabrics	166
Table E.3: Antimicrobial Efficacy	168

CHAPTER 1: INTRODUCTION

1.1 MOTIVATION

Crop agro-ecosystems are incredibly water and energy intensive, accounting for ~70% of total freshwater withdrawal in the world¹ and ~30% of global energy use.² This is, in part, because agricultural practices are inefficient. For example, up to 95% of applied micronutrients and 99% of pesticides never reach their targets and are wasted,^{3,4} running off the field, causing collateral damage, and wasting the energy and water used for their production. Sustainably meeting the world's nutritional needs will require innovative technologies that can increase crop yields and the nutritional value of foods while decreasing overall energy and water inputs. Thus, there is a critical need for innovative fertilizer systems and disease management solutions to improve the resiliency of U.S. agriculture while minimizing environmental impacts.

1.2 BACKGROUND

1.2.1. POTENTIAL FOR NANOTECHNOLOGY IN AGRICULTURE

Nanotechnology has the potential to become a valuable tool for improving agro-ecosystem efficiency by enhancing crop productivity and reducing nutrient losses (e.g. through controlled release of agrochemicals or target-specific delivery) and resiliency against major environmental stressors (e.g. drought, salinity, disease).⁵⁻⁹ First, nanoparticles (NPs) are small enough to cross important plant mechanical barriers (e.g. cuticle and cell walls) which have size exclusion limits in the μm -nm range. NPs can also cross cellular and organelle membranes and move in between cells which enables them to load into the vasculature either via apoplastic (extracellular) or symplastic (intracellular) pathways (both mechanisms have been proposed for translocation of NPs in plants).^{8,10,11} Secondly, NP surfaces are easily modifiable with a variety of coatings and, similar to drug deliv-

ery, NP surface properties can theoretically be tuned to deliver them to specific tissues or organelles in plants.^{12,13} Combined with their inherent rate-limited dissolution, many metal and metal oxide NPs could provide inherent slow release of the constituent metals in the desired locations of plants, which can be less phytotoxic than soluble forms of metals applied at the same dose.¹⁴ Finally, NPs have been shown to increase photosynthesis,^{15,16} biomass production rates,^{17,18} plant stress tolerance,¹⁹ plant resistance to diseases,^{20,21} and agrochemical utilization efficiency.²² Despite the great potential of NPs, there remains limited understanding of how NP physical and chemical properties (e.g. size, charge, solubility, coating, chemical composition) dictate NP-plant interactions. A better understanding of these NP-plant interactions is needed to design targeted and controlled delivery, which has the potential to reduce the number of applications of fertilizers and pesticides, decrease nutrient losses from fertilizers, and increase yields through optimized nutrient management.

1.2.2. INFLUENCE OF SURFACE PROPERTIES ON NANOPARTICLE-PLANT INTERACTIONS

NPs are often coated with macromolecules, such as polymers or proteins, in order to stabilize against aggregation.²³ These coatings can also increase NP functionality, such as by increasing biocompatibility or improving targeted drug delivery.^{23–27} Tailoring NP surface properties is critical for efficient, targeted delivery of agrochemicals.

1.2.2.1. Effect of Surface Charge on Metal Distribution and Uptake by Roots

Surface charge is a key property that can control NP transport in environmental and biological systems. Zhu et al. compared the uptake of functionalized gold nanoparticles (AuNPs) with well-defined surface charges into various terrestrial plants, including radish, ryegrass, rice, and pumpkin, and confirmed that while positively-charged NPs more readily attach to plant roots, negatively-charged NPs are most efficiently translocated into the plant shoots²⁸ The same trend has

been observed for AuNPs coated with variously charged organic ligands on rice and tomato²⁹ and for cationic or anionic coated CdSe/ CdSnS quantum dots on poplar trees.³⁰ Because charge can influence NP interactions with charged biological structures,²⁵ it is desirable to better understand precisely how charge affects the spatial distribution of NPs that have translocated in plants. Few studies characterize the spatial distribution of the NPs in leaves beyond total metal analysis.^(e.g.31–34)

1.2.2.2. Effect of NP Coating on Leaf Attachment

A number of studies on foliar application of NPs, including Ag,³⁵ Au,³⁶ Cu-based,^{18,37–39} CeO₂,^{18,40} iron oxides,^{41–43} MgO,⁴² MnO,³⁸ TiO₂,^{17,35,36,42} and ZnO,^{17,38,42,44,45} have demonstrated the potential uptake and translocation of metals from leaves to other tissues. Despite the breadth of NPs and plant types studied, there remains limited understanding of how these NP properties (e.g. charge, hydrophobicity, surface functional groups) influence attachment. Yu et al. demonstrated that pesticide-loaded NPs conferred with a positive charge adhered more strongly than the negative or neutral NPs primarily through hydrogen bonding and electrostatics.⁴⁶ With regards to hydrophobicity, Avellan et al. observed that while there was incomplete uptake of hydrophilic AuNPs with some NPs remaining on the outside of the cuticle layer, the fraction of these AuNPs that had penetrated the cuticle were translocated efficiently to the plant vasculature; in contrast, virtually all of the hydrophobic AuNPs crossed the cuticle layer, but its transport through the mesophyll cells to the vasculature was lower.⁴⁷ Examples of organelle-specific targeting in live plants are generally limited to chloroplasts.^{15,48,49} More studies are needed in order to fully understand how to modify NP coating properties to target specific plant features.

1.2.3. INFLUENCE OF NP TRANSFORMATIONS ON METAL INTERACTIONS WITH PLANTS

NPs often undergo biotransformation in plants, including dissolution,^{50–53} complexation,^{54–57} and reduction/oxidation.^{34,58,59} The solubility of many metal and metal oxide NPs is of interest because the dissolved metal species can be toxic. Solubility and dissolution can also influence NP persistence in soil or on plant leaves, and influences the localized delivery of dissolved vs. particulate species.

1.2.3.1. Plant-Induced Oxidation and Reduction of NPs

Many metal and metal oxide NPs are capable of being bio-reduced or bio-oxidized. Ceria, in particular, exhibits unique redox chemistry, which can potentially be used to increase photosynthesis,⁶⁰ especially if NP can be delivered to photosynthetic reaction centers in chloroplasts. CeO₂ NPs have been shown to protect cells against reactive oxygen species (ROS)-induced damage *in vitro*,^{61–63} including isolated chloroplasts.^{15,64} This is due to oxygen vacancies in the CeO₂ crystalline lattice that readily enable cycling between Ce³⁺ and Ce⁴⁺ oxidation states. However, there are limited examples of this *in vivo*. CeO₂ NPs with low Ce(III)/Ce(IV) ratios delivered via foliar infiltration have also been shown to improve plant photosynthetic rates under heat⁴⁸ and salinity^{19,65} by serving as antioxidants. In contrast, decreased photosynthetic rate and CO₂ assimilation efficiency, increased lipid peroxidation, and other stress measures have also been observed in a variety of plants exposed to CeO₂ NPs, particularly at high doses greater than 500 mg/kg soil^(eg. 66–68) and using NPs with higher Ce(III)/Ce(IV) ratios.^(eg. 69) A better understanding of the impacts of NP redox state on plant health is needed to fully leverage their benefits.

1.2.3.2. Effect of NP Dissolution on Metal Distribution and Uptake by Roots

Dissolution is an important property that influences NP behavior and mode of action. Size is generally considered the primary physiochemical property affecting NP dissolution, as dissolution rate

generally increases as particle size decreases.⁷⁰⁻⁷⁴ Other parameters such as shape, surface morphology, and crystallinity must also be considered. Numerous papers have speculated that NPs have the potential to provide a slow-release delivery of micronutrients to plants.^{3,6,75,76} This concept has already been successfully applied to drug delivery,¹² but there is limited work demonstrating this for agriculture. For example, a controlled-release polyphosphate micronutrient fertilizer containing Zn, Fe, Mn, and Cu with low solubility in water but high solubility in the presence of citric acid was able to increase rice yield by up to 17% more than conventional micronutrient salts.²² As a potential biocide, Giannousi et al. demonstrated that CuO NPs reduced the percentage of tomato plants affected by *Phytophthora infestans* better than currently available non-nano Cu agrochemicals and can be applied at a lower active ingredient rate.⁷⁷ This was further corroborated by Elmer and White who demonstrated that the antimicrobial properties of CuO NPs applied foliarly to eggplant and tomato resulted in increased resistance of the plant to *Fusarium* wilt fungus and increased yields compared to the application of bulk CuO and CuSO₄.²⁰ Differences in NP dissolution in the root rhizosphere vs bulk soil have also been observed,⁵⁰ which could be utilized in calcareous soils with high pH to selectively deliver active ingredients to the plant roots. Overall, NPs with slow-release capabilities could potentially lower the amount of micronutrients lost due to leaching from soils and increase availability to plants by releasing the active ingredient at a rate that is tuned for the plant's needs. However, detailed studies evaluating NP transformations at the root surface and subsequent NP-derived metal uptake in plants exposed to NPs of different solubilities are lacking.

1.3 OBJECTIVES AND OVERVIEW OF THIS THESIS

Improved knowledge of NP-plant interactions is needed to fully exploit their potential benefits as agrochemicals while minimizing risks. The overall motivation for this thesis is to evaluate how specific NP properties influence plant uptake and metal distribution and transformation, which will provide insight into the design of efficient and safe nano-enabled agrochemicals. Four objectives were pursued, each comprising a separate chapter of this thesis, which were focused on one of three NP properties: surface charge (**Objectives 1 and 2**), solubility (**Objective 3**) and coating (**Objective 4**).

1.3.1. OBJECTIVE 1: *Evaluate the influence of surface charge on CeO₂ NP uptake, distribution, and speciation in wheat*

To evaluate the influence of surface charge on NP uptake by plants, a model plant (*Triticum aestivum*) was exposed to ~4 nm CeO₂ NPs functionalized with positively charged, negatively charged, and neutral dextran coatings. Ce root association/uptake and leaf translocation was quantified by inductively coupled plasma mass spectrometry (ICP-MS). Additionally, the spatial distribution of the Ce within the roots and shoots was evaluated using synchrotron X-ray fluorescence mapping (XFM) and fluorescence X-ray absorption near edge structure (XANES) mapping in order to determine the Ce spatial distribution and speciation in plant tissues. This research demonstrated that different CeO₂ NP surface charge resulted in different Ce distributions in the leaves. This work resulted in a publication in *Environmental Science & Technology*.³³

1.3.2. OBJECTIVE 2: *Compare the influence of surface charge on CeO₂ NP root uptake, distribution, and speciation in monocotyledonous and dicotyledonous plants*

To determine how differences in root structure and leaf vasculature and NP surface charge influence Ce distribution and spatial distribution within plants, two monocotyledons (corn and rice) and two dicotyledons (tomato and lettuce) were exposed hydroponically to positively-charged, negatively-charged, and neutral ~4 nm CeO₂ NPs. Total Ce uptake was measured by ICP-MS, Ce reduction in roots by XANES, and Ce distribution in leaves by XFM. This research showed that dicots have higher NP translocation efficiencies than monocots and that differences in Ce distribution in the leaves due to NP surface charge are generalizable across all four plants. This work is currently being prepared for submission to *Environmental Science: Nano*.

1.3.3. OBJECTIVE 3: *Determine the influence of Cu-based NP solubility on metal distribution and speciation over time*

To evaluate the effect of solubility on NP uptake, distribution, and speciation over time, a model plant (*Triticum aestivum*) was exposed to Cu-based NPs with varying solubilities for 1h, then transferred to a Cu-free medium for a 48 h depuration period. Total Cu uptake and translocation was evaluated using ICP-MS, and changes in Cu spatial distribution and speciation in roots by ICP-MS, XFM, and XANES mapping. This research demonstrated that the initial NP composition influenced the Cu speciation within the plant roots. This research also demonstrated that NPs, by associating to the roots, have the potential to play a role in slowly providing micronutrients to plants. This work resulted in a publication in *Environmental Science & Technology*.⁷⁸

1.3.4. OBJECTIVE 4: *Determine how coating can be modified to increase NP adherence to stomata*

To evaluate the influence of targeting coating on NP attachment to stomata, gold nanoparticles were coated with a biomolecule with affinity for α -1,5-arabinan, a chemical moiety found on stomatal guard cells. *V. faba* leaves were then exposed via drop deposition, and NP distribution was evaluated using darkfield hyperspectral imaging (DF-HSI) and XFM on fresh plant tissue. This work demonstrated, for the first time, active targeted delivery of NPs to a specific site on live plants.

1.4 REFERENCES FOR CHAPTER 1

- (1) FAO (Food and Agriculture Organization of the United Nations). *FAO Statistical Pocketbook: World Food and Agriculture*; Rome, 2015.
- (2) Gerst, M. D.; Cox, M. E.; Locke, K. A.; Laser, M.; Kapuscinski, A. R. A Taxonomic Framework for Assessing Governance Challenges and Environmental Effects of Integrated Food-Energy Systems. *Environ. Sci. Technol.* **2015**, *49* (2), 734–741.
- (3) Monreal, C. M.; DeRosa, M. C.; Mallubhotla, S. C.; Bindraban, P. S.; Dimkpa, C. O. Nanotechnologies for Increasing the Crop Use Efficiency of Fertilizer-Micronutrients. *Biol. Fertil. Soils* **2016**, *52* (3), 423–437.
- (4) Castro, M. J. L.; Ojeda, C.; Cirelli, A. F. Advances in Surfactants for Agrochemicals. *Environ. Chem. Lett.* **2014**, *12* (1), 85–95.
- (5) Rodrigues, S. M.; Demokritou, P.; Dokoozlian, N.; Hendren, C. O.; Karn, B.; Mauter, M. S.; Sadik, O. A.; Safarpour, M.; Unrine, J. M.; Viers, J.; Welle, P.; White, J.C.; Wiesner, M.R.; Lowry, G.V. Nanotechnology for Sustainable Food Production: Promising Opportunities and Scientific Challenges. *Environ. Sci. Nano* **2017**, *7*, 899–904.
- (6) Servin, A. D.; Elmer, W. H.; Mukherjee, A.; De La Torre-Roche, R.; Hamdi, H.; White, J. C.; Bindraban, P. S.; Dimkpa, C. O. A Review of the Use of Engineered Nanomaterials to Suppress Plant Disease and Enhance Crop Yield. *J. Nanoparticle Res.* **2015**, *17* (2), 92.
- (7) Kah, M.; Beulke, S.; Tiede, K.; Hofmann, T. Nanopesticides: State of Knowledge, Environmental Fate, and Exposure Modeling. *Crit. Rev. Environ. Sci. Technol.* **2013**, *43* (16), 1823–1867.
- (8) Wang, P.; Lombi, E.; Zhao, F.-J.; Kopittke, P. M. Nanotechnology: A New Opportunity in Plant Sciences. *Trends Plant Sci.* **2016**, *21* (8), 699–712.
- (9) Zhao, X.; Cui, H.; Wang, Y.; Sun, C.; Cui, B.; Zeng, Z. Development Strategies and Prospects of Nano-Based Smart Pesticide Formulation. *J. Agric. Food Chem.* **2017**, *66* (26), 6504–6512.

- (10) Schwab, F.; Zhai, G.; Kern, M.; Turner, A.; Schnoor, J. L.; Wiesner, M. R. Barriers , Pathways and Processes for Uptake , Translocation and Accumulation of Nanomaterials in Plants – Critical Review. *Nanotoxicology* **2015**, *10* (3), 257–278.
- (11) Du, W.; Tan, W.; Peralta-Videa, J. R.; Gardea-Torresdey, J. L.; Ji, R.; Yin, Y.; Guo, H. Interaction of Metal Oxide Nanoparticles with Higher Terrestrial Plants: Physiological and Biochemical Aspects. *Plant Physiol. Biochem.* **2017**, *110*, 210–225.
- (12) De Jong, W. H.; Borm, P. J. A. Drug Delivery and Nanoparticles: Applications and Hazards. *Int. J. Nanomedicine* **2008**, *3* (2), 133–149.
- (13) González-Melendi, P.; Fernández-Pacheco, R.; Coronado, M.-J.; Corredor, E.; Testillano, P. S.; Risueño, M. C.; Marquina, C.; Ibarra, M. R.; Rubiales, D.; Pérez-de-Luque, A. Nanoparticles as Smart Treatment-Delivery Systems in Plants: Assessment of Different Techniques of Microscopy for Their Visualization in Plant Tissues. *Ann. Bot.* **2008**, *101* (1), 187–195.
- (14) Iavicoli, I.; Leso, V.; Beezhold, D. H.; Shvedova, A. A. Nanotechnology in Agriculture: Opportunities, Toxicological Implications, and Occupational Risks. *Toxicol. Appl. Pharmacol.* **2017**, *329*, 96–111.
- (15) Giraldo, J. P.; Landry, M. P.; Faltermeier, S. M.; McNicholas, T. P.; Iverson, N. M.; Boghossian, A. A.; Reuel, N. F.; Hilmer, A. J.; Sen, F.; Brew, J. A.; Strano, M.S. Plant Nanobionics Approach to Augment Photosynthesis and Biochemical Sensing. *Nat. Mater.* **2014**, *13* (4), 400–408.
- (16) Arora, S.; Sharma, P.; Kumar, S.; Nayan, R.; Khanna, P. K.; Zaidi, M. G. H. Gold-Nanoparticle Induced Enhancement in Growth and Seed Yield of *Brassica juncea*. *Plant Growth Regul.* **2012**, *66* (3), 303–310.
- (17) Raliya, R.; Nair, R.; Chavalmane, S.; Wang, W.-N.; Biswas, P. Mechanistic Evaluation of Translocation and Physiological Impact of Titanium Dioxide and Zinc Oxide Nanoparticles on the Tomato (*Solanum lycopersicum* L.) Plant. *Metallomics* **2015**, *7* (12), 1584–1594.
- (18) Hong, J.; Wang, L.; Sun, Y.; Zhao, L.; Niu, G.; Tan, W.; Rico, C. M.; Peralta-Videa, J. R.; Gardea-Torresdey, J. L. Foliar Applied Nanoscale and Microscale CeO₂ and CuO Alter Cucumber (*Cucumis sativus*) Fruit Quality. *Sci. Total Environ.* **2016**, *563–564*, 904–911.
- (19) Rossi, L.; Zhang, W.; Lombardini, L. L.; Ma, X. The Impact of Cerium Oxide Nanoparticles on the Salt Stress Responses of *Brassica napus* L. *Environ. Pollut.* **2016**, *219*, 28–36.
- (20) Elmer, W. H.; White, J. C. The Use of Metallic Oxide Nanoparticles to Enhance Growth of Tomatoes and Eggplants in Disease Infested Soil or Soilless Medium. *Environ. Sci. Nano* **2016**, *3* (5), 1072–1079.
- (21) Ponmurugan, P.; Manjugarunambika, K.; Elango, V.; Gnanamangai, B. M. Antifungal Activity of Biosynthesised Copper Nanoparticles Evaluated against Red Root-Rot Disease in Tea Plants. *J. Exp. Nanosci.* **2016**, *11* (13), 1019–1031.
- (22) Bandyopadhyay, S.; Ghosh, K.; Varadachari, C. Multimicronutrient Slow-Release Fertilizer of Zinc, Iron, Manganese, and Copper. *Int. J. Chem. Eng.* **2014**, *2014*, 1–7.

- (23) Louie, S. M.; Tilton, R. D.; Lowry, G. V. Critical Review: Impacts of Macromolecular Coatings on Critical Physicochemical Processes Controlling Environmental Fate of Nanomaterials. *Environ. Sci. Nano* **2016**, *3* (2), 283–310.
- (24) Cho, E. C.; Xie, J.; Wurm, P. A.; Xia, Y. Understanding the Role of Surface Charges in Cellular Adsorption versus Internalization by Selectively Removing Gold Nanoparticles on the Cell Surface with a I₂/KI Etchant. *Nano Lett.* **2009**, *9* (3), 1080–1084.
- (25) Albanese, A.; Tang, P. S.; Chan, W. C. W. The Effect of Nanoparticle Size, Shape, and Surface Chemistry on Biological Systems. *Annu. Rev. Biomed. Eng* **2012**, *14*, 1–16.
- (26) Nel, A. E.; Mädler, L.; Velegol, D.; Xia, T.; Hoek, E. M. V.; Somasundaran, P.; Klaessig, F.; Castranova, V.; Thompson, M. Understanding Biophysicochemical Interactions at the Nano-Bio Interface. *Nat. Mater.* **2009**, *8* (7), 543–557.
- (27) López-Moreno, M. L.; Cedeño-Mattei, Y.; Bailón-Ruiz, S. J.; Vazquez-Nuñez, E.; Hernandez-Viezcas, J. A.; Perales-Pérez, O. J.; la Rosa, G. De; Peralta-Videa, J. R.; Gardea-Torresdey, J. L. Environmental Behavior of Coated NMs: Physicochemical Aspects and Plant Interactions. *J. Hazard. Mater.* **2018**, *347* (347), 196–217.
- (28) Zhu, Z.-J.; Wang, H.; Yan, B.; Zheng, H.; Jiang, Y.; Miranda, O. R.; Rotello, V. M.; Xing, B.; Vachet, R. W. Effect of Surface Charge on the Uptake and Distribution of Gold Nanoparticles in Four Plant Species. *Environ. Sci. Technol.* **2012**, *46* (22), 12391–12398.
- (29) Li, H.; Ye, X.; Guo, X.; Geng, Z.; Wang, G. Effects of Surface Ligands on the Uptake and Transport of Gold Nanoparticles in Rice and Tomato. *J. Hazard. Mater.* **2016**, *314*, 188–196.
- (30) Wang, J.; Yang, Y.; Zhu, H.; Braam, J.; Schnoor, J. L.; Alvarez, P. J. J. Uptake, Translocation, and Transformation of Quantum Dots with Cationic versus Anionic Coatings by *Populus deltoides* × *nigra* Cuttings. *Environ. Sci. Technol.* **2014**, *48* (12), 6754–6762.
- (31) Li, J.; Tappero, R. V.; Acerbo, A. S.; Yan, H.; Chu, Y.; Lowry, G. V.; Unrine, J. M. Effect of CeO₂ Nanomaterial Surface Functional Groups on Tissue and Subcellular Distribution of Ce in Tomato (*Solanum lycopersicum*). *Environ. Sci. Nano* **2018**, *6*, 273–285.
- (32) Rico, C. M.; Johnson, M. G.; Marcus, M. A.; Andersen, C. P. Shifts in N and δ¹⁵N in Wheat and Barley Exposed to Cerium Oxide Nanoparticles. *NanoImpact* **2018**, *11* (June), 156–163.
- (33) Spielman-Sun, E.; Lombi, E.; Donner, E.; Howard, D. L.; Unrine, J. M.; Lowry, G. V. Impact of Surface Charge on Cerium Oxide Nanoparticle Uptake and Translocation by Wheat (*Triticum aestivum*). *Environ. Sci. Technol.* **2017**, *51* (13), 7361–7368.
- (34) Hernandez-Viezcas, J. A.; Castillo-Michel, H.; Andrews, J. C.; Cotte, M.; Rico, C. M.; Peralta-Videa, J. R.; Ge, Y.; Priester, J. H.; Holden, P. A.; Gardea-Torresdey, J. L. *In Situ* Synchrotron X-Ray Fluorescence Mapping and Speciation of CeO₂ and ZnO Nanoparticles in Soil Cultivated Soybean (*Glycine max*). *ACS Nano* **2013**, *7* (2), 1415–1423.
- (35) Larue, C.; Castillo-Michel, H.; Sobanska, S.; Cécillon, L.; Bureau, S.; Barthès, V.; Ouerdane, L.; Carrière, M.; Sarret, G. Foliar Exposure of the Crop *Lactuca sativa* to Silver

- Nanoparticles: Evidence for Internalization and Changes in Ag Speciation. *J. Hazard. Mater.* **2014**, 264 (264), 98–106.
- (36) Raliya, R.; Franke, C.; Chavalmane, S.; Nair, R.; Reed, N.; Biswas, P. Quantitative Understanding of Nanoparticle Uptake in Watermelon Plants. *Front. Plant Sci.* **2016**, 7.
- (37) Xiong, T.; Dumat, C.; Dappe, V.; Vezin, H.; Schreck, E.; Shahid, M.; Pierart, A.; Sobanska, S. Copper Oxide Nanoparticle Foliar Uptake, Phytotoxicity, and Consequences for Sustainable Urban Agriculture. *Environ. Sci. Technol.* **2017**, acs.est.6b05546.
- (38) Elmer, W. H.; White, J. Nanoparticles of CuO Improves Growth of Eggplant and Tomato in Disease Infested Soils. *R. Chem. Soc. Environ. Sci. Nano* **2016**, 3, 1072–1079.
- (39) Zhao, L.; Huang, Y.; Keller, A. A. Comparative Metabolic Response between Cucumber (*Cucumis sativus*) and Corn (*Zea mays*) to a Cu(OH)₂ Nanopesticide. *J. Agric. Food Chem.* **2018**, 66 (26), 6628–6636.
- (40) Hong, J.; Peralta-Videa, J. R.; Rico, C. M.; Sahi, S.; Viveros, M. N.; Bartonjo, J.; Zhao, L.; Gardea-Torresdey, J. L. Evidence of Translocation and Physiological Impacts of Foliar Applied CeO₂ Nanoparticles on Cucumber (*Cucumis sativus*) Plants. *Environ. Sci. Technol.* **2014**, 48 (8), 4376–4385.
- (41) Jalali, M.; Ghanati, F.; Modarres-Sanavi, A. M.; Khoshgoftarmanesh, A. H. Physiological Effects of Repeated Foliar Application of Magnetite Nanoparticles on Maize Plants. *J. Agron. Crop Sci.* **2017**, No. February.
- (42) Wang, W.-N.; Tarafdar, J. C.; Biswas, P. Nanoparticle Synthesis and Delivery by an Aerosol Route for Watermelon Plant Foliar Uptake. *J. Nanoparticle Res.* **2013**, 15 (1).
- (43) Alidoust, D.; Isoda, A. Effect of γ -Fe₂O₃ Nanoparticles on Photosynthetic Characteristic of Soybean (*Glycine max* (L.) Merr.): Foliar Spray versus Soil Amendment. *Acta Physiol. Plant.* **2013**, 35 (12), 3365–3375.
- (44) Torabian, S.; Zahedi, M.; Khoshgoftar, A. H. Effects of Foliar Spray of Two Kinds of Zinc Oxide on the Growth and Ion Concentration of Sunflower Cultivars under Salt Stress. *J. Plant Nutr.* **2016**, 39 (2), 172-180.
- (45) Subbaiah, L. V.; Prasad, T. N. V. K. V.; Krishna, T. G.; Sudhakar, P.; Reddy, B. R.; Pradeep, T. Novel Effects of Nanoparticulate Delivery of Zinc on Growth, Productivity, and Zinc Biofortification in Maize (*Zea mays* L.). *J. Agric. Food Chem.* **2016**, 64 (19), 3778–3788.
- (46) Liu, G.; Yu, M.; Wang, Y.; Yao, J.; Cui, H.; Liang, J.; Zeng, Z.; Cui, B.; Sun, C.; Zhao, X. Development of Functionalized Abamectin Poly(Lactic Acid) Nanoparticles with Regulatable Adhesion to Enhance Foliar Retention. *RSC Adv.* **2017**, 7 (19), 11271–11280.
- (47) Avellan, A.; Yun, J.; Zhang, Y.; Spielman-Sun, E.; Unrine, J. M.; Thieme, J.; Li, J.; Lombi, E.; Bland, G.; Lowry, G. V. Nanoparticle Size and Coating Chemistry Control Foliar Uptake Pathways, Translocation and Leaf-to-Rhizosphere Transport in Wheat. *ACS Nano* **2019**, *accepted*.
- (48) Wu, H.; Tito, N.; Giraldo, J. P. Anionic Cerium Oxide Nanoparticles Protect Plant Photosynthesis from Abiotic Stress by Scavenging Reactive Oxygen Species. *ACS Nano* **2017**, 11 (11), 11283–11297.

- (49) Kwak, S.-Y.; Lew, T. T. S.; Sweeney, C. J.; Koman, V. B.; Wong, M. H.; Bohmert-Tatarev, K.; Snell, K. D.; Seo, J. S.; Chua, N.-H.; Strano, M. S. Chloroplast-Selective Gene Delivery and Expression in Planta Using Chitosan-Complexed Single-Walled Carbon Nanotube Carriers. *Nat. Nanotechnol.* **2019**.
- (50) Gao, X.; Avellan, A.; Laughton, S. N.; Vaidya, R.; Rodrigues, S. M.; Casman, E. A.; Lowry, G. V. CuO Nanoparticle Dissolution and Toxicity to Wheat (*Triticum aestivum*) in Rhizosphere Soil. *Environ. Sci. Technol.* **2018**, *52* (5), 2888–2897.
- (51) Misra, S. K.; Dybowska, A.; Berhanu, D.; Luoma, S. N.; Valsami-Jones, E. The Complexity of Nanoparticle Dissolution and Its Importance in Nanotoxicological Studies. *Sci. Total Environ.* **2012**, *438*, 225–232.
- (52) Zhang, W.; Dan, Y.; Shi, H.; Ma, X. Elucidating the Mechanisms for Plant Uptake and In-Planta Speciation of Cerium in Radish (*Raphanus Sativus* L.) Treated with Cerium Oxide Nanoparticles. *J. Environ. Chem. Eng.* **2017**, *5* (1), 572–577.
- (53) Jiang, C.; Castellon, B. T.; Matson, C. W.; Aiken, G. R.; Hsu-Kim, H. Relative Contributions of Copper Oxide Nanoparticles and Dissolved Copper to Cu Uptake Kinetics of Gulf Killifish (*Fundulus grandis*) Embryos. *Environ. Sci. Technol.* **2016**, *51* (3), 1395–1404.
- (54) Schwabe, F.; Schulin, R.; Rupper, P.; Rotzetter, A.; Stark, W.; Nowack, B. Dissolution and Transformation of Cerium Oxide Nanoparticles in Plant Growth Media. *J. Nanoparticle Res.* **2014**, *16* (10), 2668.
- (55) Dimkpa, C. O.; McLean, J. E.; Latta, D. E.; Manangon, E.; Britt, D. W.; Johnson, W. P.; Boyanov, M. I.; Anderson, A. J. CuO and ZnO Nanoparticles: Phytotoxicity, Metal Speciation, and Induction of Oxidative Stress in Sand-Grown Wheat. *J. Nanoparticle Res.* **2012**, *14* (9), 1125–1129.
- (56) Ma, Y.; Zhang, P.; Zhang, Z.; He, X.; Zhang, J.; Ding, Y.; Zhang, J.; Zheng, L.; Guo, Z.; Zhang, L.; Chai, Z.; Zhao, Y. Where Does the Transformation of Precipitated Ceria Nanoparticles in Hydroponic Plants Take Place? *Environ. Sci. Technol.* **2015**, *49* (17), 10667–10674.
- (57) Sarret, G.; Smits, E. A. H. P.; Michel, H. C.; Isaure, M.-P.; Zhao, F.-J.; Tappero, R. Use of Synchrotron-Based Techniques to Elucidate Metal Uptake and Metabolism in Plants. In *Advances in Agronomy*; 2013; Vol. 119, pp 1–82.
- (58) Zhang, P.; Xie, C.; Ma, Y.; He, X.; Zhang, Z.; Ding, Y.; Zheng, L.; Zhang, J. Shape-Dependent Transformation and Translocation of Ceria Nanoparticles in Cucumber Plants. *Environ. Sci. Technol. Lett.* **2017**, *4*, 380–385.
- (59) Collin, B. E.; Auffan, M.; Johnson, A. C.; Kaur, I.; Keller, A. A.; Lazareva, A.; Lead, J. R.; Ma, X.; Merrifield, R. C.; Svendsen, C.; White, J.C.; Unrine, J.M. Environmental Release, Fate and Ecotoxicological Effects of Manufactured Ceria Nanomaterials. *Environ. Sci. Nano* **2014**, *1* (6), 533–548.
- (60) Rossi, L.; Zhang, W.; Ma, X. Cerium Oxide Nanoparticles Alter the Salt Stress Tolerance of *Brassica napus* L. by Modifying the Formation of Root Apoplastic Barriers. *Environ. Pollut.* **2017**, *229*, 132–138.

- (61) Xue, Y.; Luan, Q.; Yang, D.; Yao, X.; Zhou, K. Direct Evidence for Hydroxyl Radical Scavenging Activity of Cerium Oxide Nanoparticles. *J. Phys. Chem. C* **2011**, *115* (11), 4433–4438.
- (62) Tarnuzzer, R. W.; Colon, J.; Patil, S.; Seal, S. Vacancy Engineered Ceria Nanostructures for Protection from Radiation-Induced Cellular Damage. *Nano Lett.* **2005**, *5* (12), 2573–2577.
- (63) Pirmohamed, T.; Dowding, J. M.; Singh, S.; Wasserman, B.; Heckert, E.; Karakoti, A. S.; King, J. E. S.; Seal, S.; Self, W. T. Nanoceria Exhibit Redox State-Dependent Catalase Mimetic Activity. *Chem. Commun.* **2010**, *46* (16), 2736–2738.
- (64) Boghossian, A. A.; Sen, F.; Gibbons, B. M.; Sen, S.; Faltermeier, S. M.; Giraldo, J. P.; Zhang, C. T.; Zhang, J.; Heller, D. A.; Strano, M. S. Application of Nanoparticle Antioxidants to Enable Hyperstable Chloroplasts for Solar Energy Harvesting. *Adv. Energy Mater.* **2013**, *3* (7), 881–893.
- (65) Wu, H.; Shabala, L.; Shabala, S.; Giraldo, J. P. Hydroxyl Radical Scavenging by Cerium Oxide Nanoparticles Improves *Arabidopsis* Salinity Tolerance by Enhancing Leaf Mesophyll Potassium Retention. *Environ. Sci. Nano* **2018**, *5* (7), 1567–1583.
- (66) Conway, J. R.; Beaulieu, A. L.; Beaulieu, N. L.; Mazer, S. J.; Keller, A. A. Environmental Stresses Increase Photosynthetic Disruption by Metal Oxide Nanomaterials in a Soil-Grown Plant. *ACS Nano* **2015**, *9* (12), 11737–11749.
- (67) Zhao, L.; Peng, B.; Hernandez-Viezcas, J. A.; Rico, C. M.; Sun, Y.; Peralta-Videa, J. R.; Tang, X.; Niu, G.; Jin, L.; Varela-Ramirez, A.; et al. Stress Response and Tolerance of Zea Mays to CeO₂ Nanoparticles: Cross Talk among H₂O₂, Heat Shock Protein, and Lipid Peroxidation. *ACS Nano* **2012**, *6* (11), 9615–9622.
- (68) Cao, Z.; Stowers, C.; Rossi, L.; Zhang, W.; Lombardini, L.; Ma, X. Physiological Effects of Cerium Oxide Nanoparticles on the Photosynthesis and Water Use Efficiency of Soybean (*Glycine max* (L.) Merr.). *Environ. Sci. Nano* **2017**, *4* (5), 1086–1094.
- (69) Pulido-Reyes, G.; Rodea-Palomares, I.; Das, S.; Sakthivel, T. S.; Leganes, F.; Rosal, R.; Seal, S.; Fernández-Piñás, F. Untangling the Biological Effects of Cerium Oxide Nanoparticles: The Role of Surface Valence States. *Sci. Rep.* **2015**, *5*, 15613.
- (70) Ma, R.; Levard, C.; Marinakos, S. M.; Cheng, Y.; Liu, J.; Michel, F. M.; Brown, G. E.; Lowry, G. V. Size-Controlled Dissolution of Organic-Coated Silver Nanoparticles. *Environ. Sci. Technol.* **2012**, *46* (2), 752–759.
- (71) Bian, S. W.; Mudunkotuwa, I. A.; Rupasinghe, T.; Grassian, V. H. Aggregation and Dissolution of 4 nm ZnO Nanoparticles in Aqueous Environments: Influence of pH, Ionic Strength, Size, and Adsorption of Humic Acid. *Langmuir* **2011**, *27* (10), 6059–6068.
- (72) Radniecki, T. S.; Stankus, D. P.; Neigh, A.; Nason, J. A.; Semprini, L. Influence of Liberated Silver from Silver Nanoparticles on Nitrification Inhibition of *Nitrosomonas europaea*. *Chemosphere* **2011**, *85* (1), 43–49.
- (73) Peng, X.; Palma, S.; Fisher, N. S.; Wong, S. S. Effect of Morphology of ZnO Nanostructures on Their Toxicity to Marine Algae. *Aquat. Toxicol.* **2011**, *102* (3–4), 186–196.

- (74) Zhang, H.; Chen, B.; Banfield, J. F. Particle Size and pH Effects on Nanoparticle Dissolution. *J. Phys. Chem. C* **2010**, *114* (35), 14876–14884.
- (75) Dimkpa, C. O.; Bindraban, P. S. Fortification of Micronutrients for Efficient Agronomic Production: A Review. *Agron. Sustain. Dev.* **2016**, *36* (1), 1–26.
- (76) Milani, N.; McLaughlin, M. J.; Stacey, S. P.; Kirby, J. K.; Hettiarachchi, G. M.; Beak, D. G.; Cornelis, G. Dissolution Kinetics of Macronutrient Fertilizers Coated with Manufactured Zinc Oxide Nanoparticles. *J. Agric. Food Chem.* **2012**, *60* (16), 3991–3998.
- (77) Giannousi, K.; Avramidis, I.; Dendrinou-Samara, C. Synthesis, Characterization and Evaluation of Copper Based Nanoparticles as Agrochemicals against *Phytophthora infestans*. *RSC Adv.* **2013**, *3* (44), 21743–21752.
- (78) Spielman-Sun, E.; Lombi, E.; Donner, E.; Avellan, A.; Howard, D. L.; Etschmann, B.; Howard, D. L.; Lowry, G. V. Temporal Evolution of Copper Distribution and Speciation in Roots of *Triticum aestivum* Exposed to CuO, Cu(OH)₂, and CuS Nanoparticles. *Environ. Sci. Technol.* **2018**, *52* (17), 9777–9784.

CHAPTER 2: IMPACT OF SURFACE CHARGE ON CERIUM OXIDE NANOPARTICLE UPTAKE AND TRANSLOCATION BY WHEAT

This chapter is adapted from a publication and is citable as:

Spielman-Sun, E.; Lombi, E.; Donner, E.; Howard, D. L.; Unrine, J. M.; Lowry, G. V. Impact of Surface Charge on Cerium Oxide Nanoparticle Uptake and Translocation by Wheat (*Triticum aestivum*). *Environ. Sci. Technol.* **2017**, *51* (13), 7361–7368.

Supporting Information is provided in **Appendix A**.

ABSTRACT

Nanoparticle (NP) physiochemical properties, including surface charge, affect cellular uptake, translocation, and tissue localization. To evaluate the influence of surface charge on NP uptake by plants, wheat seedlings were hydroponically exposed to 20 mg/L of ~4 nm CeO₂ NPs functionalized with positively charged, negatively charged, and neutral dextran coatings. Fresh, hydrated roots and leaves were analyzed at various time points over 34 h using fluorescence X-ray absorption near-edge spectroscopy to provide laterally resolved spatial distribution and speciation of Ce. A 15–20% reduction from Ce(IV) to Ce(III) was observed in both roots and leaves, independent of NP surface charge. Because of its higher affinity with negatively charged cell walls, CeO₂(+) NPs adhered to the plant roots the strongest. After 34 h, CeO₂(–), and CeO₂(0) NP exposed plants had higher Ce leaf concentrations than the plants exposed to CeO₂(+) NPs. Whereas Ce was found mostly in the leaf veins of the CeO₂(–) NP exposed plant, Ce was found in clusters in the nonvascular leaf tissue of the CeO₂(0) NP exposed plant. These results provide important information for understanding mechanisms responsible for plant uptake, transformation, and translocation of NPs, and suggest that NP coatings can be designed to target NPs to specific parts of plants.

2.1 INTRODUCTION

As discussed in **Section 1.2.2.1**, surface charge is an important property dictating NP fate in plants. While positively-charged AuNPs have been shown to more readily attach to roots, negatively charged AuNPs more efficiently translocate to the shoots of radish, ryegrass, rice and pumpkin¹ and in tomato and rice.² However, few studies characterize the spatial distribution of the NPs in leaves beyond total metal analysis.^(e.g.3-5) Because charge can influence NP interactions with charged biological structures,⁶ it is desirable to better understand precisely how charge affects the spatial distribution of NPs that have translocated in plants.

To evaluate the influence of surface charge on NP uptake by plants, a model plant (*Triticum aestivum*) was exposed to ~4 nm CeO₂ NPs functionalized with positively charged, negatively charged, and neutral dextran coatings. The influence of charge on total Ce uptake into roots and translocation to shoots were determined. Additionally, the spatial distribution of the Ce within the roots and shoots was evaluated in order to gain a better understanding of the influence of surface charge on NP transformation and distribution within plant tissue.

2.2 MATERIALS AND METHODS

2.2.1. CERIUM DIOXIDE NANOPARTICLES: CeO₂ NPs with three different charges were synthesized as reported previously in Collin et al.⁷ Briefly, uncharged dextran coated CeO₂ NPs (CeO₂(0) NP) with a nominal 4 nm primary particle diameter were produced via alkaline precipitation from a solution of cerium chloride salt and dextran. This coating was then further functionalized, either with diethylaminoethyl groups to create a net positive charge (CeO₂(+) NP) or with carboxymethyl groups to create a net negative charge (CeO₂ (-) NP). The particles were diluted to 20 mg/L as Ce in the exposure medium (¼ strength Hoagland's) and probe sonicated (550 Sonic Dismembrator,

Fisher Scientific) for 1 min at 10 s intervals to ensure dispersion. The hydrodynamic diameter and electrophoretic mobility of the NPs in the exposure medium (20 mg/L as Ce in ¼ strength Hoagland's) were measured using a Nano Zetasizer (Malvern Instruments, Malvern). The initial pH and ionic strength of the exposure medium were 5.6 and 5.2 mM, respectively, and these were not further adjusted. The apparent zeta potential was calculated from the electrophoretic mobility using the Hückel approximation. NP dosing concentrations were selected to avoid acute toxicity while ensuring adequate signal for μ -XRF imaging.

2.2.2. PLANT GROWTH: For μ -XRF, wheat (*Triticum aestivum* cv. shield) seeds were surface sterilized with 10% w/v bleach (VWR Analytical) for 10 min and then thoroughly rinsed with DI water. The sterilized seeds were germinated on deionized water-moistened filter paper in a Petri dish. After four days, the seedlings were transferred to 100-mL plastic containers. Each container was filled with 80 mL of ¼ strength Hoagland's medium⁸ and covered with a plastic lid with five holes. Five seedlings were transplanted to five of the holes with the roots suspended in a continuously aerated solution. Plants were grown at 25 °C under alternating conditions of 12 h of light and 12 h of dark. Nutrient solution was renewed every 3 days. After 7 days, the plants were transferred from the University of South Australia (Adelaide, Australia) to the Australian Synchrotron (Melbourne, Australia) where the plants were hydroponically exposed to 20 mg-Ce/L of CeO₂ NPs and continuously aerated. Plant tissue was removed at 1 h, 8 h, and 34 h to analyze by μ -XRF.

Total Ce determination experiments were conducted at Carnegie Mellon University (Pittsburgh, PA). Plant growth conditions were replicated to match those used for the synchrotron experiment. At the various time points, plants were harvested in triplicate and roots and shoots separated for determination of fresh and dry mass. Briefly, dried plant tissue samples were digested overnight at room temperature in a 2:1 ratio of concentrated HNO₃ and 30% H₂O₂, then heated to

100 °C for 30 minutes (protocol adapted from EPA Method 3050b⁹). Following digestion, the samples were diluted to 5% HNO₃ using deionized water before analysis using inductively coupled plasma mass spectrometry (ICP-MS) (Agilent 7700x, Santa Clara, CA).

2.2.3. μ -XRF AND FLUORESCENCE XANES IMAGING: Following exposure, roots were rinsed in a Ce free hydroponic solution and placed between two pieces of 4 μ m-thick Ultralene, which formed a seal around the plant tissue to minimize dehydration. For each exposure solution, two replicate roots were examined, with all roots positioned vertically in the sample holder and scanned simultaneously. The tips and bases of the plant leaves were scanned separately due to the size of the sample mount. Samples were prepared and examined at the XFM beamline at the Australian Synchrotron, where an in-vacuum undulator is used to produce an X-ray beam. A Si(111) monochromator and Kirkpatrick-Baez (KB) mirror microprobe are used to obtain a monochromatic beam focused onto the specimen. The X-ray fluorescence emitted by the specimen was collected using the 384-element Maia detector (Rev C) placed in a backscatter geometry.^{10,11} For all scans, samples were analyzed continuously “on-the-fly” in the horizontal direction.

An initial large area survey scan at 15.8 keV was conducted to identify the area of interest and obtain overall elemental distributions. Step sizes and scanning velocities were adjusted so each scan took around 2 h. Details are provided in the supporting information. Subsequently, a smaller area was chosen to conduct fluorescence XANES imaging with the XANES stack itself consisting of 108 individual maps at decreasing energies across the Ce L_{III} edge. Details regarding the energy steps are provided in **Appendix A**.

The three nanoparticle types as standards were also analyzed as suspensions using fluorescence-XANES imaging. All standards were prepared to a final Ce concentration of 20 mg/L. Further details about the preparation and imaging of these standards are provided in **Appendix A**.

These XANES spectra and that of Ce(III) acetate, which was used as the model compound for Ce(III), are presented in **Appendix A (Figure A.1)**. The large peak at 5727 eV is a characteristic peak of the Ce(III) oxidation state; the two peaks at 5730 and 5737 eV are characteristic of Ce(IV). These spectral differences are an important criterion for distinguishing Ce compounds of the two different oxidation states.

μ -XRF spectra were analyzed using GeoPIXE.¹² For the fluorescence-XANES stacks, the GeoPIXE “energy association” module was used to compare the ‘concentration’ ratios between two energies: 5,727 and 5,737 eV, which are the white lines for Ce(III) and Ce(IV) respectively. Because pixels were generally parallel to the 1:1 line, particularly at the highest Ce concentrations, selected pixel populations represented absolute changes in Ce(III) and Ce(IV) concentration. (See **Figures A.3, A.5-A.6** in **Appendix A** for more details). From the selected pixel populations, XANES spectra were extracted, background subtracted, and normalized using SIXPack (Version 1.4).¹³ Linear combination fitting (LCF) was performed using the collected CeO₂ NP standards above and a Ce(III) acetate spectrum from Auffan et al.¹⁴ Because the exact oxidation state of CeO₂ NPs is difficult to characterize,¹⁵ the starting materials were assumed to be all Ce(IV) oxidation state.

2.3 RESULTS AND DISCUSSION

2.3.1. CHARACTERIZATION OF CeO₂ NPs: NPs have been previously characterized by TEM, FTIR and XRD by Collin et al.⁷ TEM indicated the CeO₂ core of the particles was ~4 nm. Additional characterization of the particles at 20 mg/L as Ce in the nutrient solution was performed as follows. The number weighted average hydrodynamic diameter of the particles in the exposure medium were 12.0 ± 3.4 , 19.4 ± 5.7 , and 14.5 ± 3.3 nm, for the CeO₂(+), CeO₂(0), and CeO₂(-)

particles, respectively. The electrophoretic mobility of the particles in the nutrient solution were 1.15 ± 0.30 , -0.02 ± 0.21 , and $-1.59 \pm 0.41 \mu\text{m}\cdot\text{cm}\cdot\text{V}^{-1}\cdot\text{s}^{-1}$ for the $\text{CeO}_2(+)$, $\text{CeO}_2(0)$, and $\text{CeO}_2(-)$ particles respectively. At pH of 5.6 and an ionic strength of 5.2 mM, this corresponds to an apparent zeta potential of $+22.0 \pm 6.1$ mV, -0.5 ± 3.9 mV, and -30.3 ± 6.6 mV, for the $\text{CeO}_2(+)$, $\text{CeO}_2(0)$, and $\text{CeO}_2(-)$ particles respectively. The particles were stable in the exposure medium; less than 0.1 % dissolution was observed over 34 hours (**Appendix A, Table A.1**); organic acid root exudates induced a small shift in the measured hydrodynamic diameter for all three particle types, but no significant difference in the aggregation behavior for the three particle types was observed (**Appendix A, Figure A.2**).

2.3.2. TOTAL CE ASSOCIATION/UPTAKE IN ROOTS AND SHOOTS: The surface charge of the CeO_2 NPs had a substantial impact on the accumulation and translocation of Ce. The Ce concentrations associated with the wheat roots and shoots from the three different treatments are shown in **Figure 2.1**. These values include all Ce that was associated with the plant roots (internal and external) after collection and rinsing in NP-free Hoagland's medium. As exposure time increased, total Ce uptake increased for all NP types in both the roots and shoots. The majority of the plant-associated Ce was sorbed on/in the roots rather than in the shoots, irrespective of the charge of the NPs (note the 1000-fold higher concentrations in the roots compared to the shoots in **Figure 2.1**). Du et al.¹⁶ and Rico et al.¹⁷ observed significantly less uptake of CeO_2 NPs in their soil exposures with wheat, which is a common difference between hydroponic and soil exposures.¹⁸ Unlike this study, Schwabe et al. observed no translocation of CeO_2 NPs in hydroponic wheat,¹⁹ though this is likely attributed to NP size differences. Numerous studies have demonstrated that smaller NPs are more likely to be internalized by plants than larger ones.^{20,21} The smallest CeO_2 NPs used by Schwabe

et al. were 9 nm by TEM, which is more than twice the diameter of the particles used in this study. Thus the observed differences are attributed to a NP size effect.

With regards to surface charge, there was an overall greater mass of the positively charged NPs associated with the roots than the neutral or negatively charged NPs, which is consistent with other studies comparing the impact of surface charge on NP uptake by plants.^{1,2,22,23} This difference in association between the differently charged particles is likely due to electrostatic interactions between the charged particles and the root surface. It is well established that plant cell walls, including epidermal cells on the root surface, are negatively charged because of the abundance of polysaccharides containing galacturonic acid residues.^{24,25} Thus, CeO₂(+) NPs accumulated on the root surface due to electrostatic attraction between the positively charged NP and the negatively charged root surface, while CeO₂(-) NPs accumulated the least due to electrostatic repulsions. The uncharged particles had an intermediate degree of interaction (possibly limited by steric impediment). While the negatively charged and neutral particles had the lowest accumulation in/on the roots, these NPs were still able to overcome this electrostatic and/or electrosteric repulsion by forming strong hydrogen or covalent bonds with the root surface, through polyvalent cation bridging, or by diffusing into the mucilage.²⁶ This distribution was confirmed with Ce maps on the wheat plant roots (**Figure 2.2**). Sufficient Ce was present on the roots exposed to negative and neutral NPs for 1 h to allow elemental mapping; the neutral particles showed some regions of concentrated Ce, likely from particle adhesion (**Figure 2.2**). Overall, the leaves contained less than 1% of the total plant associated Ce, indicating that very little of the adhered Ce was translocated from the roots to the shoots. While there was no statistically significant difference in Ce accumulation in the leaves for each treatment after 8 h, by 34 h the CeO₂(-) and CeO₂(0) NP exposed plants had accumulated significantly more Ce in the leaves than the CeO₂(+) NP exposed

plants. This is particularly noteworthy since both had accumulated significantly less Ce on/in the roots than the CeO₂(+) NP exposed plants.

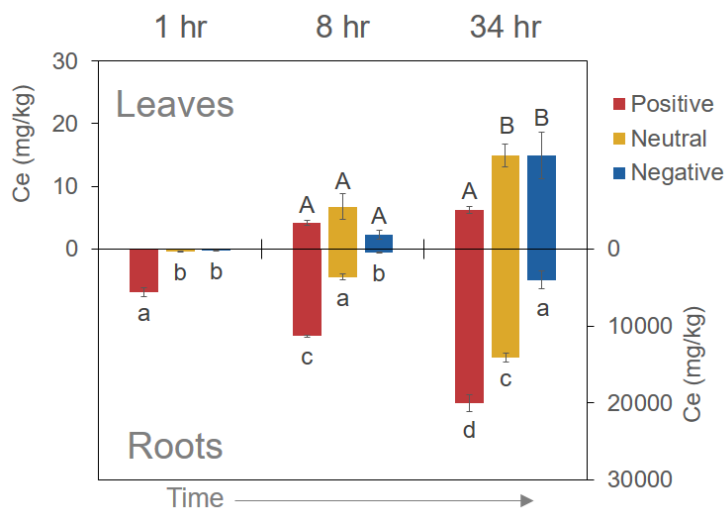


Figure 2.1. Total Ce concentrations in dried wheat plant roots (bottom) and leaves (top) after 1 h, 8 h, and 34 h. Note different scales for the roots and leaves. Total Ce uptake in the leaves after 1 h of exposure was not measured. Significant differences (based on ANOVA and Tukey HSD post hoc tests ($p < 0.05$)) are indicated by different letters with leaves indicated by uppercase letters and roots by lowercase letters.

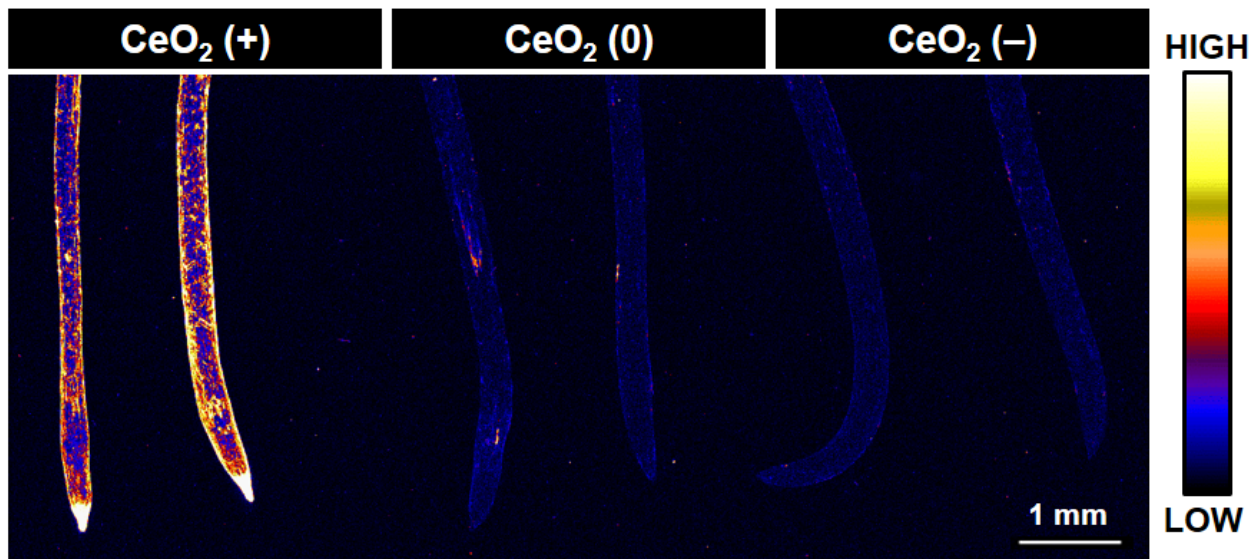


Figure 2.2. Elemental map showing total Ce distribution in wheat roots exposed hydroponically to 20 mg-Ce/L positive (+), neutral (0), or negative (-) coated CeO₂ NPs for 1 h in continuously aerated ¼ strength Hoagland's medium (pH=5.6). There are two replicate roots per treatment. Brighter colors correspond to higher Ce concentrations (see color scale at right). Later time points accumulated more Ce for all three particle types as shown below, and consistent with the measured mass (Figure 2.1).

2.3.3. CE DISTRIBUTION AND SPECIATION IN ROOTS AFTER 8 H OF EXPOSURE: The μ -XRF image of the roots after 8 h of exposure are shown in **Figure 2.3 A**. Overall the roots follow the same observed trends with regards to surface charge and total Ce uptake as observed with the ICP-MS concentrations in **Figure 2.1**. The highest concentration was observed at the tips of the $\text{CeO}_2(+)$ exposed roots. There are numerous hot spots with high Ce concentration for the $\text{CeO}_2(0)$ and $\text{CeO}_2(-)$ exposed roots. The majority of the Ce in these roots is still in the Ce(IV) oxidation state (red region, **Figure 2.3 B, C**), particularly on the $\text{CeO}_2(+)$ exposed root, however, $\sim 14\%$ of the Ce has been reduced to Ce(III) (yellow region, **Figure 2.3 B, C**). Noticeably the hotspots observed on the $\text{CeO}_2(0)$ and $\text{CeO}_2(-)$ plants remain untransformed. The hotspots are regions containing the original CeO_2 NPs, and the resulting Ce speciation is consistent with the presence of intact particles.

The second root from the right in **Figure 2.3 A**, which was exposed to $\text{CeO}_2(-)$, clearly shows Ce uptake ~ 4 mm from the tip. This significant uptake of Ce is likely due to cell rupture from selecting a damaged root rather than from natural root uptake. Looking at the potassium elemental map for these roots, which is shown in the supporting information (**Appendix A, Figure A.4**), there is noticeable potassium electrolyte leakage around these high Ce areas, which is a general indicator of cell rupture/damage.²⁷ Given that the other plant root exposed to $\text{CeO}_2(-)$ NP did not show this potassium leakage, the amount of Ce uptake is inconsistent with the ICP-MS results from **Figure 2.1**, and the distribution of Ce is so unusual, this root was likely damaged prior NP exposure, exposing internal tissue to which the Ce adhered very strongly. Similar NP uptake as a result of wounding, e.g. cut edges of plants, has previously been reported for quantum dots in ryegrass and onion²⁸ and in maize,²⁹ suggesting that damaged roots may be an entry point for NPs.

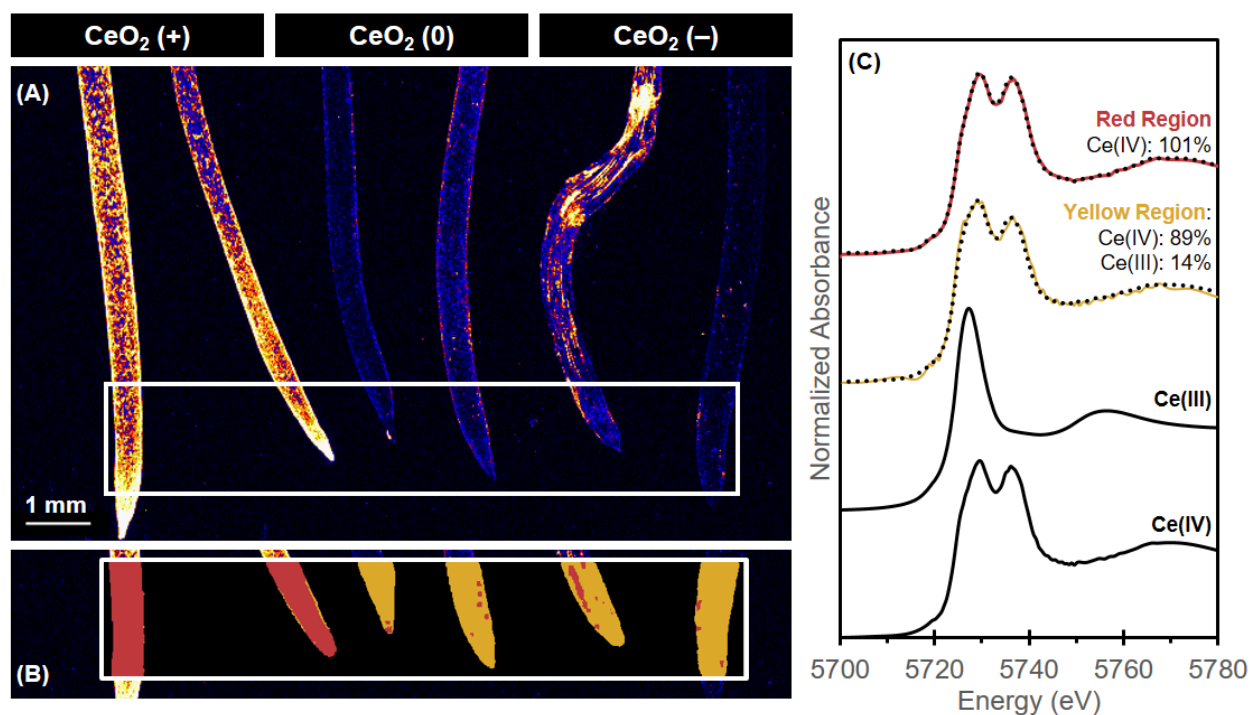


Figure 2.3. Wheat roots exposed hydroponically to 20 mg-Ce/L positive (+), neutral (0), or negative (-) coated CeO₂ NPs for 8 h in continuously aerated ¼ strength Hoagland’s medium (pH=5.6). There are two replicate roots per treatment. **(A)** Elemental survey map showing total Ce distribution, with the white box indicating the area examined by XANES imaging. Brighter colors correspond to higher Ce concentrations. **(B)** The spatial distribution of two pixel populations identified (red and yellow). **(C)** Normalized Ce L_{III} XANES spectra corresponding to the two pixel populations (red and yellow) plus the spectra for the reference compounds. The black dotted lines are fitted data while the solid lines are experimental data (see **Figure A.3** for further details on these fits).

2.3.4. CE DISTRIBUTION AND SPECIATION IN ROOTS AFTER 34 H OF EXPOSURE: The μ -XRF image of the roots after 34 h of exposure is shown in **Figure 2.4**. After 34 h of exposure, all roots showed an increased uptake of Ce and continued to follow the same observed trends with regards to surface charge and total Ce uptake with the ICP-MS concentrations in **Figure 2.1**. The roots exposed to CeO₂(0) have noticeably more Ce hot spots than at the 8 h exposure time point (**Figure 2.3 A**). Most of the Ce remains in the Ce(IV) oxidation state (red region), but ~15% of the Ce has been reduced to Ce(III) (yellow region). The projected volumetric Ce concentrations in the root cross-sections (**Appendix A, Figure A.6**) show higher projected Ce concentrations in the outer layers of the root than the inner layers, suggesting most of the Ce is adhered to the outside of the

root.³⁰ One hypothesis is that the plant roots are taking up the CeO₂ NPs, after which the NPs undergo reductive dissolution intracellularly to Ce(III). Particulate CePO₄ formation has been observed in the intracellular spaces via TEM of cucumber exposed hydroponically to CeO₂ NPs.³¹ Similar intracellular dissolution has also been observed in rat liver tissue lysosomes³² and in human HeLa cells.³³ This hypothesis that internalization is required for reduction is corroborated by the fact that no reduction was observed on the CeO₂(+) exposed roots where majority of the particles likely remained adhered to the outer root surface, while more Ce reduction was observed in the CeO₂(0) and CeO₂(-) exposed roots where more particles were likely internalized to a greater degree.

However, the observed reduction occurring at the root surface cannot be excluded. Plants alter the local pH at the root surface through the release of organic acids such as malate and citrate that can solubilize metal oxides.³⁴ It has been proposed that CeO₂ NPs are first reduced then released as Ce(III) with the assistance of reducing substances and organic acids, and then Ce(III) is precipitated with phosphates.^{31,35-37} Though the particles are stable in solution and do not readily dissolve (see **Appendix A, Table A.1**), CeO₂ NP dissolution has been observed in 20% Hoagland's solution below pH of 4.6 and in the presence of strong chelating agents at pH 8,³⁸ and studies have confirmed both CeO₂ NP and Ce(III) ion uptake in hydroponic exposures by radish³⁷ and sunflower, wheat, and pumpkin.¹⁹ The lack of reduction in the root exposed to CeO₂(+) could be attributed to the significant amount of Ce that has adhered to the root as CeO₂ therefore masking any Ce(III) signal; hence particle dissolution may also be occurring at these root interfaces that is simply not observed by this technique. This hypothesis is corroborated by the fact that local high accumulations of Ce in the (-) and (0) treatments, probably due to localized NP adsorption, correspond to areas with a prevalent Ce(IV) signal. Regardless, the speciation of Ce in the roots indicate

that some fraction of the CeO₂ NPs is becoming available as a reduced Ce(III) species, either as a free ion or located on the surface of the NPs, that can translocate to the leaves.

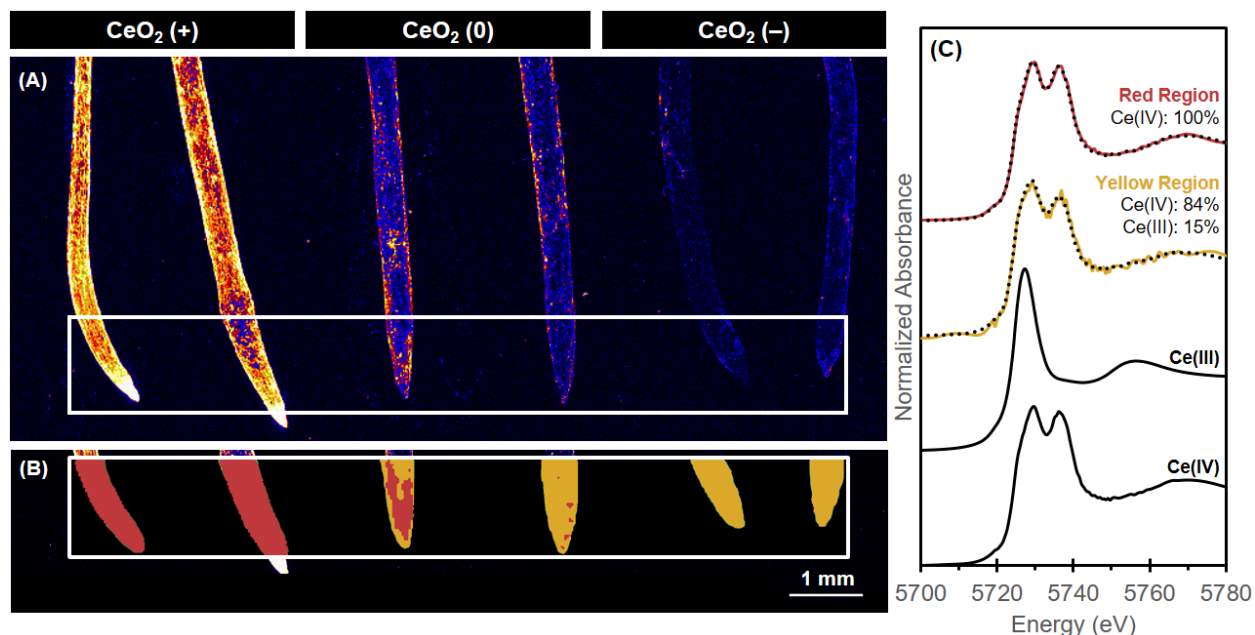


Figure 2.4. Wheat roots exposed hydroponically to 20 mg-Ce/L positive (+), neutral (0), or negative (-) coated CeO₂NPs for 34 h in continuously aerated ¼ strength Hoagland’s medium (pH=5.6). There are two replicate roots per treatment. (A) Elemental survey map showing total Ce distribution, with the white box indicating the area examined by XANES imaging. Brighter colors correspond to higher Ce concentrations. (B) The spatial distribution of two pixel populations identified (red and yellow). (C) Normalized Ce L_{III} XANES spectra corresponding to the two pixel populations (red and yellow) plus the spectra for the reference compounds. The black dotted lines are fitted data while the solid lines are experimental data (see **Figure A.5** for further details on these fits).

2.3.5. CE DISTRIBUTION AND SPECIATION IN LEAVES AFTER 34 H OF EXPOSURE: The μ -XRF image of the leaves after 34 h of exposure is shown in **Figure 2.5 A, B**. In comparison to the roots, very little Ce is present in the leaves. Ce can be seen as small discrete clusters in the CeO₂(0) leaf and at the tips of the CeO₂(-) leaf. The Ce clusters on the leaf exposed to neutral CeO₂(0) NPs are enlarged in **Figure 2.5 C, D**. There is a high association between Ce and calcium (**Figure 2.5 D**). This accumulation of calcium is hypothesized to be a plant response to reactive oxygen species (ROS) generated by the CeO₂ NPs. Zhao et al. irradiated wheat leaves to induce photo-oxidative

damage and observed that the oxidative stress and lipid peroxidation damage was reduced when the leaves were pretreated with calcium ion.³⁹ Larkindale et al. also corroborates this through their studies with *Arabidopsis* and observed that calcium channel blockers increased the effects of heat-induced oxidative damage.⁴⁰ However, the importance of this calcium response in the ability of CeO₂ and other types of NPs to promote plant health remains to be explored. There is also no visible Ce located within the xylem, as indicated by the absence of Ce signal in the leaf vasculature (**Figure 2.5 D**, areas of high zinc concentration in the leaves). Similarly, Zhang et al. demonstrated root to shoot translocation of uncoated CeO₂ NPs in hydroponically grown cucumber using radioactive isotopic tracer and detected ¹⁴¹Ce only in the non-vascular leaf tissue.²⁰

Numerous papers have also observed a variety of NP types, including CeO₂, in the intercellular space, cell walls, and xylem of plant tissue, which is evidence of apoplastic transport.^{26,41,42} From the xylem, NPs can easily translocate from the roots to shoots and distribute within the rest of the plant. One possible explanation for the absence of Ce in the xylem is that the CeO₂(0) NPs were translocated from the roots to the shoots through the xylem, but then once in the leaves became trapped and aggregated. Given that the spot size in this μ -XRF scan is 4 μm^2 , it is possible there are smaller particles that have accumulated in the leaf tissue that simply cannot be observed via this technique.

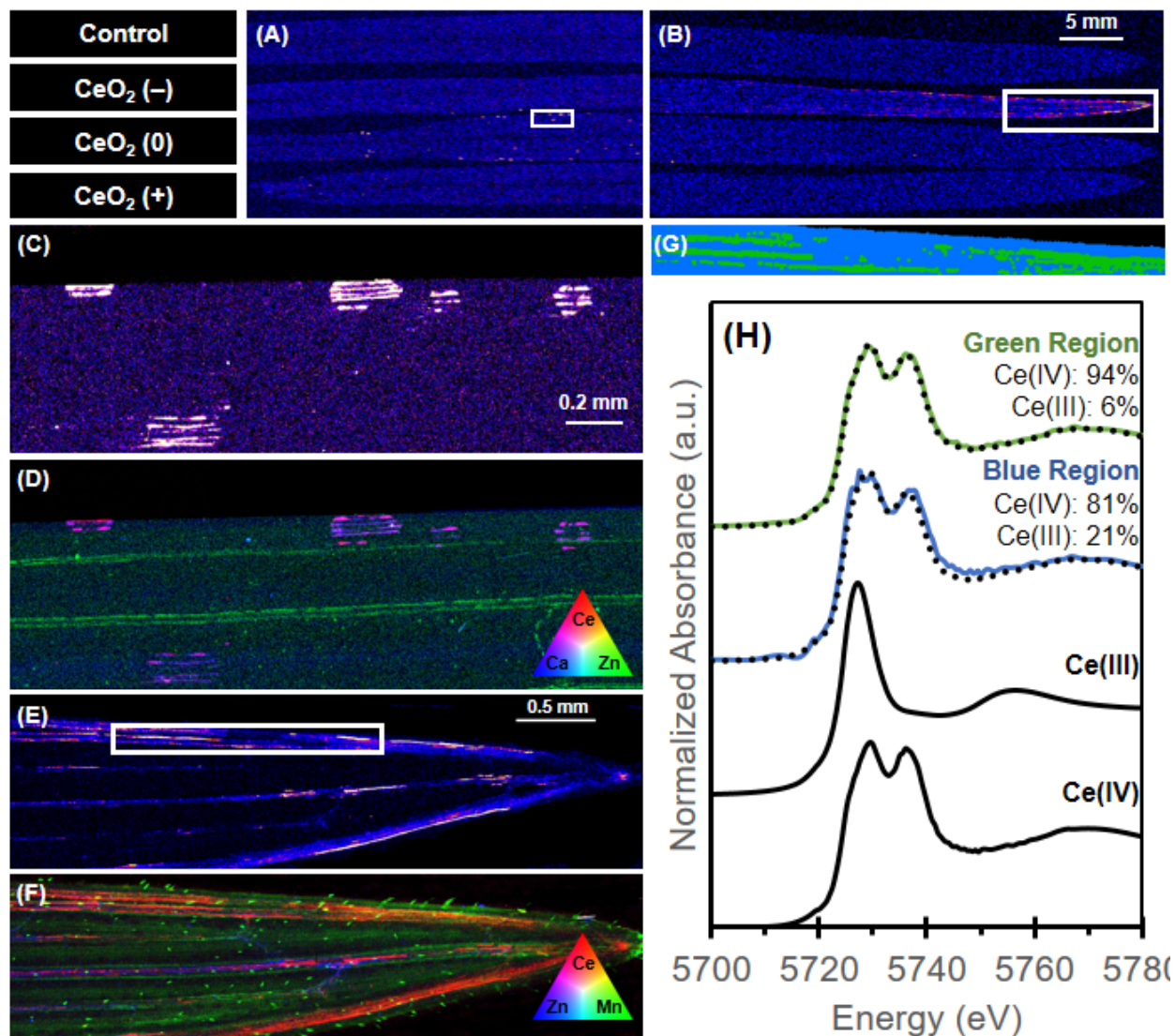


Figure 2.5. Wheat leaves exposed hydroponically to 20 mg-Ce/L positive (+), neutral (0), or negative (-) coated CeO₂NPs for 34 h in continuously aerated ¼ strength Hoagland’s medium (pH=5.6). Elemental survey map showing total Ce distribution in the (A) tips and (B) bases of leaves, which were imaged separately due to the size of the sample mount. White boxes indicates the area examined by HR-XRF. (C-D) HR-XRF on the leaf exposed to CeO₂(0) showing (C) total Ce distribution and (D) tri-colored elemental map (red= Ce, green= Zn, blue= Ca). (E-F) HR-XRF on the leaf exposed to CeO₂(-) showing (E) total Ce distribution and (F) tri-colored elemental map (red=Ce, green= Mn, blue= Zn), with the white box in (E) examined by XANES. (G) The spatial distribution of the two pixel populations identified (green and blue). (H) Normalized Ce L_{III} XANES spectra corresponding to the two pixel populations (green and blue) plus the spectra for the reference compounds. The black dotted lines are fitted data while the solid lines are experimental data (see Figure A.7 for further details on these fits).

In contrast to the neutral particles, the negatively charged NPs appeared to remain in the xylem of the leaves. The tip of the leaf exposed to $\text{CeO}_2(-)$ NPs was imaged at higher resolution and is displayed in **Figure 2.5 E,F**. Ce is not uniformly distributed throughout the leaf, but rather is located primarily in the veins of the leaf, as confirmed in **Figure A.8 (Appendix A)** by the association between Ce and zinc, which is found in higher concentrations in the xylem of plant leaves. This observation is consistent with that of Du et al. who observed Ce in the leaf veins of CeO_2 NP exposed wheat via SEM-EDX of leaf cross-sections¹⁶ and Ma et al. who observed Ce particles in the xylem sap of hydroponically exposed cucumber via TEM-EDS.⁴³ The difference in distribution between the $\text{CeO}_2(0)$ and $\text{CeO}_2(-)$ suggests that the negatively charged NPs were transported from the roots through the main vasculature of the plant into the leaves and do not as readily undergo transport or migration out of the main vasculature like the neutral CeO_2 NPs. Additionally, unlike the leaf exposed to the neutral particles, there is no association between Ce and calcium (see **Appendix A, Figure A.9**). The majority of the Ce in the veins is present as Ce(IV) (**Figure 2.5 G, H**). The remainder of the leaf tissue, with lower total Ce loads, shows significantly more bioreduction, with ~21% reduced to Ce(III). This suggests that either Ce(III) is more mobile through the plant tissue and is able to move more easily from the apoplast to the symplast than Ce(IV), or that Ce(IV) reduction primarily occurs outside of the apoplast.

2.4 ENVIRONMENTAL IMPLICATIONS

In this research, impact of surface charge on CeO_2 NP uptake and distribution was investigated in wheat plants. Results showed that $\text{CeO}_2(+)$ adhered significantly more to the roots than the $\text{CeO}_2(0)$ or $\text{CeO}_2(-)$, which is likely due to electrostatic interactions between the negatively charged root surface and the charged particles. Despite accumulating significantly less Ce on the

roots, the CeO₂(0) and CeO₂(-) exposed plants accumulated twice as much Ce in the leaves than did the CeO₂(+). Ce reduction was observed in the roots, suggesting that some Ce is taken up by the plant due to reductive dissolution.

This work also suggests there are different translocation mechanisms for differently charged particles within the plant tissue. Though the plants exposed to CeO₂(-) and CeO₂(0) accumulated the same total amount of Ce in the leaves, the overall Ce distribution was very different. The majority of the Ce in the CeO₂(-) exposed plant was found in the veins of the leaf tip, suggesting apoplastic transport through the main xylem of the plant tissue. Most of the Ce in the veins remained untransformed in the original Ce(IV) oxidation state, but the Ce outside the veins was ~20% reduced. In the CeO₂(0) exposed plants, Ce remained in clusters, co-localized with calcium, outside of the main leaf vasculature.

Overall, the present study suggests that NP surface charge plays an important role in the uptake, translocation and distribution in wheat plants. This study also suggests that NP surface charge can be used to control not only how rapidly NPs are taken up by plants, but also where the NPs end up within the plant tissues, though this has yet to be demonstrated in real soils. This knowledge of surface charge could be applied to other types of nanoparticles as part of smart delivery systems for targeted delivery of nutrients to specific plant organs.

2.5 REFERENCES FOR CHAPTER 2

- (1) Zhu, Z.-J.; Wang, H.; Yan, B.; Zheng, H.; Jiang, Y.; Miranda, O. R.; Rotello, V. M.; Xing, B.; Vachet, R. W. Effect of Surface Charge on the Uptake and Distribution of Gold Nanoparticles in Four Plant Species. *Environ. Sci. Technol.* **2012**, *46* (22), 12391–12398.
- (2) Li, H.; Ye, X.; Guo, X.; Geng, Z.; Wang, G. Effects of Surface Ligands on the Uptake and Transport of Gold Nanoparticles in Rice and Tomato. *J. Hazard. Mater.* **2016**, *314*, 188–196.
- (3) Li, J.; Tappero, R. V.; Acerbo, A. S.; Yan, H.; Chu, Y.; Lowry, G. V.; Unrine, J. M. Effect

- of CeO₂ Nanomaterial Surface Functional Groups on Tissue and Subcellular Distribution of Ce in Tomato (*Solanum lycopersicum*). *Environ. Sci. Nano* **2018**, *6*, 273–285.
- (4) Rico, C. M.; Johnson, M. G.; Marcus, M. A.; Andersen, C. P. Shifts in N and $\delta^{15}\text{N}$ in Wheat and Barley Exposed to Cerium Oxide Nanoparticles. *NanoImpact* **2018**, *11* (June), 156–163.
- (5) Hernandez-Viezcas, J. A.; Castillo-Michel, H.; Andrews, J. C.; Cotte, M.; Rico, C. M.; Peralta-Videa, J. R.; Ge, Y.; Priester, J. H.; Holden, P. A.; Gardea-Torresdey, J. L. *In Situ* Synchrotron X-Ray Fluorescence Mapping and Speciation of CeO₂ and ZnO Nanoparticles in Soil Cultivated Soybean (*Glycine max*). *ACS Nano* **2013**, *7* (2), 1415–1423.
- (6) Albanese, A.; Tang, P. S.; Chan, W. C. W. The Effect of Nanoparticle Size, Shape, and Surface Chemistry on Biological Systems. *Annu. Rev. Biomed. Eng* **2012**, *14*, 1–16.
- (7) Collin, B. E.; Oostveen, E. K.; Tsyusko, O. V.; Unrine, J. M. Influence of Natural Organic Matter and Surface Charge on the Toxicity and Bioaccumulation of Functionalized Ceria Nanoparticles in *Caenorhabditis elegans*. *Environ. Sci. Technol.* **2014**, *48* (2), 1280–1289.
- (8) Hoagland, D. R.; Arnon, D. I. *The Water-Culture Method for Growing Plants without Soil*; College of Agriculture, University of California: Berkeley, CA, 1950.
- (9) United States Environmental Protection Agency. Method 3050B - Acid Digestion of Sediments, Sludges, and Soils. *Method 3050B* **1996**.
- (10) Paterson, D. J.; de Jonge, M. D.; Howard, D. L.; Lewis, W.; McKinlay, J.; Starritt, A.; Kusel, M.; Ryan, C. G.; Kirkham, R.; Moorhead, G. F.; et al. The X-Ray Fluorescence Microscopy Beamline at the Australian Synchrotron. In *AIP Conference Proceedings*; 2011; Vol. 1365.
- (11) Ryan, C. G.; Etschmann, B. E.; Vogt, S.; Maser, J.; Harland, C. L.; Van Achterbergh, E.; Legnini, D. Nuclear Microprobe - Synchrotron Synergy: Towards Integrated Quantitative Real-Time Elemental Imaging Using PIXE and SXRF. *Nucl. Instruments Methods Phys. Res. Sect. B Beam Interact. with Mater. Atoms* **2005**, *231* (1–4), 183–188.
- (12) Ryan, C. G.; Siddons, D. P.; Kirkham, R.; Li, Z. Y.; de Jonge, M. D.; Paterson, D. J.; Kuczewski, A.; Howard, D. L.; Dunn, P. A.; Falkenberg, G.; et al. Maia X-Ray Fluorescence Imaging: Capturing Detail in Complex Natural Samples. *J. Phys. Conf. Ser.* **2014**, *499*, 012002.
- (13) Webb, S. M. SIXPack a Graphical User Interface for XAS Analysis Using IFEFFIT. *Phys. Scr.* **2005**, *T115* (0001), 1011–1014.
- (14) Auffan, M.; Masion, A.; Labille, J.; Diot, M. A.; Liu, W.; Olivi, L.; Proux, O.; Ziarelli, F.; Chaurand, P.; Geantet, C.; et al. Long-Term Aging of a CeO₂ Based Nanocomposite Used for Wood Protection. *Environ. Pollut.* **2014**, *188*, 1–7.
- (15) Cafun, J. D.; Kvashnina, K. O.; Casals, E.; Puentes, V. F.; Glatzel, P. Absence of Ce³⁺ Sites in Chemically Active Colloidal Ceria Nanoparticles. *ACS Nano* **2013**, *7* (12), 10726–10732.
- (16) Du, W.; Gardea-Torresdey, J. L.; Ji, R.; Yin, Y.; Zhu, J.; Peralta-Videa, J. R.; Guo, H. Physiological and Biochemical Changes Imposed by CeO₂ Nanoparticles on Wheat: A

- Life Cycle Field Study. *Environ. Sci. Technol.* **2015**, *49* (19), 11884–11893.
- (17) Rico, C. M.; Lee, S. C.; Rubenecia, R.; Mukherjee, A.; Hong, J.; Peralta-Videa, J. R.; Gardea-Torresdey, J. L. Cerium Oxide Nanoparticles Impact Yield and Modify Nutritional Parameters in Wheat (*Triticum aestivum* L.). *J. Agric. Food Chem.* **2014**, *62* (40), 9669–9675.
- (18) Zuverza-Mena, N.; Martínez-Fernández, D.; Du, W.; Hernandez-Viezcas, J. A.; Bonilla-Bird, N.; López-Moreno, M. L.; Komárek, M.; Peralta-Videa, J. R.; Gardea-Torresdey, J. L. Exposure of Engineered Nanomaterials to Plants: Insights into the Physiological and Biochemical Responses-A Review. *Plant Physiol. Biochem.* **2016**, *110*, 236–264.
- (19) Schwabe, F.; Tanner, S.; Schulin, R.; Rotzetter, A.; Stark, W.; Von Quadt, A.; Nowack, B. Dissolved Cerium Contributes to Uptake of Ce in the Three Crop Plants. *Metallomics* **2015**, *7*, 466–477.
- (20) Zhang, Z.; He, X.; Zhang, H.; Ma, Y.; Zhang, P.; Ding, Y.; Zhao, Y. Uptake and Distribution of Ceria Nanoparticles in Cucumber Plants. *Metallomics* **2011**, *3* (8), 816–822.
- (21) Larue, C.; Laurette, J.; Herlin-Boime, N.; Khodja, H.; Fayard, B.; Flank, A. M.; Brisset, F.; Carrière, M. Accumulation, Translocation and Impact of TiO₂ Nanoparticles in Wheat (*Triticum aestivum* spp.): Influence of Diameter and Crystal Phase. *Sci. Total Environ.* **2012**, *431*, 197–208.
- (22) Koelmel, J.; Leland, T.; Wang, H.; Amarasiriwardena, D.; Xing, B. Investigation of Gold Nanoparticles Uptake and Their Tissue Level Distribution in Rice Plants by Laser Ablation-Inductively Coupled-Mass Spectrometry. *Environ. Pollut.* **2013**, *174*, 222–228.
- (23) Wang, J.; Yang, Y.; Zhu, H.; Braam, J.; Schnoor, J. L.; Alvarez, P. J. J. Uptake, Translocation, and Transformation of Quantum Dots with Cationic versus Anionic Coatings by *Populus deltoides* × *nigra* Cuttings. *Environ. Sci. Technol.* **2014**, *48* (12), 6754–6762.
- (24) Wehr, J. B.; Blamey, F. P. C.; Menzies, N. W. Comparison between Methods Using Copper, Lanthanum, and Colorimetry for the Determination of the Cation Exchange Capacity of Plant Cell Walls. *J. Agric. Food Chem.* **2010**, *58* (8), 4554–4559.
- (25) Meychik, N. R.; Yermakov, I. P. Ion Exchange Properties of Plant Root Cell Walls. *Plant Soil* **2001**, *234*, 181–193.
- (26) Schwab, F.; Zhai, G.; Kern, M.; Turner, A.; Schnoor, J. L.; Wiesner, M. R. Barriers, Pathways and Processes for Uptake, Translocation and Accumulation of Nanomaterials in Plants – Critical Review. *Nanotoxicology* **2015**, *10* (3), 257–278.
- (27) Pandolfini, T.; Gabrielli, R.; Comparini, C. Nickel Toxicity and Peroxidase Activity in Seedlings of *Triticum aestivum* L. *Plant, Cell Environ.* **1992**, *15* (6), 719–725.
- (28) Al-Salim, N.; Barraclough, E.; Burgess, E.; Clothier, B.; Deurer, M.; Green, S.; Malone, L.; Weir, G. Quantum Dot Transport in Soil, Plants, and Insects. *Sci. Total Environ.* **2011**, *409* (17), 3237–3248.
- (29) Hu, Y.; Li, J.; Ma, L.; Peng, Q.; Feng, W.; Zhang, L.; He, S.; Yang, F.; Huang, J.; Li, L. High Efficiency Transport of Quantum Dots into Plant Roots with the Aid of Silwet L-77.

- Plant Physiol. Biochem.* **2010**, *48* (8), 703–709.
- (30) Wang, P.; Menzies, N. W.; Lombi, E.; McKenna, B. A.; de Jonge, M. D.; Donner, E.; Blamey, F. P. C.; Ryan, C. G.; Paterson, D. J.; Howard, D. L.; James, S.A.; Kpittke, P.M. Quantitative Determination of Metal and Metalloid Spatial Distribution in Hydrated and Fresh Roots of Cowpea Using Synchrotron-Based X-Ray Fluorescence Microscopy. *Sci. Total Environ.* **2013**, *463–464*, 131–139.
- (31) Zhang, P.; Ma, Y.; Zhang, Z.; He, X.; Zhang, J.; Guo, Z.; Tai, R.; Zhao, Y.; Chai, Z. Biotransformation of Ceria Nanoparticles in Cucumber Plants. *ACS Nano* **2012**, *6* (11), 9943–9950.
- (32) Graham, U. M.; Tseng, M. T.; Jasinski, J. B.; Yokel, R. A.; Unrine, J. M.; Davis, B. H.; Dozier, A. K.; Hardas, S. S.; Sultana, R.; Grulke, E. A.; et al. In Vivo Processing of Ceria Nanoparticles inside Liver: Impact on Free-Radical Scavenging Activity and Oxidative Stress. *Chempluschem* **2014**, *79* (8), 1083–1088.
- (33) Ferraro, D.; Tredici, I. G.; Ghigna, P.; Castillo-Michel, H.; Falqui, A.; Benedetto, C. Di; Alberti, G.; Ricci, V.; Anselmi-Tamburini, U.; Sommi, P. Dependence of the Ce(III)/Ce(IV) Ratio on Intracellular Localization in Ceria Nanoparticles Internalized by Human Cells. *Nanoscale* **2017**.
- (34) Jones, D. L. Organic Acids in the Rhizosphere – a Critical Review. *Plant Soil* **1998**, *205* (1), 25–44.
- (35) Ma, Y.; Zhang, P.; Zhang, Z.; He, X.; Zhang, J.; Ding, Y.; Zhang, J.; Zheng, L.; Guo, Z.; Zhang, L.; Chai, Z.; Zhao, Y. Where Does the Transformation of Precipitated Ceria Nanoparticles in Hydroponic Plants Take Place? *Environ. Sci. Technol.* **2015**, *49* (17), 10667–10674.
- (36) Rui, Y.; Zhang, P.; Zhang, Y.; Ma, Y.; He, X.; Gui, X.; Li, Y.; Zhang, J.; Zheng, L.; Chu, S.; et al. Transformation of Ceria Nanoparticles in Cucumber Plants Is Influenced by Phosphate. *Environ. Pollut.* **2015**, *198*, 8–14.
- (37) Zhang, W.; Dan, Y.; Shi, H.; Ma, X. Elucidating the Mechanisms for Plant Uptake and In-Planta Speciation of Cerium in Radish (*Raphanus sativus* L.) Treated with Cerium Oxide Nanoparticles. *J. Environ. Chem. Eng.* **2017**, *5* (1), 572–577.
- (38) Schwabe, F.; Schulin, R.; Rupper, P.; Rotzetter, A.; Stark, W.; Nowack, B. Dissolution and Transformation of Cerium Oxide Nanoparticles in Plant Growth Media. *J. Nanoparticle Res.* **2014**, *16* (10), 2668.
- (39) Zhao, H. J.; Tan, J. F. Role of Calcium Ion in Protection against Heat and High Irradiance Stress-Induced Oxidative Damage to Photosynthesis of Wheat Leaves. *Photosynthetica* **2005**, *43* (3), 473–476.
- (40) Larkindale, J.; Knight, M. R. Protection against Heat Stress-Induced Oxidative Damage in Arabidopsis Involves Calcium, Abscisic Acid, Ethylene, and Salicylic Acid. *Plant Physiol.* **2002**, *128* (2), 682–695.
- (41) Ma, X.; Geiser-Lee, J.; Deng, Y.; Kolmakov, A. Interactions between Engineered Nanoparticles (ENPs) and Plants : Phytotoxicity , Uptake and Accumulation. *Sci. Total Environ.* **2010**, *481* (1), 635.

- (42) Zhao, L.; Peralta-Videa, J. R.; Varela-Ramirez, A.; Castillo-Michel, H.; Li, C.; Zhang, J.-Y.; Aguilera, R. J.; Keller, A. A.; Gardea-Torresdey, J. L. Effect of Surface Coating and Organic Matter on the Uptake of CeO₂ NPs by Corn Plants Grown in Soil: Insight into the Uptake Mechanism. *J. Hazard. Mater.* **2012**, 225–226, 131–138.
- (43) Ma, Y.; He, X.; Zhang, P.; Zhang, Z.; Ding, Y.; Zhang, J.; Wang, G.; Xie, C.; Luo, W.; Zhang, J.; et al. Xylem and Phloem Based Transport of CeO₂ Nanoparticles in Hydroponic Cucumber Plants. *Environ. Sci. Technol.* **2017**, 51 (9), 5215–5221.

CHAPTER 3: NANOPARTICLE SURFACE CHARGE INFLUENCES UPTAKE, TRANSLOCATION, AND LEAF DISTRIBUTION IN VASCULAR PLANTS WITH CONTRASTING ANATOMY

This chapter is adapted from a publication is being prepared for submission:

Spielman-Sun, E.; Avellan, A.; Bland, G.D.; Tappero, R.V.; Acerbo, A.S.; Unrine, J.M.; Giraldo, J.P.; Lowry, G. V. Nanoparticle surface charge influences uptake, translocation, and leaf distribution in vascular plants with contrasting anatomy. *Environmental Science: Nano*. **2019**, *in preparation*.

Supporting Information is provided in **Appendix B**.

ABSTRACT

Root uptake and translocation of engineered nanoparticles (NPs) by plants is dependent on both plant species and NP physicochemical properties. To evaluate the influence of NP surface charge and differences in root structure and vasculature on cerium distribution and spatial distribution within plants, two monocotyledons (corn and rice) and two dicotyledons (tomato and lettuce) were exposed hydroponically to positively-charged, negatively-charged, and neutral ~ 4 nm CeO₂ NPs. Surface-charge mediated CeO₂ NP interactions with roots for all plant species. Positively charged CeO₂ NPs associated to the roots more than the negatively charged NPs due to electrostatic attraction/repulsion to the negatively charged root surfaces, with the highest association for the tomato. The positive NPs remained primarily adhered to the roots untransformed, while the neutral and negative NPs were more efficiently translocated from the roots to shoots. This translocation efficiency was highest for the tomato and lettuce compared to corn and rice. The positive and neutral treatments resulted in the formation of Ce clusters outside of the main vasculature in the mesophyll, while the negative treatment resulted in Ce primarily in the main vasculature of the leaves. Comparing leaf vasculature, Ce was able to move much further outside of the main vasculature in the dicot plants than monocot plants, likely due to the larger airspace volume in dicot leaves compared to monocot leaves. These results provide valuable insight into the influence of plant structure and NP properties on metal uptake, transport and distribution of NPs in plants.

3.1 INTRODUCTION

Though many published studies have focused on NP uptake by plant roots, the observations made in one plant species are often difficult to generalize to other plants. Flowering plants (angiosperms) can be classified by anatomical differences into two categories: monocotyledon (monocot) and dicotyledon (dicot) (Figure 3.1). In general, monocots are more resistant to heavy metal NP uptake than dicots.¹⁻⁴ Differences in NP uptake between monocots and dicots could be due to differences in vasculature and structural features (fibrous vs taproot system) leading to different surface area interacting with the environment, greater binding capacity and transpiration⁵ in dicots, and differences in root exudation profiles,^(e.g.6-9) as well as mucilage production at the NPs-root tip interface.¹⁰ However, the importance of each of these differences has yet to be thoroughly investigated.

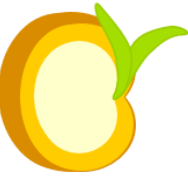
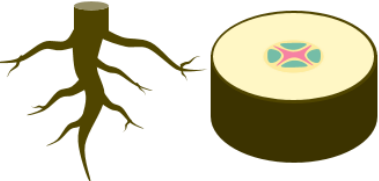
	Seed	Root	Stem	Leaf
Monocot				
	One cotyledon	Fibrous roots, vascular bundles in ring	Scattered	Parallel veins
Dicot				
	Two cotyledon	Tap root, phloem between arms of xylem	Ringed	Reticulated veins

Figure 3.1: Differences between monocot and dicot plants: (i) Seeds: the terms “monocotyledon” and “dicotyledon” directly related to the number of cotyledons (leaves) in the seed embryo; (ii) Root structure: monocots have a fibrous root system that webs off in many different directions, while dicots have a taproot from which smaller roots branch; (iii) Root cross section: vascular bundles are arranged in a ring in monocot roots, unlike dicot roots where the xylem (pink) is in the middle surrounded by the phloem (teal); (iv) Stem vascular system: vascular bundles are arranged sporadically in monocots, unlike dicots’ organized ring pattern; (v) leaf veins: veins in monocot leaves are parallel, unlike in dicots where they are branched

The goal of this study was to evaluate the observed trends in **Chapter 2** in wheat are applicable across other plant species. Using the same suite of CeO₂ NPs, two monocots (corn and rice) and two dicots (tomato and lettuce) were exposed to ~4 nm CeO₂ (+), CeO₂(0), or CeO₂(-) NPs to determine whether differences in plant anatomy and physiology influence the uptake, speciation, and spatial distribution of Ce within the plant tissue. Total Ce uptake was evaluated using ICP-MS, root reduction by Ce L_{III} XANES, and Ce distribution within leaf tissue with synchrotron X-ray fluorescence (XRF) mapping.

3.2 MATERIALS AND METHODS

3.2.1. MATERIAL CHARACTERIZATION: Cerium dioxide NPs with three different charges were synthesized as reported previously in Collin et al.¹¹ Briefly, uncharged dextran coated CeO₂ NPs (CeO₂ NP (0)) with a nominal 4 nm primary particle diameter were synthesized then further functionalized with either diethylaminoethyl groups to create a net positive charge (CeO₂ (+)) or with carboxymethyl groups to create a net negative charge (CeO₂ (-)). The particles were diluted to 50 mg/L as Ce in a basal salt solution (1 mM CaCl₂ and 5 μM H₃BO₃, pH=5.6) and probe sonicated (550 Sonic Dismembrator, Fisher Scientific) for 1 min at 10 s intervals to ensure dispersion. The hydrodynamic diameter and electrophoretic mobility of the NPs in the exposure medium at the exposure concentration (50 mg-Ce/L) were measured using a Nano Zetasizer (Malvern Instruments, Malvern).

3.2.2. PLANT GROWTH AND EXPOSURE: Crops commonly grown in the United States and easy to cultivate in lab were chosen as model plants. Corn (*Zea mays* cv. *Trinity*) and lettuce (*Lactuca sativa* cv. *Buttercrunch*) seeds were obtained from Johnny's Selected Seeds (Winslow, ME), and tomato (*Solanum lycopersicum* cv. *Roma*) from Burpee Seeds (Warminster, PA). Rice (*Oryza*

sativa cv. *Nipponbare*) were obtained from the USDA-ARS Dale Bumpers National Rice Research Center (Stuttgart, AR). Seeds were surface sterilized with commercial bleach for 10 min and then thoroughly rinsed with DI water. The sterilized seeds were germinated on deionized water-moistened filter paper in a Petri dish for 4 days for corn, 6 days for tomato and lettuce, and 7 days for rice. Germination was staggered so that all plants were transferred to hydroponic containers on the same day. Each 100-mL container was filled with 80 mL of ¼ strength Hoagland's medium and covered with a plastic lid with five holes. Five seedlings were transplanted to five of the holes with the roots suspended in a continuously aerated solution. Plants were grown in a controlled environment chamber (Binder™ Model KBWF 729; day/night photoperiod 16h/8h, day/night temperature 25 °C /21 °C and 60% humidity). Solution was renewed every 3 days with fresh ¼ strength Hoagland's medium. After 2 weeks, the plants were hydroponically exposed to 50 mg-Ce/L of CeO₂ NPs as CeO₂(+), CeO₂(0), or CeO₂(-) in a basal salt solution (1 mM CaCl₂ and 5 µM H₃BO₃, pH=5.6) and continuously aerated. Exposures were performed in this solution to reduce phosphate interference.¹² After exposure, plant roots were rinsed for 30 s in Ce-free medium to remove loosely adhered Ce. This exposure protocol was used for all subsequent measurements.

3.2.3. PLANT HEALTH MEASUREMENTS: At the end of the 48 h exposure period, photosynthetic CO₂ quantum yield (Φ_{CO_2} ; $\mu\text{mol}_{CO_2} \cdot \mu\text{mol}_{\text{photon}}^{-1}$), photosystem II quantum yield (Φ_{PSII} ; $\text{mol } e^{-} \cdot \mu\text{mol}^{-1}$), transpiration rates (E ; $\text{mol}_{H_2O} \cdot \text{m}^{-2} \cdot \text{s}^{-1}$), electron transport rates (ETR ; $\mu\text{mol}_{\text{photon}} \cdot \text{m}^{-2} \cdot \text{s}^{-1}$), and stomatal conductance (g_{sw} ; $\text{H}_2\text{O mol} \cdot \text{m}^{-2} \cdot \text{s}^{-1}$) were measured on light-adapted leaves using a LI-6800 portable gas analyzer and fluorometer (Li-COR Bio-sciences, Lincoln, NE). The leaf chamber conditions were: light intensity 600 $\mu\text{mol} \cdot \text{m}^{-2} \cdot \text{s}^{-1}$ PAR, humidity 60%, leaf temperature 25 °C, flow 500 $\mu\text{mol} \cdot \text{s}^{-1}$, and CO₂ concentration 400 $\mu\text{mol} \cdot \text{mol}^{-1}$. Measurements were made 3 h after sunrise to ensure similar stomatal aperture between samples. Leaves were left to equilibrate

for 2 min for stabilization in the Li-COR chamber before reading. Leaf PSII fluorescence was measured using a fluorometer using a flash of saturated light ($1500 \mu\text{mol}\cdot\text{m}^{-2}\cdot\text{s}^{-1}$). For plant root surface area (SA) approximations, four sets of plant roots per species were scanned using an EPSON Perfection V19 scanner. The images were processed using *ImageJ* to calculate the 2-D surface area.

3.2.4. TOTAL CE ASSOCIATION AND UPTAKE: After exposure, plants were harvested, and roots and shoots separated and lyophilized. Dried plant tissue samples were digested overnight at room temperature in concentrated HNO_3 and 30% H_2O_2 , then heated to 95°C for 30 minutes, then allowed to cool down and 30% H_2O_2 was added to obtain a 2:1 HNO_3 : H_2O_2 (v/v) ratio and heated again at 95°C for 2 h (protocol adapted from EPA Method 3050b¹³). Following digestion, the samples were diluted to 5% (v/v) HNO_3 using deionized water and filtered through a $0.45 \mu\text{m}$ filter before analysis using inductively coupled plasma mass spectrometry (ICP-MS) (Agilent 7700x, Santa Clara, CA). Blanks and standard reference material (Environmental Express, Charleston, SC) were used to validate the digestion and analytical method. The calibration curve consisted of the following concentrations: 0, 1, 10, 50, 100, 500, 1000 $\mu\text{g}/\text{kg}$. All samples either fell within the range of the calibration curve or were diluted to be within the range. Blanks were run every 10 samples. The detection limit was $0.5 \mu\text{g}/\text{kg}$. Samples were measured five times and averaged to give an output concentration with an RSD.

3.2.5. X-RAY ABSORPTION SPECTROSCOPY: After exposure, roots from two plants were lyophilized, combined, ground and homogenized, and pressed into a pellet. Cerium L_{III} X-ray absorption near edge structure (XANES) spectroscopy data were collected at the Stanford Synchrotron Radiation Lightsource (SSRL) on Beamline 11-2. Beam energy was calibrated using a Cr foil (5.989 keV). A double crystal monochromator (Si [220], crystal $\phi=90$) equipped with a

harmonic rejector was used in conjunction with a 100-element solid-state Ge detector. Measurements were collected at 77 K using a liquid N₂ cryostat. All scans were energy calibrated, deadtime corrected, and averaged using the SIXPACK software package (v1.2.10).¹⁴ Scans were then background subtracted, normalized, and fit using linear combination fitting (LCF) using ATHENA (Demeter v0.9.24).¹⁵ For the purposes of LCF, we assume that the starting materials are all Ce(IV) oxidation state.¹⁶

3.2.6. X-RAY FLUORESCENCE (XRF) IMAGING AND μ -XANES COLLECTION AND ANALYSIS:

After exposure, fresh plant leaves were placed between two pieces of 4 μ m-thick Ultralene®, which formed a seal around the plant tissue to minimize dehydration. μ -XRF maps and μ -XANES were acquired at National Synchrotron Light Source (NSLS-II) at Brookhaven National Laboratory on SRX (5-ID) for the CeO₂(0) and CeO₂(-) NP exposures and XFM (4-BM) for the CeO₂(+) NP exposures. On SRX, samples were oriented 45° to incoming beam and to a three-element Vortex-ME3 silicon-drift detector. Elemental maps with an incident energy of 14 keV were collected via fly-scanning using a step size of 4 μ m and a dwell time of 0.1 s, and spectral fitting was performed using the PyXRF spectral fitting program.¹⁷ On XFM, samples were oriented 45° to incoming beam and to a four-element Vortex-ME4 silicon-drift detector. Large area (> 1mm) elemental maps with an incident energy of 11 keV were created using a step size of 20 μ m and a dwell time of 0.2 s, and spectral fitting was performed using GSE MapViewer in Larch (v 0.9.40).¹⁸ μ -XANES were then collected at locations of interest across the Ce L_{III}-edge (5.623-5.823 keV) and data analysis was performed using ATHENA as detailed above.

3.3 RESULTS AND DISCUSSION

3.3.1. NP CHARACTERIZATION: NPs have previously been characterized by transmission electron microscopy (TEM), Fourier-transform infrared spectroscopy (FTIR), and x-ray diffraction (XRD) by Collin et al.¹¹ The primary crystallite diameters, as measured by TEM, are between 2 and 4 nm. Here, the number-weighted average hydrodynamic diameters of the particles in the exposure medium were 30.3 ± 2.8 , 22.9 ± 2.2 , and 27.9 ± 2.2 nm for the $\text{CeO}_2(+)$, $\text{CeO}_2(0)$, and $\text{CeO}_2(-)$ particles, respectively. Volume- and intensity- weighted distribution and averages are presented in **Appendix B (Figure B.1)**. The electrophoretic mobility of the particles in the nutrient solution were $+1.69 \pm 0.50$, -0.14 ± 0.50 , and $-2.48 \pm 0.60 \mu\text{m} \cdot \text{cm} \cdot \text{V}^{-1} \cdot \text{s}^{-1}$ for the $\text{CeO}_2(+)$, $\text{CeO}_2(0)$, and $\text{CeO}_2(-)$ particles, respectively. This corresponds to apparent zeta potentials using the Hückel approximation of $+32.2 \pm 9.6$ mV, -2.6 ± 8.6 mV, and -52.3 ± 12.7 mV, for the $\text{CeO}_2(+)$, $\text{CeO}_2(0)$, and $\text{CeO}_2(-)$ particles, respectively. Generally, a ζ -potential between -10 mV and $+10$ mV is considered to be relatively neutral, while absolute values greater than 10 mV are considered to be cationic ($> +10$ mV) or anionic (< -10 mV). At the end of the exposure, $<0.1\%$ of the Ce remaining in the exposure solution was dissolved (**Appendix B, Table B.1**).

3.3.2. TOTAL CE UPTAKE: The Ce concentrations associated with plant roots and shoots from the three different treatments are shown in **Figure 3.2 A**. Irrespective of plant species, $\text{CeO}_2(+)$ NPs adhered more readily to the plant roots than $\text{CeO}_2(-)$ NPs due to electrostatic attraction to the negatively charged root surface or repulsion for the negatively charged particle, which is consistent with numerous other studies comparing the impact of surface charge in plants.^{10,19–23} Across the plant species, the tomato accumulated the most Ce in/on the roots for all NP treatments, with the highest being from the $\text{CeO}_2(+)$ NP treatment ($47,300 \pm 3,100$ mg/kg). Neutral particles had an intermediate degree of interaction.

The dicots generally show more Ce in the shoots than the monocots (**Figure 3.2**). This trend is consistent with trends observed by Lopez-Moreno, et al.²⁴ between dicots (alfalfa, tomato, cucumber) and a monocot (corn) exposed hydroponically to 7 nm CeO₂ NP and by Schwabe et al.⁵ between a dicot (pumpkin) and a monocot (wheat) to 9 nm CeO₂ NPs. With regards to surface charge, corn, rice, and lettuce followed previously observed statistically significant trends,^{20,22,23} in which plants accumulated higher amounts of metal in the shoots from the negatively charged NP exposure compared to the positively charged NP exposure. The tomato plant, however, followed the opposite trend, with the highest Ce accumulation from the CeO₂(+) NP treatment and the lowest from the CeO₂(-) NP treatment. This is due to high accumulation of Ce in/on the roots from the CeO₂(+) NP exposure compared to the CeO₂(-) NP which enabled more Ce to translocate, albeit less efficiently. The speciation of Ce that is translocating is discussed later in the paper.

Translocation efficiency was also calculated as a ratio of total Ce in shoots to total Ce in/on roots to better compare the capability of different particles to move from the roots to shoots (**Figure 3.2 B**). All plants had the highest translocation efficiencies for the CeO₂(-) NP treatment and the lowest for the CeO₂(+) NP treatment, further suggesting that the positively charged particles adhere too strongly to the root surface to translocate. The CeO₂(-) NP treatment for lettuce had the largest value (24%). Regarding the high Ce leaf concentration in the CeO₂(+) NP exposure in tomato, the lower translocation efficiency for the positive treatment than the negative treatment further corroborates the hypothesis that negatively charged particles are able to more efficiently translocate than positively charged particles. The two dicots translocated Ce more efficiently than the monocots for all particle types (though the tomato neutral treatment was not statistically significantly higher). This is likely due to the high transpiration rate in the dicots compared to monocots (see **Section 3.3.3**). The trends in uptake observed here for the NPs follow the trends

observed in a field study using soil contaminated with Cd, Pb, Cu, and Zn with ten different plants. Lettuce and other leaf vegetables had higher translocation factors than tomato and other fruit vegetables, which were higher than corn and other grains.²⁵

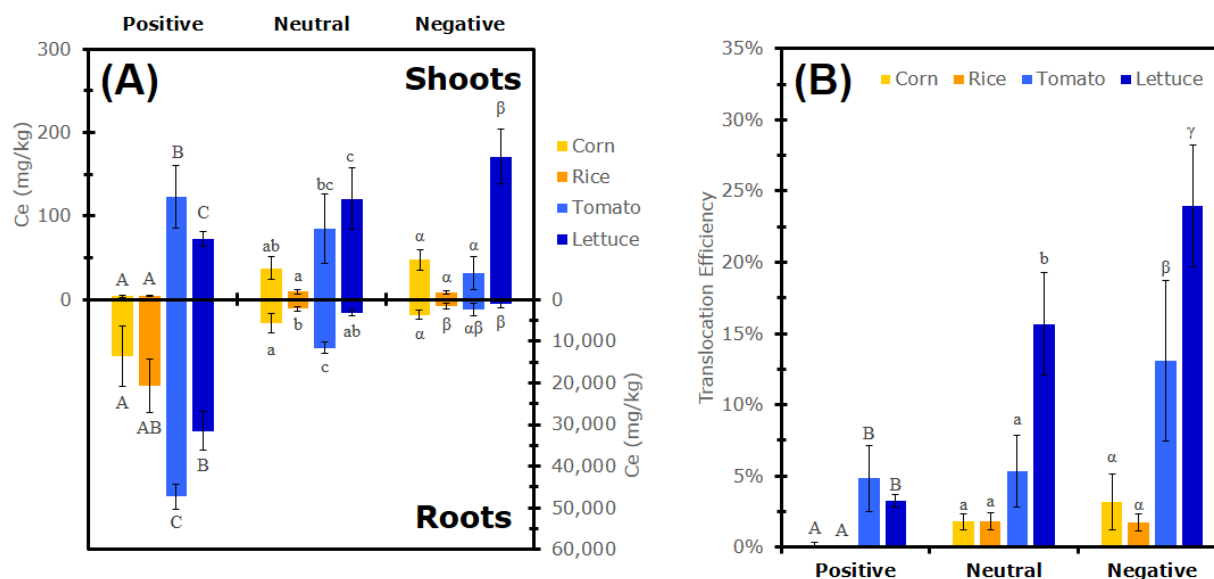


Figure 3.2. (A) Ce concentration (mg-Ce per kg of dried plant tissue) on/in dried roots (bottom) and shoots (top) and (B) translocation efficiency (%; $\text{Tot Ce}_{\text{shoots}} / \text{Tot Ce}_{\text{roots}}$) of corn (yellow), rice (orange), tomato (light blue), and lettuce (dark blue) after 48 h of hydroponic exposure to 50 mg-Ce/L as $\text{CeO}_2(+)$, $\text{CeO}_2(0)$, or $\text{CeO}_2(-)$ NPs in continuously aerated basal salt solution (pH=5.6). Roots were rinsed for 30s in Ce-free medium prior to lyophilization and analysis. The means are averaged from four replicates. Error bars correspond to standard deviation. Significant differences [based on ANOVA and Tukey HSD post hoc tests ($p < 0.05$)] between plant species for the same NP treatment for either the roots or shoots are indicated by capital letters, lower-case letters, and Greek letters for the positive, neutral, and negative treatments, respectively.

Calculated root SA for the corn, rice, tomato, and lettuce were $6.6 \pm 1.2 \text{ cm}^2$, $0.6 \pm 0.2 \text{ cm}^2$, $11.3 \pm 3.2 \text{ cm}^2$, and $1.3 \pm 1.0 \text{ cm}^2$, respectively (**Appendix B, Table B.2**). There was no correlation between root surface area and Ce root uptake/attachment for the $\text{CeO}_2(+)$ NP or $\text{CeO}_2(-)$ NP exposure (**Figure 3.3**), emphasizing the importance of this electrostatic attraction/repulsion between the charged NPs and the charged root surface. The roots of dicots generally have greater cation exchange capacities than monocots,²⁶ which likely explains the higher Ce association for the tomato and lettuce compared to the corn and rice for the $\text{CeO}_2(+)$ NP treatment. In contrast,

higher root surface area correlated with higher Ce root attachment/uptake for the CeO₂(0) NP exposure (**Figure 3.3**), suggesting primarily a sorption interaction when NPs are relatively uncharged.

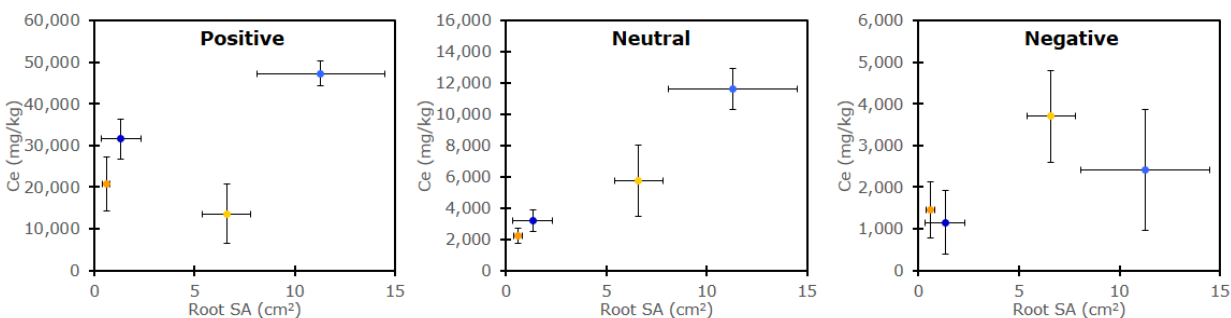


Figure 3.3. Correlation between root surface area (SA) and Ce associated with roots of corn (yellow), rice (orange), tomato (light blue), and lettuce (dark blue) after 48 h of hydroponic exposure to 50 mg-Ce/L as CeO₂(+), CeO₂(0), or CeO₂(-) NPs in continuously aerated basal salt solution (pH=5.6). Roots were rinsed for 30s in Ce-free medium prior to lyophilization and analysis. The means are averaged from four replicates. Error bars correspond to standard deviation. Raw values are reported in **Appendix B (Table B.2)**.

3.3.3. PLANT HEALTH: Physiological measurements of plant health are presented in (**Figure 3.4**).

No statistically significant changes in dry biomass were observed for exposed vs. control plants. No differences were observed for any of the plant health parameters measured for rice, likely due to low uptake into the leaves compared to the other plants. In contrast, the most significant changes to plant photosynthesis (ΦCO_2 , $\Phi PSII$, ETR) and gas exchange (E , gsw) were observed for corn with all NP treatments. Interestingly, these changes were observed in the positive NP treatment despite accumulating ~10 times less Ce in the shoots than the neutral and negative NP treatments. We hypothesize that the NPs induce changes to the root water potential, permeability, or conductivity to water. This in turn could result in a higher stomatal conductance and therefore increased CO₂ uptake and subsequently $\Phi PSII$.

For tomato, increases to ΦCO_2 , $\Phi PSII$, E , ETR , and gsw were observed for the CeO₂(0) NP treatment. Negatively charged CeO₂ NPs have been previously reported to boost photosynthesis

rates in soil-grown soybean under non-stressed conditions (soil exposure; ζ -potential= -51.57 mV)²⁷ and salt-stressed canola (hydroponic; ζ -potential= -51.8 mV)²⁸, and boost carbon assimilation rates and $\Phi PSII$ *Arabidopsis* plants exposed to salt-stress, heat, and high light (foliar infiltration; ζ -potential= -17 ± 2.7 mV).²⁹ Wu et al.³⁰ observed almost two times higher localization of negatively charged (ζ -potential= -16.9 ± 6.1 mV) than neutral/moderately-positive (ζ -potential= $+9.7 \pm 1.2$ mV) CeO₂ NPs within chloroplasts in *Arabidopsis* leaf mesophyll cells exposed via foliar infiltration. Though the observed increase in plant health was not statistically significant for the CeO₂(-) NP treatment, Ce accumulation from this exposure was almost three times lower than from the CeO₂(0) NP exposure. The reported increases in plant photosynthesis by CeO₂(-) NP were observed in stressed *Arabidopsis* plants experiencing ROS accumulation whereas in this study, plants were exposed to CeO₂ NPs under normal growing conditions. It is likely that oxidative stress levels in tomato were not high enough for CeO₂ NPs to provide a beneficial impact on plant health through ROS scavenging. In general, the dicots have higher transpiration rates, indicating higher water uptake, which could contribute to their higher Ce uptake.

Negative impacts on ΦCO_2 , E , and g_{sw} were observed for the lettuce CeO₂(+) NP exposure. Positively charged CeO₂ NPs (ζ -potential= $+32.8 \pm 1.0$ mV) have been shown to decrease ΦCO_2 and intercellular CO₂ concentration in *Clarkia unguiculata*.³¹ Considering ΦCO_2 and not $\Phi PSII$ is impacted, the NPs are likely causing the plant to divert energy for stress response mechanisms rather than the typical plant processes.³² Cationic NPs in general have been shown to be more toxic in a variety of cells compared to their neutral or anionic counterparts.^{11,16,33,34} Asati et al.³⁴ observed that CeO₂ surface charge influenced toxicity in normal and cancer mammalian cell lines: positively charged nanocerium would generally localize in lysosomes and release ROS-generating

Ce³⁺ due to an acidic microenvironment, while neutral particles localized in the cytoplasm and remained untransformed and displayed no toxicity. In this study, the highest Ce accumulation in leaves from the CeO₂(+) NP treatment was observed in tomato and lettuce, which were the only treatments that observed decreases to plant health, though this decrease was only statistically significant for the lettuce exposure. Lettuce has been shown to be more sensitive to CeO₂ NPs compared to cabbage, wheat, cucumber, radish, tomato, and rape.^{2,35}

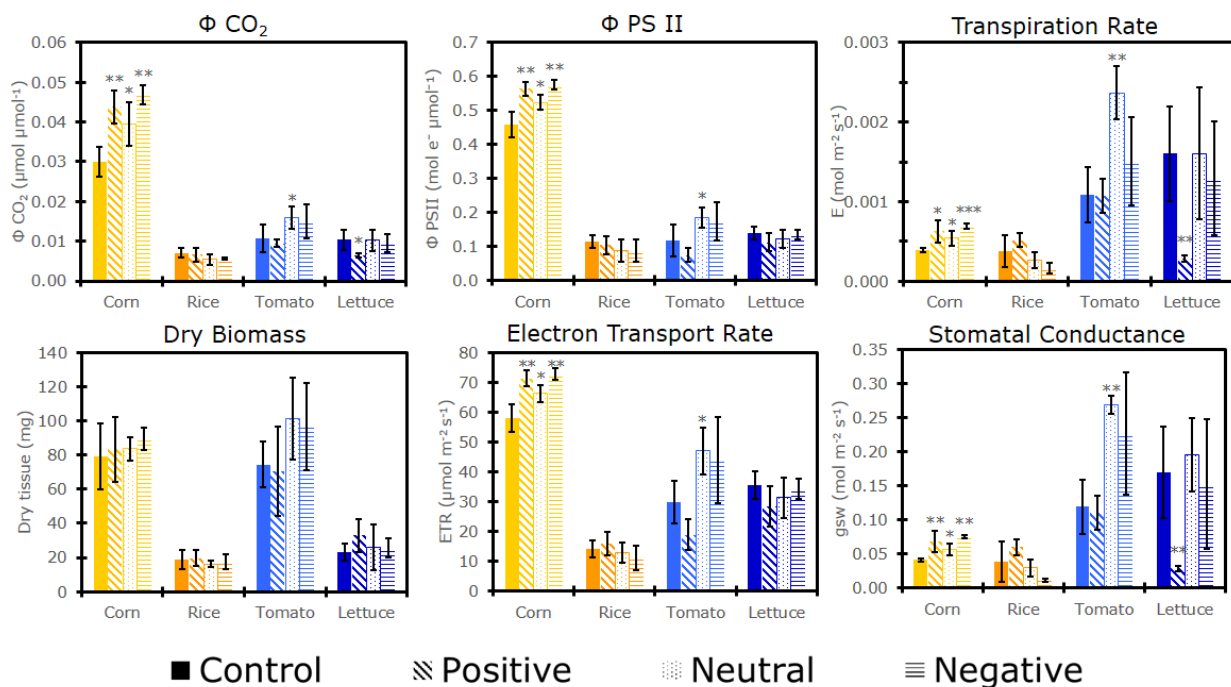


Figure 3.4. Measurements of quantum yield of CO₂ uptake (ΦCO_2) and photosystem II quantum yield ($\Phi PSII$), transpiration rates (E), dry biomass, electron transport rate (ETR), and stomatal conductance (g_{sw}) after 48 h of hydroponic exposure to 50 mg-Ce/L as CeO₂(+), CeO₂(0), or CeO₂(-) NPs in continuously aerated basal salt solution (pH=5.6). The means are averaged from four replicates. Error bars correspond to standard deviation. Asterisks indicate statistically significant differences relative to the control (2-sample *t*-test; * $p \leq 0.05$, ** $p \leq 0.01$).

3.3.4. CE REDUCTION IN ROOTS: No evidence for Ce reduction in/on roots was observed in any plant for the CeO₂(+) NP treatment, while the CeO₂(0) and CeO₂(-) NP treatments show up to ~30% reduction to Ce(III), with the most reduction observed for lettuce (**Figure 3.5**). In agreement with these results, previous XANES maps on wheat roots exposed to these same particles show no

reduction from the CeO₂(+) NP treatment and ~15% from the CeO₂(0) and CeO₂(-) NP treatments.²⁰ Furthermore, bulk XANES on hydroponically exposed cucumber (ζ -potential= -10 mV) roots have been shown to undergo some reduction to Ce(III) (<20%).³⁶⁻³⁸

The exact location of this biotransformation and the mechanisms occurring are still under debate. We hypothesize that the plant roots are taking up the CeO₂ NPs, after which the NPs undergo reductive dissolution intracellularly to Ce(III), as discussed below. The Ce(III)/Ce(IV) equilibrium mostly involves the atoms on the surface of CeO₂ NPs,^{39,40} thus we posit that the Ce(III) is not truly dissolved, but rather that Ce(IV) reduction happens at the NP surface, likely as CePO₄. HR-TEM images by Singh et al⁴¹ showed no significant changes to average crystal size of CeO₂ NPs incubated in PBS buffer for 72 h, but the XPS and UV-Vis spectra suggest the formation of amorphous Ce(III) phosphate at the particle surface. This was further corroborated by Schwabe et al.⁴² who found less released Ce when phosphate was present in the media, indicating that the Ce(III) is not released from the surface but most likely trapped by the formation of CePO₄ on the NP surface. Where majority of the particles remained adhered to the root outer surface from the CeO₂(+) NP exposure, no reduction was observed, while Ce reduction was observed in the CeO₂(0) and CeO₂(-) NP exposed roots where more particles were likely internalized to a greater degree (as suggested by translocation efficiencies in **Figure 3.2 B**).

However, reductive dissolution at the root surface cannot be entirely excluded. Though the particles are stable in solution and do not significantly dissolve (see **Appendix B, Table B.2**), CeO₂ NP dissolution has been observed in the presence of low molecular weight organic acids,^{9,42} and studies have confirmed both CeO₂ NP and Ce(III) ion uptake in hydroponic exposures by radish,⁹ and sunflower, wheat, and pumpkin.⁶ Additionally, Schwabe et al.⁴² observed greater

solution acidification for the dicot (pumpkin) compared to the monocot (wheat) exposed to CeO₂ NPs.

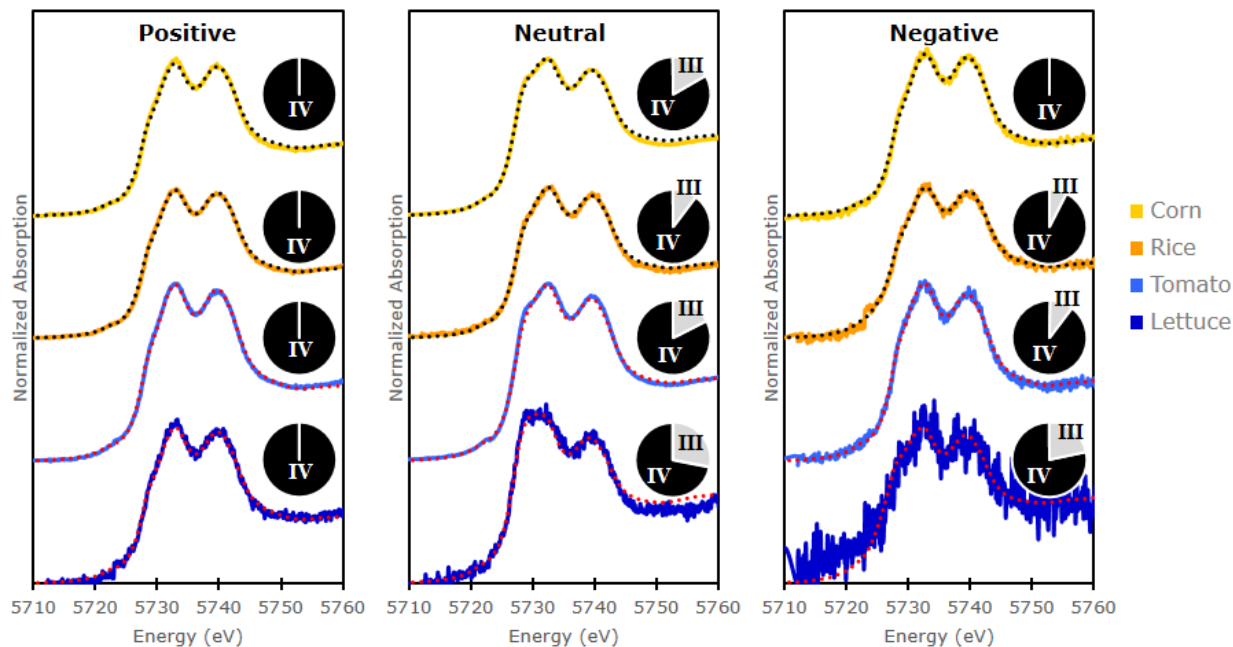


Figure 3.5. Change in Ce oxidation state, presented as pie charts, in root tissue of corn (yellow), rice (orange), tomato (light blue), and lettuce (dark blue) after 48 h of hydroponic exposure to 50 mg-Ce/L as CeO₂(+), CeO₂(0), or CeO₂(-) NPs in continuously aerated basal salt solution (pH=5.6). Roots were rinsed for 30s in Ce-free medium prior to lyophilization and analysis. Normalized Ce L_{III} XANES experimental spectra (solid) are presented with LCF fits (dotted). Fitting statistics are provided in **Appendix B (Table B.3)**.

3.3.5 CE DISTRIBUTION IN LEAVES: Both NP charge and plant vasculature affected the distribution of CeO₂ NPs in plant leaves. XFM maps of exposed monocots (corn and rice) are shown in **Figure 3.6**. For corn, the Ce from the CeO₂(-) NP exposure accumulated in parallel lines with Zn, suggesting the Ce is primarily located in the leaf veins. No Ce fluorescence signal was detected in the leaves of plants for the CeO₂(0) NP treatment. For rice, Ce fluorescence signal from the CeO₂(-) NP treatment formed clusters within the leaf veins as 30% Ce(III). The CeO₂(0) NP treatment in rice induced a non-uniform distribution of Ce; a large aggregate (100 μm x 30 μm) of Ce was detected outside the vasculature. These results are consistent with our previous results in

wheat using the same particles where the neutral treatment resulted in clusters outside of the main vasculature and the negative resulted in Ce accumulation in the veins primarily as Ce(IV) with some reduction (~20%) outside of the vasculature.²⁰

XFM maps of dicots (lettuce and tomato) are shown in **Figures 3.7** and **3.8**. Unlike the monocots, where the Ce was located in small clusters or in the vasculature, Ce is found throughout the leaf. Dicots generally have larger airspace volume than monocots,⁴³ which may have allowed the Ce to spread further out of the vasculature through the leaf. Previous XRF images of tomato exposed to the same CeO₂(-) NP particles for 14 days showed Ce accumulation within the vascular tissue in relatively large foci as ~40% Ce(III) from the CeO₂(-) NP treatment.²³ Similar accumulation in the primary and secondary veins was observed for tomato CeO₂(-) NP treatment (**Appendix B, Figure B.9**), though less reduction was observed here (13%), possibly due to the shorter exposure period. The observed clusters outside of the vasculature from the CeO₂(0) NP are similar to those observed in cucumber exposed to CeO₂ NP (ζ -potential=8.8 mV; relatively neutral), where Ce concentrations in the veins and leaf stalks were lower compared to other areas of the leaves.⁴⁴ Interestingly, similar distinct spots were observed in Arabidopsis exposed hydroponically to cationic quantum dots.⁴⁵ In contrast, both the lettuce and tomato CeO₂(+) NP exposures showed minimal Ce in the primary vasculature, instead they have Ce clusters around minor veins, suggesting the Ce migrates out of the vasculature at the end of minor veins and accumulates in the cells at this point of exit.

In the tomato CeO₂(+) NP exposure in **Figure 3.7**, there is evidence of Ce-trichome colocalization (see **Appendix B, Figure B.14** for larger images of these regions). Trichomes are involved in various secretory and uptake functions, and it has been proposed that metal NPs can be excreted through trichomes.⁴⁶ Many types of trichomes have been shown to accumulate

internalized or airborne metals as a detoxification mechanism.⁴⁶⁻⁴⁸ Tobacco exposed to cadmium accumulated cadmium in trichome tips as a Cd-substituted calcite type compound.⁴⁹⁻⁵¹ Similar accumulation of nickel have also been observed in the leaf trichomes of an *Alyssum* Ni-hyperaccumulator species.⁵² With specific regards to NPs, pumpkin trichomes have been shown to excrete NPs after C-coated nano-Fe_xO_y particles were injected in the leaf petiole, as visualized by TEM.⁵³ Similar accumulation for the same C-coated nano-Fe_xO_y particles has been observed in wheat trichomes after NP exposure to the roots.⁵⁴ Nano- TiO₂ has also been observed to be translocated from the roots of cucumber into leaf trichomes.⁵⁵ Thus, the CeO₂ NPs could have been translocated from the roots to the shoots through the vascular tissue before being sequestered in the trichomes of the leaves to be further exuded from the plant.

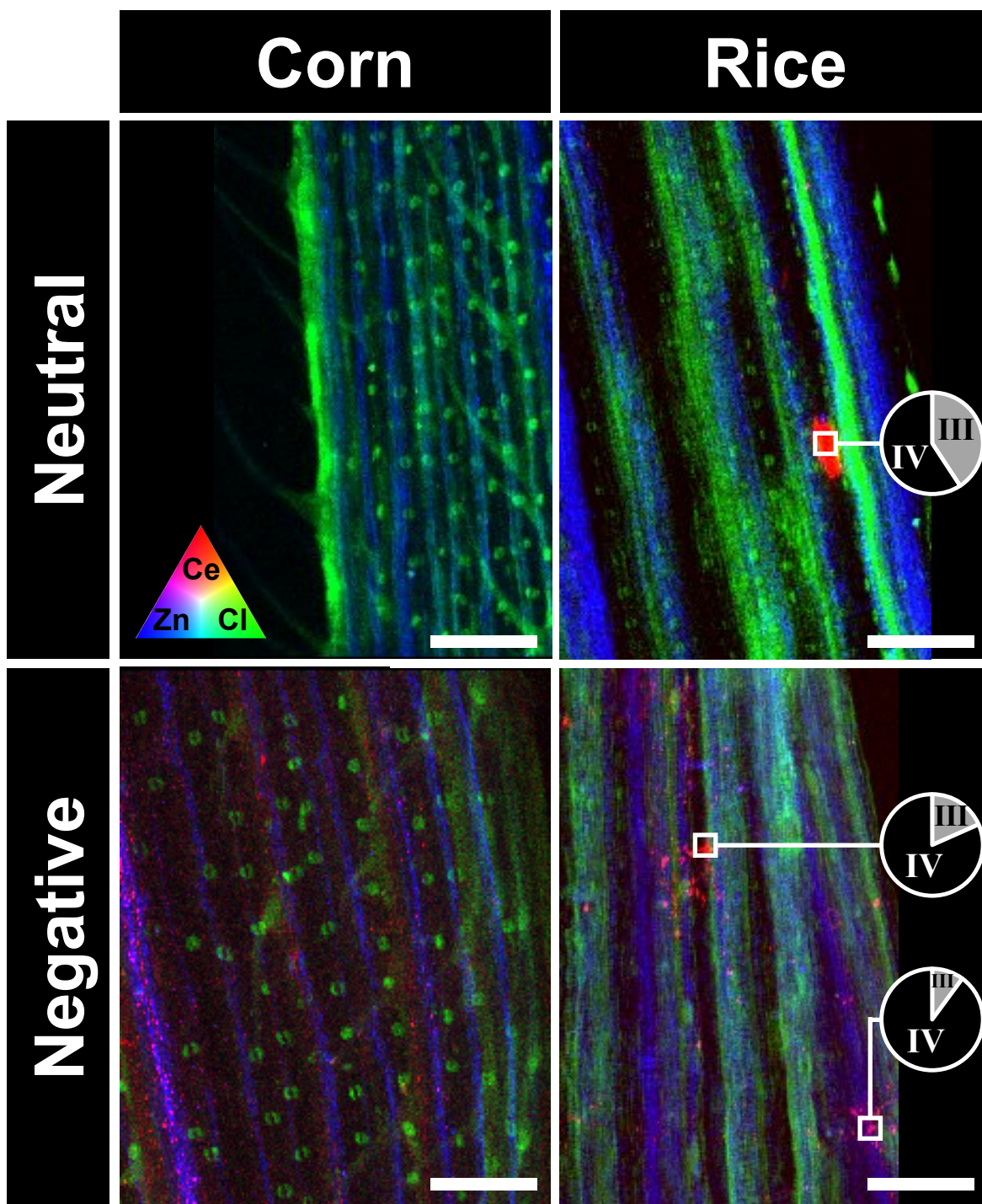


Figure 3.6. Tri-colored XRF maps of monocot leaves showing Ce (red), Zn (blue), and Cl (green) distribution in corn and rice after 48 h of hydroponic exposure to 50 mg-Ce/L as $\text{CeO}_2(0)$ or $\text{CeO}_2(-)$ NPs in continuously aerated basal salt solution (pH=5.6). Ce signal in the leaves exposed to $\text{CeO}_2(+)$ NPs was too low for imaging. White boxes indicate where μ -XANES were acquired, with the LCF results presented as a pie chart. Ce signal was too low to acquire μ -XANES for either corn exposure. XRF maps of individual elements and XANES spectra and fitting statistics are provided in **Appendix B, Figures B.2-5**. Scale bar=200 μm .

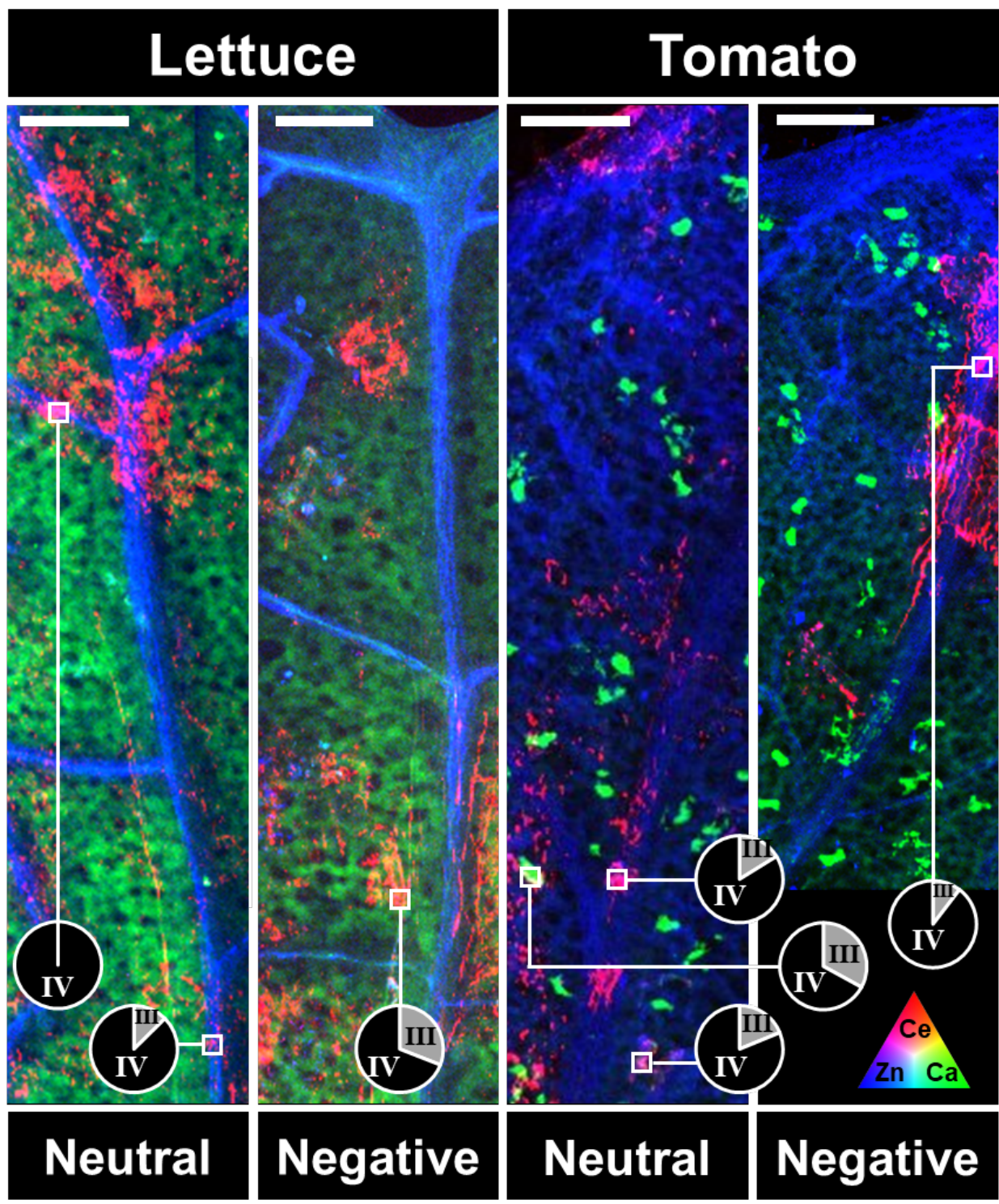


Figure 3.7. Tri-colored XRF maps of dicot leaves showing Ce (red), Zn (blue), and Ca (green) distribution in lettuce and tomato after 48 h of hydroponic exposure to 50 mg-Ce/L as CeO₂(0), or CeO₂(-) NPs in continuously aerated basal salt solution (pH=5.6). White boxes indicate where μ -XANES were acquired, with the LCF results presented as a pie chart. XRF maps of individual elements and XANES spectra and fitting statistics are provided in **Appendix B, Figures B.6-10**. Scale bar=200 μ m.

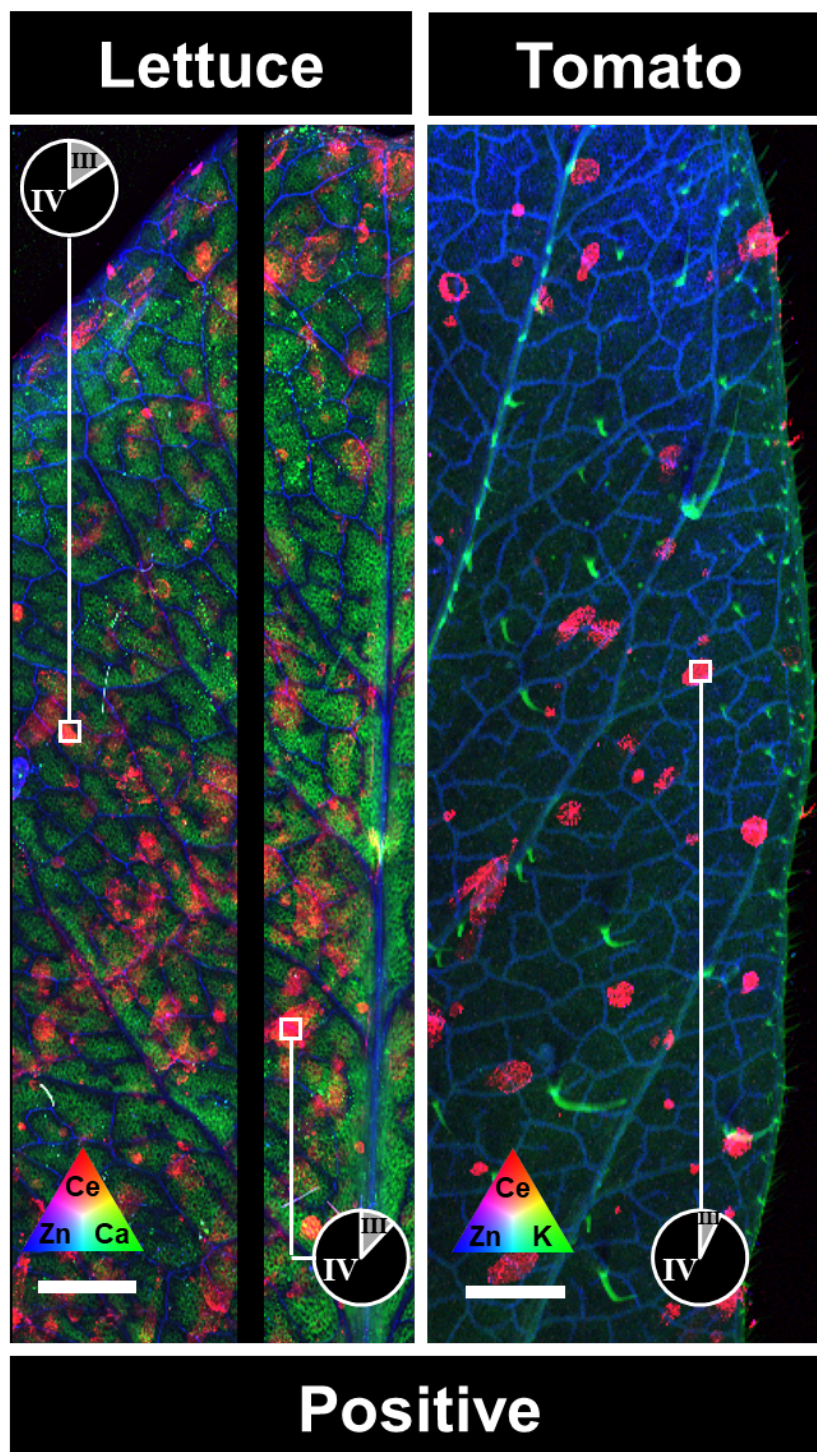


Figure 3.8. Tri-colored XRF maps of dicot leaves showing Ce (red), Zn (blue), and either Ca (green) for lettuce or K (green) for tomato distribution in lettuce and tomato after 48 h of hydroponic exposure to 50 mg-Ce/L as CeO₂(+) in continuously aerated basal salt solution (pH=5.6). White boxes indicate where μ -XANES were acquired, with the LCF results presented as a pie chart. XRF maps of individual elements and XANES spectra and fitting statistics are provided in **Appendix B, Figures B.11-13**. The lettuce map was completed as two scans. Scale bar=1 mm.

3.4 ENVIRONMENTAL IMPLICATIONS

Both surface chemistry and plant species have a significant impact on the uptake and distribution of CeO₂ NPs. Positively charged CeO₂ NPs remained primarily adhered to the negatively charged roots via electrostatics as Ce(IV), with poor Ce translocation efficiency to the shoots. In contrast, negatively charged CeO₂ NPs accumulated significantly less on the roots but had the highest translocation efficiency. Overall, tomato and lettuce were able to translocate Ce more efficiently to the shoots than rice and corn. This correlates with higher transpiration rates, and thus water uptake. Increases in plant photosynthesis were observed in corn plants exposed to CeO₂ NPs of all charges that were accompanied by enhanced stomatal aperture and therefore CO₂ uptake. Some reduction to plant photosynthesis was observed in plants under CeO₂(+) NP exposure, potentially a result of the different spatial distribution of the CeO₂(+) NPs in the leaves. Once in the leaves, CeO₂(-) remained primarily in the veins, while (0) and (+) formed clusters outside of the vasculature. Comparing leaf vasculature, Ce was able to move much further outside of the main vasculature in the dicot plants than monocot plants, likely due to the larger airspace volume in dicot leaves compared to monocot leaves. The different Ce distribution as a function of particle surface chemistry suggests that NPs may potentially be engineered for targeted, NP mediated delivery of agrochemicals to different plant organs.

3.5 REFERENCES FOR CHAPTER 3

- (1) Judy, J. D.; Unrine, J. M.; Rao, W.; Wirick, S.; Bertsch, P. M. Bioavailability of Gold Nanomaterials to Plants: Importance of Particle Size and Surface Coating. *Environ. Sci. Technol.* **2012**, *46* (15), 8467–8474.
- (2) Ma, Y.; Kuang, L.; He, X.; Bai, W.; Ding, Y.; Zhang, Z.; Zhao, Y.; Chai, Z. Effects of Rare Earth Oxide Nanoparticles on Root Elongation of Plants. *Chemosphere* **2010**, *78* (3), 273–279.
- (3) Wang, P.; Lombi, E.; Sun, S.; Scheckel, K. G.; Malysheva, A.; McKenna, B. A.; Menzies,

- N. W.; Zhao, F.-J.; Kopittke, P. M. Characterizing the Uptake, Accumulation and Toxicity of Silver Sulfide Nanoparticles in Plants. *Environ. Sci. Nano* **2017**, *4* (2), 448–460.
- (4) Sun, D.; Hussain, H. I. H. I.; Yi, Z.; Siegele, R.; Cresswell, T.; Kong, L.; Cahill, D. M. Uptake and Cellular Distribution, in Four Plant Species of Fluorescently Labeled Mesoporous Silica Nanoparticles. *Plant Cell Rep.* **2014**, *33* (8), 1389–1402.
- (5) Schwabe, F.; Schulin, R.; Limbach, L. K.; Stark, W.; Bürge, D.; Nowack, B. Influence of Two Types of Organic Matter on Interaction of CeO₂ Nanoparticles with Plants in Hydroponic Culture. *Chemosphere* **2013**, *91* (4), 512–520.
- (6) Schwabe, F.; Tanner, S.; Schulin, R.; Rotzetter, A.; Stark, W.; Von Quadt, A.; Nowack, B. Dissolved Cerium Contributes to Uptake of Ce in the Three Crop Plants. *Metallomics* **2015**, *7*, 466–477.
- (7) Zhang, W.; Ebbs, S. D.; Musante, C.; White, J. C.; Gao, C.; Ma, X. Uptake and Accumulation of Bulk and Nanosized Cerium Oxide Particles and Ionic Cerium by Radish (*Raphanus sativus* L.). *J. Agric. Food Chem.* **2015**, *63* (2), 382–390.
- (8) Rossi, L.; Zhang, W.; Schwab, A. P.; Ma, X. Uptake, Accumulation and in-Planta Distribution of Co-Existing Cerium Oxide Nanoparticles and Cadmium in *Glycine max* (L.) Merr. *Environ. Sci. Technol.* **2017**, *51* (21), 12815–12824.
- (9) Zhang, W.; Dan, Y.; Shi, H.; Ma, X. Elucidating the Mechanisms for Plant Uptake and In-Planta Speciation of Cerium in Radish (*Raphanus sativus* L.) Treated with Cerium Oxide Nanoparticles. *J. Environ. Chem. Eng.* **2017**, *5* (1), 572–577.
- (10) Avellan, A.; Schwab, F.; Masion, A.; Chaurand, P.; Borschneck, D.; Vidal, V.; Rose, J.; Santaella, C.; Levard, C. Nanoparticle Uptake in Plants: Gold Nanomaterial Localized in Roots of *Arabidopsis thaliana* by X-Ray Computed Nanotomography and Hyperspectral Imaging. *Environ. Sci. Technol.* **2017**, *51* (15), 8682–8691.
- (11) Collin, B. E.; Oostveen, E. K.; Tsyusko, O. V.; Unrine, J. M. Influence of Natural Organic Matter and Surface Charge on the Toxicity and Bioaccumulation of Functionalized Ceria Nanoparticles in *Caenorhabditis elegans*. *Environ. Sci. Technol.* **2014**, *48* (2), 1280–1289.
- (12) Zhang, P.; Ma, Y.; Xie, C.; Guo, Z.; He, X.; Valsami-Jones, E.; Lynch, I.; Luo, W.; Zheng, L.; Zhang, Z. Plant Species Dependent Transformation and Translocation of Ceria Nanoparticles. *Environ. Sci. Nano* **2019**, *6*, 60–67.
- (13) United States Environmental Protection Agency. Method 3050B - Acid Digestion of Sediments, Sludges, and Soils. *Method 3050B* **1996**.
- (14) Webb, S. M. SIXPack a Graphical User Interface for XAS Analysis Using IFEFFIT. *Phys. Scr.* **2005**, *T115* (0001), 1011–1014.
- (15) Ravel, B.; Newville, M. ATHENA, ARTEMIS, HEPHAESTUS: Data Analysis for X-Ray Absorption Spectroscopy Using IFEFFIT. *J. Synchrotron Radiat.* **2005**, *12* (4), 537–541.
- (16) Graham, U. M.; Tseng, M. T.; Jasinski, J. B.; Yokel, R. A.; Unrine, J. M.; Davis, B. H.; Dozier, A. K.; Hardas, S. S.; Sultana, R.; Grulke, E. A.; et al. In Vivo Processing of Ceria Nanoparticles inside Liver: Impact on Free-Radical Scavenging Activity and Oxidative Stress. *Chempluschem* **2014**, *79* (8), 1083–1088.

- (17) Yan, H.; Xu, W.; Yu, D.; Heroux, A.; Lee, W.-K.; Li, L.; Campbell, S.; Chu, Y. PyXRF: Python-Based X-Ray Fluorescence Analysis Package. *X-Ray Nanoimaging Instruments Methods III* **2017**, No. September 2017, 30.
- (18) Newville, M. Larch: An Analysis Package for XAFS and Related Spectroscopies. In *Journal of Physics: Conference Series*; IOP Publishing, 2013; Vol. 430, p 012007.
- (19) Li, H.; Ye, X.; Guo, X.; Geng, Z.; Wang, G. Effects of Surface Ligands on the Uptake and Transport of Gold Nanoparticles in Rice and Tomato. *J. Hazard. Mater.* **2016**, *314*, 188–196.
- (20) Spielman-Sun, E.; Lombi, E.; Donner, E.; Howard, D. L.; Unrine, J. M.; Lowry, G. V. Impact of Surface Charge on Cerium Oxide Nanoparticle Uptake and Translocation by Wheat (*Triticum aestivum*). *Environ. Sci. Technol.* **2017**, *51* (13), 7361–7368.
- (21) Wang, J.; Yang, Y.; Zhu, H.; Braam, J.; Schnoor, J. L.; Alvarez, P. J. J. Uptake, Translocation, and Transformation of Quantum Dots with Cationic versus Anionic Coatings by *Populus deltoides* × *nigra* Cuttings. *Environ. Sci. Technol.* **2014**, *48* (12), 6754–6762.
- (22) Zhu, Z.-J.; Wang, H.; Yan, B.; Zheng, H.; Jiang, Y.; Miranda, O. R.; Rotello, V. M.; Xing, B.; Vachet, R. W. Effect of Surface Charge on the Uptake and Distribution of Gold Nanoparticles in Four Plant Species. *Environ. Sci. Technol.* **2012**, *46* (22), 12391–12398.
- (23) Li, J.; Tappero, R. V.; Acerbo, A. S.; Yan, H.; Chu, Y.; Lowry, G. V.; Unrine, J. M. Effect of CeO₂ Nanomaterial Surface Functional Groups on Tissue and Subcellular Distribution of Ce in Tomato (*Solanum lycopersicum*). *Environ. Sci. Nano* **2018**, *6*, 273–285.
- (24) Lopez-Moreno, M. L.; de la Rosa, G.; Hernandez-Viezcas, J. A.; Castillo-Michel, H.; Botez, C. E.; Peralta-Videa, J. R.; Gardea-Torresdey, J. L. Evidence of the Differential Biotransformation and Genotoxicity of ZnO and CeO₂ Nanoparticles on Soybean (*Glycine max*) Plants. *Environ. Sci. Technol.* **2010**, *44* (19), 7315–7320.
- (25) Mirecki, N.; Agič, R.; Šunić, L.; Milenković, L.; Ilić, Z. S. Transfer Factor as Indicator of Heavy Metals Content in Plants. *Fresenius Environ. Bull.* **2015**, *24* (11C), 4212–4219.
- (26) Crooke, W. M. The Measurement of the Cation-Exchange Capacity of Plant Roots. *Plant Soil* **1964**, *21* (1), 43–49.
- (27) Cao, Z.; Rossi, L.; Stowers, C.; Zhang, W.; Lombardini, L.; Ma, X. The Impact of Cerium Oxide Nanoparticles on the Physiology of Soybean (*Glycine max* (L.) Merr.) under Different Soil Moisture Conditions. *Environ. Sci. Pollut. Res.* **2018**, *25*, 930–939.
- (28) Rossi, L.; Zhang, W.; Lombardini, L. L.; Ma, X. The Impact of Cerium Oxide Nanoparticles on the Salt Stress Responses of *Brassica napus* L. *Environ. Pollut.* **2016**, *219*, 28–36.
- (29) Wu, H.; Shabala, L.; Shabala, S.; Giraldo, J. P. Hydroxyl Radical Scavenging by Cerium Oxide Nanoparticles Improves *Arabidopsis* Salinity Tolerance by Enhancing Leaf Mesophyll Potassium Retention. *Environ. Sci. Nano* **2018**, *5* (7), 1567–1583.
- (30) Wu, H.; Tito, N.; Giraldo, J. P. Anionic Cerium Oxide Nanoparticles Protect Plant Photosynthesis from Abiotic Stress by Scavenging Reactive Oxygen Species. *ACS Nano* **2017**, *11* (11), 11283–11297.

- (31) Conway, J. R.; Beaulieu, A. L.; Beaulieu, N. L.; Mazer, S. J.; Keller, A. A. Environmental Stresses Increase Photosynthetic Disruption by Metal Oxide Nanomaterials in a Soil-Grown Plant. *ACS Nano* **2015**, *9* (12), 11737–11749.
- (32) Loriaux, S. D.; Avenson, T. J.; Welles, J. M.; Mcdermitt, D. K.; Eckles, R. D.; Riensche, B.; Genty, B. Closing in on Maximum Yield of Chlorophyll Fluorescence Using a Single Multiphase Flash of Sub-Saturating Intensity. *Plant, Cell Environ.* **2013**, *36* (10), 1755–1770.
- (33) Feng, Z. V.; Gunsolus, I. L.; Qiu, T. A.; Hurley, K. R.; Nyberg, L. H.; Frew, H.; Johnson, K. P.; Vartanian, A. M.; Jacob, L. M.; Lohse, S. E.; et al. Impacts of Gold Nanoparticle Charge and Ligand Type on Surface Binding and Toxicity to Gram-Negative and Gram-Positive Bacteria. *Chem. Sci.* **2015**, *6* (9), 5186–5196.
- (34) Asati, A.; Santra, S.; Kaittanis, C.; Perez, J. M. Surface-Charge-Dependent Cell Localization and Cytotoxicity of Cerium Oxide Nanoparticles. *ACS Nano* **2010**, *4* (9), 5321–5331.
- (35) Zhang, P.; Ma, Y.; Zhang, Z.; He, X.; Li, Y.; Zhang, J.; Zheng, L.; Zhao, Y. Species-Specific Toxicity of Ceria Nanoparticles to *Lactuca* Plants. *Nanotoxicology* **2015**, *9* (1), 1–8.
- (36) Ma, Y.; He, X.; Zhang, P.; Zhang, Z.; Ding, Y.; Zhang, J.; Wang, G.; Xie, C.; Luo, W.; Zhang, J.; et al. Xylem and Phloem Based Transport of CeO₂ Nanoparticles in Hydroponic Cucumber Plants. *Environ. Sci. Technol.* **2017**, *51* (9), 5215–5221.
- (37) Zhang, P.; Ma, Y.; Zhang, Z.; He, X.; Zhang, J.; Guo, Z.; Tai, R.; Zhao, Y.; Chai, Z. Biotransformation of Ceria Nanoparticles in Cucumber Plants. *ACS Nano* **2012**, *6* (11), 9943–9950.
- (38) Zhang, P.; Xie, C.; Ma, Y.; He, X.; Zhang, Z.; Ding, Y.; Zheng, L.; Zhang, J. Shape-Dependent Transformation and Translocation of Ceria Nanoparticles in Cucumber Plants. *Environ. Sci. Technol. Lett.* **2017**, *4*, 380–385.
- (39) Baalousha, M.; Le Coustumer, P.; Jones, I.; Lead, J. R. Characterisation of Structural and Surface Speciation of Representative Commercially Available Cerium Oxide Nanoparticles. *Environ. Chem.* **2010**, *7* (4), 377–385.
- (40) Wu, L.; Wiesmann, H. J.; Moodenbaugh, A. R.; Klie, R. F.; Zhu, Y.; Welch, D. O.; Suenaga, M. Oxidation State and Lattice Expansion of CeO_{2-x} Nanoparticles as a Function of Particle Size. *Phys. Rev. B* **2004**, *69* (12), 125415.
- (41) Singh, S.; Dosani, T.; Karakoti, A. S.; Kumar, A.; Seal, S.; Self, W. T. A Phosphate-Dependent Shift in Redox State of Cerium Oxide Nanoparticles and Its Effects on Catalytic Properties. *Biomaterials* **2011**, *32* (28), 6745–6753.
- (42) Schwabe, F.; Schulin, R.; Rupper, P.; Rotzetter, A.; Stark, W.; Nowack, B. Dissolution and Transformation of Cerium Oxide Nanoparticles in Plant Growth Media. *J. Nanoparticle Res.* **2014**, *16* (10), 2668.
- (43) Byott, G. S. Leaf Air Space Systems in C₃ and C₄ Species. *New Phytol.* **1976**, *76*, 295–299.
- (44) Zhang, Z.; He, X.; Zhang, H.; Ma, Y.; Zhang, P.; Ding, Y.; Zhao, Y. Uptake and

- Distribution of Ceria Nanoparticles in Cucumber Plants. *Metallomics* **2011**, 3 (8), 816–822.
- (45) Koo, Y.; Wang, J.; Zhang, Q.; Zhu, H.; Chehab, E. W.; Colvin, V. L.; Alvarez, P. J. J.; Braam, J. Fluorescence Reports Intact Quantum Dot Uptake into Roots and Translocation to Leaves of *Arabidopsis thaliana* and Subsequent Ingestion by Insect Herbivores. *Environ. Sci. Technol.* **2015**, 49 (1), 626–632.
- (46) Schwab, F.; Zhai, G.; Kern, M.; Turner, A.; Schnoor, J. L.; Wiesner, M. R. Barriers , Pathways and Processes for Uptake , Translocation and Accumulation of Nanomaterials in Plants – Critical Review. *Nanotoxicology* **2015**, 10 (3), 257–278.
- (47) Gutierrez-Alcala, G.; Gotor, C.; Meyer, A. J.; Fricker, M.; Vega, J. M.; Romero, L. C. Glutathione Biosynthesis in *Arabidopsis* Trichome Cells. *Proc. Natl. Acad. Sci. U. S. A.* **2000**, 97 (20), 11108–11113.
- (48) Wagner, G. J. Secreting Glandular Trichomes: More than Just Hairs. *Plant Physiol.* **1991**, 96 (3), 675–679.
- (49) Choi, Y.-E.; Harada, E.; Wada, M.; Tsuboi, H.; Morita, Y.; Kusano, T.; Sano, H. Detoxification of Cadmium in Tobacco Plants: Formation and Active Excretion of Crystals Containing Cadmium and Calcium through Trichomes. *Planta* **2001**, 213 (1), 45–50.
- (50) Choi, Y.-E.; Harada, E.; Kim, G.-H.; Yoon, E.-S.; Sano, H. Distribution of Elements on Tobacco Trichomes and Leaves under Cadmium and Sodium Stresses. *J. Plant Biol.* **2004**, 47 (2), 75–82.
- (51) Isaure, M.-P.; Sarret, G.; Harada, E.; Choi, Y.-E.; Marcus, M. A.; Fakra, S. C.; Geoffroy, N.; Pairis, S.; Susini, J.; Clemens, S.; et al. Calcium Promotes Cadmium Elimination as Vaterite Grains by Tobacco Trichomes. *Geochim. Cosmochim. Acta* **2010**, 74 (20), 5817–5834.
- (52) Broadhurst, C. L.; Chaney, R. L.; Angle, J. S.; Mangel, T. K.; Erbe, E. F.; Murphy, C. A. Simultaneous Hyperaccumulation of Nickel, Manganese, and Calcium in Alyssum Leaf Trichomes. *Environ. Sci. Technol.* **2004**, 38 (21), 5797–5802.
- (53) Corredor, E.; Testillano, P. S.; Coronado, M.-J.; González-Melendi, P.; Fernández-Pacheco, R.; Marquina, C.; Ibarra, M. R.; De La Fuente, J. M.; Rubiales, D.; Pérez-de-Luque, A.; et al. Nanoparticle Penetration and Transport in Living Pumpkin Plants: *In Situ* Subcellular Identification. *BMC Plant Biol.* **2009**, 9 (1), 45.
- (54) Cifuentes, Z.; Custardoy, L.; De La Fuente, J. M.; Marquina, C.; Ibarra, M. R.; Rubiales, D.; Pérez-de-Luque, A. Absorption and Translocation to the Aerial Part of Magnetic Carbon-Coated Nanoparticles through the Root of Different Crop Plants. *J. Nanobiotechnology* **2010**, 8 (1), 26.
- (55) Servin, A. D.; Castillo-Michel, H.; Hernandez-Viezcas, J. A.; Diaz, B. C.; Peralta-Videa, J. R.; Gardea-Torresdey, J. L. Synchrotron Micro-XRF and Micro-XANES Confirmation of the Uptake and Translocation of TiO₂ Nanoparticles in Cucumber (*Cucumis sativus*) Plants. *Environ. Sci. Technol.* **2012**, 46 (14), 7637–7643.

CHAPTER 4: TEMPORAL EVOLUTION OF COPPER DISTRIBUTION AND SPECIATION IN ROOTS OF *TRITICUM AESTIVUM* EXPOSED TO CuO, Cu(OH)₂, AND CuS NANOPARTICLES

This chapter is adapted from a publication and is citable as:

Spielman-Sun, E.; Lombi, E.; Donner, E.; Avellan, A.; Howard, D. L.; Etschmann, B.; Howard, D. L.; Lowry, G. V. Temporal Evolution of Copper Distribution and Speciation in Roots of *Triticum aestivum* Exposed to CuO, Cu(OH)₂, and CuS Nanoparticles. *Environ. Sci. Technol.* **2018**, 52 (17), 9777–9784.

The Supporting Information is provided in **Appendix C**.

ABSTRACT

Utilization of nanoparticles (NP) in agriculture as fertilizers or pesticides requires an understanding of the NP properties influencing their interactions with plant roots. To evaluate the influence of the dissolution of Cu-based NP on Cu uptake and NP association with plant roots, wheat seedlings were hydroponically exposed to 1 mg/L of Cu NPs with different 1-h solubilities (CuO, CuS, and Cu(OH)₂) for 1 h, then transferred to a Cu free medium for 48 h. Fresh, hydrated roots were analyzed using micro X-ray fluorescence (μ -XRF) and imaging fluorescence X-ray absorption near edge spectroscopy (XANES imaging) to provide laterally resolved distribution and speciation of Cu in roots. Higher 1-h solubility Cu(OH)₂ NPs provided more uptake of Cu after 1 h of exposure, but the lower 1-h solubility materials (CuO and CuS) were more persistent on the roots, and continued to deliver Cu to plant leaves over the 48h depuration period. These results demonstrate that NPs, by associating to the roots, have the potential to play a role in slowly providing micronutrients to plants. Thus tuning the dissolution of NPs may provide a long-term slow delivery of micronutrients to plants and provide important information for understanding mechanisms responsible for plant uptake, transformation, and translocation of NPs.

4.1 INTRODUCTION

Copper (Cu) is a micronutrient essential for plant carbohydrate metabolism and lignin synthesis (which is needed for cell wall strengthening).¹ Cu is also associated with crop resilience to pathogens, either directly by killing the pathogen or indirectly by evoking various physiological responses in the plant involved in pathogen attack.^{1,2} Improved Cu uptake could also have implications for the survival of plants under abiotic stresses of wilting, windiness, or rainstorm conditions where plant rigidity is important.² Therefore, an important challenge is how to package micronutrients like Cu in such a way that their bioavailability by plants is enhanced, they are safer for the environment with minimal losses, and they are affordable for growers.

Currently, micronutrients are commonly applied to plants as soluble species (e.g. CuSO_4 , Cu-EDTA).³ The widespread use of these forms of micronutrients for fertilizers implies that the nutrients are delivered as soluble ions, which are readily plant-bioavailable in typical agriculture soils that are slightly acidic. However, in alkaline and calcareous soils Cu can undergo rapid transformation with hydroxides and carbonates to form chemical precipitates (e.g. $\text{Cu}(\text{OH})_2$; $\text{Cu}_2\text{CO}_3(\text{OH})_2$),⁴ become bound to organic matter,^{5,6} rendering them unavailable to crops.⁷⁻⁹ While particulate metals and metal oxides have longer soil availability times,¹⁰ they must first dissolve, which can occur very slowly depending on soil and rhizosphere properties, prior to plant uptake.³ As discussed in **Section 1.2.3.2**, numerous papers have posited the theory that NPs have the potential to provide a slow-release delivery of micronutrients to plants.^{3,11-13} This concept has already been successfully applied to drug delivery,¹⁴ but there is limited work demonstrating this for agriculture.

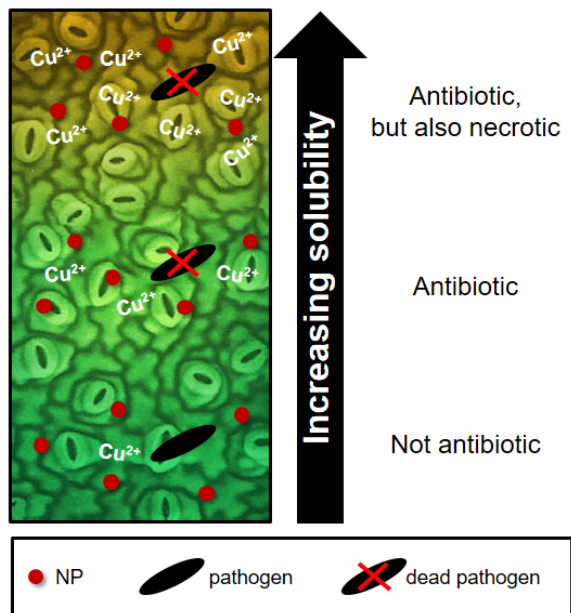


Figure 4.1. NP solubility can be tuned to deliver antibiotics at a rate high enough to be effective, but low enough to avoid necrosis (phytotoxicity)

The main goal of this study was to evaluate the influence of Cu-based NP solubility on the evolution of Cu uptake, Cu depuration, distribution, and speciation over 48 hours, using wheat (*Triticum aestivum*) as a model plant. Plants were exposed under highly controlled hydroponic conditions in order to remove confounding interactions between the NPs and soil and to be able to conserve root integrity. Fluorescence-XANES imaging was used to investigate the *in situ* laterally resolved speciation of Cu within fresh roots with the overarching goal of gaining a better understanding of how NP solubility can be engineered to be more efficient nanofertilizers or nanopesticides.

4.2 MATERIALS AND METHODS

4.2.1 CHEMICALS: CuO NPs (~50 nm), $\text{Cu}(\text{NO}_3)_2 \cdot 2.5\text{H}_2\text{O}$, polyvinylpyrrolidone (PVP, MW=10,000), ethylene glycol, and H_2O_2 solution (30%) were purchased from Signal Aldrich. $\text{Cu}(\text{OAc})_2$, and $\text{Na}_2\text{S}_2\text{O}_3$ were purchased from Fisher Chemical. Trace-metal grade HNO_3 was

purchased from VWR Analytical. Cu(OH)₂ NPs were obtained from the Center for Environmental Implications of Nanotechnology (CEINT).

4.2.2 CuS NP SYNTHESIS: CuS NPs were synthesized using the procedure described by Kundu and Pradhan.¹⁵ Briefly, in a 100-mL round bottom flask, 340 mg of Cu(OAc)₂ was dissolved in 10 mL of a 3:1 N₂-purged solution of ethylene glycol: DI water. Then, 496 mg of Na₂S₂O₃ was added to the solution. The flask was manually stirred until a yellowish green color was obtained. The flask was then heated at 70 °C for 4 hours with constant stirring. Final product was isolated via filtration, washed multiple times with ethanol and water, then oven dried overnight at 60 °C. The crystal structure for all NPs were confirmed by X-ray diffraction (XRD; Panalytical X'Pert Pro MPD X-ray Diffractometer) and peak matched using PANalytical X'Pert High Score software.

4.2.3 CU NP CHARACTERIZATION: All NPs were coated with PVP to ensure good dispersion in solution. 500 mg of NP was combined with 2 g of PVP in 10 mL of water. This suspension was bath sonicated for 30 min, then probe sonicated (550 Sonic Dismembrator, Fisher Scientific) on ice for 2 min at 10 s intervals. The suspension was then washed to remove residual PVP via centrifugation (7,500 g for 30 min), decanting the supernatant and resuspending in DI water four times. The final product was then lyophilized to yield a powder.

The primary particle size distribution of the NPs was characterized by transmission electron microscopy (TEM; JEOL JEM-2000EX operating at 200 keV). NPs were suspended in methanol and probe sonicated on ice for 5 minutes, then an aliquot was placed on a lacey coated gold grid (Ted Pella, CA) and allowed to dry. Number-weighted hydrodynamic radius and the electrophoretic mobility of the NPs in the exposure medium (see details below) were measured using a Nano Zetasizer (Malvern Instruments, Malvern). The suspension was probe sonicated on

ice for 2 min at 10 s intervals to ensure dispersion. The initial pH and ionic strength of the exposure medium was 5.6 and 5.2 mM and were not further adjusted. The apparent zeta potential was calculated from the electrophoretic mobility using the Smoluchowski approximation. The specific surface area of the particles was measured by the multipoint N₂-BET method (Quantachrome® ASiQwin™, Quantachrome Instruments, Boynton Beach, FL).

The 1-h solubility of the NPs in the exposure medium (see details below) was determined in triplicate by mixing solutions on an end-over-end rotator for 1 h, after which aliquots were removed and the dissolved Cu was isolated using an Amicon-Ultra, 3 kDa centrifugal filter (Sigma Aldrich). The filtrate was then acidified to 2% HNO₃ and analyzed by inductively coupled plasma mass spectrometry (ICP-MS) (Agilent 7700x, Santa Clara, CA). The instrument was calibrated with a mixed calibration standard (Environmental Express, Charleston, SC) and a Ge internal standard (Agilent Technologies, Santa Clara, CA).

4.2.4 PLANT EXPOSURE: For μ -XRF, wheat (*Triticum aestivum* cv. Shield) seeds were surface sterilized with commercial bleach (8.5% active chlorine) for 10 min and then thoroughly rinsed with DI water. The sterilized seeds were germinated on deionized water moistened filter paper in a Petri dish. After four days, the seedlings were transferred to 100-mL plastic containers. Each container was filled with 80 mL of copper-free ¼ strength modified Hoagland's medium¹⁶ and covered with a plastic lid with five holes. One seedling was transplanted in each hole with the roots suspended in a continuously aerated solution. Plants were grown at 25 °C under alternate 12 h of light and 12 h of dark. Nutrient solution was renewed every 3 days. After 7 days, the plants were transferred from the University of South Australia (Adelaide, Australia) to the Australian Synchrotron (Melbourne, Australia) where the plants were hydroponically exposed for one hour to either 1 mg-Cu/L as NPs or to Cu(NO₃)₂ at 1 mg-Cu/L and 50 μ g-Cu/L as a high and low ionic

control. The concentration for the low ionic control was chosen to be the amount of dissolved Cu from the 1-h solubility experiment for the least soluble NP (CuO), while the high ionic control represents a 100% soluble particle. Roots were briefly rinsed in Cu-free hydroponic media to remove loosely adhered NPs and imaged. The remaining plants were then transferred to Cu-free hydroponic medium (herein referred to as the “depuration solution”) and imaged after 12 h and 48 h. Remaining Cu in solution was quantified by ICP-MS, and dissolved and nanoparticulate fractions were determined using the methods stated above.

Total Cu uptake measurements were conducted at Carnegie Mellon University (Pittsburgh, PA). Plant growth conditions were replicated to match those used for the synchrotron exposures. At the various time points, plants were harvested in triplicate, roots were briefly rinsed in Cu-free hydroponic medium, and roots and shoots were separated, weighed, and lyophilized. Plant tissue was digested in a 1:1 solution of DI water: concentrated HNO₃ at 95°C for 30 minutes, and then allowed to return to room temperature. Solution was then brought to a 2:1 ratio of concentrated HNO₃: H₂O₂, heated to 95°C for 2 hours, then allowed to return to room temperature (protocol adapted from EPA Method 3050b¹⁷). Following digestion, the samples were diluted to 2% HNO₃ using deionized water, spiked with a Ge internal standard, and filtered through a 0.45 μm filter before analysis using ICP-MS for total Cu.

4.2.5 μ-XRF AND FLUORESCENCE XANES IMAGING: Following exposure, roots were briefly rinsed in a Cu-free hydroponic solution, positioned vertically in the sample holder, and sealed between two pieces of 4 μm-thick Ultralene, which formed a tight seal around the roots to prevent dehydration. Roots were scanned at the XFM beamline at the Australian Synchrotron, where an in-vacuum undulator is used to produce an X-ray beam. A Si(111) monochromator and Kirkpatrick-Baez (KB) mirror microprobe are used to obtain a monochromatic beam focused onto

the specimen (approximately 2x2 μ m). The X-ray fluorescence emitted by the specimen was collected using the 384-element Maia detector (Rev C) placed in a backscatter geometry.¹⁸

First, an initial large area survey scan at 15.8 keV was conducted to identify the area of interest and obtain overall elemental distributions. Step size in the vertical direction and scanning velocity were adjusted so each scan took around 2 hours (details provided in **Appendix C**). Subsequently, a smaller area around the tips of the roots and the elongation zone were chosen to conduct fluorescence-XANES imaging with the XANES stack itself consisting of 95 individual maps at decreasing energies across the Cu K-edge. Details regarding the energy steps are provided in **Appendix C**.

The three nanoparticle standards were also analyzed using fluorescence-XANES imaging. All standards were prepared to a final Cu concentration of 100 mg/L. Further details about the preparation and imaging of these standards are provided in the supporting information. These XANES spectra and that of other Cu-models are presented in **Appendix C (Figure C.1)**. To allow easier interpretation of the results of the XAS fitting, similar reference compounds were grouped and referred to as the type of species (e.g. Cu-phosphate and Cu-sulfate were grouped and reported as Cu-O-R, while Cu-cysteine and Cu-glutathione were grouped and reported as Cu-S-R).

μ -XRF spectra from the root tips and root elongation zones were extracted and analyzed using GeoPIXE.¹⁹ XANES spectra were averaged from selected pixel populations (see **Appendix C, Figures C.5-7**), and then background subtracted and normalized using the Athena software package.²⁰ Linear combination fitting (LCF) was performed using the starting NPs and the reference compounds described in **Appendix C, Figure C.1**. Inclusion of a reference spectrum into the combination fit required at least a 10% decrease in the Rf-value, indicating a significant change to the quality of the fit.

XANES spectra were also fit pixel-by-pixel using a linear combination of Cu-O and Cu-S models. To improve the signal to noise ratio, the XANES spectrum at each pixel was smoothed over two pixels with both the *x* and *y* directions. Details regarding this code are described in Etschmann, et al.²¹ Only the roots after 1 h of exposure had adequate Cu signal for this analysis.

4.3 RESULTS AND DISCUSSION

4.3.1 NP CHARACTERIZATION: TEM images and XRD spectra of the Cu-based NPs are provided in the **Appendix C (Figure C.2)**. The CuO and Cu(OH)₂ NPs were identified by XRD as tenorite and spertiniite, respectively. The CuS NP was identified as primarily covellite, although a chalcantite (CuSO₄·5H₂O) phase was also identified. The presence of this sulfate phase indicates that some of the sulfide was oxidized, likely during the drying process.^{22,23} The CuO and CuS NPs were spherical, while the Cu(OH)₂ NPs were spindle-shaped. Additional measured particle properties are displayed in **Table 4.1**.

Table 4.1. Summary of PVP-coated NP characterization in ¼ strength Hoagland’s medium (pH=5.6; ionic strength=5.2 mM). Hydrodynamic diameter and electrophoretic mobility (and calculated zeta potential) were performed at 50 mg-Cu/L in order to obtain adequate signal. The 1h solubility was determined at the experimental dosing concentration of 1 mg-Cu/L. TEM diameter of Cu(OH)₂ NPs was measured at the narrowest point of the spindles.

NP	TEM Diameter (nm)	BET Surface Area (m ² /g)	Hydrodynamic Diameter (nm)	Electrophoretic mobility (µm·cm·V ⁻¹ ·s ⁻¹)	Zeta potential (mV)	1 h solubility
CuO	56.4 ± 19.4	8.6	141.3 ± 28.1	-1.28 ± 0.32	-16.4 ± 4.1	6.6 ± 0.5 %
CuS	25.5 ± 4.7	11.5	115.9 ± 29.3	-1.36 ± 0.31	-17.3 ± 3.9	15.3 ± 0.6 %
Cu(OH) ₂	16.0 ± 4.7	99.4	159.3 ± 30.6	-0.74 ± 0.26	-9.4 ± 3.4	64.6 ± 1.6 %

4.3.2 TOTAL CU ASSOCIATION/UPTAKE IN ROOTS AND SHOOTS: The Cu concentrations associated with and in the wheat roots and in the leaves with the different dosing scenarios are shown in **Figure 4.2**. No visual signs of toxicity (e.g. chlorosis, wilting, root damage) were observed during the experiment. After the 1 h exposure, Cu significantly accumulated on/in the

plant roots for all treatments except for the low ionic dose compared to the control. The three NP treatments, especially the CuO NP treatment, all had higher Cu association to the root compared to the soluble Cu (high dose), suggesting that NPs had attached to or entered the roots. The observed Cu sorbed on or in roots (~1000 mg/kg DW) is relatively high compared to other hydroponic studies at similar NP dosing concentrations and over longer exposure periods; Shi et al. exposed duckweed to 1 mg/L of CuO NPs for 96 hours and observed similar values to this study (~800 mg-Cu/kg DW of roots).²⁴ The high Cu attachment/uptake is likely due to the fact that in this study, the roots were only briefly washed with Cu-free ¼ strength Hoagland’s medium before measuring Cu, unlike other studies which have more extensive washing protocols to remove all adhered NPs on the outside of the root.

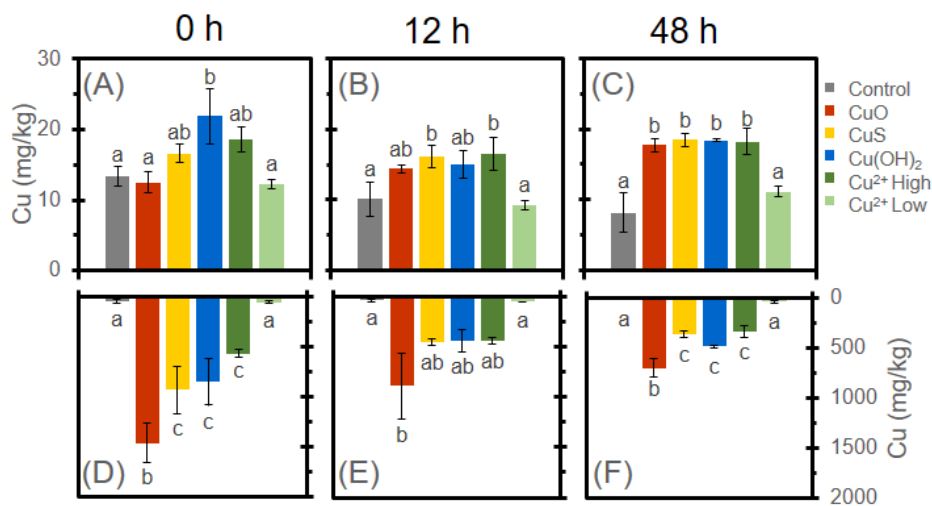


Figure 4.2. Total Cu concentrations in dried wheat leaves (top; **A, B, C**) and roots (bottom; **D, E, F**) after 1 h of exposure and then 0 (**A, D**), 12 h (**B, E**) or 48 h (**C, F**) of depuration in Cu-free solution. Note difference scales for the roots and leaves. The means are averaged from three replicates. Error bars correspond to standard deviation. Significant differences (based on ANOVA and Tukey HSD post hoc tests ($p < 0.05$)) between the treatments at the same time point for the same plant section are indicated by different lowercase letters. Individual values are reported in **Appendix C, Table C.1**.

As the roots recovered in the Cu-free depuration solution, the amount of Cu adhering to the roots decreased (**Figure 4.2 d, e, f**). By the end of the depuration period, statistically significant

differences in leaf Cu concentrations were also found between control and all the treatments (except for the low ionic dose) (**Figure 4.2, a, b, c**). The CuO NPs, the lowest soluble particles, display the most distinct increase in Cu concentration in the leaves over time. After 1 h of exposure (t=0 depuration), the CuO dosed plants had not accumulated a significantly higher amount of Cu in leaves in comparison to the control plants, despite have a greater adhered mass of Cu on the roots. However, by the end of the 48 h period, the CuO NP exposed plants had accumulated a similar amount of Cu in the leaves, as had all the other treatments excluding the control and low ionic treatment, suggesting that Cu is steadily being translocated from the roots to the leaves despite being in a Cu-free medium. This implies either direct CuO NP uptake and translocation, or the ability of the CuO NPs to continually supply Cu ions into the roots. This is based on the fact that more Cu is delivered by the CuO NPs than for the low ionic Cu dose that is equal to the total amount of dissolved Cu released from CuO NPs during the 1h exposure time. In general, the amount of Cu in the leaves from the other treatments (i.e. the more soluble Cu(OH)₂ NPs, CuS NPs, and the high ionic dose) stayed relatively constant over the exposure period, suggesting that at this Cu dose the plant is able to regulate the uptake and translocation of Cu ions to the leaves.²⁵ The uptake, intracellular translocation, and storage of essential metals is known to be tightly regulated by plant homeostasis.²⁶ By the end of the 48 h depuration period, the NP treatments have similar total amount of Cu adhered to and in the roots, but the distribution and speciation of the Cu in these roots is significantly different (as discussed in **Section 4.3.4**).

Remaining Cu in solution was also quantified, and the remaining nanoparticulate and dissolved Cu in the hydroponic medium at the end of the 1 h exposure period follow the solubility trends of the NPs. At the end of the CuO NP, CuS NP, Cu(OH)₂ NP exposures, the dissolved fraction of Cu was 13.2±1.8%, 19.2±0.1%, 90.2±2.8%, respectively. It should be noted that the dissolved fraction

post-exposure is higher than the dissolved fraction observed in plant-free medium (**Table 4.1**), likely due to root exudate assisted dissolution.²⁷ This difference is particularly pronounced for the CuO and Cu(OH)₂ NP exposures, but less so for the CuS exposure. This dissolution pH sensitivity is further discussed later in the paper.

4.3.3 CHANGE IN CU DISTRIBUTION OVER TIME: XRF images of the roots at the various time points are shown in **Figure 4.3**. There are substantial differences in the distributions of Cu for the various NPs over time. After 1 h of exposure, all NPs resulted in significant Cu accumulation at the root apex in the root cap and meristematic zone, as was observed for cowpea,²⁸ cucumber,²⁹ and rice³⁰ exposed to ionic Cu. This accumulation at the tip is particularly prominent for the Cu(OH)₂ NP treatment. Unlike the Cu(OH)₂ NP treatment, the CuO and CuS NP treatments resulted in Cu accumulation additionally along the root elongation zone in a spotted pattern, suggesting that the adhered Cu is particulate (see later discussion of the XANES spectra for more details). After transferring to the Cu-free medium, the overall Cu distribution for the CuO and CuS exposures did not significantly change, while the Cu(OH)₂ exposed root showed a significant decrease in Cu fluorescence signal likely due to rapid Cu translocation. The root tips under all exposure scenarios continued to show significant Cu, which is consistent with the idea that the meristematic region of the root tip is the most active zone for heavy metal absorption.²⁹⁻³¹ Throughout the depuration period, all roots continue to show high concentrations of Cu at the tip, likely due to high affinity of Cu with hard ligands of the cell walls³² or to a different potential for mucilage exudation and trapping efficiency depending on the root zone and the NP surface.³³ Given that these wheat roots are continually growing at ~1 mm/h,³⁴ it is particularly noteworthy that the Cu is persistent over the 48 h period.

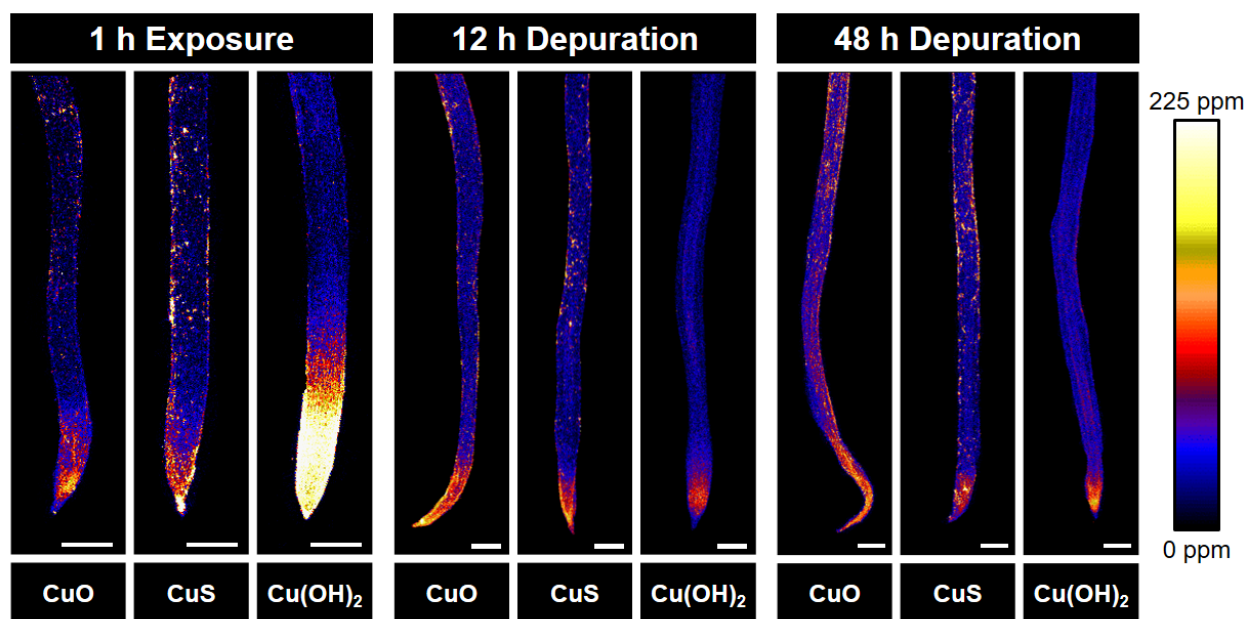


Figure 4.3. XRF Elemental maps showing total Cu distribution in wheat roots exposed hydroponically to 1 mg-Cu/L as Cu-based NPs in continuously aerated $\frac{1}{4}$ strength Hoagland's medium (pH=5.6) for 1 h, rinsed, then placed in a Cu-free medium for 12 and 48 hours. Scale bar = 500 μ m. Note larger scale bar for 1 h exposure than 12 h and 48 h depuration scenarios.

Projected volumetric Cu concentrations in the root cross-sections were calculated using GeoPIXE and are shown in (Appendix C, Figure C.3). The plots for the CuO (Appendix C, Figure C.3 a-c) and CuS (Appendix C, Figure C.3 d-f) treatments consistently show higher Cu concentrations on the outer edges, suggesting that most of the Cu is adhered to the outside of the roots cells.³² In contrast, the Cu(OH)₂ NP exposure (Appendix C, Figure C.3 g-i) showed changes in the Cu distribution over time. After 12 h of depuration, most of the Cu has moved from the outside of the root to inside the main vasculature. By 48 hours, majority of the Cu has moved into the internal vasculature. These changes in distribution suggest that the less soluble NPs are able to remain on the root for longer periods of time compared to the higher soluble NPs.

4.3.4 CHANGE IN CU SPECIATION OVER TIME. Extracted XANES spectra at the root tips and root elongation zone and fitting statistics are shown in Appendix C (Figures C.4-6; Table C.2). The temporal changes in Cu speciation are graphically shown in Figure 4.4. After 1h of exposure to

CuO NPs, a significant amount of Cu remains as CuO NPs (40-80%) with some transformation to a Cu(II)-O-R species. This Cu(II)-O-R species is hypothesized to be Cu bound to polygalacturonic acid or other oxygen and nitrogen rich ligands found in the plant root cell walls.^{28,35} The observed high percent of CuO NP, in combination with the observed Cu concentrations in root cross-sections (**Figure C.3**), further suggests that these relatively insoluble particles remain sorbed or associated with the outside of the root surface. In the elongation zone, as time increases, the overall percent of CuO decreases, suggesting a slow biotransformation outside and/or in the first cell layers and subsequent translocation to the leaves. Differences between the elongation zone and root tip are likely due to differences in biotransformation rates.

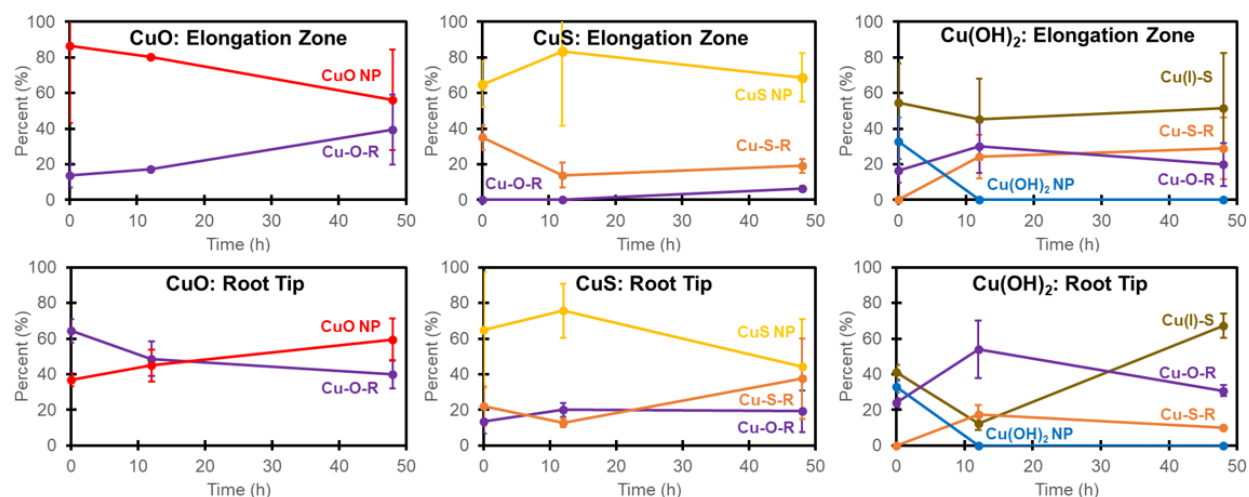


Figure 4.4. Wheat roots were exposed hydroponically to 1 mg-Cu/L as Cu-based NPs in continuously aerated ¼ strength Hoagland’s medium (pH=5.6) for 1 h, rinsed, then placed in a Cu-free medium for 12 and 48 hours. Components of the extracted XANES spectra from **Figures C.4-6** are plotted for each region over the exposure period. See **Table C.2** for details regarding the LCF results. LCF results are presented with an implicit ± 20%.

Despite being twice as soluble as CuO NPs in plant free media, the CuS NPs were similarly persistent as the CuO NPs. CuS NPs remain the dominant species throughout the entire exposure period (40-80%), particularly in the elongation zone, with some biotransformed mostly to a Cu(I,II)-S-R species and some Cu(II)-O-R or Cu(I,II)-S-R type complexes. This apparent

discrepancy can potentially be explained by the pH at the root surface. The 1-h solubility measurements presented in **Table 4.1** were conducted at an initial pH of 5.6. Plants exude low molecular weight organic acids into the rhizosphere,³⁶ which can lower the pH at the root surface and promote the dissolution of NPs.^{27,37-41} While little CuO NP dissolution occurs at neutral pH, significant dissolution is observed at lower pH.⁴² In comparison, CuS NP dissolution is less sensitive to pH than CuO NPs,⁴³ so it is possible that the CuO NPs are dissolving at the root tip surface more than the CuS NPs and thus the CuS NPs are more persistent.

Unlike the CuO NP and CuS NPs which are less soluble and persist over the 48 h period, the Cu(OH)₂ NPs disappeared after the roots were transferred to the Cu-free medium. After 1 h of exposure, ~33% the Cu is in the original Cu(OH)₂ NP form. The remaining ~67% Cu is transformed to Cu(I)S, Cu(II)-O-R, and Cu-S-R type complexes. Similarly, Kopittke et al.²⁸ observed by XAS in cowpea hydroponically exposed to ionic Cu that ~45-60% of Cu is bound in a Cu(I,II)-S-R type species and the remainder Cu(II)-O-R. Song et al.²⁹ observed in hydroponic cucumber exposed to ionic Cu that only ~20% of the Cu was bound as Cu(I,II)-S-R and the remaining as Cu(II)-O-R. The high degree of thiolation is likely a plant detoxification pathway to sequester Cu with metallothionein-type proteins.^{1,2,44} The lower Cu exposure concentration used here compared to other studies may have allowed the plant to respond better to the toxicity, complexing a greater fraction of the Cu with thiol groups. This is consistent with the lack of visually observable toxicity. Isotope fractionation analysis of Cu uptake suggests preferential uptake of the light Cu isotope, which has been proposed to be the result of a reductive uptake mechanism via the Cu specific carrier protein COPT.^{45,46} The observed Cu(I) species in the highly soluble Cu(OH)₂ NP treatment supports this idea that Cu(II) reduction to Cu(I) occurs at the root cell membrane prior to ionic Cu uptake. Other proposed uptake mechanisms include via Cu non-

specific transport proteins in the ZIP family, which mostly transport Zn^{2+} and Fe^{2+} but may also be capable of transporting Cu^{2+} .⁴⁷⁻⁴⁹

Pixel-by-pixel fitting performed on the roots after the 1 h exposure period confirmed these observations (**Figure 4.5**). The Cu in the CuO exposed roots is present mostly as a Cu-O species, while the Cu in the CuS is mostly Cu-S with some Cu-O. On the outside of the root for the $Cu(OH)_2$ NP exposure, the Cu is mostly present as a Cu-O species, suggesting that the Cu is either dissolved or bound to the cell wall as has been observed in cowpea,²⁸ cucumber,²⁹ and rice.²⁷ The center of the roots exposed to $Cu(OH)_2$ NPs, however, is mostly reduced Cu as Cu-S species, likely bound to a thiol group which is a common plant response to Cu.^{1,2}

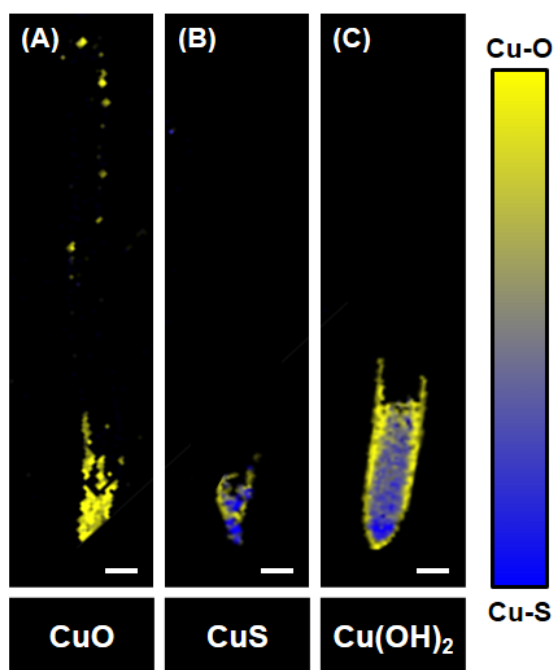


Figure 4.5. Pixel-by-pixel XANES analysis for wheat roots exposed hydroponically to 1 mg-Cu/L as (A) CuO NP, (B) CuS NP, or (C) $Cu(OH)_2$ NPs for 1 h in continuously aerated $\frac{1}{4}$ strength Hoagland's medium (pH=5.6). Using the dataset smoothed over 2×2 pixels, XANES spectra were fit to two components: Cu-O model (yellow) and Cu-S model (blue) (see color scale at right). Black pixels were excluded based on low Cu counts. Cu signal was too low to perform this analysis at other time points. Scale bar= 200 μ m

4.4 ENVIRONMENTAL IMPLICATIONS

In this research, the impact of the speciation of Cu-based NPs and their resulting 1-h solubility on Cu uptake and distribution was investigated in wheat plants. Results showed that the higher 1-h solubility $\text{Cu}(\text{OH})_2$ NPs provided more immediate Cu to the plant after 1 h of exposure, and the Cu was quickly reduced and/or sulfidized. The lower 1-h solubility CuO and CuS NPs, on the other hand, were more persistent over the 48 h post-exposure period, with as much as 80% of the Cu on the root surfaces remaining as the untransformed NP.

The initial NP composition influenced Cu speciation within the plant roots. Despite having similar solubilities (~15% vs 7%), the Cu in plants exposed to CuS NPs was mostly reduced and/or sulfidized Cu while the Cu in the CuO NP exposed plants remained oxidized. These differences in Cu speciation may subsequently affect the bioavailability of the Cu and the health of the plants depending on natural plant strategies for transporting/sequestering Cu, since plants have different translocation mechanisms for Cu(I) vs Cu(II).^{44,50} Therefore, these observed speciation differences also suggests that plant uptake may be controllable by engineering the initial speciation of the Cu-based NP.

This persistence of untransformed NP on roots has potential implications for improving micronutrient utilization efficiency in agricultural systems. Commercial hydroponic systems often recirculate and reuse nutrient solutions in order to reduce environmental and economic costs.⁵¹ By using persistent, slow delivery materials such as these low soluble NPs, micronutrients can potentially be applied directly to the roots and less frequently than conventional ionic materials, which would save costs on application and improve utilization efficiency. Additional studies are needed to determine the concentrations of adhered Cu-based particles that can be applied without toxicity, though a recent study indicated that the toxicity of CuO NPs adhered to wheat roots in

soil were less toxic than Cu salt treatments at 1.6 times the dose.⁵² Though these results cannot be directly extrapolated to other matrices, the benefits of these slow release particles could potentially be realized in soils assuming the NP-root interactions are similar in soils and hydroponics. Low soluble NP could theoretically also persist in soils slowly delivering micronutrients over an extended period of time, unlike highly soluble NP or ionic doses which quickly decrease in bioavailability over time due to various short- and long-term soil aging processes such as precipitation and solid state diffusion.^{4,53,54} Several studies have demonstrated that upon aging, total dissolved Cu concentrations increase in the soils spiked with CuO NPs but decrease in the soils spiked with ionic Cu.^{55,56} In this hydroponic system, all three NP treatments provided the same amount of Cu to the leaves over the 48 h, which is very short compared to the overall lifetime of agricultural crops, thus we can only posit that low soluble NPs can better deliver micronutrients over an extended period of time compared to highly soluble NPs. A long term exposure study in soil encompassing the entire lifecycle would be needed to verify these hypotheses.

Overall, the present study demonstrates that NP speciation and dissolution plays an important role in the rate of transformation on/in plant roots and to the resulting speciation and fate of Cu in wheat plants. This study also suggests that NP solubility can be tuned via composition to control how rapidly NPs, or metals derived from them, can be made phytoavailable. This knowledge of solubility could also be applied to other types of NPs as part of smart delivery systems for sustained delivery of nutrients.

4.5 REFERENCES FOR CHAPTER 4

- (1) Yruela, I. Copper in Plants: Acquisition, Transport and Interactions. *Funct. Plant Biol.* **2009**, *36* (5), 409–430.
- (2) Yruela, I. Copper in Plants. *Brazilian J. Plant Physiol.* **2005**, *17* (1), 145–156.

- (3) Dimkpa, C. O.; Bindraban, P. S. Fortification of Micronutrients for Efficient Agronomic Production: A Review. *Agron. Sustain. Dev.* **2016**, *36* (1), 1–26.
- (4) Ma, Y.; Lombi, E.; Oliver, I. W.; Nolan, A. L.; McLaughlin, M. J. Long-Term Aging of Copper Added to Soils. *Environ. Sci. Technol.* **2006**, *40* (20), 6310–6317.
- (5) Strawn, D. G.; Baker, L. L. Speciation of Cu in a Contaminated Agricultural Soil Measured by XAFS, μ -XAFS, and μ -XRF. *Environ. Sci. Technol.* **2008**, *42* (1), 37–42.
- (6) Sauve, S.; McBride, M. B.; Norvell, W. A.; Hendershot, W. H. Copper Solubility and Speciation of In Situ Contaminated Soils: Effects of Copper Level, pH, and Organic Matter. *Water. Air. Soil Pollut.* **1997**, *100*, 133–149.
- (7) Sims, J. T. Soil pH Effects on the Distribution and Plant Availability of Manganese, Copper, and Zinc. *Soil Sci. Soc. Am. J.* **1986**, *50* (2), 367–373.
- (8) Zhou, L. X.; Wong, J. W. C. Effect of Dissolved Organic Matter from Sludge and Sludge Compost on Soil Copper Sorption. *J. Environ. Qual.* **1999**, *30* (3), 878–883.
- (9) Sinha, M. K.; Dhillon, S. K.; Dhillon, K. S.; Dyanand, S. Solubility Relationships of Iron, Manganese, Copper and Zinc in Alkaline and Calcareous Soils. *Aust. J. Soil Res.* **1978**, *16* (1), 19–26.
- (10) Sekine, R.; Marzouk, E. R.; Khaksar, M.; Scheckel, K. G.; Stegemeier, J. P.; Lowry, G. V.; Donner, E.; Lombi, E. Aging of Dissolved Copper and Copper-Based Nanoparticles in Five Different Soils: Short-Term Kinetics vs. Long-Term Fate. *J. Environ. Qual.* **2017**, *46* (6), 1198–1205.
- (11) Servin, A. D.; Elmer, W. H.; Mukherjee, A.; De La Torre-Roche, R.; Hamdi, H.; White, J. C.; Bindraban, P. S.; Dimkpa, C. O. A Review of the Use of Engineered Nanomaterials to Suppress Plant Disease and Enhance Crop Yield. *J. Nanoparticle Res.* **2015**, *17* (2), 92.
- (12) Milani, N.; McLaughlin, M. J.; Stacey, S. P.; Kirby, J. K.; Hettiarachchi, G. M.; Beak, D. G.; Cornelis, G. Dissolution Kinetics of Macronutrient Fertilizers Coated with Manufactured Zinc Oxide Nanoparticles. *J. Agric. Food Chem.* **2012**, *60* (16), 3991–3998.
- (13) Monreal, C. M.; DeRosa, M. C.; Mallubhotla, S. C.; Bindraban, P. S.; Dimkpa, C. O. Nanotechnologies for Increasing the Crop Use Efficiency of Fertilizer-Micronutrients. *Biol. Fertil. Soils* **2016**, *52* (3), 423–437.
- (14) De Jong, W. H.; Borm, P. J. A. Drug Delivery and Nanoparticles: Applications and Hazards. *Int. J. Nanomedicine* **2008**, *3* (2), 133–149.
- (15) Kundu, J.; Pradhan, D. Controlled Synthesis and Catalytic Activity of Copper Sulfide Nanostructured Assemblies with Different Morphologies. *ACS Appl. Mater. Interfaces* **2014**, *6* (3), 1823–1834.
- (16) Hoagland, D. R.; Arnon, D. I. *The Water-Culture Method for Growing Plants without Soil*; College of Agriculture, University of California: Berkeley, CA, 1950.
- (17) United States Environmental Protection Agency. Method 3050B - Acid Digestion of Sediments, Sludges, and Soils. *Method 3050B* **1996**.
- (18) Paterson, D. J.; de Jonge, M. D.; Howard, D. L.; Lewis, W.; McKinlay, J.; Starritt, A.; Kusel, M.; Ryan, C. G.; Kirkham, R.; Moorhead, G. F.; et al. The X-Ray Fluorescence

- Microscopy Beamline at the Australian Synchrotron. In *AIP Conference Proceedings*; 2011; Vol. 1365.
- (19) Ryan, C. G.; Siddons, D. P.; Kirkham, R.; Li, Z. Y.; de Jonge, M. D.; Paterson, D. J.; Kuczewski, A.; Howard, D. L.; Dunn, P. A.; Falkenberg, G.; et al. Maia X-Ray Fluorescence Imaging: Capturing Detail in Complex Natural Samples. *J. Phys. Conf. Ser.* **2014**, *499*, 012002.
- (20) Ravel, B.; Newville, M. ATHENA, ARTEMIS, HEPHAESTUS: Data Analysis for X-Ray Absorption Spectroscopy Using IFEFFIT. *J. Synchrotron Radiat.* **2005**, *12* (4), 537–541.
- (21) Etschmann, B. E.; Donner, E.; Brugger, J.; Howard, D. L.; De Jonge, M. D.; Paterson, D. J.; Naidu, R.; Scheckel, K. G.; Ryan, C. G.; Lombi, E. Speciation Mapping of Environmental Samples Using XANES Imaging. *Environ. Chem.* **2014**, *11* (3), 341–350.
- (22) Ma, R.; Stegemeier, J. P.; Levard, C.; Dale, J. G.; Noack, C. W.; Yang, T.; Brown, G. E.; Lowry, G. V. Sulfidation of Copper Oxide Nanoparticles and Properties of Resulting Copper Sulfide. *Environ. Sci. Nano* **2014**, *1* (4), 347–357.
- (23) Luther, G. W.; Theberge, S. M.; Rozan, T. F.; Rickard, D.; Rowlands, C. C.; Oldroyd, A. Aqueous Copper Sulfide Clusters as Intermediates during Copper Sulfide Formation. *Environ. Sci. Technol.* **2002**, *36* (3), 394–402.
- (24) Shi, J.; Abid, A. D.; Kennedy, I. M.; Hristova, K. R.; Silk, W. K. To Duckweeds (*Landoltia punctata*), Nanoparticulate Copper Oxide Is More Inhibitory than the Soluble Copper in the Bulk Solution. *Environ. Pollut.* **2011**, *159* (5), 1277–1282.
- (25) Li, H.; Fan, R.; Li, L.; Wei, B.; Li, G.; Gu, L.; Wang, X.; Zhang, X. Identification and Characterization of a Novel Copper Transporter Gene Family *TaCT1* in Common Wheat. *Plant. Cell Environ.* **2014**, *37* (7), 1561–1573.
- (26) Grotz, N.; Guerinot, M. Lou. Molecular Aspects of Cu, Fe and Zn Homeostasis in Plants. *Biochim. Biophys. Acta - Mol. Cell Res.* **2006**, *1763* (7), 595–608.
- (27) Peng, C.; Duan, D.; Xu, C.; Chen, Y.; Sun, L.; Zhang, H.; Yuan, X.; Zheng, L.; Yang, Y.; Yang, J.; et al. Translocation and Biotransformation of CuO Nanoparticles in Rice (*Oryza sativa* L.) Plants. *Environ. Pollut.* **2015**, *197*, 99–107.
- (28) Kopittke, P. M.; Menzies, N. W.; de Jonge, M. D.; McKenna, B. A.; Donner, E.; Webb, R. I.; Paterson, D. J.; Howard, D. L.; Ryan, C. G.; Glover, C. J.; et al. In Situ Distribution and Speciation of Toxic Copper, Nickel, and Zinc in Hydrated Roots of Cowpea. *Plant Physiol.* **2011**, *156* (June), 663–673.
- (29) Song, J.; Yang, Y.; Zhu, S. H.; Chen, G. C.; Yuan, X. F.; Liu, T. T.; Yu, X. H.; Shi, J. Spatial Distribution and Speciation of Copper in Root Tips of Cucumber Revealed by μ -XRF and μ -XANES. *Biol. Plant.* **2013**, *57* (3), 581–586.
- (30) Lu, L.; Xie, R.; Liu, T.; Wang, H.; Hou, D.; Du, Y.; He, Z.; Yang, X.; Sun, H.; Tian, S. Spatial Imaging and Speciation of Cu in Rice (*Oryza Sativa* L.) Roots Using Synchrotron-Based X-Ray Microfluorescence and X-Ray Absorption Spectroscopy. *Chemosphere* **2017**, *175*, 356–364.
- (31) Walker, T. S.; Bais, H. P.; Grotewold, E.; Vivanco, J. M. Root Exudation and Rhizosphere Biology. *Plant Physiol.* **2003**, *132* (1), 44–51.

- (32) Wang, P.; Menzies, N. W.; Lombi, E.; McKenna, B. A.; de Jonge, M. D.; Donner, E.; Blamey, F. P. C.; Ryan, C. G.; Paterson, D. J.; Howard, D. L.; et al. Quantitative Determination of Metal and Metalloid Spatial Distribution in Hydrated and Fresh Roots of Cowpea Using Synchrotron-Based X-Ray Fluorescence Microscopy. *Sci. Total Environ.* **2013**, *463–464*, 131–139.
- (33) Avellan, A.; Schwab, F.; Masion, A.; Chaurand, P.; Borschneck, D.; Vidal, V.; Rose, J.; Santaella, C.; Levard, C. Nanoparticle Uptake in Plants: Gold Nanomaterial Localized in Roots of *Arabidopsis thaliana* by X-Ray Computed Nanotomography and Hyperspectral Imaging. *Environ. Sci. Technol.* **2017**, *51* (15), 8682–8691.
- (34) Pritchard, J.; Tomos, A. D.; Wyn Jones, R. G. Control of Wheat Root Elongation Growth. *J. Exp. Bot.* **1987**, *38* (191), 948–959.
- (35) Guigues, S.; Bravin, M. N.; Garnier, C.; Masion, A.; Chevassus-Rosset, C.; Cazevielle, P.; Doelsch, E. Involvement of Nitrogen Functional Groups in High-Affinity Copper Binding in Tomato and Wheat Root Apoplasts: Spectroscopic and Thermodynamic Evidence. *Metallomics* **2016**, *8* (3), 366–376.
- (36) Jones, D. L. Organic Acids in the Rhizosphere – a Critical Review. *Plant Soil* **1998**, *205* (1), 25–44.
- (37) Schwabe, F.; Tanner, S.; Schulin, R.; Rotzetter, A.; Stark, W.; Von Quadt, A.; Nowack, B. Dissolved Cerium Contributes to Uptake of Ce in the Three Crop Plants. *Metallomics* **2015**, *7*, 466–477.
- (38) Zhang, P.; Ma, Y.; Zhang, Z.; He, X.; Guo, Z.; Tai, R.; Ding, Y.; Zhao, Y.; Chai, Z. Comparative Toxicity of Nanoparticulate/Bulk Yb₂O₃ and YbCl₃ to Cucumber (*Cucumis sativus*). *Environ. Sci. Technol.* **2012**, *46* (3), 1834–1841.
- (39) Lv, J.; Zhang, S.; Luo, L.; Zhang, J.; Yang, K.; Christie, P. Accumulation, Speciation and Uptake Pathway of ZnO Nanoparticles in Maize. *Environ. Sci. Nano* **2015**, *2* (1), 68–77.
- (40) Ma, Y.; He, X.; Zhang, P.; Zhang, Z.; Guo, Z.; Tai, R.; Xu, Z.; Zhang, L.; Ding, Y.; Zhao, Y.; et al. Phytotoxicity and Biotransformation of La₂O₃ Nanoparticles in a Terrestrial Plant Cucumber (*Cucumis sativus*). *Nanotoxicology* **2011**, *5* (4), 743–753.
- (41) Peng, C.; Zhang, H.; Fang, H.; Xu, C.; Huang, H.; Wang, Y.; Sun, L.; Yuan, X.; Chen, Y.; Shi, J. Natural Organic Matter-Induced Alleviation of the Phytotoxicity to Rice (*Oryza sativa* L.) Caused by Copper Oxide Nanoparticles. *Environ. Toxicol. Chem.* **2015**, *34* (9), 1996–2003.
- (42) Wang, Z.; Von Dem Bussche, A.; Kabadi, P. K.; Kane, A. B.; Hurt, R. H. Biological and Environmental Transformations of Copper-Based Nanomaterials. *ACS Nano* **2013**, *7* (10), 8715–8727.
- (43) Kent, R. D.; Vikesland, P. J. Dissolution and Persistence of Copper-Based Nanomaterials in Undersaturated Solutions with Respect to Cupric Solid Phases. *Environ. Sci. Technol.* **2016**, *50* (13), 6772–6781.
- (44) Printz, B.; Lutts, S.; Hausman, J.-F.; Sergeant, K. Copper Trafficking in Plants and Its Implication on Cell Wall Dynamics. *Front. Plant Sci.* **2016**, *7* (May), 1–16.
- (45) Jouvin, D.; Weiss, D. J.; Mason, T. F. M.; Bravin, M. N.; Louvat, P.; Zhao, F.; Ferec, F.;

- Hinsinger, P.; Benedetti, M. F. Stable Isotopes of Cu and Zn in Higher Plants: Evidence for Cu Reduction at the Root Surface and Two Conceptual Models for Isotopic Fractionation Processes. *Environ. Sci. Technol.* **2012**, *46* (5), 2652–2660.
- (46) Ryan, B. M.; Kirby, J. K.; Degryse, F.; Harris, H. H.; McLaughlin, M. J.; Scheiderich, K. Copper Speciation and Isotopic Fractionation in Plants: Uptake and Translocation Mechanisms. *New Phytol.* **2013**, *199* (2), 367–378.
- (47) Guerinot, M. Lou. The ZIP Family of Metal Transporters. *Biochim. Biophys. Acta - Biomembr.* **2000**, *1465* (1–2), 190–198.
- (48) Grotz, N.; Fox, T.; Connolly, E.; Park, W.; Guerinot, M. Lou; Eide, D. Identification of a Family of Zinc Transporter Genes from *Arabidopsis* That Respond to Zinc Deficiency. *Proc. Natl. Acad. Sci.* **1998**, *95* (12), 7220–7224.
- (49) Wintz, H.; Fox, T.; Wu, Y.-Y.; Feng, V.; Chen, W.; Chang, H.-S.; Zhu, T.; Vulpe, C. Expression Profiles of *Arabidopsis thaliana* in Mineral Deficiencies Reveal Novel Transporters Involved in Metal Homeostasis. *J Biol Chem* **2003**, *278* (48), 47644–47653.
- (50) Schulten, A.; Krämer, U. Interactions Between Copper Homeostasis and Metabolism in Plants. In *Progress in Botany*; Canovas, F., Luttge, U., R., M., Eds.; Springer, Cham, 2017; Vol. 79, pp 111–146.
- (51) Bugbee, B. Nutrient Management in Recirculating Hydroponic Culture. In *Acta Horticulturae*; 2004; Vol. 648, pp 99–112.
- (52) Gao, X.; Avellan, A.; Laughton, S. N.; Vaidya, R.; Rodrigues, S. M.; Casman, E. A.; Lowry, G. V. CuO Nanoparticle Dissolution and Toxicity to Wheat (*Triticum aestivum*) in Rhizosphere Soil. *Environ. Sci. Technol.* **2018**, *52* (5), 2888–2897.
- (53) Anxiang, L.; Shuzhen, Z.; Xiangyang, Q.; Wenyong, W.; Honglu, L. Aging Effect on the Mobility and Bioavailability of Copper in Soil. *J. Environ. Sci.* **2009**, *21* (2), 173–178.
- (54) Zeng, S.; Li, J.; Wei, D.; Ma, Y. A New Model Integrating Short- and Long-Term Aging of Copper Added to Soils. *PLoS One* **2017**, *12* (8), e0182944.
- (55) Gao, X.; Spielman-Sun, E.; Rodrigues, S. M.; Casman, E. A.; Lowry, G. V. Time and Nanoparticle Concentration Affect the Extractability of Cu from CuO NP Amended Soil. *Environ. Sci. Technol.* **2017**, *51* (4), 2226–2234.
- (56) Qiu, H.; Smolders, E. Nanospecific Phytotoxicity of CuO Nanoparticles in Soils Disappeared When Bioavailability Factors Were Considered. *Environ. Sci. Technol.* **2017**, *51* (20), 11976–11985.

CHAPTER 5: ACTIVE TARGETED DELIVERY OF NANOPARTICLES TO STOMATAL GUARD CELLS

Supporting Information is provided in **Appendix D**.

ABSTRACT

Plant nanobiotechnology promises transformative solutions to the most vexing problems threatening global food security, e.g. drought, disease, and soil nutrient deficiencies. However, the lack of effective methods to deliver the nanomaterials to the precise locations in plants where they are needed to be active (e.g. points of disease entry on leaves) impedes these technological innovations. Gold nanoparticles (AuNP) were coated with LM6-M, an antibody with an affinity for functional groups unique to stomata on leaf surfaces to target their delivery to stomata. One-month-old *Vicia fava* leaves were exposed via drop deposition to aqueous suspensions of LM6-M-coated AuNPs and allowed to air dry. After 2 min of rinsing with a basal salt solution, only NPs strongly adhered to the stomata remained on the leaf surface, as confirmed by darkfield-based hyperspectral imaging (DF-HSI) and x-ray fluorescence mapping (XFM). To the authors' knowledge, this is the first reported active targeting of NPs in plants *in vivo* by coating NPs with molecular recognition molecules. This proof-of-concept study provides a strategy for future targeted nanopesticide delivery research.

5.1 INTRODUCTION

The ability to tune NP surface properties has led to significant developments in the use of surface-functionalized nanoparticles as nanocarriers for targeted delivery in medical and biological research. A growing number of studies have demonstrated that “active targeting” of nanoscale drug carriers conjugated with cell-specific targeting ligands (e.g. antibodies, aptamers, peptides) can increase drug delivery to the desired site while decreasing unwanted delivery elsewhere.^{1,2} Recently, there has also been some interest in the use of NPs as delivery vehicles into plants, though most have an emphasis on tuning coating to improve plant uptake.^(e.g.3-6) Examples of organelle-specific targeting in live plants are generally limited to chloroplasts.⁷⁻⁹

Pathogen entry into host tissue is a critical first step leading to infection. Many plant pathogens are known to enter plants through natural openings (e.g. stomata, trichomes, hydathodes) or artificial openings (e.g. points of injury).¹⁰⁻¹² While spraying uncoated NPs onto leaf surfaces results in a random distribution of NPs with low affinity to any particular leaf structure, targeting antimicrobial NPs directly to these disease entry points (e.g. stomatal guard cells; **Figure 5.1**) can increase the probability of contact between the pathogen and NP. This target-specific delivery, however, requires a fundamental understanding of the surface chemistry of stomatal guard cells and its interactions with different types of NP coatings.

Plant leaves are covered with a lipophilic waxy layer (cuticle) 0.1-10 μm thick,¹³ but this layer can be thinner on the surface of guard cells and is absent on the stomatal opening.¹⁴ Though the exact chemical composition of guard cells varies between plant species, plant cell walls are generally pectin-rich.¹⁵⁻¹⁷ Using FTIR, Jones et al. identified that guard cells of *Vicia faba* are enriched in phenolic esters of pectin compared to the surrounding epidermal cells, which had a higher unesterified pectin content.¹⁸ In particular, they identified arabinose sugar content in the

stomata as being particularly high. Recently, Cornuault et al.¹⁹ have designed a monoclonal antibody with high avidity to pectic α -1,5-arabinan, which have been fluorescently tagged to image stomatal guard cell walls in fixed tissue.^{20,21} Similarly to how monoclonal antibodies tethered to NPs have been used as targeting ligands in medicine, we hypothesize that these antibodies coated onto a NP can provide targeted affinity to stomata on live plants.

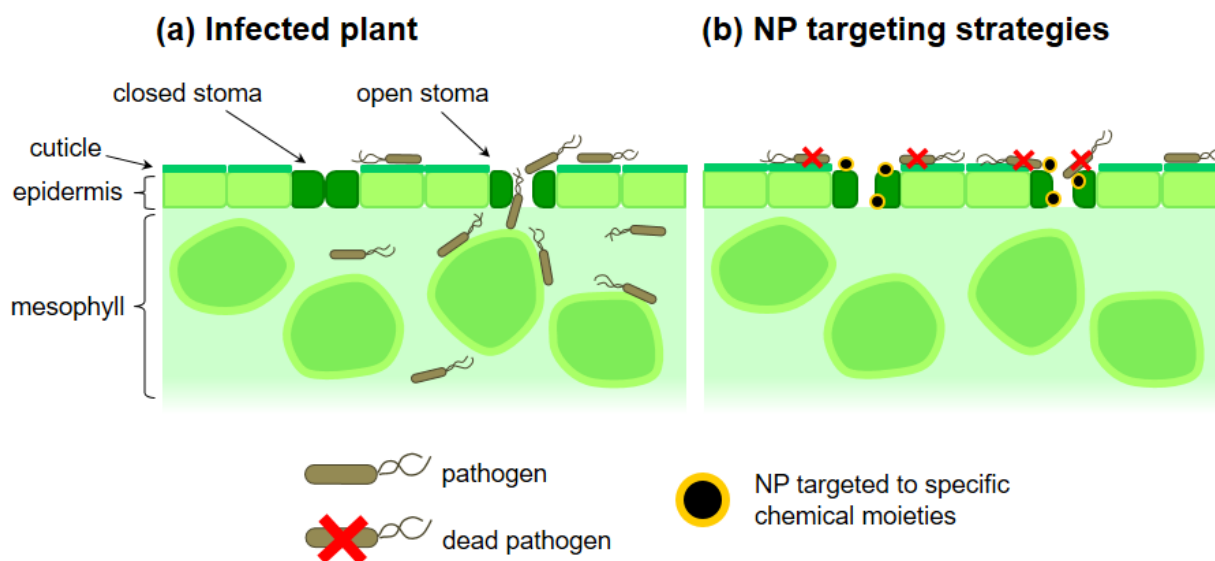


Figure 5.1 (A) Pathogens on a leaf surface can penetrate open stoma, colonizing the apoplast and spreading to other parts of the plant. (B) NPs can potentially be targeted directly to specific guard cell wall chemical moieties to prevent pathogen entry.

Overall, the goal of this study was to demonstrate targeted delivery of NPs to stomata onto live plants. Gold nanoparticles were coated with a biomolecule with affinity for α -1,5-arabinan, a chemical moiety found on stomatal guard cells. *V. faba* leaves were exposed via drop deposition, and NP distribution was evaluated using darkfield hyperspectral imaging (DF-HSI) and synchrotron X-ray fluorescence mapping (XFM) on live plant tissue. To the authors' knowledge, this is the first reported active targeting of NPs onto live plants by coating NPs with molecular recognition molecules.

5.2 MATERIALS AND METHODS

5.2.1. MATERIALS: Citrate-reduced gold were obtained from the Center for the Environmental Implications of Nanotechnology (CEINT). AuNPs were chosen for the absence of Au background in plant tissue, its stability against oxidation to ensure the absence of dissolution, and the ease of coating its metallic surface. Three monoclonal antibodies, LM6-M, LM6, and LM13, that have affinities for different epitopes of α -1,5-arabinan were purchased from Kerafast (Boston, MA) and are summarized in **Appendix D (Table D.1)**.^{19,20,22}

5.2.2. COATING ATTACHMENT PROTOCOL: The antibodies were attached to AuNPs via sorption. The antibody solution was combined with citrate-AuNP solution (200 mg/L) in a 1:1 (v/v) ratio and mixed in the dark for 48 h. Solutions were centrifuged, supernatant decanted, and resuspended twice to remove non-adhered antibody.

5.2.3. NANOPARTICLE CHARACTERIZATION: All characterization was performed on the NPs in the exposure solution. Electrophoretic mobility and number-weighted hydrodynamic diameter were measured using a Nano Zetasizer (Malvern Instruments, Malvern). UV-Vis spectra were measured using Cary Series UV-Vis-NIR spectrophotometer (Agilent, Santa Clara, CA). The primary particle size distribution was characterized by transmission electron microscopy (TEM; JEOL JEM-2000EX operating at 200 keV).

5.2.4. PLANT GROWTH AND EXPOSURE: Broad bean (*Vicia faba* cv. Windsor) seeds were obtained from Jonny's Selected Seeds (Winslow, ME). *V. faba* was chosen because it is a commonly used model plant in stomatal studies and therefore is well characterized. Seeds were surface sterilized with 10% (w/v) bleach (VWR Analytical) for 10 minutes, thoroughly rinsed with DI water, and then soaked in DI water overnight. The seeds were then planted in glass beakers with acid-washed

sand (50-70 mesh; Sigma-Aldrich). Plants were grown in a controlled environment chamber (Binder™ Model KBWF 729; day/night photoperiod 16h/8h, day/night temperature 25 °C /21 °C and 60% humidity) for 3 weeks and were watered as needed with ¼ strength Hoagland's nutrient solution. 5 µL of NP solution was dropped on the adaxial side of the plant leaf and allowed to air dry on the bench-top for 4 h. The exposed leaf was then cut-off and rinsed in a 50 mL centrifuge tube filled with a 1 mM CaCl₂ basal salt solution under gentle agitation for 2 minutes to remove loosely adhered NPs prior to further analysis.

5.2.5. DARKFIELD HYPERSPECTRAL IMAGING: The NP distribution on the leaves were visualized using darkfield-based hyperspectral imaging (DF-HSI) system. This enhanced resolution dark-field microscope system (BX51, Olympus, USA) was equipped with a 150 W halogen light source for the dark-field sample illumination (Fiber-Lite®, Dolan-Jenner, USA), and a hyperspectral camera (CytoViva Hyperspectral Imaging System 1.4). The leaves were observed with 60× magnification. Hyperspectral images were acquired using 60% light source intensity and 0.5 s acquisition time per line. Each pixel of the hyperspectral image contains its light reflectance spectrum ranging from 400 to 1000 nm with a step of 1.5 nm.

5.2.6. X-RAY FLUORESCENCE IMAGING: After exposure to LM6M-AuNPs (the most successful antibody based on hyperspectral images), fresh plant leaves were placed between two pieces of 4 µm-thick Ultralene®, which formed a seal around the plant tissue to minimize dehydration. Prior to synchrotron XFM mapping, microscope images of the drop deposition zone were taken using a Nikon Eclipse LVDIA-N in transmission bright field mode. µ-XRF maps were acquired at National Synchrotron Light Source (NSLS-II) at Brookhaven National Laboratory on XFM (4-BM). Samples were oriented 45° to incoming beam and to a four-element Vortex-ME4 silicon-drift detector. Large area (> 1 mm) maps with an incident energy of 14.5 keV were created using

a step size of 5 μm and a dwell time of 500 ms. Using GSE MapViewer in Larch (v 0.9.40),²³ Au maps were obtained using the Au L β fluorescence peak (11.4 keV) rather than the Au L α (9.7 keV) which overlaps with Zn K β (9.6 keV).

5.3 RESULTS AND DISCUSSION

5.3.1. MATERIALS CHARACTERIZATION: The TEM images of the citrate-AuNPs and LM6M-NPs shown in **Figure 5.2 A** and **B**, confirm the presence of a heterogeneous organic coating \sim 1-5 nm thick. Additional particle characteristics are presented in **Table 5.1**. The primary particle diameter remained the same after being coated. The increase in hydrodynamic radii and λ_{max} shift in the UV-Vis spectra (**Figure 5.2 C**) confirm the presence of the coating. There is a slight decrease in electrophoretic mobility (and calculated zeta potential), but the difference is not statistically significant. Nonetheless, a lower EPM (and therefore zeta potential) is consistent with the adsorption of a macromolecule like the LM6-M.^{24,25}

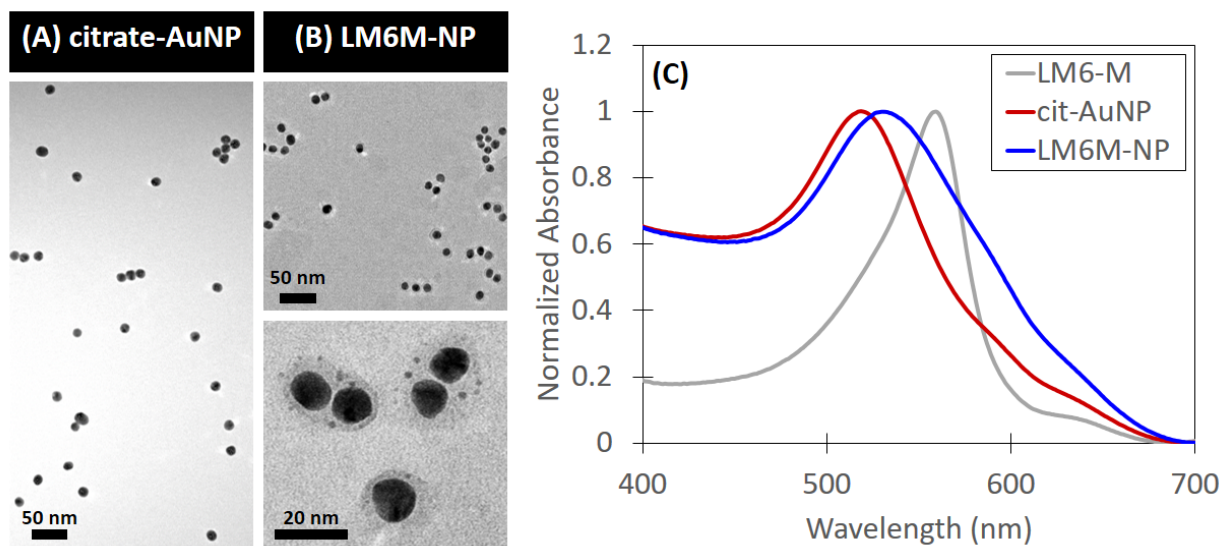


Figure 5.2: TEM images of (A) citrate-NPs and (B) LM6M-NPs. (C) Normalized UV-Vis spectra of LM6-M antibody, citrate-AuNP, and LM6M-NP. No measurements were made for the other antibodies.

Table 5.1: Summary of citrate-AuNP and LM6M-NP solution characterization. No measurements were made for the other antibodies.

Sample	TEM Diameter (nm)	Hydrodynamic diameter (nm)	Electrophoretic mobility ($\mu\text{m}\cdot\text{cm}\cdot\text{V}^{-1}\cdot\text{s}^{-1}$)	Zeta Potential (mV)	UV-Vis λ_{max} (nm)
citrate-AuNP	12.6 ± 1.0	25.8 ± 7.6	-2.77 ± 0.38	-35.5 ± 4.9	519
LM6M-NP	11.6 ± 1.2	81.2 ± 25.4	-2.42 ± 0.43	-31.0 ± 5.5	531

5.3.2. MICROSCOPE IMAGES OF AUNPS ON LEAF SURFACE: Light microscope images of *V. faba* leaves are shown in **Figure 5.3**, with stomata indicated with red arrows. Stomata were identified by their distinct, kidney-bean shaped cells.

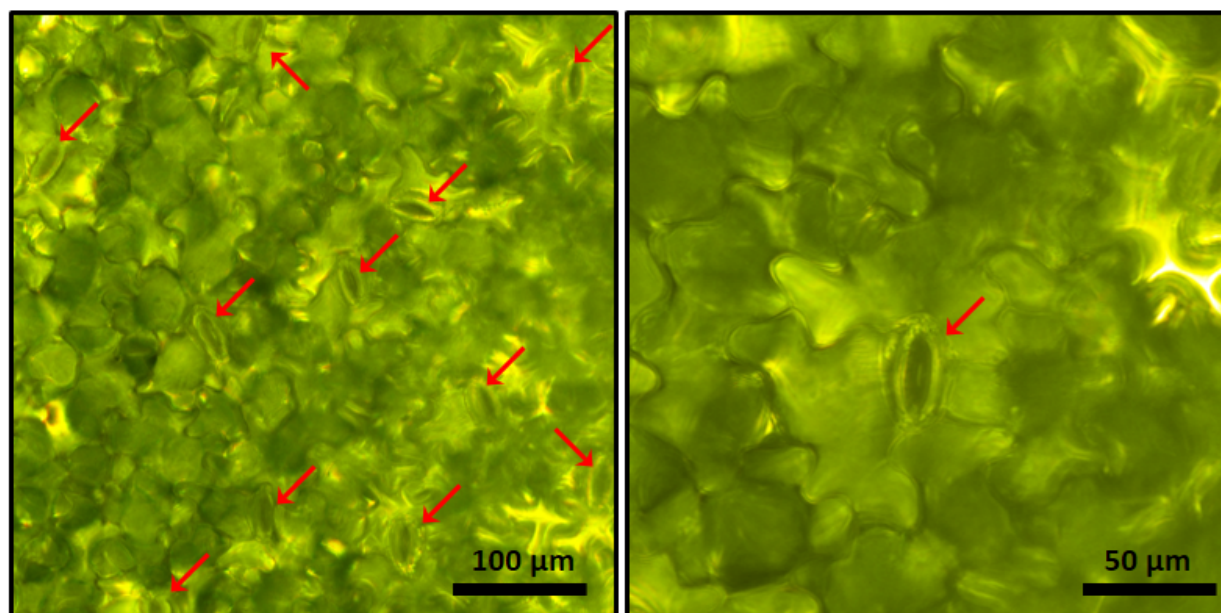


Figure 5.3. Light microscope images of the adaxial side of a *V. faba* leaf exposed via drop deposition to DI water as a control. Stomata are indicated with red arrows.

Darkfield microscopy images of *V. faba* leaves exposed to LM6M-NP, LM6-NP, LM13-NP or DI water (as a control) are shown in **Figure 5.4**. While in all treatments there was colocalization of NPs and stomata, only the LM6M-NP treatment showed isolated accumulation around the stomata and not elsewhere on the leaf. In contrast, LM13-NP, which prefers longer, linear arabinans,²⁰ primarily accumulated along the spaces between the epidermal cells where the cuticle

can be thinner¹⁴ and possibly enabling greater interaction with the antibody. LM6-M has a higher avidity (binding strength between the antibody and antigen) than LM6,¹⁹ which likely explains the selectivity of LM6M-NPs to stomata and not to other structures. Because LM6M-NP was the most successful, this coating was further analyzed by XFM.

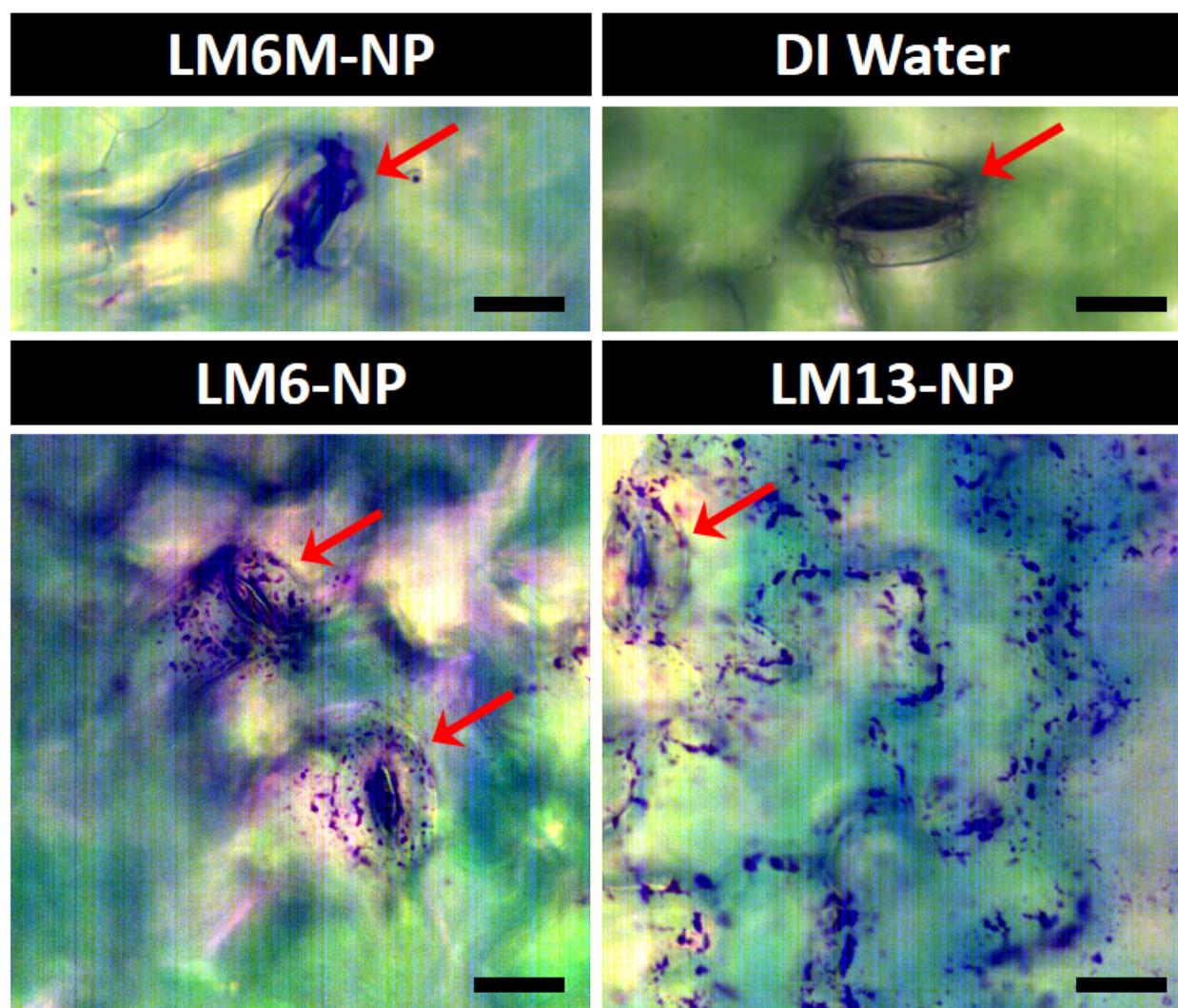


Figure 5.4. Darkfield microscopy images of the adaxial side of a *V. faba* leaf exposed via drop deposition to LM6M-NP, DI water (control), LM13-NP, or LM6-NP, then rinsed for 2 min in a basal salt solution. Stomata are indicated with red arrows. Scale bar = 20 μm .

5.3.3. X-RAY FLUORESCENCE MAPS: XFM map showing Au distribution after exposure to LM6M-NP is shown in **Figure 5.5**. Au clearly accumulates around numerous stomata (stomata

are indicated by red arrows), though there is also some additional adherence to other leaf features, possibly trichomes or other protein-rich features of the leaf where the cuticle is thin/absent.¹⁴ Higher magnification light microscope image confirming the accumulation of Au with a stomata is shown in **Appendix D (Figure D.1)**. This suggests that the antibody coating was successfully able to deliver NPs to the stomata in a targeted manner. However, a control using BSA-coated or other protein-coated NPs would be needed to confirm that the attachment is due to antibody-antigen specific interactions and not due to hydrophilic or other non-specific interactions.

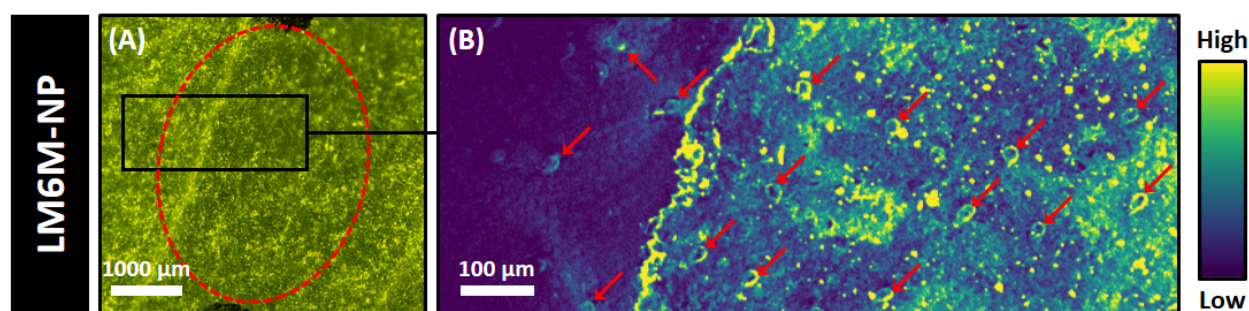


Figure 5.5. Adaxial side of a *V. faba* leaf exposed via drop deposition to LM6M-NP solution then rinsed for 2 min in a basal salt solution. (A) Light microscope image of drop deposition zone (region between the black pen dots, indicated with red dashed oval) and region analyzed by XFM (indicated by the black box). (B) Elemental maps showing total Au distribution, with color scale shown on the right. Targeted stomata are indicated with red arrows.

5.4 FUTURE WORK

This chapter demonstrated the successful targeted delivery of AuNPs to stomata on fresh *V. faba* leaves by coating NPs with an antibody with an affinity for α -1,5-arabinan, a chemical moiety found on stomatal guard cells. Though similar targeting has been used in nanomedicine, this is the first proof-of-concept study with plants. This is the first step in testing the hypothesis that a targeted approach is more effective than conventional pesticide applications. Future studies can build off this work by using either antimicrobial NPs (e.g. CuO, Ag) or nanocarriers loaded with a pesticide.

Overall, massive innovations in pesticide and nutrient delivery systems in agriculture are needed to minimize wasted energy and water inputs resulting from inefficient use of fertilizers and pesticides. The ability to provide delivery of pesticides to precise locations in the plant will revolutionize the way that agrochemicals are applied, providing greater efficacy, higher yields, and fewer off-target side effects (e.g. environmental degradation).

5.5 REFERENCES FOR CHAPTER 5

- (1) Dai, Q.; Bertleff-Zieschang, N.; Braunger, J. A.; Björnmalm, M.; Cortez-Jugo, C.; Caruso, F. Particle Targeting in Complex Biological Media. *Adv. Healthc. Mater.* **2017**, *7* (1), 1700575.
- (2) McClements, D. J. Delivery by Design (DbD): A Standardized Approach to the Development of Efficacious Nanoparticle- and Microparticle-Based Delivery Systems. *Compr. Rev. Food Sci. Food Saf.* **2018**, *17* (1), 200–219.
- (3) Karny, A.; Zinger, A.; Kajal, A.; Shainsky-Roitman, J.; Schroeder, A. Therapeutic Nanoparticles Penetrate Leaves and Deliver Nutrients to Agricultural Crops. *Sci. Rep.* **2018**, *8* (1), 7589.
- (4) Torney, F.; Trewyn, B. G.; Lin, V. S.-Y.; Wang, K. Mesoporous Silica Nanoparticles Deliver DNA and Chemicals into Plants. *Nat. Nanotechnol.* **2007**, *2* (5), 295–300.
- (5) Liu, G.; Yu, M.; Wang, Y.; Yao, J.; Cui, H.; Liang, J.; Zeng, Z.; Cui, B.; Sun, C.; Zhao, X. Development of Functionalized Abamectin Poly(Lactic Acid) Nanoparticles with Regulatable Adhesion to Enhance Foliar Retention. *RSC Adv.* **2017**, *7* (19), 11271–11280.
- (6) Avellan, A.; Yun, J.; Zhang, Y.; Spielman-Sun, E.; Unrine, J. M.; Thieme, J.; Li, J.; Lombi, E.; Bland, G.; Lowry, G. V. Nanoparticle Size and Coating Chemistry Control Foliar Uptake Pathways, Translocation and Leaf-to-Rhizosphere Transport in Wheat. *ACS Nano* **2019**, *accepted*.
- (7) Wu, H.; Tito, N.; Giraldo, J. P. Anionic Cerium Oxide Nanoparticles Protect Plant Photosynthesis from Abiotic Stress by Scavenging Reactive Oxygen Species. *ACS Nano* **2017**, *11* (11), 11283–11297.
- (8) Giraldo, J. P.; Landry, M. P.; Faltermeier, S. M.; McNicholas, T. P.; Iverson, N. M.; Boghossian, A. A.; Reuel, N. F.; Hilmer, A. J.; Sen, F.; Brew, J. A.; et al. Plant Nanobionics Approach to Augment Photosynthesis and Biochemical Sensing. *Nat. Mater.* **2014**, *13* (4), 400–408.
- (9) Kwak, S.-Y.; Lew, T. T. S.; Sweeney, C. J.; Koman, V. B.; Wong, M. H.; Bohmert-Tatarev, K.; Snell, K. D.; Seo, J. S.; Chua, N.-H.; Strano, M. S. Chloroplast-Selective Gene Delivery and Expression in Planta Using Chitosan-Complexed Single-Walled Carbon Nanotube Carriers. *Nat. Nanotechnol.* **2019**.

- (10) Melotto, M.; Underwood, W.; He, S. Y. Role of Stomata in Plant Innate Immunity and Foliar Bacterial Diseases. *Annu. Rev. Phytopathol.* **2008**, *46* (1), 101–122.
- (11) Melotto, M.; Underwood, W.; Koczan, J.; Nomura, K.; Yang He, S.; He, S. Y. Plant Stomata Function in Innate Immunity against Bacterial Invasion. *Cell* **2006**, *126* (5), 969–980.
- (12) Sundin, G. W.; Castiblanco, L. F.; Yuan, X.; Zeng, Q.; Yang, C. H. Bacterial Disease Management: Challenges, Experience, Innovation and Future Prospects: Challenges in Bacterial Molecular Plant Pathology. *Mol. Plant Pathol.* **2016**, *17* (9), 1506–1518.
- (13) Kirkwood, R. C. Recent Developments in Our Understanding of the Plant Cuticle as a Barrier to the Foliar Uptake of Pesticides. *Pestic. Sci.* **1999**, *55* (1), 69–77.
- (14) Bird, S. M.; Gray, J. E. Signals from the Cuticle Affect Epidermal Cell Differentiation. *New Phytol.* **2003**, *157* (1), 9–23.
- (15) Burton, R. A.; Gidley, M. J.; Fincher, G. B. Heterogeneity in the Chemistry, Structure and Function of Plant Cell Walls. *Nat. Chem. Biol.* **2010**, *6* (10), 724–732.
- (16) Harholt, J.; Suttangkakul, A.; Vibe Scheller, H. Biosynthesis of Pectin. *Plant Physiol.* **2010**, *153* (2), 384–395.
- (17) Shtein, I.; Shelef, Y.; Marom, Z.; Zelinger, E.; Schwartz, A.; Popper, Z. A.; Bar-On, B.; Harpaz-Saad, S. Stomatal Cell Wall Composition: Distinctive Structural Patterns Associated with Different Phylogenetic Groups. *Ann. Bot.* **2017**, *119* (6), 1021–1033.
- (18) Jones, L.; Milne, J. L.; Ashford, D.; McCann, M. C.; McQueen-Mason, S. J. A Conserved Functional Role of Pectic Polymers in Stomatal Guard Cells from a Range of Plant Species. *Planta* **2005**, *221* (2), 255–264.
- (19) Cornuault, V.; Buffet, F.; Marcus, S. E.; Fabienne, M. C.; Ralet, G. M.; Knox, J. P. LM6-M: A High Avidity Rat Monoclonal Antibody to Pectic α -1,5-L-Arabinan. *bioRxiv* **2017**, 1–11.
- (20) Verhertbruggen, Y.; Marcus, S. E.; Haeger, A.; Verhoef, R.; Schols, H. A.; McCleary, B. V.; McKee, L.; Gilbert, H. J.; Knox, J. P. Developmental Complexity of Arabinan Polysaccharides and Their Processing in Plant Cell Walls. *Plant J.* **2009**, *59* (3), 413–425.
- (21) Rossez, Y.; Holmes, A.; Lodberg-Pedersen, H.; Birse, L.; Marshall, J.; Willats, W. G. T.; Toth, I. K.; Holden, N. J. *Escherichia coli* Common Pilus (ECP) Targets Arabinosyl Residues in Plant Cell Walls to Mediate Adhesion to Fresh Produce Plants. *J. Biol. Chem.* **2014**, *289* (49), 34349–34365.
- (22) Willats, W. G. T.; Marcus, S. E.; Knox, J. P. Generation of a Monoclonal Antibody Specific to (1→5)- α -l-Arabinan. *Carbohydrate Research.* **1998**, *308* (1-2), 149–152.
- (23) Newville, M. Larch: An Analysis Package for XAFS and Related Spectroscopies. In *Journal of Physics: Conference Series*; IOP Publishing, 2013; Vol. 430, p 012007.
- (24) Louie, S. M.; Tilton, R. D.; Lowry, G. V. Critical Review: Impacts of Macromolecular Coatings on Critical Physicochemical Processes Controlling Environmental Fate of Nanomaterials. *Environ. Sci. Nano* **2016**, *3* (2), 283–310.
- (25) Louie, S. M.; Phenrat, T.; Small, M. J.; Tilton, R. D.; Lowry, G. V. Parameter

Identifiability in Application of Soft Particle Electrokinetic Theory to Determine Polymer and Polyelectrolyte Coating Thicknesses on Colloids. *Langmuir* **2012**, 28 (28), 10334–10347.

**CHAPTER 6: SUMMARY OF MAJOR
CONTRIBUTIONS AND PERSPECTIVES FOR
FUTURE RESEARCH**

6.1 SUMMARY OF MAJOR CONTRIBUTIONS

This dissertation has made several major contributions that improve our understanding of plant uptake, transformation, and translocation of NP. Novel insights from this work are summarized here.

6.1.1. MAJOR CONTRIBUTIONS OF OBJECTIVE 1: *Evaluate the influence of surface charge on CeO₂ NP uptake, distribution, and speciation in wheat.*

1. Cerium dioxide nanoparticle surface charge has a significant impact on Ce distribution in wheat leaves. Though previous studies have demonstrated that positively charged NPs adhere to roots more strongly but negatively charged NPs translocate more efficiently,¹⁻³ this is the first study to compare differences in NP spatial distribution in leaf tissue due to NP surface charge. The majority of the Ce in the CeO₂(-) NP exposed plant was found in the veins of the leaf tip, suggesting apoplastic transport through the main xylem of the plant tissue. In the CeO₂(0) exposed plant, Ce remained in clusters outside of the main leaf vasculature. More broadly, these results suggest that there are different translocation routes for differently charged particles within the plant tissue. Possible mechanisms for these observed differences are discussed in **Section 6.2.1**.

6.1.2. MAJOR CONTRIBUTIONS OF OBJECTIVE 2: *Compare the influence of surface charge on CeO₂ NP root uptake, distribution, and speciation in monocotyledonous and dicotyledonous plants*

2. While surface charge plays an important role in NP uptake (as discussed in Objective 1), different plant architectures between monocots and dicots also lead to different uptake rates and NP distribution in leaves. Though many published studies have focused on NP uptake by plant roots, the observations made in one plant species are often difficult to generalize

to other plants. Across the four plant species analyzed in this study, higher Ce uptake correlated with higher transpiration rates. With regards to surface charge, the positive and neutral treatments resulted in the formation of Ce clusters outside of the main vasculature in the mesophyll of the leaves, while the negative treatment resulted in Ce primarily in the main vasculature. Comparing leaf vasculature, Ce was able to move much further outside of the main vasculature in the dicot plants than monocot plants, likely due to the larger airspace volume in dicot leaves compared to monocot leaves. This knowledge of surface charge could be applied to other types of nanoparticles as part of smart delivery systems for targeted delivery of nutrients to specific plant organs for different types of plants.

6.1.3. MAJOR CONTRIBUTIONS OF OBJECTIVE 3: *Determine the influence of Cu-based NP solubility on metal distribution and speciation over time*

3. Low-solubility copper nanoparticles are able to persist on the root surface. Numerous papers have posited the theory that NPs have the potential to provide a slow-release delivery of micronutrients to plants.⁴⁻⁷ However, there is limited work demonstrating this for agriculture.^(eg 8-10) In particular, detailed studies comparing the NP- plant associations and NP-derived metal uptake in plants exposed to NPs of different solubility are lacking. Higher 1-h solubility Cu(OH)₂ NPs provided more immediate Cu to the plant after 1 h of exposure and the Cu was quickly biotransformed. In contrast, the lower 1-h solubility CuO and CuS NPs were more persistent over the 48 h post-exposure period, with as much as 80% of the Cu NP on the root surfaces untransformed. These results suggest that NP solubility can be tuned via composition to control how rapidly NPs, or metals derived from them, can be made bioavailable.

4. The initial nanoparticle composition influences copper speciation within plant roots.

Though numerous hydroponic studies have investigated the accumulation and translocation of CuO NPs in plants, generally with an emphasis on toxicity,^(e.g. 11–14) few provide insight into the changes in Cu speciation.^{15,16} Despite having similar solubilities, the Cu in plants exposed to CuS NPs was mostly reduced and/or sulfidized Cu while the Cu in the CuO NP exposed plants remained oxidized. These differences in Cu speciation will subsequently affect the bioavailability of the Cu depending on natural plant strategies for transporting/sequestering Cu, since plants have different translocation mechanisms for Cu(I) vs Cu(II).^{17,18} Overall, these observed speciation differences suggests that Cu toxicity to plants and Cu uptake and translocation by plants may be controllable by engineering the initial speciation of the Cu-based NP.

6.1.4 MAJOR CONTRIBUTIONS OF OBJECTIVE 4: *Determine how coating can be modified to increase NP adherence to stomata*

5. Tuning NP surface properties can provide stomata targeting by increasing stomatal guard

cell-NP association. In medicine, “active targeting” of nanoscale drug carriers conjugated with cell-specific targeting ligands (e.g. antibodies, aptamers, peptides) can increase drug delivery to the desired site.^{19,20} Though there has also been some interest in the use of NPs as delivery vehicles into plants, examples of organelle-specific targeting in live plants are limited.^{21–23} This study is the first report of active targeting of NPs in plants *in vivo* by coating NPs with molecular recognition molecules. This proof-of-concept study provides a strategy for future research into targeted nanopesticide delivery that is more efficient.

6.2 PERSPECTIVES FOR FUTURE RESEARCH

Meeting the world's growing demand for food and energy without undue pollution pressures on soil, air and water is one of the greatest challenges of our age. Massive innovations in pesticide and nutrient delivery systems in agriculture are needed to achieve an atom-efficient system where each nutrient and pesticide input is translated into healthy crop growth rather than being lost to the surrounding ecosystem. This thesis provides valuable mechanistic insight into the influence of fundamental NP properties on NP-plant interactions in highly controlled systems and adds to the growing body of literature touting the proposed benefits of nanotechnology for agriculture. Despite this significant progress, there are still limited examples of successful field trials and very few products that actually reach the market. Outlined here are some key challenges that will need to be overcome before any of these novel technologies can be implemented on agricultural scales.

6.2.1 FUTURE RESEARCH FOR OBJECTIVE 1: *Evaluate the influence of surface charge on CeO₂ NP uptake, distribution, and speciation in wheat*

As summarized in **Section 6.1.1**, the Ce in the leaves was found mostly in the veins of the CeO₂(-) NP exposed plant while Ce was found in clusters in the nonvascular leaf tissue of the CeO₂(0) NP exposed plant. However, the exact mechanism for this difference in distribution requires further investigation. Charge can affect transport through plants depending on the transport pathway. Majority of studies using isolated plant cells have suggested that endocytosis (active) pathways are involved in NP uptake. Though these mechanisms are well characterized in animal cells, they are less so in plants. In clathrin-dependent (or receptor-mediated) endocytosis, the substrate binds to receptors on the plasma membrane is absorbed via inward budding into the formation of clathrin-coated vesicles.²⁴ This mechanism, which has been observed for variously charged NPs in isolated plant protoplasts (plant cells without a cell wall), favors positively-charged

NPs over negatively-charged NPs.²⁵⁻²⁸ If the CeO₂(+) and CeO₂(0) NPs are more effectively endocytosed, these particles may be able to move out of the vasculature more easily, thus explaining the observed clustering of Ce outside of the veins in the plant leaves. Further studies using plant cells with intact cell walls would be needed to confirm that this charge-related selectivity still holds.

NP surface charge also plays a role in passive transport. The few examples of passive transport of NPs into plant cells suggest that highly negative or positive particles are able to cross cell membranes more easily than neutral particles by perturbing the membrane potential.²⁹⁻³¹ Giraldo et al. observed higher uptake of charged single-walled carbon nanotubes (CNTs; ζ -potentials of -44.6 mV and +48.5 mV) than neutral CNTs (ζ -potential= -6.4 mV) into chloroplasts of *Spinacia oleraceae* L.³² Wu et al also observed higher transport of CeO₂ NPs into chloroplasts in *Arabidopsis thaliana* that were anionic (ζ -potential= -16.9 mV) compared to NPs that were relatively neutral/ cationic (ζ -potential= +9.6 mV).³³ Proper design of NP coating for targeted delivery to different plant organelles will require a better understanding of the relative importance of these cellular uptake and intracellular tracking processes.

6.2.2 FUTURE RESEARCH FOR OBJECTIVE 2: *Compare the influence of surface charge on CeO₂ NP root uptake, distribution, and speciation in monocotyledonous and dicotyledonous plants*

The distinct spatial distribution in leaves depending on NP surface charge has implications for improved pesticide delivery. Because many plant-pathogenic bacteria are known to infect the phloem and xylem tissues, many attempts have been made to develop phloem-mobile pesticides. However, most of these efforts have been on structural modifications of existing pesticide structures with phloem-mobile derivatives.³⁴ As an example, *Xanthomonas campestris* pv *campestris* (*Xcc*) is a vascular pathogen that causes black rot in cruciferous vegetables that does

not respond well to traditional chemical/pesticide control methods^{35,36} but could potentially be better managed with antimicrobial NPs (e.g. silver or copper based) or nanocarriers loaded with pesticides that are coated to target the plant vasculature. Further experiments would be needed to confirm if manipulating surface functionality to promote xylem/phloem loading protects plants against these vascular pathogens better than commercial products.

6.2.3 FUTURE RESEARCH FOR OBJECTIVE 3: *Determine the influence of Cu-based NP solubility on metal distribution and speciation over time*

This persistence of untransformed NP on roots has potential implications for improving micronutrient utilization efficiency in commercial hydroponics systems. Many hydroponics systems recirculate and reuse nutrient solutions in order to reduce environmental and economic costs.³⁷ By using persistent, slow delivery materials such as low solubility NPs, micronutrients can potentially be applied directly to the roots and less frequently than conventional ionic materials, which would save costs on application and improve utilization efficiency. A long term study using a larger hydroponic setup would be needed to evaluate if these low soluble materials reduce the number of needed applications and/or improve nutrient use efficiency in a cost-effective way.

Given how complex NP-soil interactions can be, extending the results of this study from hydroponics to soil matrices is difficult, particularly with the numerous limitations of soil application (e.g. poor nutrient availability in neutral to basic soils,^{38,39} losses due to soil leaching^{40,41}). These soil application limitations, however, can potentially be overcome through the use of foliar application, which have been shown to increase plant growth,^{42,43} protect against reactive oxygen species generation,³³ improve photosynthesis,³² and reduce crop losses in infested soils.^{10,44,45} In particular, relatively low solubility NPs, similar to the CuO or CuS NPs used in this study, have been shown to slowly provide nutrients and could potentially minimize leaf burn or

other phytotoxic effects often observed with foliarly applied salts.^{46,47} Further experiments would be needed to compare the ability of foliarly applied Cu-NPs and ionic Cu to deliver micronutrients to plants over an entire plant's life cycle.

6.2.4 FUTURE RESEARCH FOR OBJECTIVE 4: *Determine how coating can be modified to increase NP adherence to stomata*

The work presented in Chapter 5 is the first step in testing the hypothesis that a targeted pesticide approach is more effective than conventional application methods. Future studies can build off this work by using either antimicrobial NPs (e.g. Ag- or Cu-based) or nanocarriers loaded with a pesticide. To determine targeting efficiency, the amount of adhered NP as a percent of total applied NP would need to be measured. Antimicrobial efficacy against model pathogens, such as *Pseudomonas syringae* or other foliar pathogens known to enter via stomata,⁴⁸ would need to be compared with non-coated NPs, bulk formulations of the chemical materials, and a chemical pesticide.

Finally, many novel technologies in the nanoagro-field are prohibitively expensive, which prevents their widespread use.^{49,50} In the case of human medical applications, a (relatively) high production cost can be accepted, but that is not possible for agriculture. Antibodies, though ideal for research on determining the types of chemical moieties that can afford targeted delivery, are relatively expensive and impractical for a commercial agrochemical product. Future experiments would need to experiment with other antibodies to gain enough insight into the binding patterns between the NP coating and stomatal guard cells in order to design polymers or aptamers⁵¹ that are able to provide the same targeting at a lower cost.

6.3 REFERENCES FOR CHAPTER 6

- (1) Zhu, Z.-J.; Wang, H.; Yan, B.; Zheng, H.; Jiang, Y.; Miranda, O. R.; Rotello, V. M.; Xing, B.; Vachet, R. W. Effect of Surface Charge on the Uptake and Distribution of Gold Nanoparticles in Four Plant Species. *Environ. Sci. Technol.* **2012**, *46* (22), 12391–12398.
- (2) Wang, J.; Yang, Y.; Zhu, H.; Braam, J.; Schnoor, J. L.; Alvarez, P. J. J. Uptake, Translocation, and Transformation of Quantum Dots with Cationic versus Anionic Coatings by *Populus deltoides* × *nigra* Cuttings. *Environ. Sci. Technol.* **2014**, *48* (12), 6754–6762.
- (3) Li, H.; Ye, X.; Guo, X.; Geng, Z.; Wang, G. Effects of Surface Ligands on the Uptake and Transport of Gold Nanoparticles in Rice and Tomato. *J. Hazard. Mater.* **2016**, *314*, 188–196.
- (4) Servin, A. D.; Elmer, W. H.; Mukherjee, A.; De La Torre-Roche, R.; Hamdi, H.; White, J. C.; Bindraban, P. S.; Dimkpa, C. O. A Review of the Use of Engineered Nanomaterials to Suppress Plant Disease and Enhance Crop Yield. *J. Nanoparticle Res.* **2015**, *17* (2), 92.
- (5) Dimkpa, C. O.; Bindraban, P. S. Fortification of Micronutrients for Efficient Agronomic Production: A Review. *Agron. Sustain. Dev.* **2016**, *36* (1), 1–26.
- (6) Milani, N.; McLaughlin, M. J.; Stacey, S. P.; Kirby, J. K.; Hettiarachchi, G. M.; Beak, D. G.; Cornelis, G. Dissolution Kinetics of Macronutrient Fertilizers Coated with Manufactured Zinc Oxide Nanoparticles. *J. Agric. Food Chem.* **2012**, *60* (16), 3991–3998.
- (7) Monreal, C. M.; DeRosa, M. C.; Mallubhotla, S. C.; Bindraban, P. S.; Dimkpa, C. O. Nanotechnologies for Increasing the Crop Use Efficiency of Fertilizer-Micronutrients. *Biol. Fertil. Soils* **2016**, *52* (3), 423–437.
- (8) Bandyopadhyay, S.; Ghosh, K.; Varadachari, C. Multimicronutrient Slow-Release Fertilizer of Zinc, Iron, Manganese, and Copper. *Int. J. Chem. Eng.* **2014**, *2014*, 1–7.
- (9) Giannousi, K.; Avramidis, I.; Dendrinou-Samara, C. Synthesis, Characterization and Evaluation of Copper Based Nanoparticles as Agrochemicals against *Phytophthora infestans*. *RSC Adv.* **2013**, *3* (44), 21743–21752.
- (10) Elmer, W. H.; White, J. C. The Use of Metallic Oxide Nanoparticles to Enhance Growth of Tomatoes and Eggplants in Disease Infested Soil or Soilless Medium. *Environ. Sci. Nano* **2016**, *3* (5), 1072–1079.
- (11) Adams, J.; Wright, M.; Wagner, H.; Valiente, J.; Britt, D. W.; Anderson, A. J. Cu from Dissolution of CuO Nanoparticles Signals Changes in Root Morphology. *Plant Physiol. Biochem.* **2017**, *110*, 108–117.
- (12) Hong, J.; Rico, C. M.; Zhao, L.; Adeleye, A. S.; Keller, A. A.; Peralta-Videa, J. R.; Gardea-Torresdey, J. L. Toxic Effects of Copper-Based Nanoparticles or Compounds to Lettuce (*Lactuca sativa*) and Alfalfa (*Medicago sativa*). *Environ. Sci. Process. Impacts* **2015**, *17* (1), 177–185.
- (13) Wang, Z.; Xie, X.; Zhao, J.; Liu, X.; Feng, W.; White, J. C.; Xing, B. Xylem- and Phloem-Based Transport of CuO Nanoparticles in Maize (*Zea mays* L.). *Environ. Sci. Technol.* **2012**, *46* (8), 4434–4441.

- (14) Dimkpa, C. O.; McLean, J. E.; Latta, D. E.; Manangon, E.; Britt, D. W.; Johnson, W. P.; Boyanov, M. I.; Anderson, A. J. CuO and ZnO Nanoparticles: Phytotoxicity, Metal Speciation, and Induction of Oxidative Stress in Sand-Grown Wheat. *J. Nanoparticle Res.* **2012**, *14* (9), 1125–1129.
- (15) Lu, L.; Xie, R.; Liu, T.; Wang, H.; Hou, D.; Du, Y.; He, Z.; Yang, X.; Sun, H.; Tian, S. Spatial Imaging and Speciation of Cu in Rice (*Oryza sativa* L.) Roots Using Synchrotron-Based X-Ray Microfluorescence and X-Ray Absorption Spectroscopy. *Chemosphere* **2017**, *175*, 356–364.
- (16) Peng, C.; Duan, D.; Xu, C.; Chen, Y.; Sun, L.; Zhang, H.; Yuan, X.; Zheng, L.; Yang, Y.; Yang, J.; et al. Translocation and Biotransformation of CuO Nanoparticles in Rice (*Oryza sativa* L.) Plants. *Environ. Pollut.* **2015**, *197*, 99–107.
- (17) Printz, B.; Lutts, S.; Hausman, J.-F.; Sergeant, K. Copper Trafficking in Plants and Its Implication on Cell Wall Dynamics. *Front. Plant Sci.* **2016**, *7* (May), 1–16.
- (18) Schulten, A.; Krämer, U. Interactions Between Copper Homeostasis and Metabolism in Plants. In *Progress in Botany*; Canovas, F., Luttge, U., R., M., Eds.; Springer, Cham, 2017; Vol. 79, pp 111–146.
- (19) Dai, Q.; Bertleff-Zieschang, N.; Braunger, J. A.; Björnmalm, M.; Cortez-Jugo, C.; Caruso, F. Particle Targeting in Complex Biological Media. *Adv. Healthc. Mater.* **2017**, *7* (1), 1700575.
- (20) McClements, D. J. Delivery by Design (DbD): A Standardized Approach to the Development of Efficacious Nanoparticle- and Microparticle-Based Delivery Systems. *Compr. Rev. Food Sci. Food Saf.* **2018**, *17* (1), 200–219.
- (21) Cunningham, F. J.; Goh, N. S.; Demirer, G. S.; Matos, J. L.; Landry, M. P. Nanoparticle-Mediated Delivery towards Advancing Plant Genetic Engineering. *Trends Biotechnol.* **2018**, *36* (9), 882–897.
- (22) Kwak, S.-Y.; Lew, T. T. S.; Sweeney, C. J.; Koman, V. B.; Wong, M. H.; Bohmert-Tatarev, K.; Snell, K. D.; Seo, J. S.; Chua, N.-H.; Strano, M. S. Chloroplast-Selective Gene Delivery and Expression in Planta Using Chitosan-Complexed Single-Walled Carbon Nanotube Carriers. *Nat. Nanotechnol.* **2019**.
- (23) Giraldo, J. P.; Weidman, M. C.; Landry, M. P.; Wong, M. H.; Kwak, S.-Y.; Lew, T. T. S.; Koman, V. B.; Ell, J.; Tisdale, W. A.; Strano, M. S. A Nanobionic Light-Emitting Plant. *Nano Lett.* **2017**, *17* (12), 7951–7961.
- (24) Gratton, S. E. A.; Ropp, P. A.; Pohlhaus, P. D.; Luft, J. C.; Madden, V. J.; Napier, M. E.; DeSimone, J. M. The Effect of Particle Design on Cellular Internalization Pathways. *Proc. Natl. Acad. Sci. U. S. A.* **2008**, *105* (33), 11613–11618.
- (25) Onelli, E.; Prescianotto-Baschong, C.; Caccianiga, M.; Moscatelli, A. Clathrin-Dependent and Independent Endocytic Pathways in Tobacco Protoplasts Revealed by Labelling with Charged Nanogold. *J. Exp. Bot.* **2008**, *59* (11), 3051–3068.
- (26) Etxeberria, E.; Gonzalez, P.; Baroja-Fernandez, E.; Romero, J. P. Fluid Phase Endocytic Uptake of Artificial Nano-Spheres and Fluorescent Quantum Dots by Sycamore Cultured Cells: Evidence for the Distribution of Solutes to Different Intracellular Compartments.

- Plant Signal. Behav.* **2006**, *1* (4), 196–200.
- (27) Torney, F.; Trewyn, B. G.; Lin, V. S.-Y.; Wang, K. Mesoporous Silica Nanoparticles Deliver DNA and Chemicals into Plants. *Nat. Nanotechnol.* **2007**, *2* (5), 295–300.
- (28) Moscatelli, A.; Ciampolini, F.; Rodighiero, S.; Onelli, E.; Cresti, M.; Santo, N.; Idilli, A. Distinct Endocytic Pathways Identified in Tobacco Pollen Tubes Using Charged Nanogold. *J. Cell Sci.* **2007**, *120* (Pt 21), 3804–3819.
- (29) Wong, M. H.; Misra, R. P.; Giraldo, J. P.; Kwak, S. Y.; Son, Y.; Landry, M. P.; Swan, J. W.; Blankschtein, D.; Strano, M. S. Lipid Exchange Envelope Penetration (LEEP) of Nanoparticles for Plant Engineering: A Universal Localization Mechanism. *Nano Lett.* **2016**, *16* (2), 1161–1172.
- (30) Arvizo, R. R.; Miranda, O. R.; Thompson, M. A.; Pabelick, C. M.; Bhattacharya, R.; David Robertson, J.; Rotello, V. M.; Prakash, Y. S.; Mukherjee, P. Effect of Nanoparticle Surface Charge at the Plasma Membrane and Beyond. *Nano Lett.* **2010**, *10* (7), 2543–2548.
- (31) Lin, J.; Zhang, H.; Chen, Z.; Zheng, Y. Penetration of Lipid Membranes by Gold Nanoparticles: Insights into Cellular Uptake, Cytotoxicity, and Their Relationship. *ACS Nano* **2010**, *4* (9), 5421–5429.
- (32) Giraldo, J. P.; Landry, M. P.; Faltermeier, S. M.; McNicholas, T. P.; Iverson, N. M.; Boghossian, A. A.; Reuel, N. F.; Hilmer, A. J.; Sen, F.; Brew, J. A.; Strano, M.S. Plant Nanobionics Approach to Augment Photosynthesis and Biochemical Sensing. *Nat. Mater.* **2014**, *13* (4), 400–408.
- (33) Wu, H.; Tito, N.; Giraldo, J. P. Anionic Cerium Oxide Nanoparticles Protect Plant Photosynthesis from Abiotic Stress by Scavenging Reactive Oxygen Species. *ACS Nano* **2017**, *11* (11), 11283–11297.
- (34) Sheng, Q.; Liu, X.; Xie, Y.; Lin, F.; Zhang, Z.; Zhao, C.; Xu, H. Synthesis of Novel Amino Acid–Fipronil Conjugates and Study on Their Phloem Loading Mechanism. *Molecules* **2018**, *23* (4), 1–14.
- (35) Nuñez, A. M. P.; Rodríguez, G. A. A.; Monteiro, F. P.; Faria, A. F.; Silva, J. C. P.; Monteiro, A. C. A.; Carvalho, C. V.; Gomes, L. A. A.; Souza, R. M.; De Souza, J. T.; et al. Bio-Based Products Control Black Rot (*Xanthomonas campestris* pv. *campestris*) and Increase the Nutraceutical and Antioxidant Components in Kale. *Sci. Rep.* **2018**, *8* (1), 10199.
- (36) Vicente, J. G.; Holub, E. B. *Xanthomonas campestris* pv. *campestris* (Cause of Black Rot of Crucifers) in the Genomic Era Is Still a Worldwide Threat to *Brassica* Crops. *Mol. Plant Pathol.* **2013**, *14* (1), 2–18.
- (37) Bugbee, B. Nutrient Management in Recirculating Hydroponic Culture. In *Acta Horticulturae*; 2004; Vol. 648, pp 99–112.
- (38) Fernández, V.; Brown, P. H. From Plant Surface to Plant Metabolism: The Uncertain Fate of Foliar-Applied Nutrients. *Front. Plant Sci.* **2013**, *4*.
- (39) Qiu, H.; Smolders, E. Nanospecific Phytotoxicity of CuO Nanoparticles in Soils Disappeared When Bioavailability Factors Were Considered. *Environ. Sci. Technol.* **2017**,

- 51 (20), 11976–11985.
- (40) Ma, Y.; Lombi, E.; Nolan, A. L.; McLaughlin, M. J. Short-Term Natural Attenuation of Copper in Soils: Effects of Time, Temperature, and Soil Characteristics. *Environ. Toxicol. Chem.* **2006**, *25* (3), 652–658.
 - (41) Ma, Y.; Lombi, E.; Oliver, I. W.; Nolan, A. L.; McLaughlin, M. J. Long-Term Aging of Copper Added to Soils. *Environ. Sci. Technol.* **2006**, *40* (20), 6310–6317.
 - (42) Alidoust, D.; Isoda, A. Effect of $\gamma\text{Fe}_2\text{O}_3$ Nanoparticles on Photosynthetic Characteristic of Soybean (*Glycine max* (L.) Merr.): Foliar Spray versus Soil Amendment. *Acta Physiol. Plant.* **2013**, *35* (12), 3365–3375.
 - (43) Tarafdar, J. C.; Raliya, R.; Mahawar, H.; Rathore, I. Development of Zinc Nanofertilizer to Enhance Crop Production in Pearl Millet (*Pennisetum americanum*). *Agric. Res.* **2014**, *3* (3), 257–262.
 - (44) Imada, K.; Sakai, S.; Kajihara, H.; Tanaka, S.; Ito, S. Magnesium Oxide Nanoparticles Induce Systemic Resistance in Tomato against Bacterial Wilt Disease. *Plant Pathol.* **2016**, *65* (4), 551–560.
 - (45) Choudhary, R. C.; Kumaraswamy, R. V.; Kumari, S.; Sharma, S. S.; Pal, A.; Raliya, R.; Biswas, P.; Saharan, V. Cu-Chitosan Nanoparticle Boost Defense Responses and Plant Growth in Maize (*Zea mays* L.). *Sci. Rep.* **2017**, *7* (1), 9754.
 - (46) Drissi, S.; Houssa, A. A.; Bamouh, A.; Benbella, M. Corn Silage (*Zea mays* L.) Response to Zinc Foliar Spray Concentration When Grown on Sandy Soil. *J. Agric. Sci.* **2015**, *7* (2), 68–79.
 - (47) Li, C.; Wang, P.; Ent, A. Van Der; Cheng, M.; Jiang, H.; Read, T. L.; Lombi, E.; Tang, C.; Jonge, M. D. De; Menzies, N. W.; et al. Absorption of Foliar-Applied Zn in Sunflower (*Helianthus annuus*): Importance of the Cuticle, Stomata and Trichomes. *Ann. Bot.* **2018**, 1–12.
 - (48) Melotto, M.; Underwood, W.; He, S. Y. Role of Stomata in Plant Innate Immunity and Foliar Bacterial Diseases. *Annu. Rev. Phytopathol.* **2008**, *46* (1), 101–122.
 - (49) Li, Q.; Zimmerman, J.; Alvarez, P.; Westerhoff, P.; Gardea-Torresdey, J. Overcoming Implementation Barriers for Nanotechnology in Drinking Water Treatment. *Environ. Sci. Nano* **2016**, *3* (6), 1241–1253.
 - (50) Kumar, S.; Nehra, M.; Dilbaghi, N.; Marrazza, G.; Hassan, A. A.; Kim, K. H. Nano-Based Smart Pesticide Formulations: Emerging Opportunities for Agriculture. *J. Control. Release* **2019**, *294* (November 2018), 131–153.
 - (51) Aptagen <https://www.aptagen.com/>.

APPENDIX A

Supporting Information for **Chapter 2:**

Impact of Surface Charge on Cerium Oxide Nanoparticle Uptake and Translocation by Wheat

(Triticum aestivum)

A.1. Synchrotron Methods

For the plant roots, an initial large area survey scan at 15.8 keV was conducted to identify the area of interest and obtain overall elemental distributions. The step sizes were 3 x 3 μm , 5 x 5 μm , and 4 x 4 μm (horizontal x vertical) with scanning velocities of 3 mm/s, 4 mm/s, and 2.5 mm/s for the 1 h, 8 h, and 34 h time points respectively. Subsequently, a smaller area was chosen to conduct fluorescence XANES imaging with the XANES stack itself consisting of 108 individual maps at decreasing energies across the Ce L_{III} edge (see details below).

For the plant leaves, an initial large area survey scan was conducted to identify the region of interest and obtain overall elemental distributions. Then, a smaller area was chosen to conduct HR fluorescence imaging. Finally, an even smaller area was chosen to conduct the fluorescence XANES imaging (see details below). For the larger survey scans, the step sizes were 25 x 25 μm with a scanning velocity of 8 mm/s and an incident energy of 15.8 keV. For the HR scan, the step size was reduced to 2x2 μm and the scanning velocity slowed to 1 mm/s. For each standard solution at 20 mg/L-Ce, a strip of filter paper (~2 mm wide) was immersed for 30 s. The three strips were then wrapped in polyimide film and placed vertically on the sample holder for analysis using fluorescence-XANES imaging.

The fluorescence-XANES imaging consists of “stacks” of 108 μ -XRF maps collected at decreasing incident energies from 5973 eV to 5673 eV across the Ce L_{III}-edge. The energies of these 108 progressive scans were selected as follows: 5973-5873 in 25 eV decrements (five energies), 5863-5813 in 10 eV decrements (six energies), 5808-5768 in 5 eV decrements (nine energies), 5767-5751 in 1 eV decrements (seventeen energies), 5750-5718 in 0.5 eV decrements (sixty-five energies), 5713-5703 in 5 eV decrements (three energies), and 5693-5673 in 10 eV decrements (three energies). Step sizes were 25 x 25 μm , 30 x 30 μm , and 5x5 μm for the 8 h roots, 34 h roots, and 34 h leaves, respectively. Scanning velocities were 9 mm/s, 12 mm/s and 2 mm/s respectively. For the standards, the step size was 20 x 20 μm with a scanning velocity of 12 mm/s.

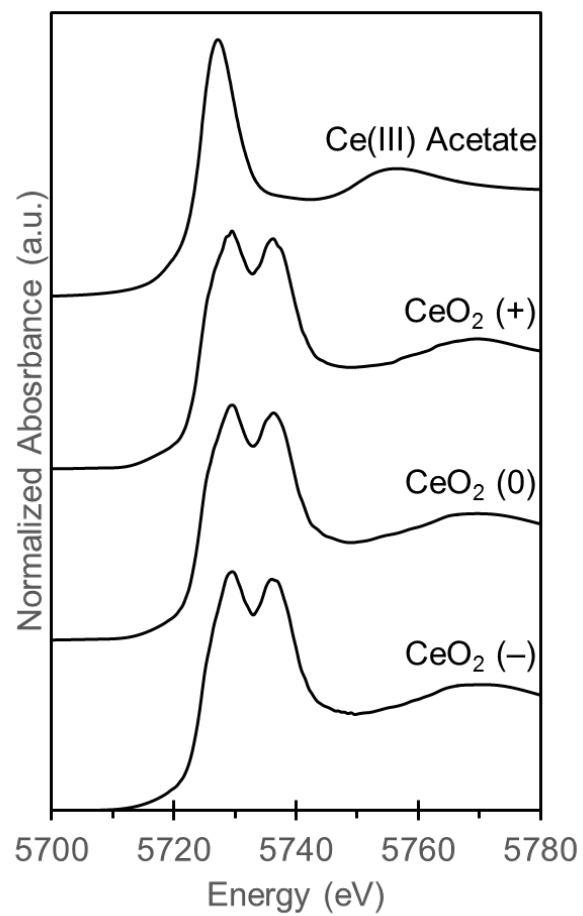


Figure A.1: Ce L_{III} XANES of CeO₂ NPs and model compounds

Treatment	Percent Dissolved
CeO ₂ (+)	0.01 ± 0.01 %
CeO ₂ (0)	0.03 ± 0.02 %
CeO ₂ (-)	0.09 ± 0.09 %

Table A.1: CeO₂ NP solubility was measured in 20 mg/L-Ce CeO₂ NP suspensions in continuously aerated ¼ strength Hoagland’s medium (pH=5.6) after 34 hours. The dissolved fraction (± SD) was calculated as a percent of the Ce concentration in ultra-filtered (3 kDa cutoff) suspensions after 34 hours divided by the total Ce concentration of the solution. Measurements were made in duplicate.

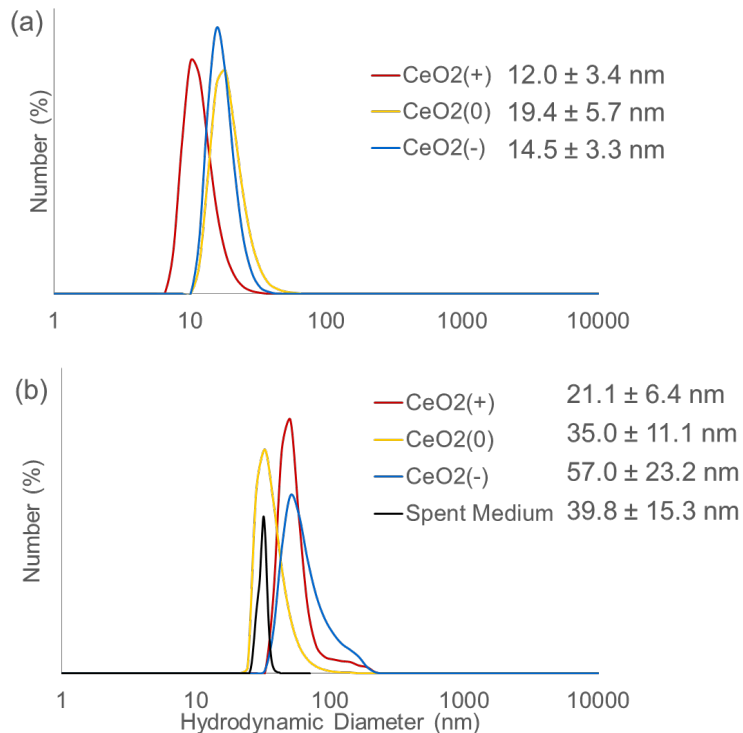


Figure A.2: Number-weighted distribution of the hydrodynamic diameters of positive (+), neutral (0), or negative (-) coated CeO₂ NPs in continuously aerated ¼ strength Hoagland’s medium (pH=5.6) **(A)** before exposure, and **(B)** after incubation in spent hydroponic medium* for 34 h. Spent medium contains some small particles that are likely influencing the size distribution of the NPs, but do not cause significant aggregation.

*Wheat was grown for two days in hydroponic medium, then this used nutrient solution was filtered through a 0.45 µm filter. Particles were then suspended in this spent media and mixed on an end-over-end rotator for 34 hours.

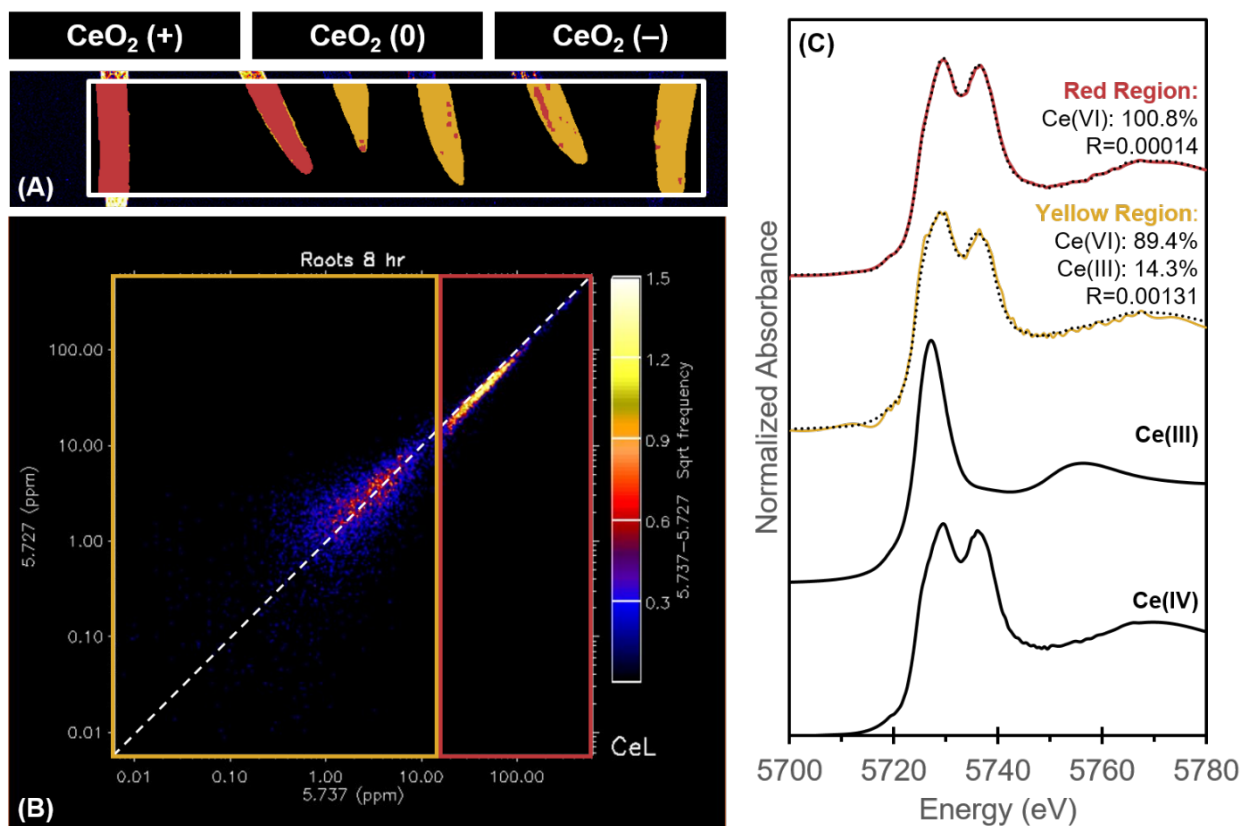


Figure A.3: Wheat roots exposed hydroponically to 20 mg-Ce/L positive (+), neutral (0), or negative (-) coated CeO_2 NPs in continuously aerated $\frac{1}{4}$ strength Hoagland's medium (pH=5.6) for 8 h. There are two replicates per treatment. (A) The spatial distribution of the two pixel populations identified (red and yellow) from XANES maps at the root tips. (B) An energy association plot from the XANES imaging showing the relationship between energies (5.737 and 5.727 keV—these being the white line for Ce(III) and Ce(IV), the dashed line is 1:1). The two colored rectangles in (B) represent the populations of pixels highlighted in (A) from which XANES data were obtained. (C) Normalized Ce L_{III} XANES spectra corresponding to the two pixel populations (red and yellow) plus the spectra for the reference compounds. The black dotted lines are fitted data while the solid lines are experimental data.

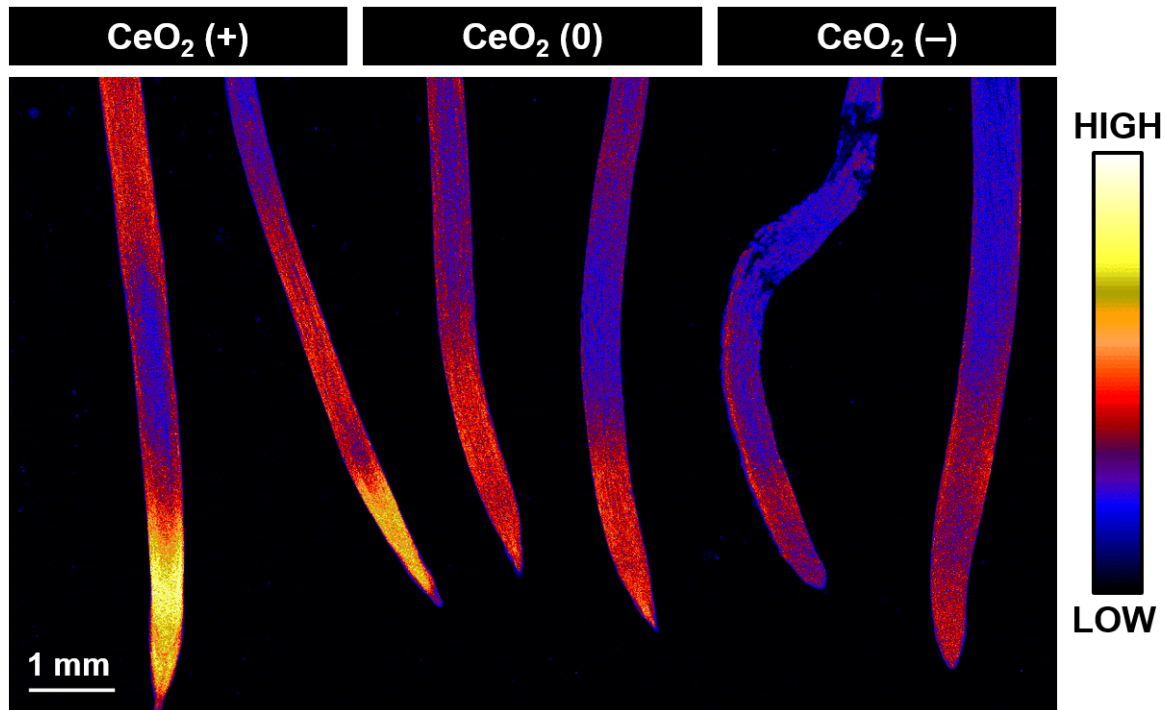


Figure A.4: XRF elemental survey map showing total potassium (K) distribution in wheat roots exposed hydroponically to 20 mg-Ce/L positive (+), neutral (0), or negative (-) coated CeO_2 NPs in continuously aerated $\frac{1}{4}$ strength Hoagland's medium (pH=5.6) for 8 h. There are two replicate roots per treatment. Brighter colors correspond to higher K concentrations (see color scale at right). Note the K leakage in the left CeO_2 (-) root, indicating root damage.

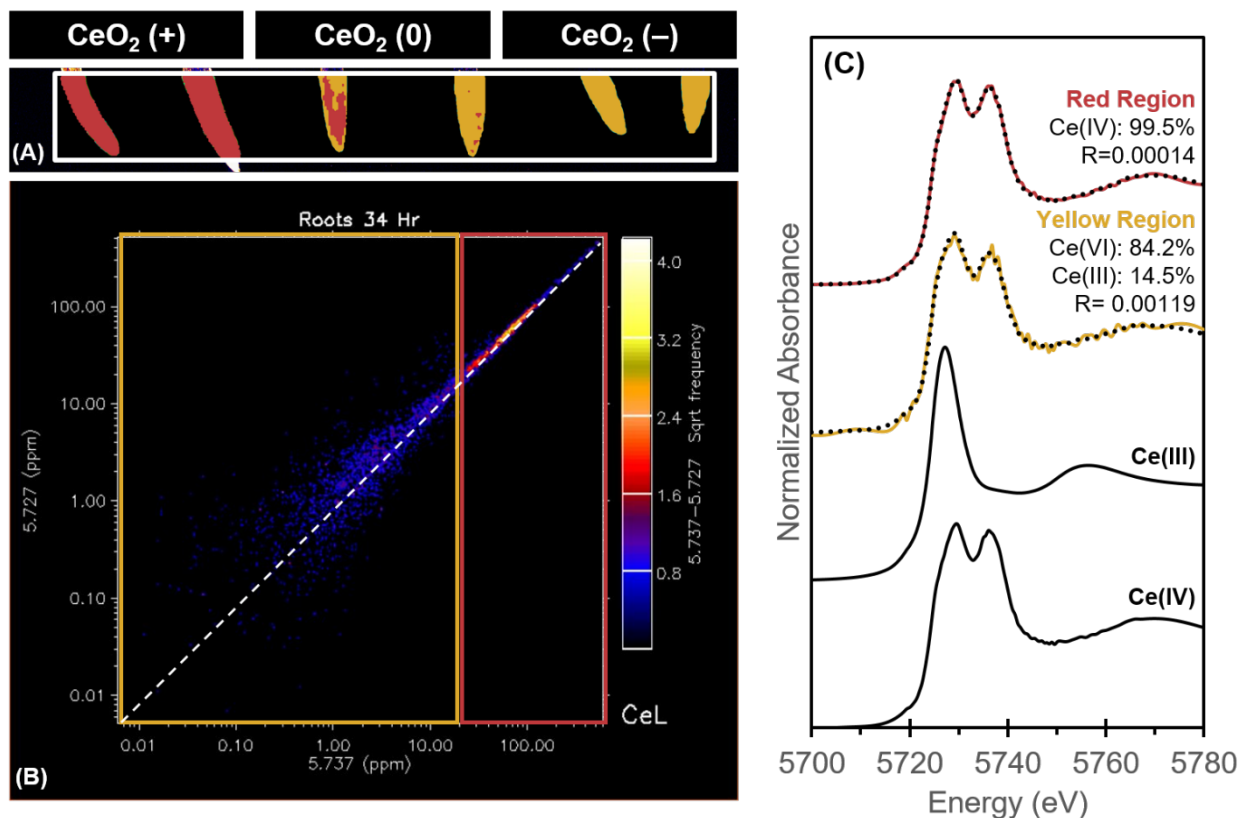


Figure A.5: Wheat roots exposed hydroponically to 20 mg-Ce/L positive (+), neutral (0), or negative (-) coated CeO₂NPs in continuously aerated ¼ strength Hoagland’s medium (pH=5.6) for 34 h. There are two replicates per treatment. **(A)** The spatial distribution of the two pixel populations identified (red and yellow) from XANES maps at the root tips. **(B)** An energy association plot from the XANES imaging showing the relationship between energies (5.737 and 5.727 keV—these being the white line for Ce(III) and Ce(IV), the dashed line is 1:1). The two colored rectangles in **(B)** represent the populations of pixels highlighted in **(A)** from which XANES data were obtained. **(C)** Normalized Ce L_{III} XANES spectra corresponding to the two pixel populations (red and yellow) plus the spectra for the reference compounds. The black dotted lines are fitted data while the solid lines are experimental data

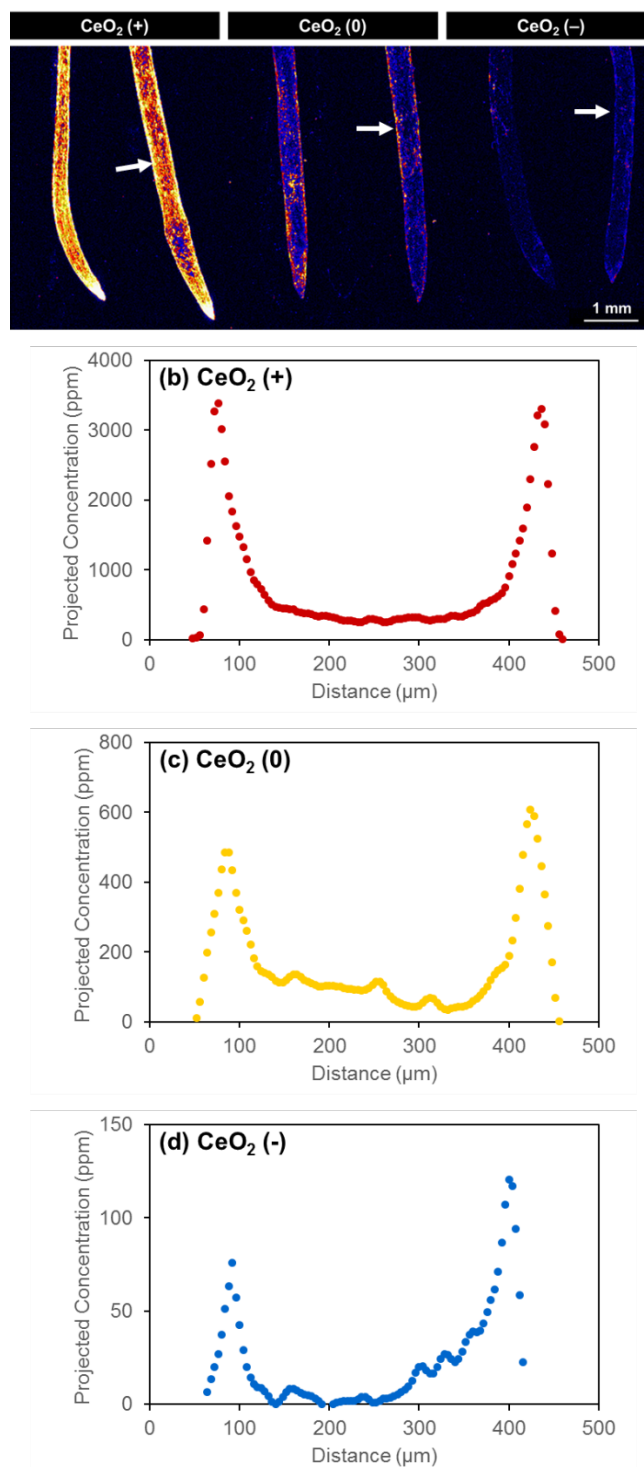


Figure A.6: Wheat roots exposed hydroponically to 20 mg-Ce/L positive (+), neutral (0), or negative (-) coated CeO_2 NPs in continuously aerated $\frac{1}{4}$ strength Hoagland's medium (pH=5.6) for 34 h. (A) XRF elemental survey map of total Ce distribution, with arrows indicating where the traverse Ce concentrations for the (B) positive, (C) neutral, and (D) negative coated CeO_2 NP exposed plants were calculated using GeoPIXE's traverse projection function.

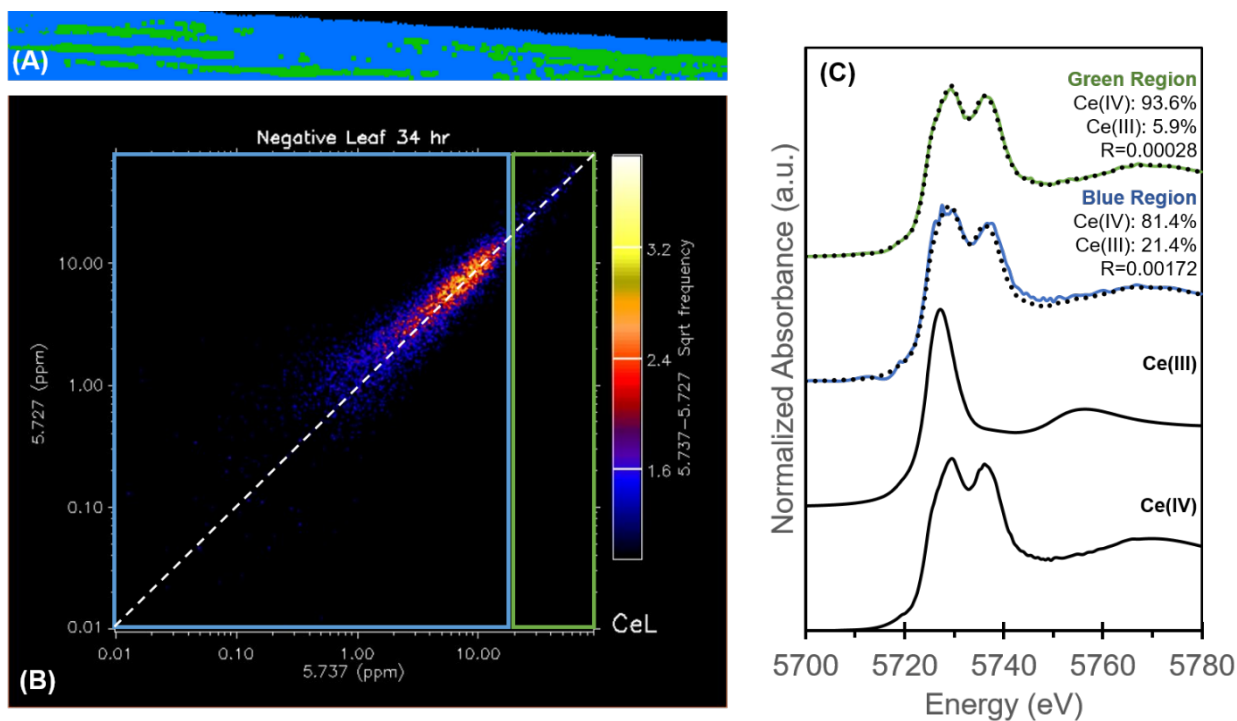


Figure A.7: Wheat leaf exposed hydroponically to 20 mg-Ce/L negative (-) coated CeO₂NPs in continuously aerated ¼ strength Hoagland’s medium (pH=5.6) for 34 h. (A) The spatial distribution of the two pixel populations identified (green and blue) from XANES maps at the root tips. (B) An energy association plot from the XANES imaging showing the relationship between energies (5.737 and 5.727 keV—these being the white line for Ce(III) and Ce(IV), the dashed line is 1:1.) The two colored rectangles in (B) represent the populations of pixels highlighted in (A) from which XANES data were obtained. (C) Normalized Ce L_{III} XANES spectra corresponding to the two pixel populations (blue and green) plus the spectra for the reference compounds. The black dotted lines are fitted data while the solid lines are experimental data.

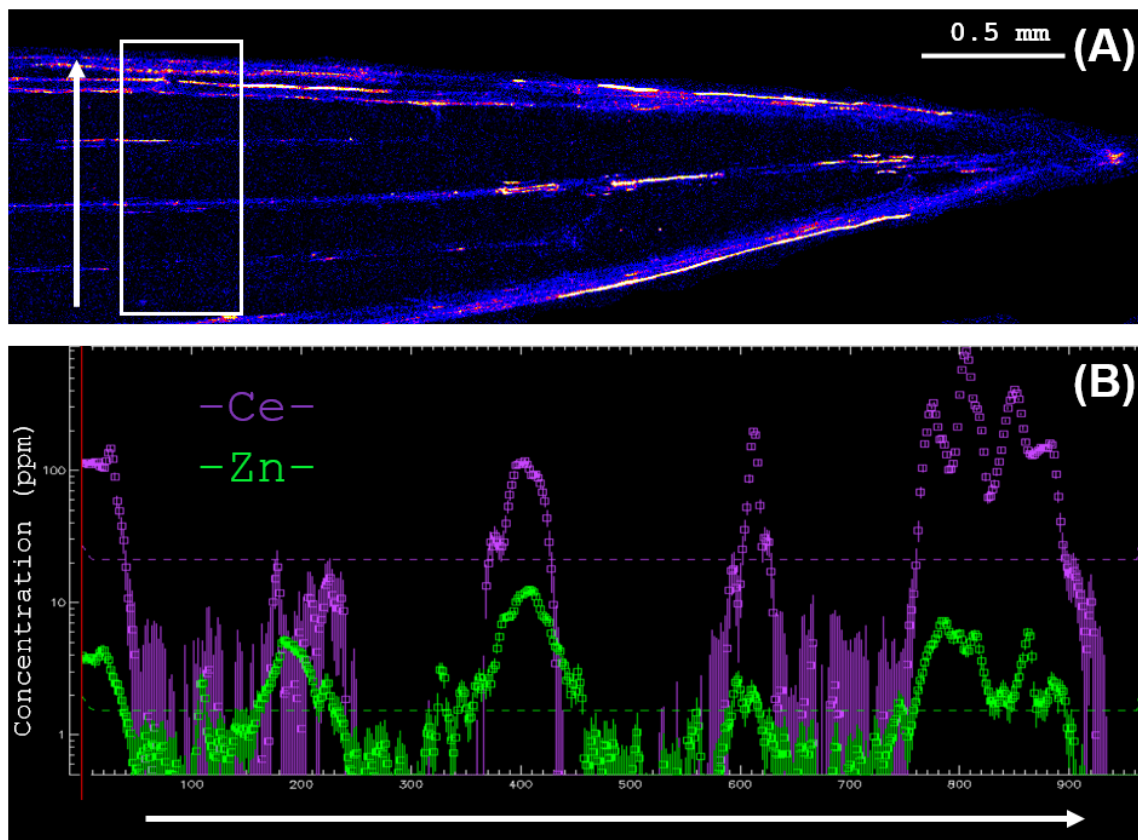


Figure A.8: Wheat leaf tip exposed hydroponically to 20 mg-Ce/L negative (-) coated CeO₂ NPs in continuously aerated ¼ strength Hoagland’s medium (pH=5.6) for 34 h. (A) XRF elemental survey map showing total Ce distribution in the leaf tip, with the white box indicating where (B) the transverse Ce and zinc (Zn) concentrations were calculated using GeoPIXE’s traverse projection function.

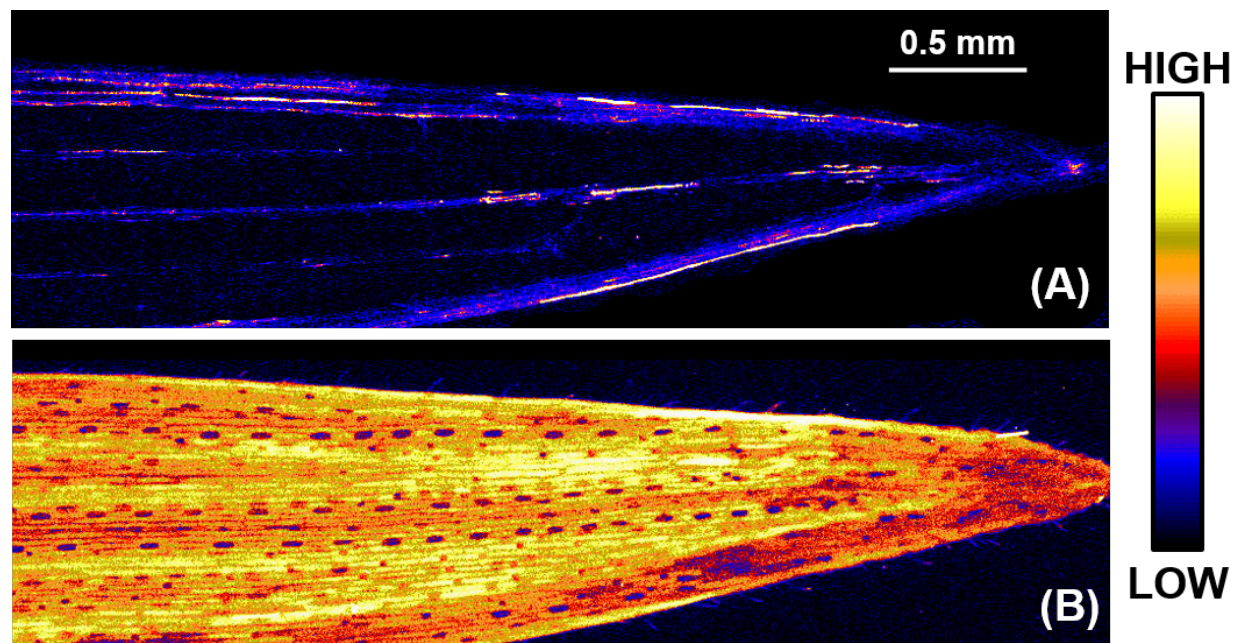


Figure A.9: Cerium (A) and calcium (B) XRF elemental maps of wheat leaf tip exposed hydroponically to 20 mg-Ce/L negative (-) coated CeO₂ NPs in continuously aerated ¼ strength Hoagland's medium (pH=5.6) for 34 h. Note: images are not to the same color scale. There is no obvious association between Ce and calcium

APPENDIX B

Supporting Information for **Chapter 3**:

Nanoparticle Surface Charge Influences Uptake, Translocation, and Leaf Distribution in
Vascular Plants with Contrasting Anatomy

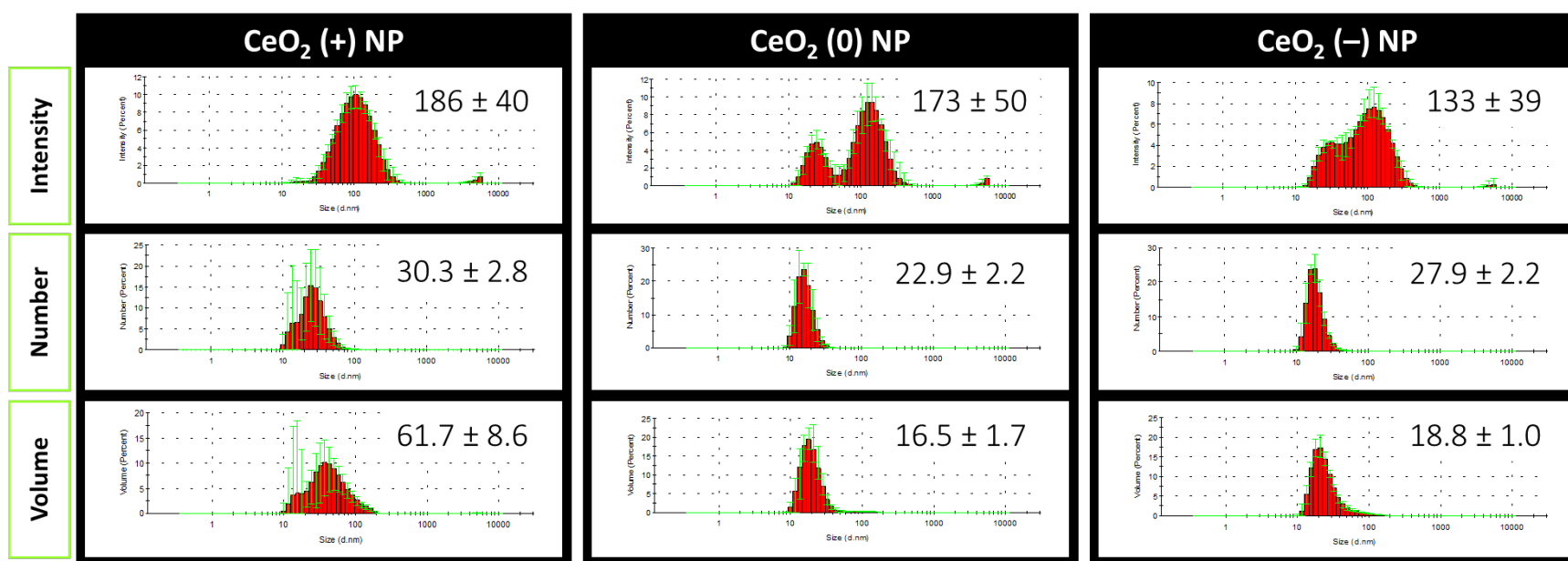


Figure B.1. Intensity, number, and volume weighted distributions of the hydrodynamic diameters (nm) of CeO₂(+), CeO₂(0), and CeO₂(-) NPs at 50 mg-Ce/L in exposure medium (basal salt solution, pH=5.6). Values are presented with standard deviation over 5 replicates.

Table B.1: Dissolved fraction of Ce remaining in solution after 48 h of hydroponic exposure to 50 mg-Ce/L as CeO₂(+), CeO₂(0) or CeO₂(-) NPs (basal salt solution, pH=5.6). The dissolved fraction was calculated as a percent of Ce concentration in ultra-filtered (3 kDa cutoff) suspensions divided by the total Ce concentration of the solution. Measurements were made in triplicate. Majority of the remaining Ce is not dissolved.

	Positive	Neutral	Negative
Corn	0.14 ± 0.08 %	0.02 ± 0.01 %	0.01 ± 0.01 %
Rice	0.04 ± 0.01 %	0.00 ± 0.01 %	0.05 ± 0.01 %
Tomato	0.04 ± 0.01 %	0.04 ± 0.01 %	0.02 ± 0.01 %
Lettuce	0.12 ± 0.01 %	0.03 ± 0.01 %	0.01 ± 0.01 %

Table B.2: Total Ce concentrations on/in dried plant roots after 48 h of hydroponic exposure to 50 mg-Ce/L as CeO₂(+), CeO₂(0) or CeO₂(-) NPs (basal salt solution, pH=5.6). The reported values are means averaged from four replicates ± SD. Plant root surface area (SA) approximations were also averaged over four sets of plant roots per species.

Plant Species	Root SA (cm²)	NP Surface Charge	Ce association with roots (mg/kg)
Corn	6.6 ± 1.2	(+)	13,640 ± 7,200
		(0)	5,730 ± 2,270
		(-)	3,700 ± 1,110
Rice	0.6 ± 0.2	(+)	20,780 ± 6,380
		(0)	2,230 ± 500
		(-)	1,470 ± 670
Tomato	11.3 ± 3.2	(+)	47,330 ± 3,100
		(0)	11,640 ± 1,320
		(-)	2,410 ± 1,450
Lettuce	1.3 ± 1.0	(+)	31,530 ± 4,690
		(0)	1,470 ± 670
		(-)	1,150 ± 770

Table B.3: Ce L_{III} XANES linear combination fitting (LCF) results of roots after 48 h of hydroponic exposure to 50 mg-Ce/L as CeO₂(+), CeO₂(0) or CeO₂(-) NPs (basal salt solution, pH=5.6). Roots were rinsed for 30s in Ce-free medium prior to lyophilization and analysis. Spectra are shown in **Figure 3.5**.

	Positive				Neutral				Negative			
	Corn	Rice	Tomato	Lettuce	Corn	Rice	Tomato	Lettuce	Corn	Rice	Tomato	Lettuce
Ce(III)	-	-	-	-	18.0%	10.5%	18.8%	31.5%	-	7.6%	10.4%	23.9%
Ce(IV)	98.8%	96.9%	100.5%	89.4%	88.5%	89.8%	87.9%	80.6%	105.5%	94.3%	93.7%	85.8%
R Factor	0.0025	0.0008	0.0007	0.0035	0.0018	0.0018	0.0015	0.0094	0.0026	0.0032	0.0024	0.1910
Red. χ^2	0.0011	0.0003	0.0004	0.0017	0.0008	0.0007	0.0084	0.0048	0.0013	0.0013	0.0014	0.0410

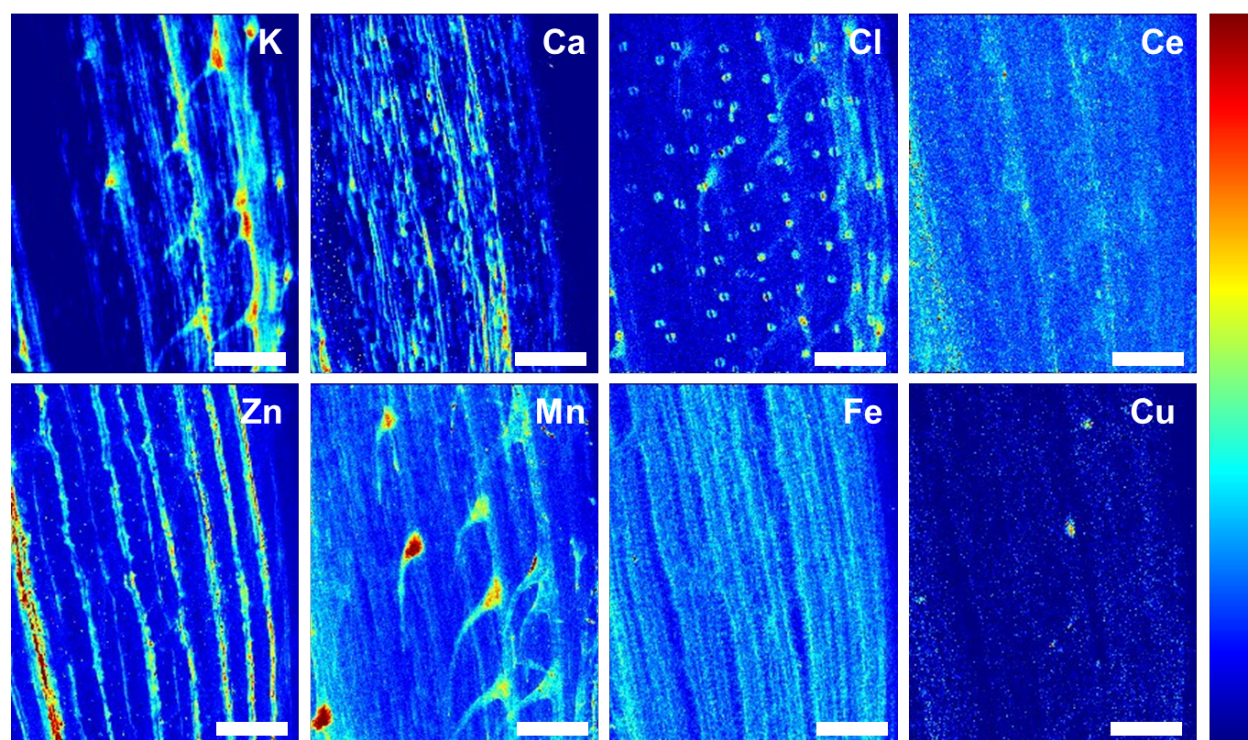


Figure B.2. XRF maps showing elemental distribution in a corn leaf after 48 h of hydroponic exposure to 50 mg-Ce/L as CeO₂(-) NPs (basal salt solution, pH=5.6). Ce signal was not sufficient to perform μ -XANES. Scale bar=200 μ m.

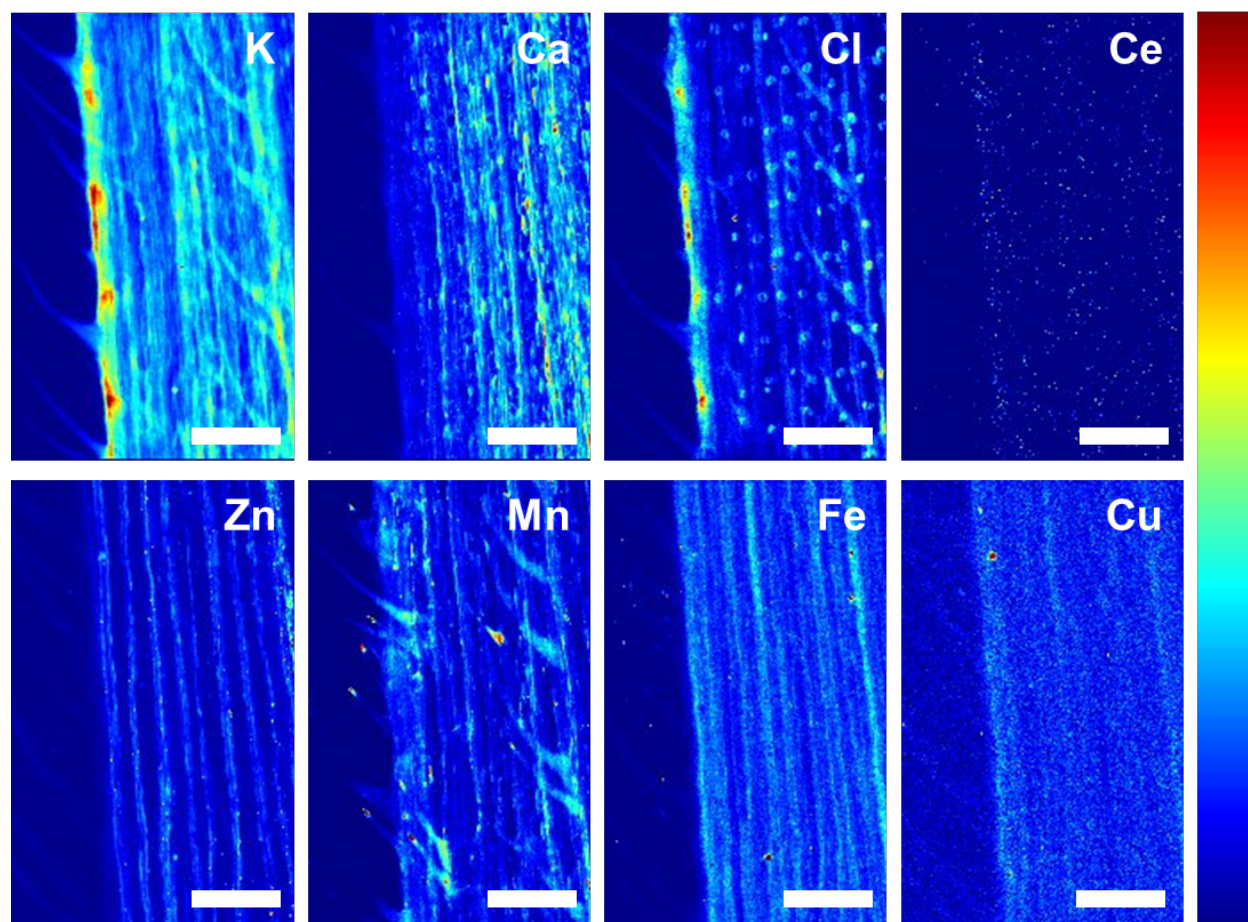


Figure B.3. XRF maps showing elemental distributions in a corn leaf after 48 h of hydroponic exposure to 50 mg-Ce/L as $\text{CeO}_2(0)$ NPs (basal salt solution, pH=5.6). Ce signal was not sufficient to perform μ -XANES. Scale bar=200 μm .

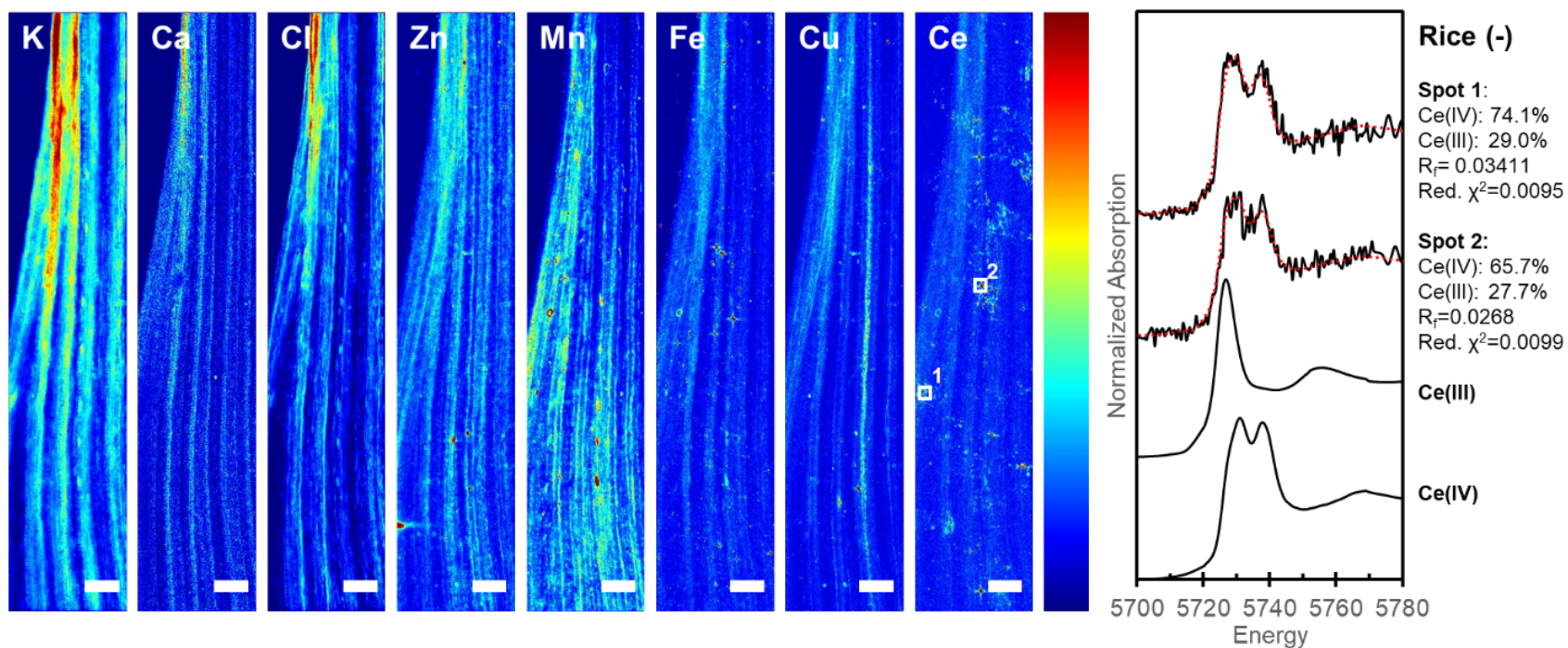


Figure B.4. XRF maps showing elemental distributions in a rice leaf after 48 h of hydroponic exposure to 50 mg-Ce/L as CeO₂(-) NPs (basal salt solution, pH=5.6). Ce L(III) μ -XANES spectra (solid, black) from high intensity spots are indicated with white boxes on the Ce map. LCF results (dotted, red) are presented with fitting statistics and Ce(III) and Ce(IV) model compounds. Scale bar=200 μ m

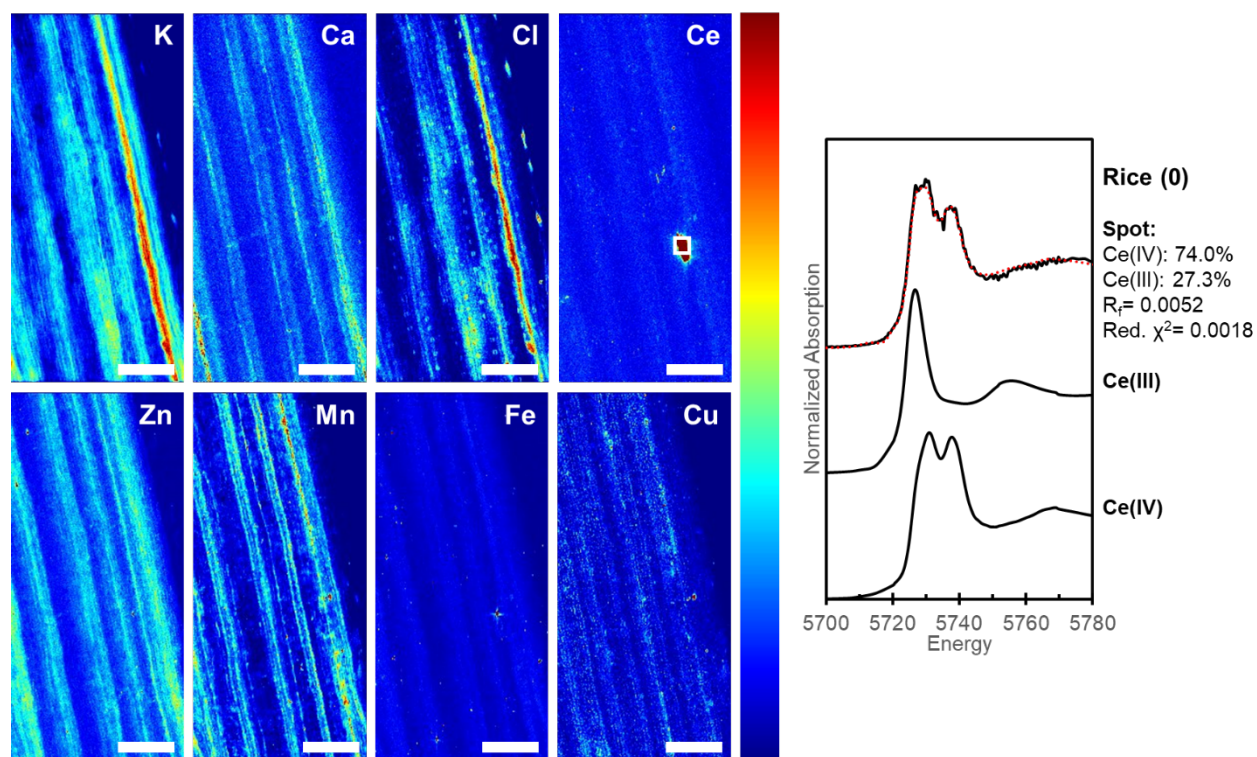


Figure B.5. XRF maps showing elemental distributions in a rice leaf after 48 h of hydroponic exposure to 50 mg-Ce/L as $\text{CeO}_2(0)$ NPs (basal salt solution, pH=5.6). Ce L(III) μ -XANES spectrum (solid, black) from high intensity spot is indicated with a white box on the Ce map. LCF result (dotted, red) is presented with fitting statistics and Ce(III) and Ce(IV) model compounds. Scale bar=200 μm

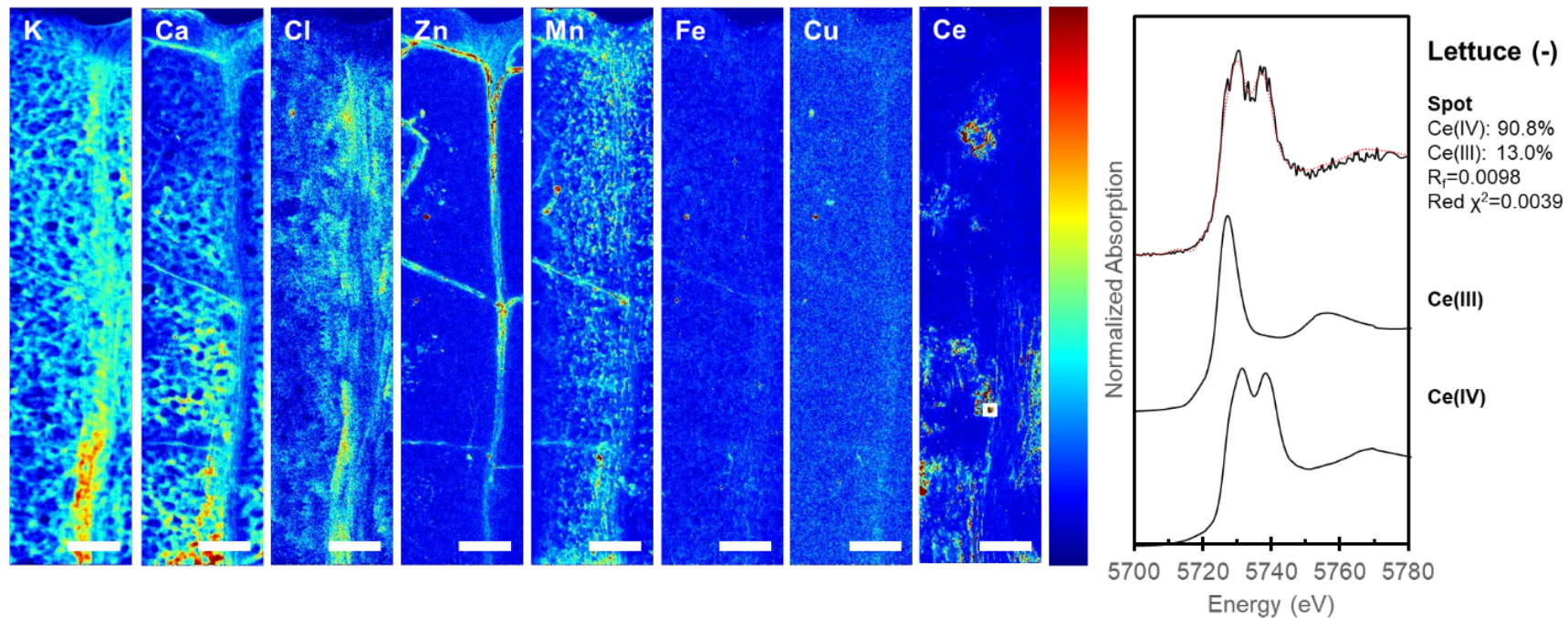


Figure B.6. XRF maps showing elemental distribution in a lettuce leaf after 48 h of hydroponic exposure to 50 mg-Ce/L as CeO₂(-) NPs (basal salt solution, pH=5.6). Ce L(III) μ -XANES spectrum (solid, black) from high intensity spot is indicated with a white box on the Ce map. LCF result (dotted, red) is presented with fitting statistics and Ce(III) and Ce(IV) model compounds. Scale bar=200 μ m.

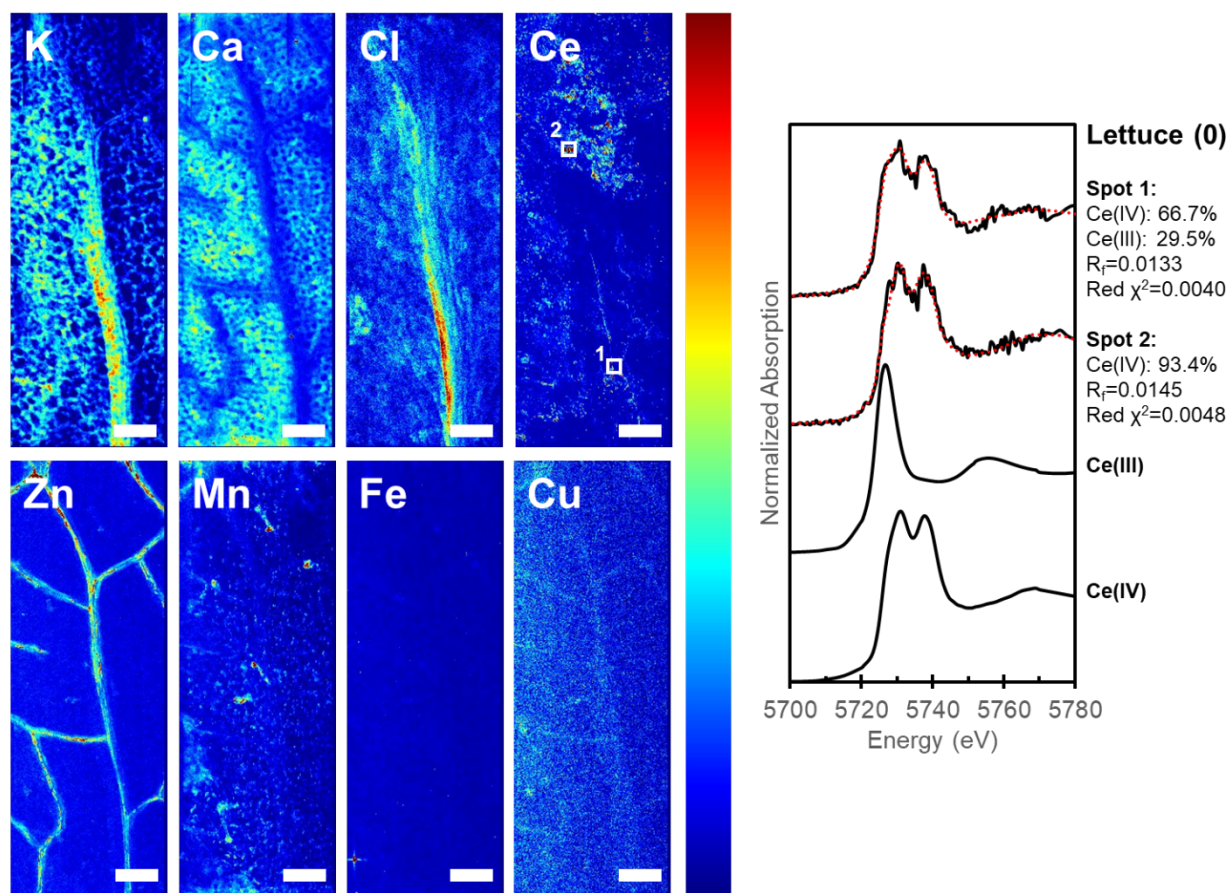


Figure B.7. XRF maps showing elemental distribution in a lettuce leaf after 48 h of hydroponic exposure to 50 mg-Ce/L as $\text{CeO}_2(0)$ NPs (basal salt solution, pH=5.6). Ce L(III) μ -XANES spectra (solid, black) from high intensity spots are indicated with white boxes on the Ce map. LCF results (dotted, red) are presented with fitting statistics and Ce(III) and Ce(IV) model compounds. Scale bar=200 μm .

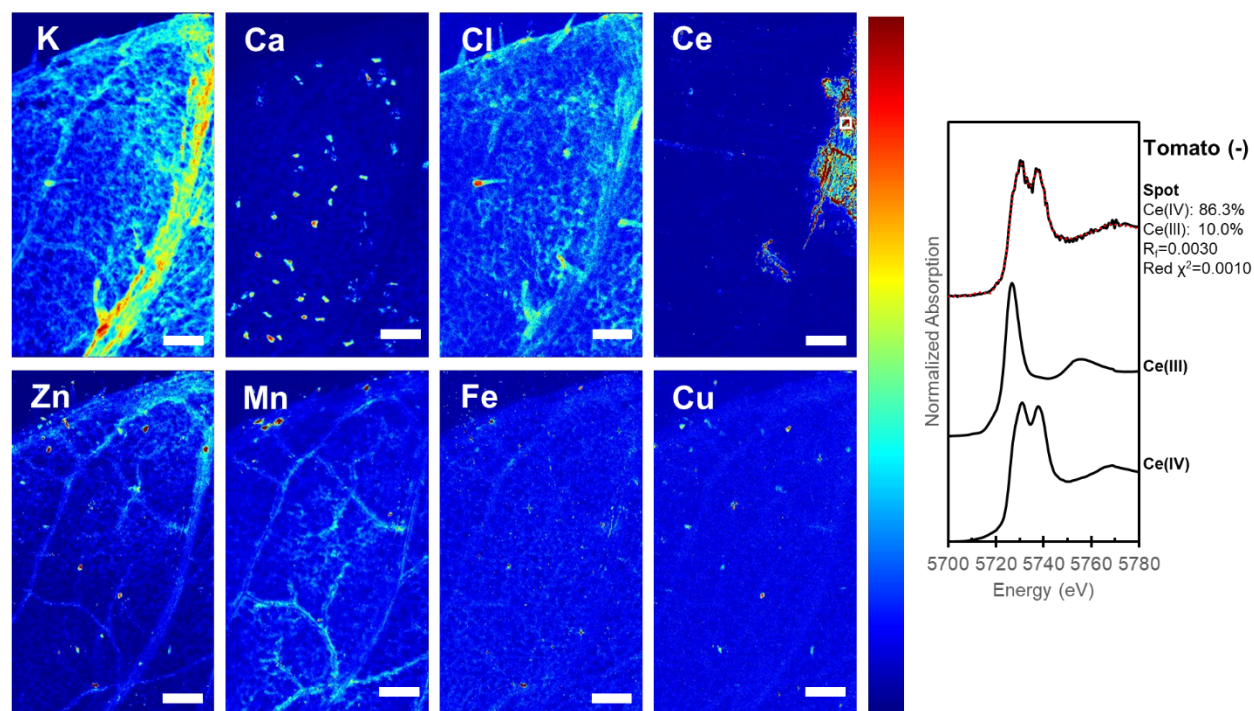


Figure B.8. XRF maps showing elemental distributions in a tomato leaf after 48 h of hydroponic exposure to 50 mg-Ce/L as CeO₂ (-) NPs (basal salt solution, pH=5.6). Ce L(III) μ -XANES spectrum (solid, black) from high intensity spot is indicated with a white box on the Ce map. LCF result (dotted, red) is presented with fitting statistics and Ce(III) and Ce(IV) model compounds. Scale bar=200 μ m

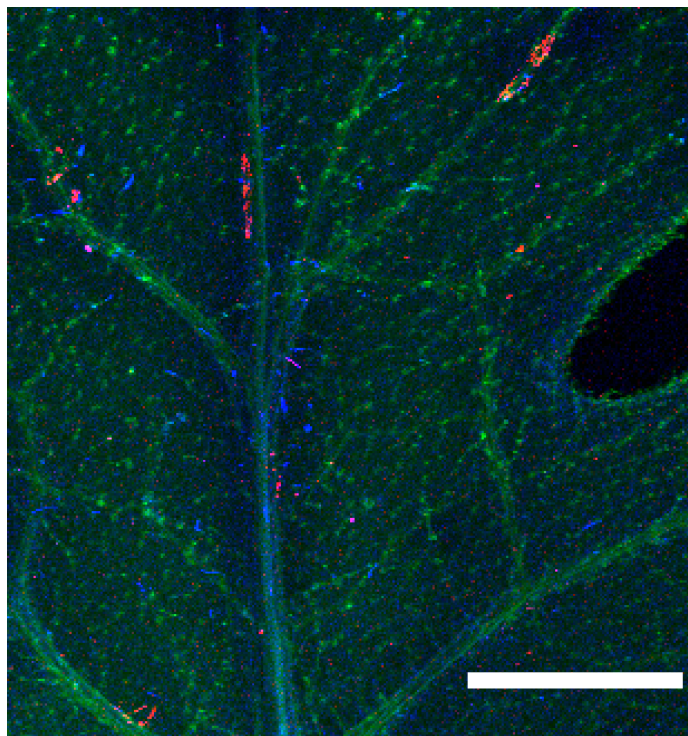


Figure B.9. Tri-colored XRF map showing Ce (red), K (green), and Mn (blue) distributions in a tomato leaf after 48 h of hydroponic exposure to 50 mg-Ce/L as CeO₂ (-) NP (basal salt solution, pH=5.6). Elemental maps were collected at NSLS-II on BL 4-BM using a step size of 15 μm and a dwell time of 0.1 s. Scale bar=1 mm

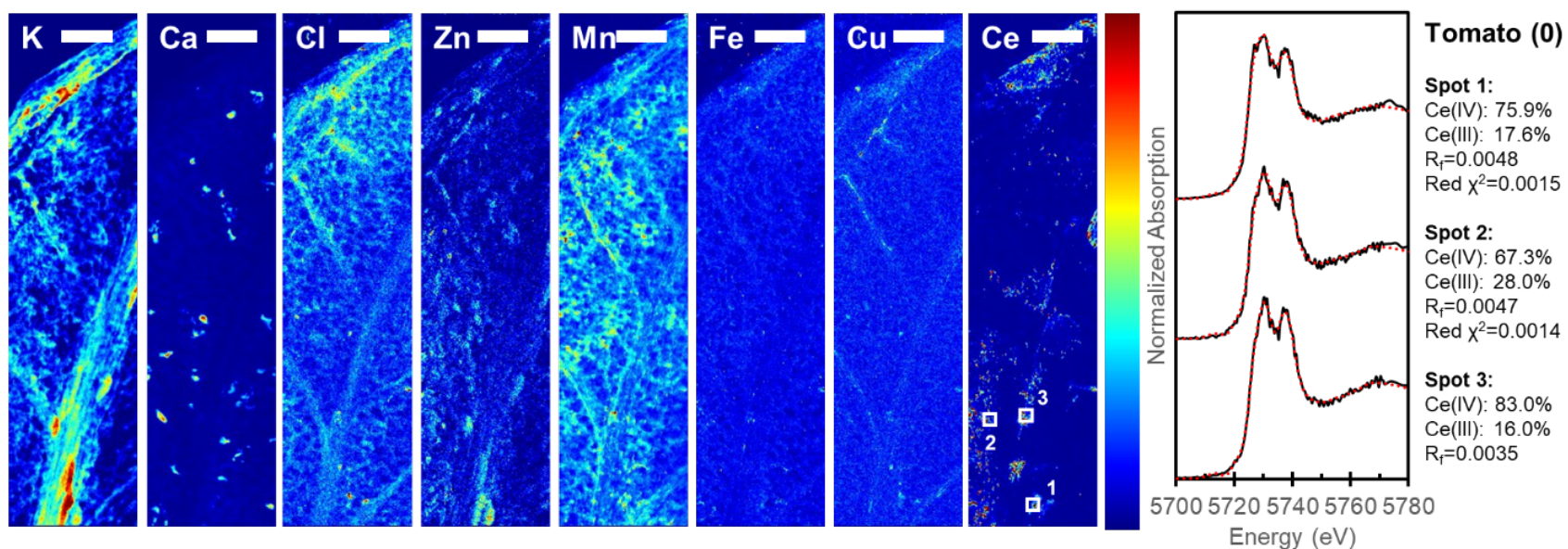


Figure B.10. XRF maps showing elemental distributions in a tomato leaf after 48 h of hydroponic exposure to 50 mg-Ce/L as CeO₂(0) NPs (basal salt solution, pH=5.6). Ce L(III) μ -XANES spectra (solid, black) from high intensity spots are indicated with white boxes on the Ce map. LCF results (dotted, red) are presented with fitting statistics. Scale bar=200 μ m.

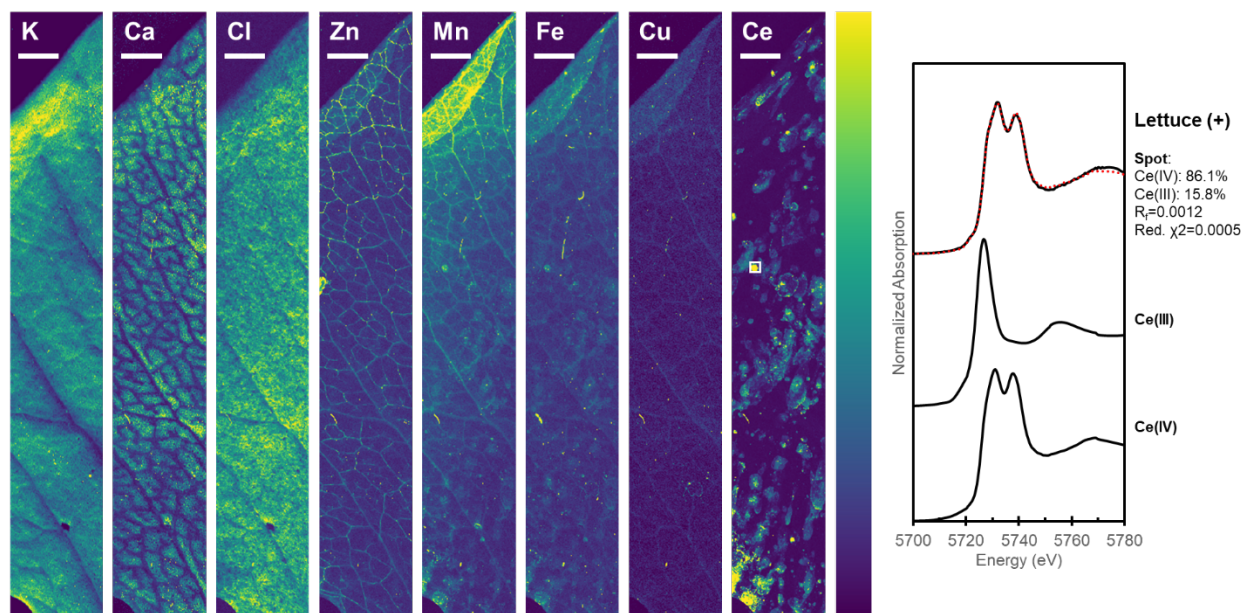


Figure B.11. XRF maps showing elemental distributions in a lettuce leaf after 48 h of hydroponic exposure to 50 mg-Ce/L as CeO₂ (+) NPs (basal salt solution, pH=5.6). Ce L(III) μ -XANES spectrum (solid, black) from high intensity spot is indicated with a white box on the Ce map. LCF result (dotted, red) is presented with fitting statistics and Ce(III) and Ce(IV) model compounds. Scale bar= 1 mm.

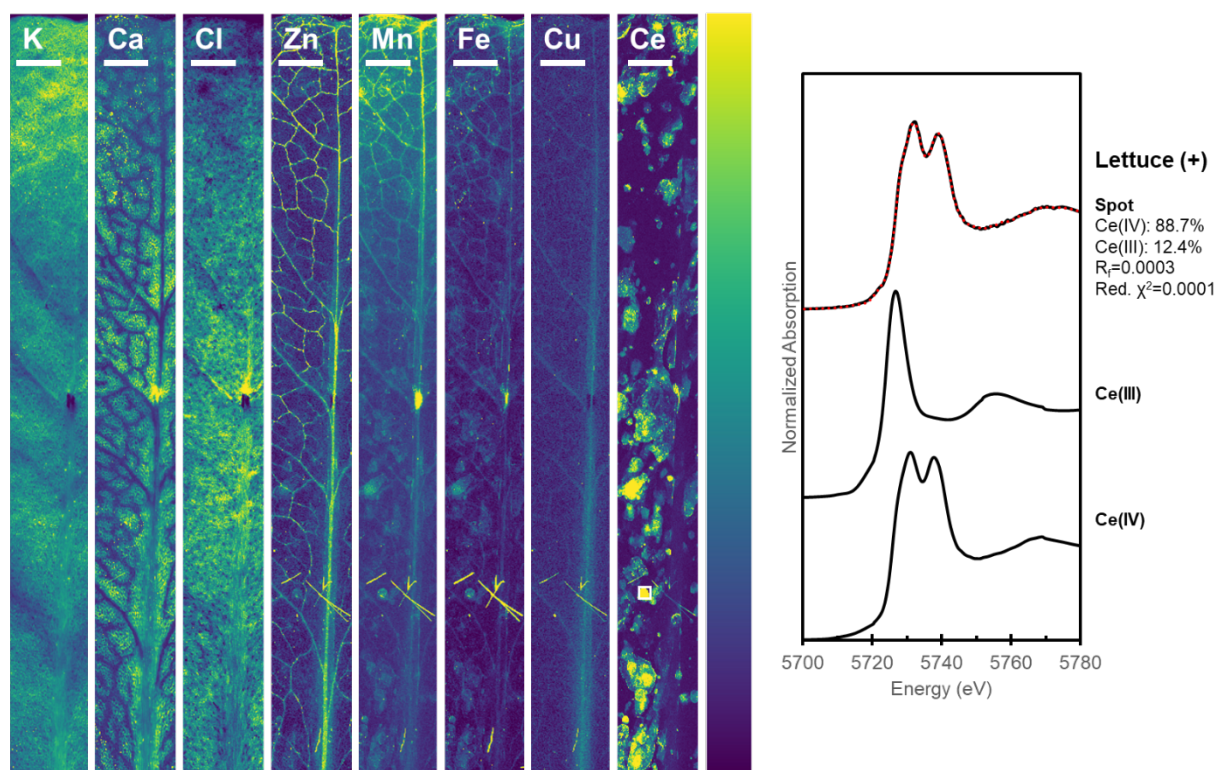


Figure B.12. XRF maps showing elemental distributions in the central vein of a lettuce leaf after 48 h of hydroponic exposure to 50 mg-Ce/L as CeO₂ (+) NPs (basal salt solution, pH=5.6). Ce L(III) μ -XANES spectrum (solid, black) from high intensity spot is indicated with a white box on the Ce map. LCF result (dotted, red) is presented with fitting statistics and Ce(III) and Ce(IV) model compounds. Scale bar= 1 mm.

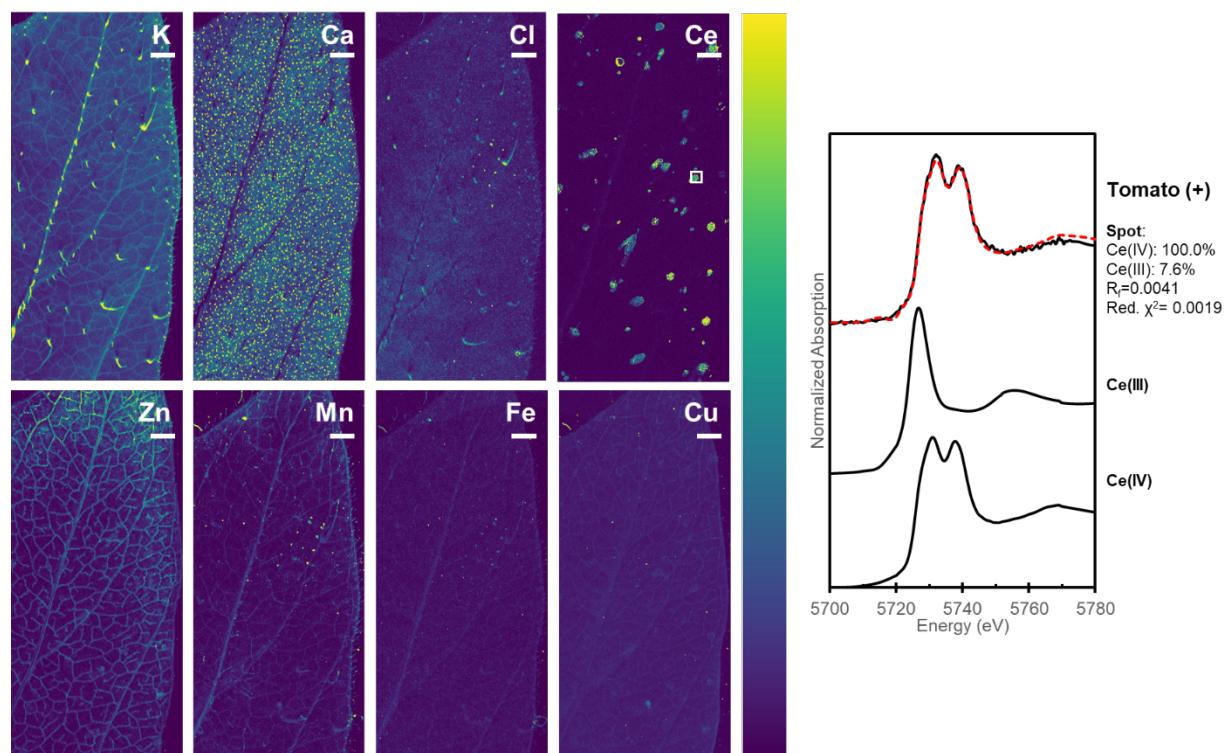


Figure B.13. XRF maps showing elemental distributions in a tomato leaf after 48 h of hydroponic exposure to 50 mg-Ce/L as CeO₂ (+) NPs (basal salt solution, pH=5.6). Ce L(III) μ -XANES spectrum (solid, black) from high intensity spot is indicated with a white box on the Ce map. LCF result (dotted, red) is presented with fitting statistics and Ce(III) and Ce(IV) model compounds. Scale bar= 1 mm.

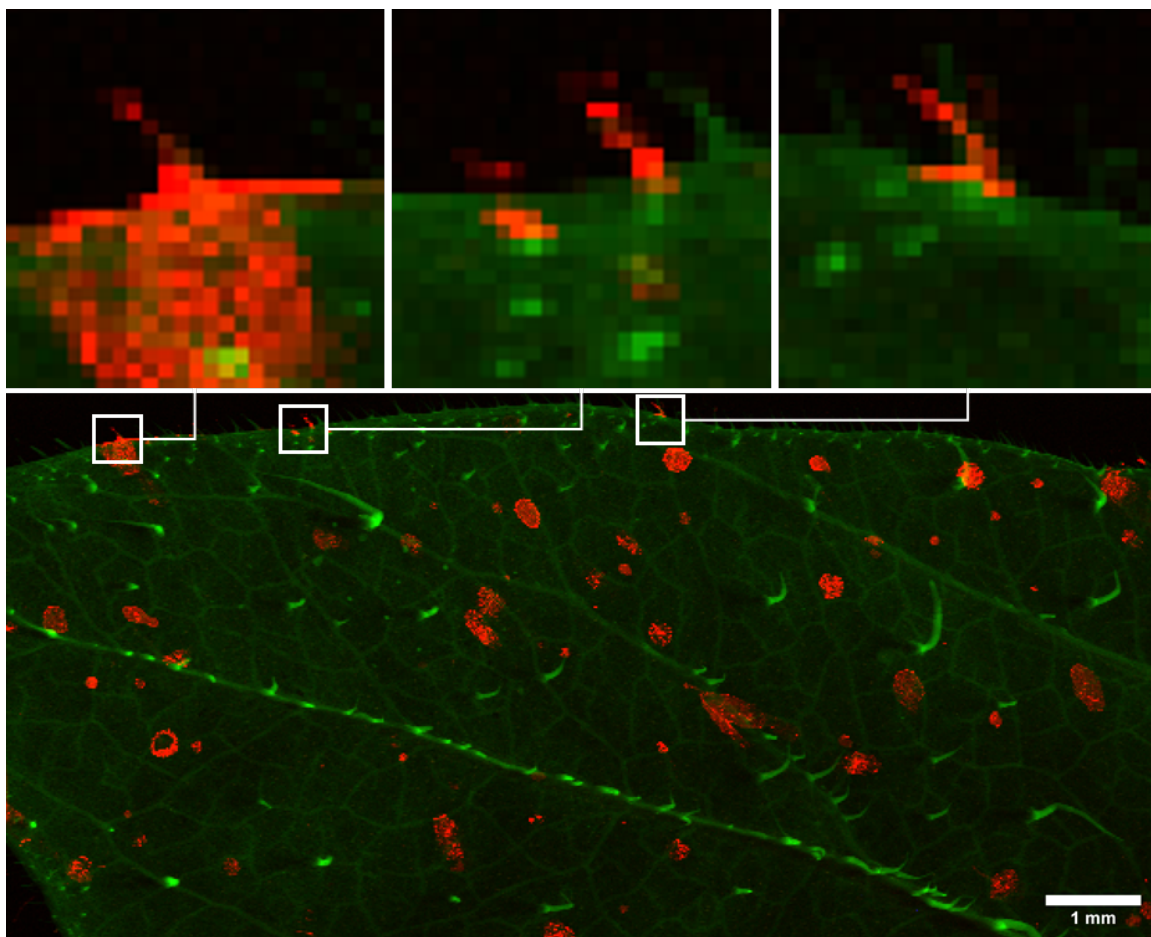


Figure B.14. Dual-colored XRF map showing Ce (red) and K (green) distribution in a tomato leaf after 48 h of hydroponic exposure to 50 mg-Ce/L of CeO₂(+) NPs (basal salt solution, pH=5.6). White boxes (500 μ m x 500 μ m) indicate Ce-trichome colocalization.

APPENDIX C

Supporting Information for **Chapter 4:**

Temporal Evolution of Copper Distribution and Speciation in Roots of *Triticum aestivum*

Exposed to CuO, Cu(OH)₂, and CuS Nanoparticles

C.1. Synchrotron X-ray Analysis

For the plant roots, an initial large area survey scan at 15.8 keV was conducted to identify the area of interest and obtain overall elemental distributions (~2 h per time point). The scanning velocities were 4 mm/s, with dwell times of 1.25 ms and step size of 5 μm in the x and y directions. Subsequently, a smaller area was chosen to conduct fluorescence XANES imaging with the XANES stack itself consisting of 95 individual maps at decreasing energies across the Cu K edge (see details below). The scanning velocities of these XANES maps were 12 mm/s and 6 mm/s for the root tips and root elongation zones, respectively. Step sizes for the root tips was 25 μm in the x and y directions, and step sizes for the root elongation zones were 12.5 μm in the x and y directions. Dwell times were 2.08 ms.

The three nanoparticle types as standards were also analyzed as solutions using fluorescence-XANES imaging. All standards were prepared to a final copper concentration of 100 mg/L in $\frac{1}{4}$ strength Hoagland's medium. For each standard solution, a strip of filter paper (~2 mm wide) was immersed for 30 s, allowing the solution to wick up the paper. The strips were then wrapped in polyimide film and placed vertically on the sample holder for analysis using fluorescence-XANES imaging with a scanning velocity of 4 mm/s, a step size of 50 μm in the x and y directions, and a dwell time of 12.5 ms.

The fluorescence-XANES imaging consists of "stacks" of 95 $\mu\text{-XRF}$ maps collected at decreasing incident energies from 9300 eV to 8900 eV across the Cu K edge. The energies of these 95 progressive scans are as follows: 9300-9100 in 25 eV decrements (nine energies), 9090-9050 in 10 eV decrements (five energies), 9046-9010 in 4 eV decrements (ten energies), 9009-9000 in 1 eV decrements (ten energies), 8999.5-8976 in 0.5 eV decrements (forty-eight energies), 8975-8970 in 1 eV decrements (six energies), 8960-8900 in 10 eV decrements (seven energies).

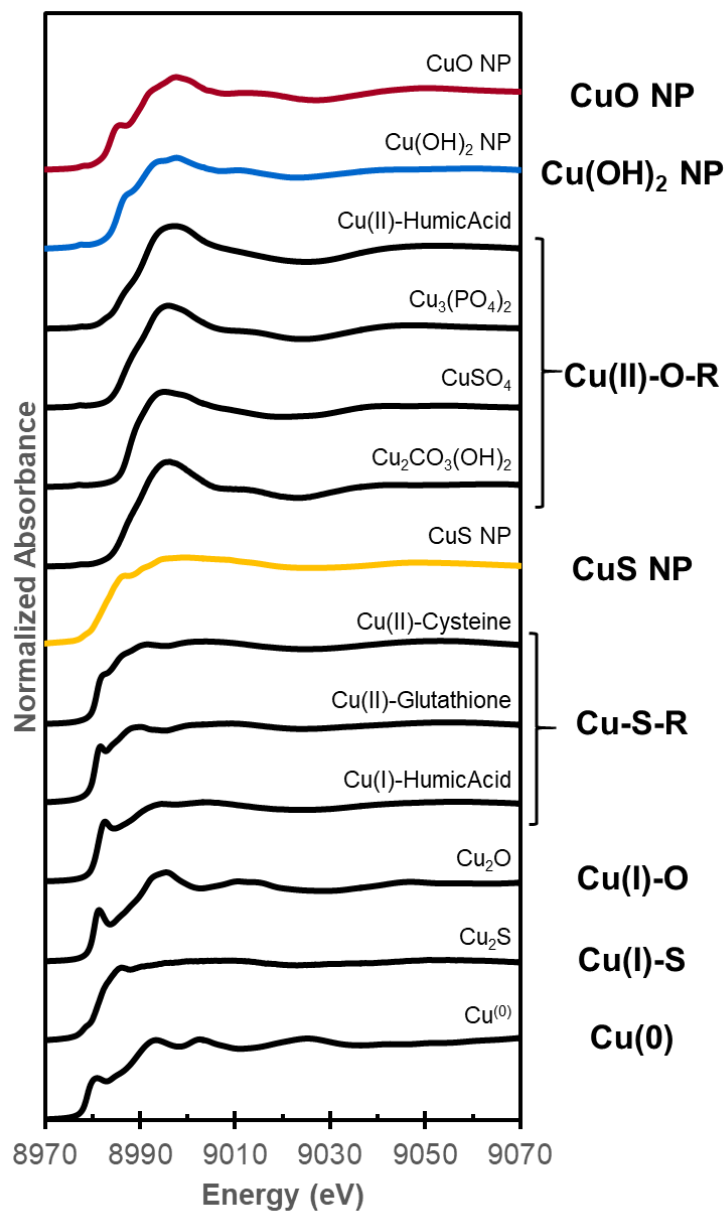


Figure C.1: Normalized Cu K-edge XANES spectra of starting NPs and model compounds. Spectra are also labeled with the simplified binding environment used for explanation of fits. NP standards were collected for this study. Cu(I)-HA model was obtained from Fulda et al. All other models were obtained from Stegemeier et al. Compounds grouped together have white lines within 1 eV and thus not distinguishable.

Fulda, B.; Voegelin, A.; Ehlert, K.; Kretzschmar, R. Redox Transformation, Solid Phase Speciation and Solution Dynamics of Copper during Soil Reduction and Reoxidation as Affected by Sulfate Availability. *Geochim. Cosmochim. Acta* **2013**, *123*, 385–402.

Stegemeier, J. P.; Avellan, A.; Lowry, G. V. Effect of Initial Speciation of Copper- and Silver-Based Nanoparticles on Their Long-Term Fate and Phytoavailability in Freshwater Wetland Mesocosms. *Environ. Sci. Technol.* **2017**, *51* (21), 12114–12122.

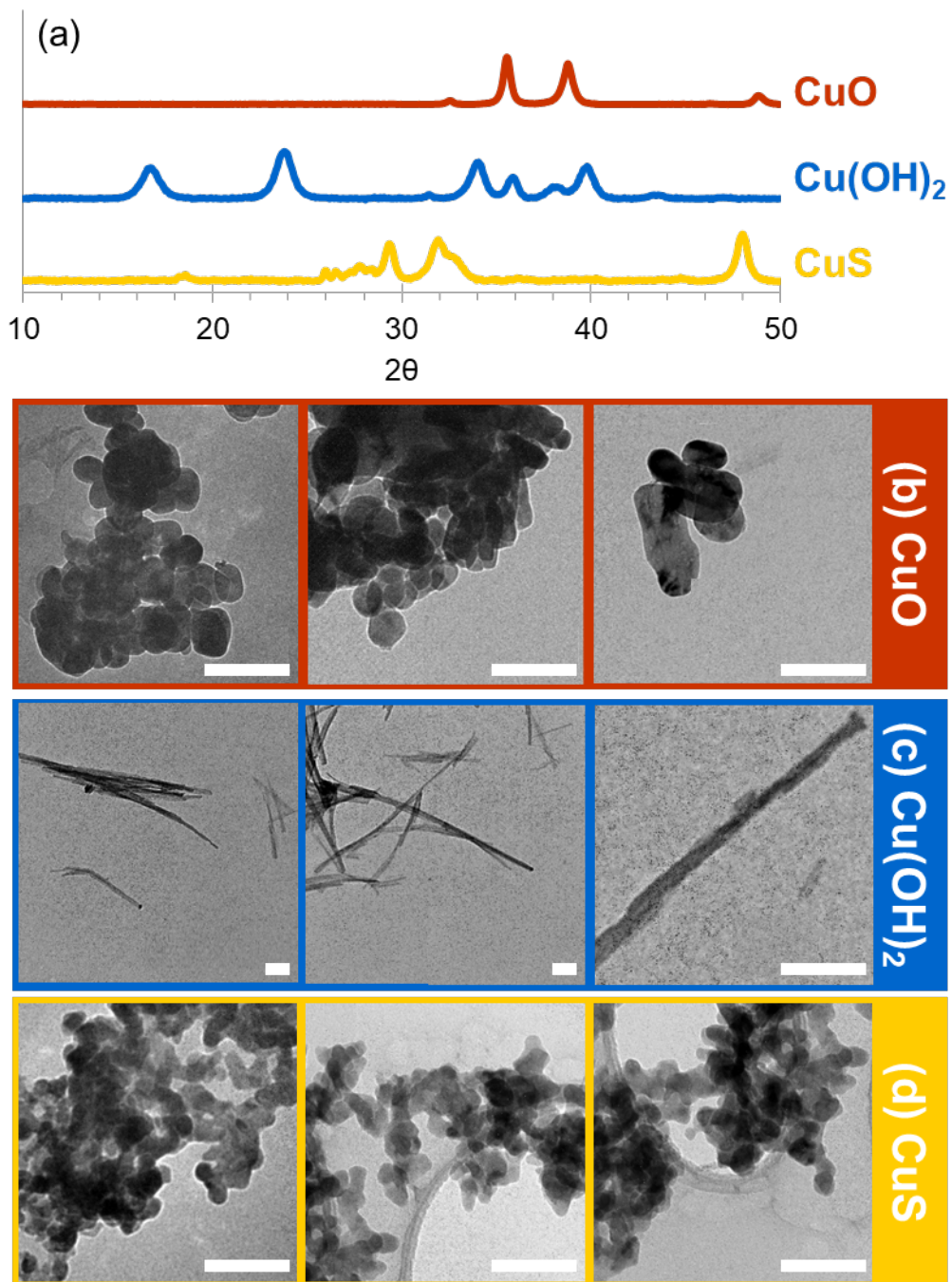


Figure C.2: NP characterization consisting of (A) XRD spectra of NPs and TEM images of (B) CuO NPs, (C) Cu(OH)₂ NPs, and (D) CuS NPs. Scale bar = 100 nm.

Table C.1: Total Cu concentrations on/in dried wheat roots (**top**) and leaves (**bottom**) after 1 h of exposure and after 12 h and 48 h depuration in Cu-free solution (continuously aerated). The reported values are means averaged from three replicates \pm SD

Cu Concentration in Roots (mg/kg DW)				
	0 h	1 h exposure	12 h depuration	48 h depuration
Control		42 \pm 20	36.6 \pm 8.6	10.1 \pm 2.4
CuO		1460 \pm 200	890 \pm 330	700 \pm 89
CuS	17.3 \pm 1.0	930 \pm 440	450 \pm 28	359 \pm 29
Cu(OH) ₂		840 \pm 230	440 \pm 110	483 \pm 11
Cu ⁺² High		569 \pm 41	437 \pm 31	338 \pm 57
Cu ⁺² Low		54.3 \pm 9.2	50.4 \pm 4.3	39 \pm 11

Cu Concentration in Leaves (mg/kg DW)				
	0 h	1 h exposure	12 h depuration	48 h depuration
Control		13.4 \pm 1.3	10.1 \pm 2.4	8.2 \pm 2.8
CuO		12.5 \pm 1.5	14.4 \pm 0.5	17.7 \pm 0.9
CuS	10.8 \pm 2.3	16.6 \pm 1.3	16.1 \pm 1.6	18.5 \pm 1.0
Cu(OH) ₂		21.9 \pm 3.9	15.1 \pm 2.0	18.4 \pm 0.2
Cu ⁺² High		18.7 \pm 1.8	16.6 \pm 2.4	18.2 \pm 1.8
Cu ⁺² Low		12.3 \pm 0.6	9.3 \pm 0.7	11.1 \pm 0.7

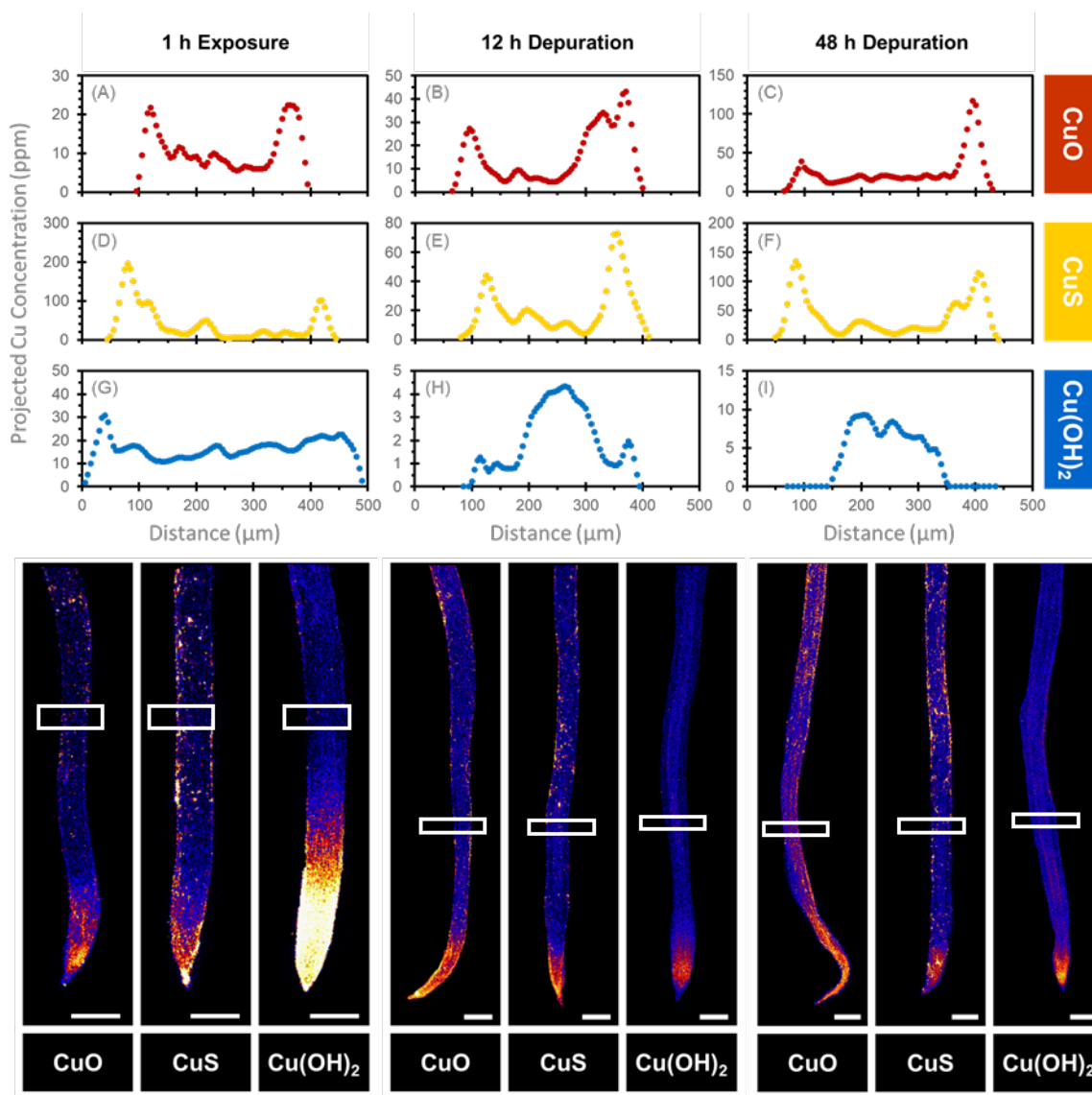


Figure C.3: XRF maps of Cu distribution in wheat roots (continuously aerated) exposed hydroponically to 1 mg-Cu/L as (A-C) CuO NP, (D-F) CuS NP, or (G-I) Cu(OH)₂ NPs for (A,D,G) 1 h, rinsed, then placed in a Cu-free medium (depuration period) for (B,E,H) 12 h or (C,F,I) 48 h. Scale bar is 500 μm. White boxes (250 μm in height) on the XRF maps indicate where the Cu concentrations were calculated at ~3 mm from the root tip using GeoPIXE's traverse projection junction.

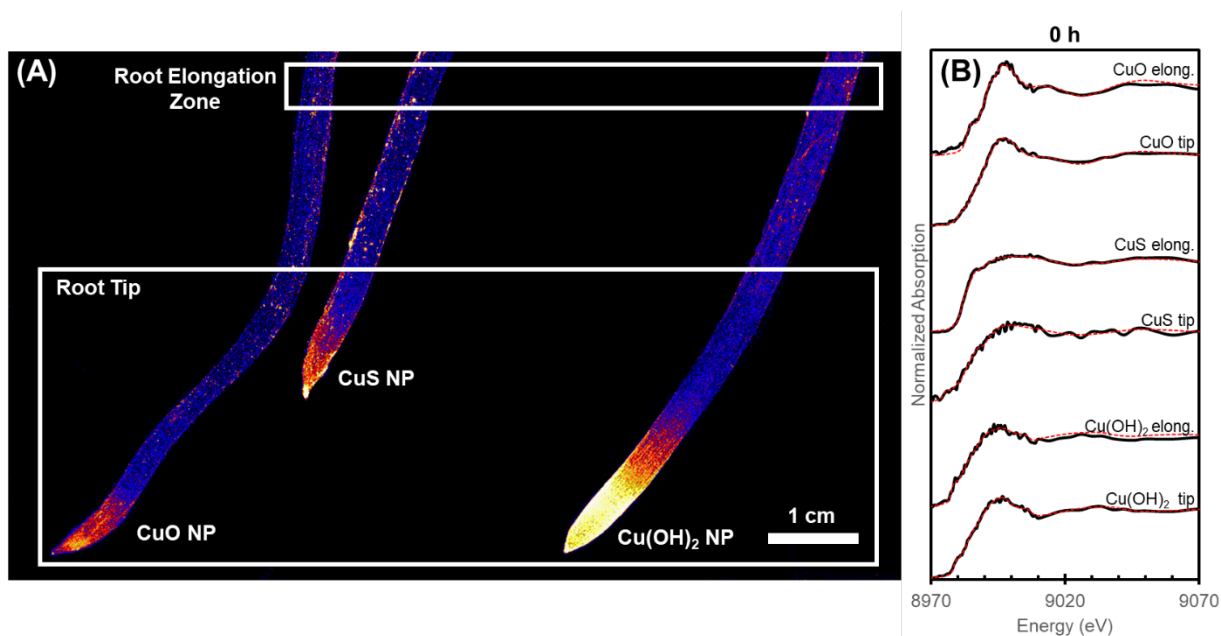


Figure C.4: (A) XRF elemental map showing total Cu distribution in wheat roots (continuously aerated) exposed hydroponically to 1 mg-Cu/L as Cu-based NPs for 1 h, with white boxes indicating the area examined by XANES imaging. (B) Normalized Cu K-edge XANES sample spectra. Red dashed lines are the fitted spectra while the solid black lines are experimental data. Details regarding the fits are presented in **Table C.2**.

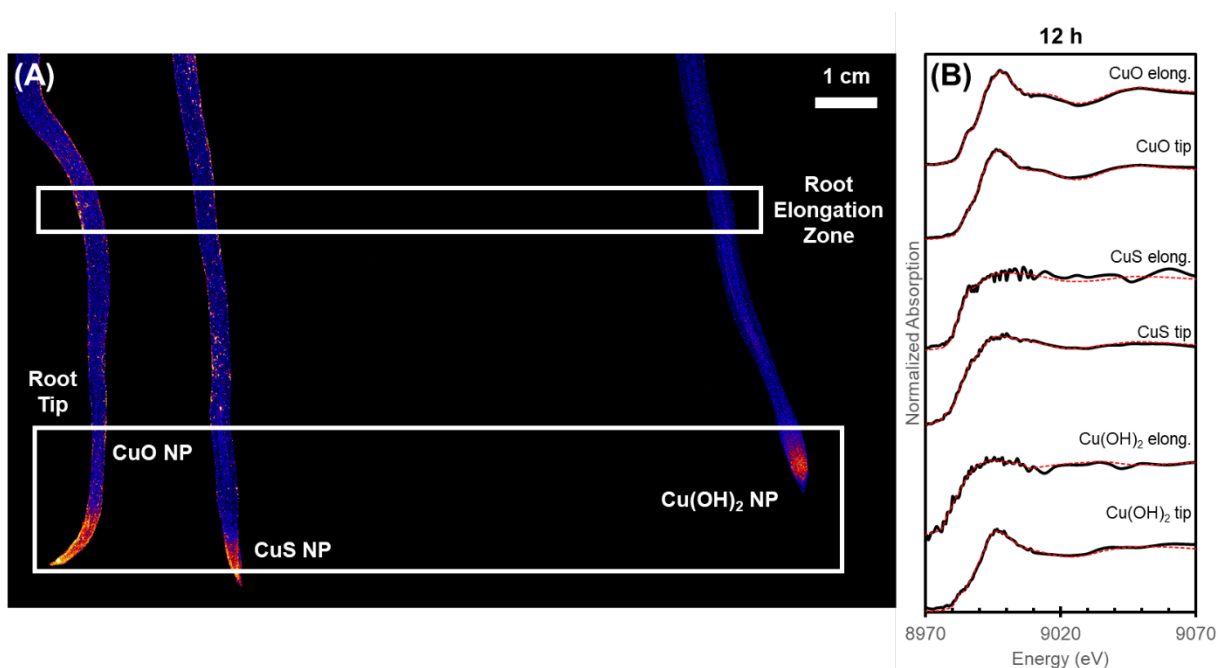


Figure C.5: (A) XRF elemental map showing total Cu distribution in wheat roots (continuously aerated) exposed hydroponically to 1 mg-Cu/L as Cu-based NPs for 1 h, rinsed, then placed in a Cu free medium (deuration solution) for 12 h, with white boxes indicating the area examined by XANES imaging. (B) Normalized Cu K-edge XANES sample spectra. Red dashed lines are the fitted spectra while the solid black lines are experimental data. Details regarding the fits are presented in **Table C.2**.

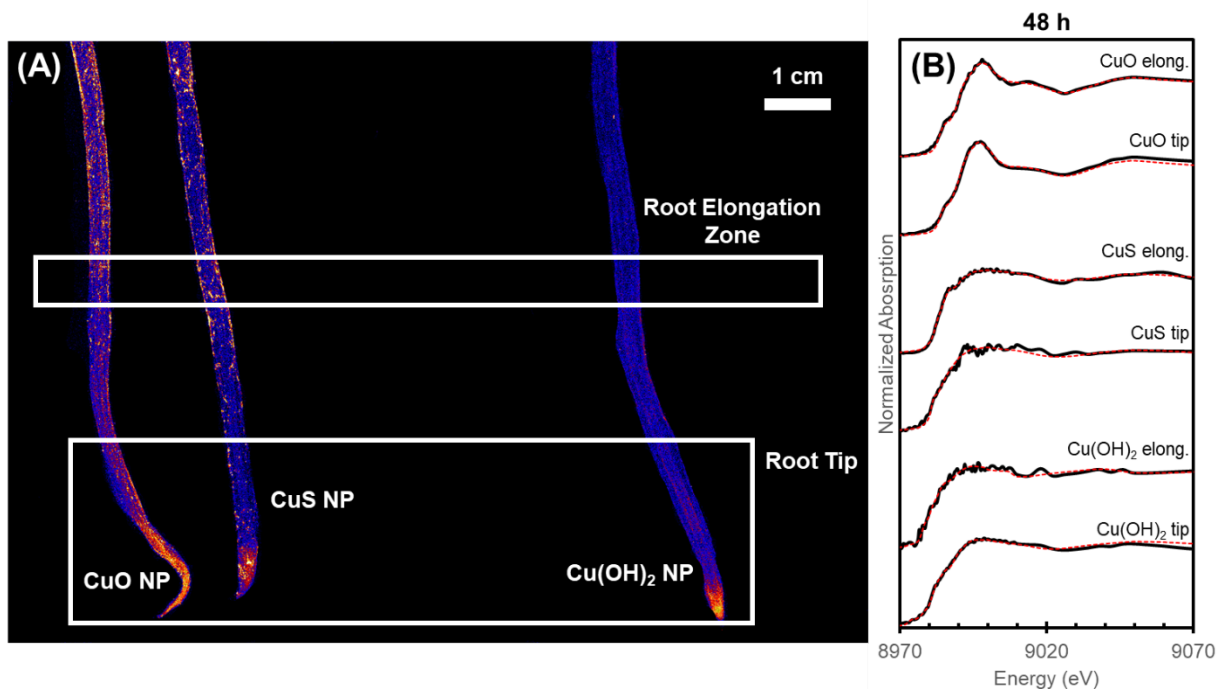


Figure C.6: (A) XRF elemental map showing total Cu distribution in wheat roots (continuously aerated) exposed hydroponically to 1 mg-Cu/L as Cu-based NPs for 1 h, rinsed, then placed in a Cu free medium (deuration solution) for 48 h, with white boxes indicating the area examined by XANES imaging. (B) Normalized Cu K-edge XANES sample spectra. Red dashed lines are the fitted spectra while the solid black lines are experimental data. Details regarding the fits are presented in **Table C.2**.

Table C.2: Linear combination fitting results of Cu K-edge XANES spectra (**Figure C.4, 5, 6**) for plant roots. Presented with the R-factor and reduced χ^2 parameters.

Treatment	CuO NP (%)	Cu(OH) ₂ NP (%)	Cu-O-R (%)	CuS NP (%)	Cu ₂ S (%)	Cu-S-R (%)	Sum	Reduced χ^2	R Factor
<i>CuO</i>									
0 h tip	36.9		64.3				101.2	0.00033	0.00149
0 h elong	86.4		13.8				100.2	0.00187	0.00842
12 h tip	44.9		48.7				93.6	0.00040	0.00189
12 h elong	80.2		17.4				97.6	0.00031	0.00137
48 h tip	59.3		39.9				99.2	0.00058	0.00286
48 h elong	56.2		39.4				95.6	0.00069	0.00336
<i>CuS</i>									
0 h tip			13.4	65.0		22.0	100.4	0.00146	0.00973
0 h elong				64.9		35.1	100.0	0.00041	0.00232
12 h tip			20.0	75.6		12.9	108.5	0.00034	0.00295
12 h elong				83.3		13.9	97.2	0.00171	0.01132
48 h tip			19.3	44.4		37.5	101.2	0.00180	0.01226
48 h elong			8.6	68.8		19.1	96.5	0.00030	0.00182
<i>Cu(OH)₂</i>									
0 h tip		33.1	24.0			41.1	98.2	0.000473	0.00237
0 h elong		33.0	16.5			54.6	104.1	0.001059	0.00631
12 h tip			53.8		12.5	27.5	93.8	0.000588	0.00429
12 h elong			30.2		45.4	24.3	99.9	0.001339	0.00845
48 h tip			30.7		67.2	10.0	107.9	0.000283	0.00170
48 h elong			19.9		51.4	28.8	100.1	0.001896	0.01254

APPENDIX D

Supporting Information for **Chapter 5:**

Active Targeted Delivery of Nanoparticles to Stomatal Guard Cells

Table D.1. Summary of monoclonal antibodies to (1-5)- α -L-arabinan

Antibody	Isotype	Specificity	Reference
LM6-M	IgM	Recognizes linear (1-5)- α -L-arabinan. It has no cross-reactivity with gum arabic but it may recognize arabinogalactan-proteins in some species. LM6-M has similar specificity to LM6, but is a different isotype.	[3]
LM6	IgG	Recognizes a linear pentasaccharide in (1-5)- α -L-arabinans. It can recognize pectic polysaccharides in several species. It has no cross-reactivity with gum arabic but it may recognize arabinogalactan-proteins in some species.	[1,3]
LM13	IgM	Recognizes linear epitope in (1-5)- α -L-arabinans. This antibody binds to a specific subset of pectic arabinans, and to longer stretches of 1,5-linked arabinosyl residues that are likely to be more abundant in unbranched arabinans. LM13 is more sensitive to arabinanase action than LM6	[2]

- [1] Willats, W. G. T.; Marcus, S. E.; Knox, J. P. Generation of a Monoclonal Antibody Specific to (1 \rightarrow 5)- α -L-Arabinan. *Carbohydrate Research*. **1998**, 149–152.
- [2] Verhertbruggen, Y.; Marcus, S. E.; Haeger, A.; Verhoef, R.; Schols, H. A.; McCleary, B. V.; McKee, L.; Gilbert, H. J.; Knox, J. P. Developmental Complexity of Arabinan Polysaccharides and Their Processing in Plant Cell Walls. *Plant J*. **2009**, 59 (3), 413–425.
- [3] Cornuault, V.; Buffetto, F.; Marcus, S. E.; Fabienne, M. C.; Ralet, G. M.; Knox, J. P. LM6-M : A High Avidity Rat Monoclonal Antibody to Pectic α -1,5-L-Arabinan. *bioRxiv* **2017**, 1–11

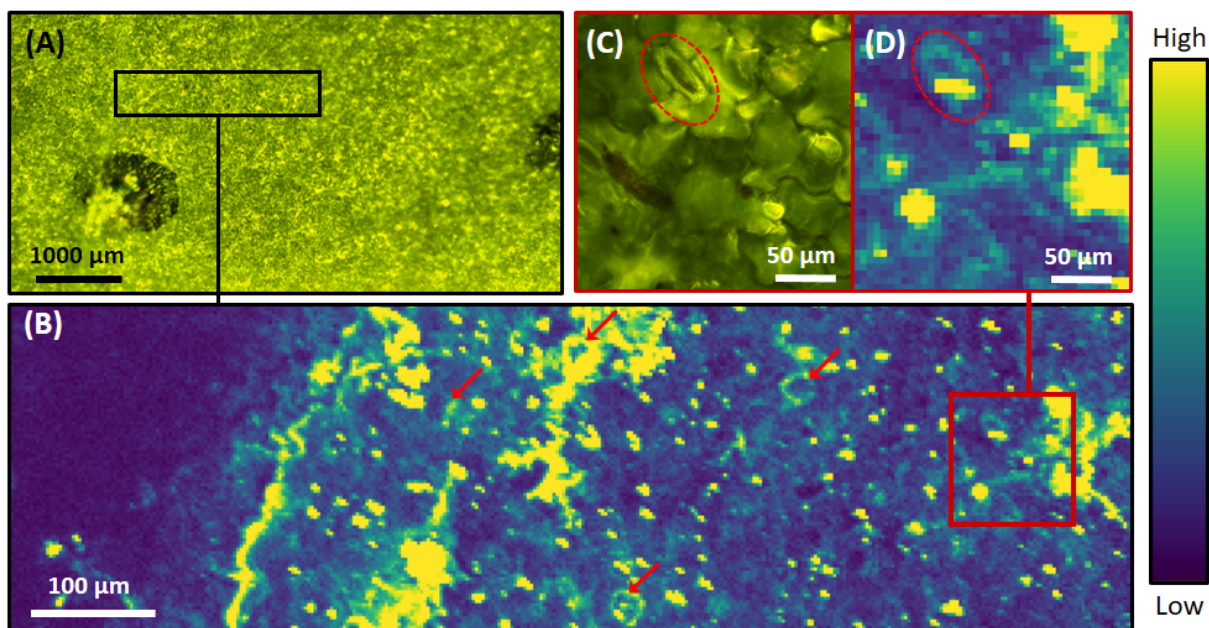


Figure D.1. *V. faba* leaf exposed via drop deposition to LM6M-NP solution, then rinsed for 1 min in a basal salt solution. **(A)** Light microscope image of drop deposition zone (region between the two black dots) with region analyzed by XFM indicated by a black rectangle. **(B)** Elemental map showing total Au distribution (see color scale to right). Several stomata that were successfully targeted are indicated by red arrows. The region inside the red box is enlarged both as a **(C)** light microscope image and a **(D)** Au XFM map, with one stoma indicated inside the red dashed oval.

APPENDIX E

This chapter is adapted from a publication and is citable as:

Spielman-Sun, E.; Zaikova, T.; Dankovich, T. A.; Yun, J.; Ryan, M.; Hutchison, J. E.; Lowry, G.

V. Effect of Silver Concentration and Chemical Transformations on Release and Antibacterial

Efficacy in Silver-Containing Textiles. *NanoImpact* **2018**, *11* (November 2017), 51–57.

ABSTRACT

Silver-enabled fabrics may be transformed during use in ways that may affect their release characteristics and antibacterial efficacy. Here, we assess how chemical transformations of silver in fabrics treated with Ag nanoparticles or AgCl particles, or containing interwoven Ag⁰ fibers affect silver leaching and their antibacterial efficacy under different use and end-of-life scenarios. Fabrics were exposed to artificial sweat (use phase) or artificial landfill leachate (sodium chloride, sodium sulfide, or acetic acid; end of life phase). Chemical transformations induced by exposure to sodium chloride, sodium sulfide and acetic acid result in variations in Ag release and corresponding changes in bactericidal properties of the Ag-treated textiles. Exposure to solutions containing chloride ions (sodium chloride and artificial sweat) generally increased leaching compared to deionized water. Conversely, exposure to sodium sulfide and acetic acid solutions decreased Ag release. Exposure to artificial sweat did not affect antibacterial efficacy for fabrics with greater than ~10 µg Ag (g fabric)⁻¹. Sulfide solution exposure decreased antibacterial performance for all but the 500 µg Ag (g fabric)⁻¹. The lower efficacy was consistent with chemical transformation of elemental Ag to AgCl/Ag⁰ or Ag₂S, respectively for chloride and sulfide exposure. AgCl-coated fabrics were more resilient to chemical attack than Ag⁰-enabled fabrics. These results indicate that fabrics with as low as ~10 µg Ag (g fabric)⁻¹ can maintain high antibacterial efficacy under normal use phase conditions, but below this concentration efficacy significantly decreases. Taken together, the data permit a comparison of the benefits (antimicrobial efficacy) in the context of the impacts (silver release) and inform selection and design of materials and loadings that give the best overall lifecycle benefit.

E.1 INTRODUCTION

The functional properties of textiles can be modified by the addition of nanomaterials that can improve the properties of textiles,^{1,2} such as antibacterial properties^{3,4}, UV protection,⁵ abrasion resistance,⁶ and hydrophobicity.⁷ To be economically viable and environmentally sustainable, the functional improvements to the textile properties introduced by the nanomaterial need to out-weigh the additional manufacturing costs and the potential impacts over the lifecycle of the textiles. The use of silver (Ag) in textiles is a good example: the antibacterial properties of that material must remain sufficiently high over the lifetime of the product to warrant the cost and environmental impacts of Ag.⁸ To ensure maximum functional performance, i.e. antibacterial activity, the optimal amount of Ag, the form of nano-Ag, and the attachment methods of Ag to the fiber surfaces should be selected to reduce impacts and enhance performance.⁹ This study assesses the role of chemical transformations of different silver forms on the functional benefit (antibacterial activity) and impacts (silver release) of silver-enabled consumer textiles.

During the functional usage and end-of-life phases of these nano-enabled textiles, chemical transformations may affect the functional performance of such products or the potential for human exposure to the incorporated nanoparticles (NPs).¹⁰⁻¹³ For example, during the nano-Ag textile's lifecycle, the Ag can undergo various chemical changes, including dissolution^{9,13-16} and sulfidization¹⁷ due to ambient hydrogen sulfide in air, or other alterations that can limit Ag antibacterial efficacy. Such transformations may also affect the release of Ag from the textile and the potential for human exposure during use or release to the environment.^{13,18} The effects of these transformations on both the performance and potential release of Ag is required for the different silver attachment approaches and silver loadings to determine the impact-benefit ratio for different Ag use scenarios in fabrics.

Significant research has been conducted on Ag release from AgNP enabled fabrics under various use-phase scenarios. Most of these studies have focused on the behavior of AgNPs in fabrics through detergent washing tests and observed particulate release. Such studies determined that detergent composition, particle size, and fabric attachment method strongly affect particulate release^{16,19,20} and final speciation of Ag (combination of Ag⁰, AgCl, and Ag₂S).^{10,15,21} Several papers have also tested usage scenarios, such as sweat,^{11,16,19,22–26} though there is no established standard method for this. Notably, only a few papers have evaluated the potential environmental effects of Ag containing textiles at the “end-of-life” phase,^{9,13} though there exist standardized methods by the Environmental Protection Agency (EPA) for this e.g. toxicity characteristic leaching protocol (TCLP; acetic acid at pH=4.9).²⁷ Additionally, little work has been done to evaluate the impact of AgNP enabled fabrics on antimicrobial activity of Ag on the biological landfill operations.^{28–30}

Importantly, product efficacy testing is often limited to the “as produced” product and does not consider how transformations throughout the lifecycle may influence efficacy and/or release. The evaluation of bactericidal properties due to changes in the speciation of the embedded Ag during the product usage and end-of-life phases is highly important to understand the potential for long-term product performance and potential hazards to the human environment, respectively. Measuring Ag release from the fabrics without considering the potential transformations of the Ag in the fabrics, as is often done, may lead to overestimates or underestimates of Ag release depending on the use phase or end of life chemical environment. Apart from Reed et al.⁹, previous studies have not examined both the Ag release and subsequent changes in Ag availability for the intended function of biocidal activity towards bacteria. The latter is typically only completed as a proof-of-concept on the as-manufactured materials at the research stage, or during product

registration, as a demonstration of the efficacy of a new form of a bactericidal material. Such lifecycle efficacy testing is needed to determine if assumptions made in lifecycle benefits-impacts analyses are reasonable.

The objective of this study was to investigate how transformations in the silver species on the textiles influence antibacterial activity and release in order to assess the benefits versus potential impacts of different Ag-containing textiles. Laboratory models were used to simulate product usage and disposal conditions commonly encountered for such products. The effect of the Ag speciation (metallic Ag⁰ vs. AgCl vs NP), the Ag concentration, and the method of Ag attachment to the textile were assessed to determine the influence on the fabric's ability to maintain its antibacterial efficacy during the simulated use-phase. Use-phase conditions included exposure to acidic and alkaline sweat exposure and simulated landfill disposal conditions included the TCLP and exposure to chlorides and sulfides. Product usage and end-of-life conditions were evaluated over time ranging from one hour for sweat solutions to one week for end-of-life solutions. Following these model exposure scenarios, the release of Ag from the textile, transformation of the remaining Ag in the textile, and the antibacterial efficacy of the remaining Ag in the textile were determined. This work has been published in *NanoImpact*.³¹

E.2 MATERIALS AND METHODS

E.2.1. AG-ENABLED TEXTILES: Two commercially available and two custom-synthesized AgNP-functionalized polyester textiles were studied. Two commercially available polyester textiles used were Ag-coated fibers woven into a shirt (X-Static[®], referred to as “Ag⁰-coated”) and AgCl applied to the fabric (Polygiene[®], referred to as “AgCl-coated”). The synthesized textiles used either electrostatic attachment of AgNPs to fibers, referred to as “Electrostatic-AgNP”, or attachment

based on proprietary linker molecule that tethers AgNPs to the fibers, referred to as “Tethered-AgNP”. Details regarding synthesis and characterization of custom-synthesized textiles are provided in Reed et al.⁹ The average diameter of the AgNPs used was 20.0 ± 7.0 nm as determined by TEM.⁹ The fabrics studied contained between 1 and 500 $\mu\text{g Ag/g}$ textile (**Table E.1**)

Table E.1. Description of textiles investigated in this study. Ag content in the control textile was below the detection limit (BDL).

Source	Label	Product Description	Silver content ($\mu\text{g Ag/g}$ fabric)
Commercial product	Ag ⁰ -coated	Fibers are permanently bonded with a layer of 99.9% pure metallic silver	492 ± 21
	AgCl-coated	Polygiene [®] AgCl particles are more than 100 times larger than nanoparticles	22.7 ± 1.3
	Control	100% Polyester	BDL
Synthesized for study	Electrostatic-AgNP	Tween stabilized AgNPs linked via electrostatic forces	1.08 ± 0.19
	Tethered-AgNP	Tween stabilized AgNPs linked via proprietary linker	21.2 ± 1.2

E.2.2. TEXTILE EXPOSURE: To simulate the “use-phase” scenario, acidic (pH=3.5) and alkaline (pH=8.0) artificial sweat solutions were prepared as described in AATCC Method 15.³² Briefly, the acidic sweat solution contains 0.25 g of histidine, 1 g of lactic acid (85%), 10 g of NaCl, and 1 g of Na₂HPO₄ per L of DI water. The alkaline sweat solution contains 0.25 g of histidine, 4 g of (NH₄)₂CO₃, 10 g of NaCl, and 1 g of Na₂HPO₄ per L of DI water. pH was adjusted using 1 M HCl or 1 M NaOH. ~4 cm² fabric swatches were exposed to 20 mL of artificial sweat solution or DI water in a polypropylene container and incubated quiescently for 60 minutes at 37 °C. As per the AATCC Method, the fabric swatches were then removed from the solution and pressed between paper towels with ~3 kg weight overnight to remove residual solution before being air dried. To simulate “end-of-life” scenarios, ~4 cm² fabric swatches were exposed to 50 mL of an exposure solution (500 mM NaCl, 10 mM Na₂S, TCLP, or DI water) in a polypropylene container in the

dark at 20 °C for 1 week. The fabric swatches were air dried, and set aside for subsequent experiments. The total amount of Ag leached into the solution during the test, remaining in the fabrics, and absorbed into the paper towels during the test was determined by ICP-MS. All exposure scenarios were performed in triplicate. To determine total Ag in the untreated fabrics, five 4-cm² swatches of each textile were taken from random parts of the larger fabric (in order to account for fabric heterogeneity).

Using established methods,^{33,34} exposure solutions and fabrics were spiked with concentrated HNO₃, heated to 95 °C for 30 min, and then spiked with concentrated HCl to give a 3:1 ratio of HNO₃: HCl. Samples were heated at 95 °C for 2 hours, allowed to cool, and diluted to a final concentration of 5% HNO₃ with DI water. Samples were centrifuged and the top 10 mL of supernatant was removed for total metals analysis using Inductively Coupled Plasma - Mass Spectrometry (ICP-MS, Agilent 7700x, Santa Clara, CA). Blanks and standard reference material (Environmental Express, Charleston, SC) were used to validate the digestion and analytical method. The calibration curve consisted of the following concentrations: 0, 10, 100, and 1000 ppb. All samples either fell within the range of the calibration curve or were diluted to be within the range. The detection limit was 0.1 ppb. Samples were measured five times and averaged to give an output concentration with an RSD. Blanks were run every 10 samples. Ag concentrations in the paper towels from the “use-phase” exposure scenarios were not significant.

E.2.3. DETERMINATION OF AG TRANSFORMATIONS IN TEXTILES: Ag transformations in the textiles under end-of-life scenarios were analyzed by Ag K-edge X-Ray Absorption Near Edge Spectroscopy (XANES) at the Stanford Synchrotron Radiation Light Source (SSRL) on Beamline 4-1 using a Si (220) monochromator crystal across the Ag K-edge (25,514 eV). Only the Ag⁰-coated textile contained enough Ag for evaluation of the speciation. The Ag⁰-coated textile was

analyzed pre- and post-1 week exposure. Harmonic rejection was achieved by detuning the monochromator by 20%. The samples were loaded into aluminum holders, enclosed in Kapton® tape, and transferred to a liquid nitrogen cryostat (77 K) to minimize thermal vibration and improve the quality of the spectra. Spectra were collected on a 32-element germanium detector in fluorescence mode. The scans were averaged, energy corrected using a metallic Ag foil standard, deadtime-corrected, background subtracted with E_0 defined at 25,534 eV, and de-glitched using SixPack data analysis software.³⁵ Spectra were analyzed by linear combination fitting (LCF) using the following reference spectra: metallic Ag, Ag₂S, Ag-acetate, and AgCl. Inclusion of a reference spectrum into the combination fit required at least a 10% decrease in the R-value, indicating a significant change to the quality of the fit.

E.2.4. ANTIBACTERIAL EFFICACY OF TEXTILES: The antibacterial efficacy of the textiles was tested in triplicate using a modified protocol based on the AATCC Test Method 100.³⁶ The viable *E. coli* cell count on the untreated control polyester fabric was assessed at two time points: immediately after fabric inoculation ($t=0$), and 24 hours after fabric inoculation. Standard deviation is reported for all samples. A saturated culture of *E. coli* XL1-Blue (Agilent Technologies/Stratagene, Santa Clara, CA) was raised in LB-H broth (1% tryptone, 0.5% yeast extract, 0.5% NaCl, 0.001 N NaOH, pH 7) by overnight incubation at 37 °C with shaking. The saturated culture (3.4×10^9 CFU/mL) was diluted in 0.85% NaCl. Swatches of ~ 1 cm² from each exposed (aged) fabric were weighed (~ 20 mg each) and placed into sterile Petri dishes and then inoculated with 50 μ L of the diluted culture (6.0×10^6 CFU/mL). Petri dishes were sealed and incubated for 24 h at 37 °C. After 24 h, fabric swatches were placed into 5 mL of PBS buffer (126 mM NaCl, 3.22 mM NaH₂PO₄, 7.18 mM Na₂HPO₄, pH \sim 7.1) and vortex mixed for 1 minute. Serial dilutions were performed and samples were plated.³⁷ Plates were inverted and incubated for 19 h

at 37 °C and colonies were counted. An untreated fabric (no Ag added) was used as a control sample for all experiments to make sure that bacteria reduction is due Ag present and not to exposure solutions. The viable *E. coli* cell count on the untreated control polyester fabric was assessed at two time points: immediately after fabric inoculation (t=0), and 24 hours after fabric inoculation. Bacteria reduction was calculated using number of bacteria eluted from fabrics at t=0 for all experiments. Standard deviation is reported for all samples.

E.3. RESULTS AND DISCUSSION

E.3.1. AG RELEASE FROM TEXTILES UNDER “USE-PHASE” SCENARIO: The total Ag released, normalized to surface area of fabric after one-hour exposure to both types of artificial sweat, are reported in **Figure E.1**. Previous work with these fabrics has shown that only a small fraction of released Ag (~8%) was present as Ag nanoparticulates.^{9,11,13} The total Ag release was generally greatest with the Ag⁰-coated textile ($0.73 \pm 0.04 \mu\text{g Ag/cm}^2$ for acidic sweat and $2.46 \pm 0.03 \mu\text{g Ag/cm}^2$ for alkaline sweat), which also had the highest initial Ag content. The Ag release for both the Ag⁰-coated textile and AgCl-coated textiles was greater into the alkaline sweat than the acidic sweat. There was no statistical difference (two-sample *t*-Test) in Ag release between acid and alkaline sweat for the Electrostatic-AgNP or Tethered-AgNP textiles. It would be expected for Ag to be more soluble in the acidic sweat solutions because AgNPs dissolve more readily in acidic solutions.³⁸ However, other factors such as particle size, type, and precipitation of AgCl_(s) may also be affecting the dissolution rates for the different particle types.³⁹ Kulthong et al. also found the effect of pH on Ag release from Ag-enabled textiles exposed to artificial sweat to be negligible²² and Wagener et al. found no correlation between Ag release and artificial sweat pH for AgNP-enabled polyester/polyester blend fabrics.²⁵

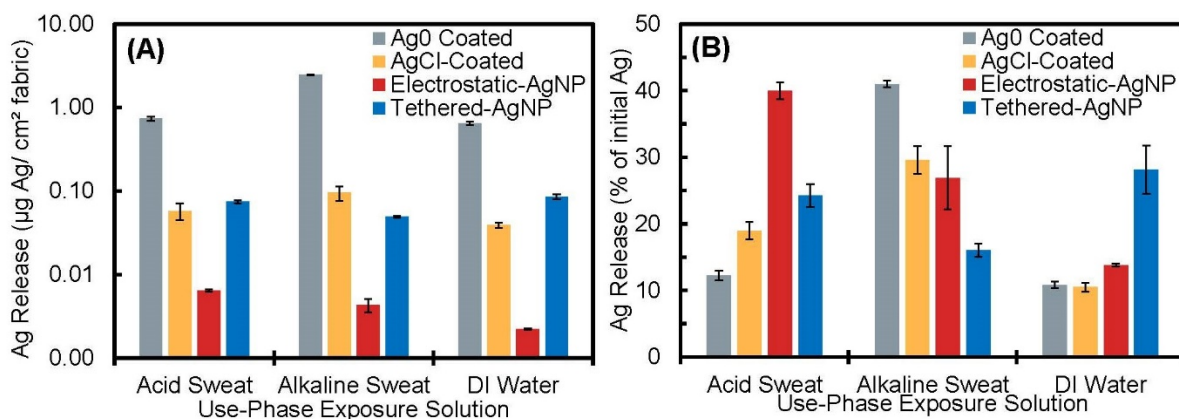


Figure E.1: Ag release from Ag-enabled textiles during “Use-Phase” exposure scenarios normalized to the (A) surface area of the textile and (B) initial Ag content of the textile. Note that Figure 1A y-axis is in a log scale. Error bars are \pm one standard deviation of triplicate experiments, i.e. three separate fabric swatches per solution.

To provide a more thorough understanding of Ag release from these textiles in the context of potential for Ag exposure and the impact on product efficacy, the total Ag release was normalized to the initial Ag loading (**Figure E.1 b**). The Electrostatic-AgNP textile, which had the lowest starting Ag concentration (**Table E.1**) and the lowest levels of total Ag release (**Figure E.1 a**), showed significantly higher percent release of the initial Ag loading, particularly under the acidic sweat exposure (**Figure E.1 b**). The low total mass of Ag release suggests limited overall environmental impacts but larger percentage release fails to maintain sufficient Ag in the fabrics for antimicrobial activity for extended times (assuming that one sweat simulation is equivalent to one usage period). Balakumaran et al observed similar percentages of silver release from AgNP treated cotton fabrics exposed to acidic (pH=4.3; 49%) and alkaline (pH=8.0; 19%) artificial sweat.²⁴ In contrast, the Ag⁰-coated textile showed the highest overall total Ag release per cm² and the highest percentage of Ag retained. This suggests a greater potential for repeated Ag release and prolonged efficacy due to the majority of the Ag remaining in the Ag⁰-coated textile. However,

as discussed later in **Section E.3.3**, the silver release and efficacy also depend on resulting speciation of the Ag in the fabrics.

E.3.2. AG RELEASE FROM TEXTILES UNDER “END-OF-LIFE” SCENARIO: The total Ag release varied considerably with respect to the corrosive agent and the means of Ag attachment to the fabrics (**Figure E.2 a**). For all fabrics, the Ag release per cm² of fabric was the least for solutions containing Na₂S (**Figure E.2 a**). This suggests that an Ag₂S corrosion layer is forming on the surface that prevents further leaching of silver into the solution. The Ag⁰-coated textile with the highest initial loading of Ag leached the highest levels of Ag in the 500 mM NaCl solution. The textile with the lowest initial loading of Ag, the Electrostatic-AgNP textile, released significantly less Ag but a higher overall percentage of Ag than the Ag⁰-coated fabric into the 500 mM NaCl solution (**Figure E.2 b**). This is likely due to the lower total Ag loading, higher dissolution rate (due to the increased surface-to-volume ratio of the small AgNPs compared to the larger Ag⁰-coated fibers) and weaker attachment of the NP to the textile.⁴⁰ The leached Ag concentration was below 15 µg/L for all samples, which is several orders of magnitude lower than the 5 mg/L Resource Conservation and Recovery Act (RCRA) regulatory limit for leached Ag.⁴¹ Given that the released Ag is likely largely dissolved^{9,11,13} and the releases are significantly lower than the regulatory allowable standards, the disposal of these products should not threaten the operation of landfills, assuming that the current standards are protective. More Ag release (~50-60%) from the NP-enabled fabrics is observed under the TCLP exposure scenario than in the literature by Mitrano et al. (10-30%), which is attributed to the longer exposure time (18 h vs 1 week).¹³

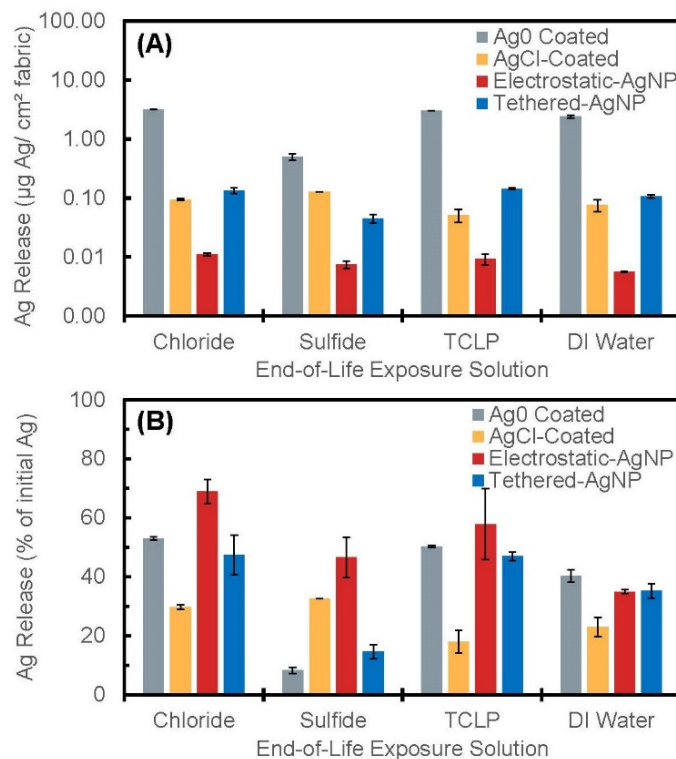


Figure E.2: Ag release from Ag-enabled textiles during “End-of-Life” exposure scenarios normalized to the (A) surface area of the textile and (B) initial Ag content of the textile. Error bars are \pm one standard deviation of triplicate experiments, i.e. three separate fabric swatches per solution.

Exposure to NaCl solutions and to artificial sweat provide insight into how the form of Ag incorporated into the fabrics can affect their performance. Both the 500 mM NaCl solution and the artificial sweat solutions contain chloride that can react with Ag to form soluble $\text{AgCl}_x^{[1-x]}_{(aq)}$ species.⁴² Accordingly, both the NaCl exposure and artificial sweat increased leaching of Ag compared to DI water for the Ag^0 -enabled fabrics. The AgCl-coated fabric was less affected by the presence of chloride ion than the Ag^0 -enabled fabrics. Thermodynamically, these two systems should behave the same given that there is excess chloride relative to Ag in all systems. Thus, the dissolution rate of AgCl particles in the presence of chloride must be slower than for the Ag^0 . This appears to be the case in general for all exposure solutions. The released mass of Ag from the AgCl-coated fabric was relatively constant across all treatments, except for the Na_2S (**Figure E.2**

a). This resulted in a more robust antibacterial fabric, regardless of the Ag concentration remaining in the material. The apparent resilience of AgCl particles in fabrics against aging in artificial sweat and other chloride-containing solutions suggests that this may be a preferred species of Ag for modifying fabrics for antibacterial properties, though this would need to be further demonstrated with a different amounts of Ag loading and exposure scenarios.

E.3.3. AG TRANSFORMATION IN AG⁰-COATED TEXTILES: : Synchrotron-based experiments were performed to quantify and identify new phase(s) formed on the Ag⁰-coated textiles after exposure to aqueous Na₂S, NaCl, and TCLP solutions for 1 week to better understand the chemical reactions responsible for changes in ion release after exposure. The exposure of the fabrics to the different solutions changed the Ag speciation in the fabrics. Unexposed Ag⁰-coated fabric was initially predominantly metallic Ag⁰ (**Figure E.3, Table E.2**). Exposure to the Na₂S solution resulted in complete sulfidation of the Ag to acanthite (Ag₂S). Exposure to the 500 mM NaCl solution resulted in approximately 50% conversion of the Ag to AgCl_(s). Exposure to the TCLP solution altered the speciation of Ag in the sample as well. The presence of Ag⁰ in the sample is evident from the characteristic peaks for Ag⁰ at 25,550 eV and 25,580 eV. However these peaks have a lower magnitude than the Ag⁰ model compound, indicating that there is a second phase in addition to the Ag⁰. None of the organic-Ag model compounds known (including Ag-acetate) matched the remainder of the spectra well, so the second phase remains unidentified. Regardless, there is a component of Ag⁰ remaining in this fabric. The Ag fibers in these Ag⁰-coated textiles have larger dimensions than the attached AgNPs (Electrostatic and Tethered) and the solid AgCl. Thus, even though the Ag in those textiles could not be speciated due to the lower Ag concentrations, they are expected to also be fully sulfidized under the Na₂S exposure conditions given the higher surface-to-volume ratio of the NPs compared to the fibers. Similarly, the partial transformation observed

for exposure of Ag^0 -coated fabrics in 500 mM NaCl or the TCLP solutions suggests that these transformations are also likely for the Tethered-AgNP and Electrostatic-AgNP fabrics, perhaps to a greater extent due to the increased surface-to-volume ratio of the small AgNPs compared to the non-nano Ag^0 coated fibers.⁴⁰

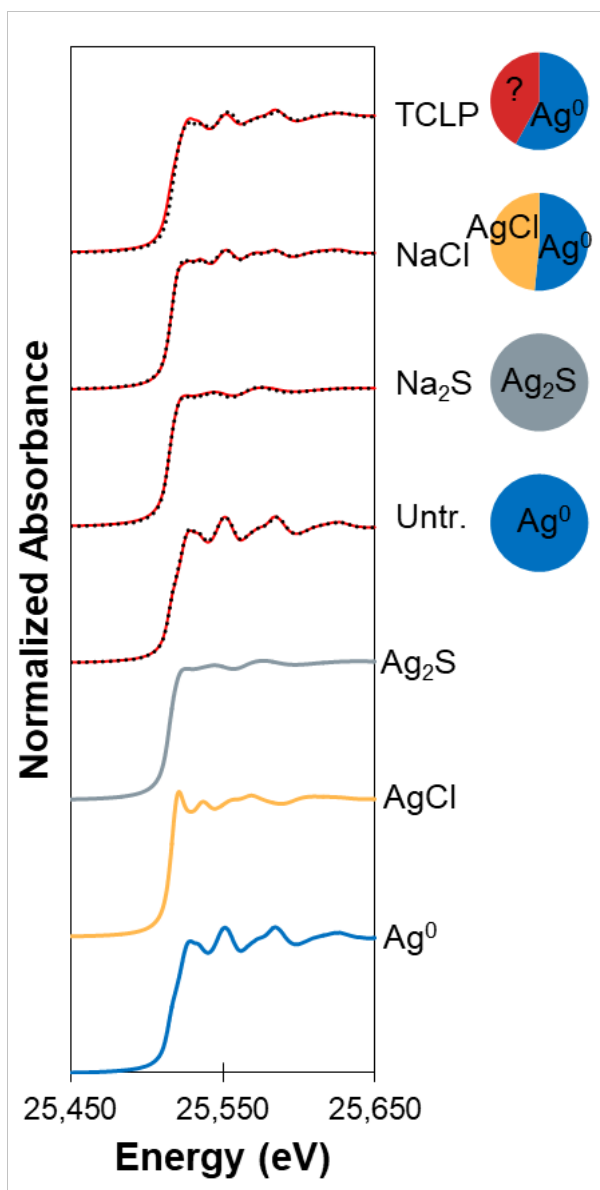


Figure E.3: XANES spectra of Ag standards and Ag^0 -coated textile after exposure to the different “end-of-life” exposure solutions. The red solid lines are fits while the black dotted lines are experimental data. Model compounds used for the fits are below the experimental spectra. The TCLP fits are relatively poor using Ag^0 alone ($R=8 \times 10^{-4}$) or Ag^0 and Ag-acetate ($R=2.8 \times 10^{-4}$). Thus the second species present in this exposure was not identified.

Table E.2: XANES fitting results for the woven textile exposed to the “end-of-life” scenarios

Treatment	% Ag ⁰	% Ag ₂ S	% AgCl	% Ag-acetate	R-value
Untreated	100	-	-	-	4.8x10 ⁻⁵
NaCl (500 mM)	52	-	49	-	4.1x10 ⁻⁵
Na ₂ S (10 mM)	-	100	-	-	3.3x10 ⁻⁵
TCLP	58	-	-	42*	2.8x10 ⁻⁴

*The best fit was obtained using an Ag-acetate model compound. However, the relatively poor XANES fit using Ag-acetate as a reference compounds prevents positive identification of this species as noted in **Figure E.3**.

E.3.4. ANTIMICROBIAL EFFECTIVENESS OF TEXTILES: Silver treated fabrics were exposed to usage or aging solutions and then evaluated for their bactericidal activities by measuring the number of viable bacteria recovered from the fabrics after 24 h of contact time. To account for any effect of exposure solutions on the fabric characteristics, a control fabric without Ag was also exposed to usage and aging solutions in parallel and evaluated. Finally, the reduction in viability of bacteria on untreated polyester fabric that *had not been exposed* to usage or aging solutions was compared to the exposed fabrics. The number of *E. coli* bacteria that were recovered from this untreated fabric swatch immediately after inoculation (t = 0 hours) was 260,000 CFU per cm² and was the baseline for comparison, i.e. set as 0% reduction in viability (0 log₁₀ reduction value, LRV). For fabrics exposed only to DI water, high levels of antibacterial activity were observed even at relatively low concentrations of Ag in the fabrics. After soaking the various textiles in DI water, viable *E. coli* bacteria were completely eliminated after 24 h of treatment with the AgCl-coated fabric, Tethered-AgNP fabric, and Ag⁰-coated fabric, with LRVs as high as 4.7, this value corresponds to the detection limit in our assay (**Figure E.4 a**). Variable, but lower, biocidal activity was seen with the Electrostatic-AgNP fabric, with an LRV of only 0.3, similar to the control fabric without Ag addition (**Figure E.4 a**). This inconsistency could be due to poor spatial coverage of

AgNPs on the fabric surface due to the low Ag concentration, which appears to have resulted in insufficient Ag release and uptake into the bacteria to be biocidal. This is consistent with the low amounts of released Ag measured for the Electrostatic-AgNP fabric (**Figure E.1**).

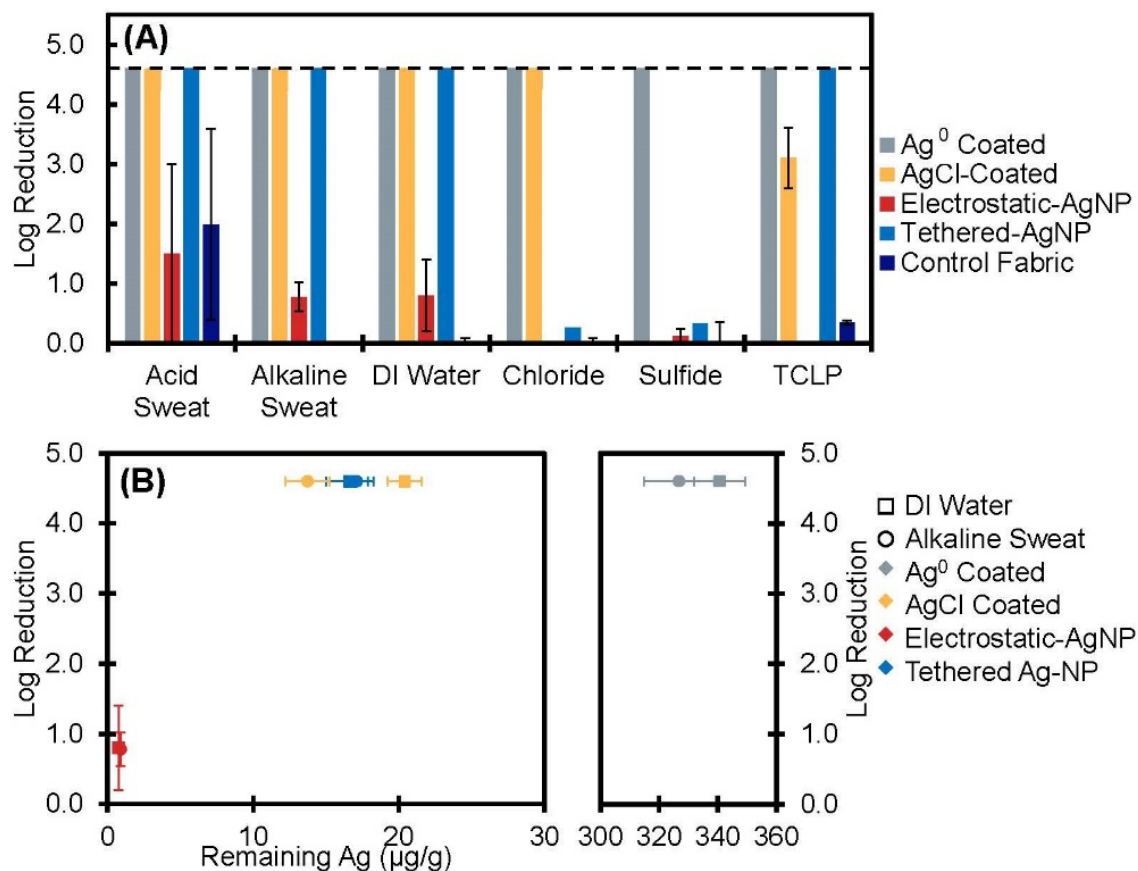


Figure E.4: *E. coli* antibacterial efficacy of Ag-enabled textiles during various exposure scenarios. (A) Comparison of log reduction of *E. coli* bacteria after 24 hours of incubation on various textile surfaces. The control fabric here was 100% polyester with no Ag that was exposed to the listed treatment solutions. The dashed line at 4.6 indicates the bacterial detection limit. (B) Efficacy of Ag-enabled textiles with respect to remaining silver content on the textile surfaces.

Table E-3: Bacteria cell counts after 24 hours of incubation on treated silver textiles.

Treatment	Fabric	Remaining Ag ($\mu\text{g/g}$ fabric)	CFU per cm^2	% reduction in <i>E. coli</i> viability	Log Reduction (\pm stdev)
DI Water	Ag ⁰ -coated	340.8	< 5	> 99.998 %	4.6*
	AgCl-coated	20.4	< 5	> 99.998 %	4.6*
	Electrostatic-AgNP	0.8	40,900	85 %	0.8 \pm 0.6
	Tethered-AgNP	16.6	< 5	> 99.998 %	4.6*
	Untreated	BDL	260,000	8.8 %	0.04 \pm 0.04
Acid Sweat Exposure	Ag ⁰ -coated	313.7	< 5	> 99.998 %	4.6*
	AgCl-coated	15.0	< 5	> 99.998 %	4.6*
	Electrostatic-AgNP	0.8	9,000	96.4 %	1.5 \pm 1.5
	Tethered-AgNP	12.9	<5	> 99.998 %	4.6*
	Untreated	BDL	3,000	98.99 %	1.99 \pm 1.6
Alkaline Sweat Exposure	Ag ⁰ -coated	326.8	< 5	> 99.998 %	4.6*
	AgCl-coated	13.7	< 5	> 99.998 %	4.6*
	Electrostatic-AgNP	0.9	44,000	85.4 %	0.78 \pm 0.24
	Tethered-AgNP	17.1	< 5	> 99.998 %	4.6*
	Untreated	BDL	270,000	1.2 %	0.01 \pm 0.01
Chloride	Ag ⁰ -coated	336.0	< 5	> 99.998 %	4.6*
	AgCl-coated	13.7	< 5	> 99.998 %	4.6*
	Electrostatic-AgNP	0.7	680,000	0.0 %	N/A
	Tethered-AgNP	8.8	121,000	44.9 %	0.26 \pm 0.26
	Untreated	BDL	330,000	0 %	N/A
Sulfide	Ag ⁰ -coated	343.6	< 5	> 99.998%	4.6*
	AgCl-coated	18.5	730,000	0.0 %	N/A
	Electrostatic-AgNP	0.2	177,000	24.8 %	0.12 \pm 0.12
	Tethered-AgNP	22.6	102,000	53.8 %	0.34 \pm 0.34
	Untreated	BDL	360,000	0.0 %	N/A
TCLP	Ag ⁰ -coated	342.7	< 5	> 99.998%	4.6*
	AgCl-coated	14.2	250	99.93 %	3.1 \pm 0.5
	Electrostatic-AgNP	0.7	520,000	0 %	N/A
	Tethered-AgNP	11.2	<5	99.998%	4.6*
	Untreated	BDL	128,000	55.0 %	0.35 \pm 0.04

BDL= below ICP-MS detection limit.

*Bacterial detection limit

E.3.4.1 Antimicrobial Efficacy Under “Use-Phase” Scenario: Following fabric soaking in both types of artificial sweat solutions, the three fabrics that were highly antibacterial after soaking in DI water (Ag⁰-coated, Tethered-AgNP, and AgCl-coated) continued to show complete (>99.998%) reduction of *E. coli* bacteria. On the Electrostatic-AgNP fabric, less bacterial reduction was observed, comparable to control fabric without Ag, except for a slightly higher potency after alkaline sweat treatment compared to the control fabric. However, post-soaking in the *acidic* sweat solution, the polyester control and Electrostatic-AgNP fabrics had higher levels of antibacterial activity compared to the *alkaline* sweat solution or DI water. This decline in viable bacteria cells on the fabrics soaked in acidic sweat was unexpected, but can be explained by the poor growth conditions for *E. coli* due to the artificial acidic sweat recipe which has a combination of low pH of 3.5 and lactic acid. It has been reported that either the presence of lactic acid or a pH less than 4.0 can have detrimental effects on the growth rate of *E. coli*, and other species of bacteria.⁴³ The standard AATCC protocol for artificial sweat tests on textiles is designed to examine the potential changes in the textile color due to dye or colorant release into the sweat solution, not necessarily to examine bacterial growth rates. Thus, the experimental conditions for the AATCC acid sweat test for colorfastness (which has previously been used to test the release of Ag from fabrics^{9,11,22,44}) did not appear to represent an ideal simulation for assessing the effects of human sweat on the fabric’s antibacterial efficacy. Alternative protocols which more closely resemble the sweat excretion chemical composition have been considered,⁴³ but not yet evaluated for experiments similar to this study. Either a better chemical approximation of acid sweat is needed for these efficacy tests, or a different test microorganism should be considered, such as *micrococci* or *coryneforms* that better mimic the bacteria in the skin microbiome.⁴⁵

E.3.4.2 Antimicrobial Efficacy after Exposure to Simulated Environmental Conditions:

Following fabric exposure to the end-of-life proxies, including TCLP, NaCl, and Na₂S, only the Ag⁰-coated textile completely eliminated the *E. coli* bacteria (**Figure E.4 A**). For the other textiles, exposure to the sulfide solutions resulted in much lower log reduction in bacterial viability. For the AgCl-coated textile in particular, the bacteria count increased by a factor of 2.2 relative to the control fabric after sulfide exposure (**Figure E.4 A, Table E.3**). This suggests that the Ag₂S is less effective of an antibacterial as has been previously shown for *E. coli*.⁴⁶ Ag₂S has a very low solubility product constant ($K_{sp}=10^{-50}$).⁴⁷ The low Ag release rates and low antibacterial efficiency of most of the textiles is consistent with the low solubility of Ag₂S.⁴⁷

Exposure of the Tethered-AgNP textile to the NaCl solution also rendered them no longer antibacterial. In contrast, the AgCl-coated textile remained highly bactericidal after exposure to the NaCl solution (**Figure E.4 A, Table E.3**). The AgCl-coated textile had lower levels of Ag release into the NaCl solution than the Tethered-AgNP textile (0.09 µg/cm² compared to 0.13 µg/cm², respectively), which resulted in higher levels of Ag remaining in the AgCl-coated textile following the NaCl aging than the Tethered-AgNP textile. This implies that these fabrics could be approaching the threshold level of Ag in textiles that is necessary for bactericidal activity.

Surprisingly, the Ag⁰-coated textile continued to completely eliminate the *E. coli* bacteria in the Na₂S exposure (**Figure E.4 A**). The Ag₂S-transformed Ag⁰-coated textile (**Figure E.2**) showed the same high level of bactericidal activity as the DI exposed Ag⁰-coated textile (**Figure E.4 A**), which has not been observed before for Ag₂S. A possible interpretation for this result is that the organisms are interacting directly with the Ag₂S threads in the fabric. This direct contact with the Ag₂S might allow it to remain antibacterial despite being fully sulfidized. It is also possible that the large mass of Ag₂S provides enough dissolved Ag or Ag-S complexes locally at the cell surface

that it can remain antibacterial. Interactions between Ag-S complexes and biomolecules have been shown to occur in aquatic environments, and this transfer from the Ag₂S textile to the bacterial cells likely involves the cysteine sulfhydryl groups of proteins.⁴⁸

TCLP treatment, consisting of acetic acid at pH=4.9 and no NaCl, increased the Ag leaching compared to DI water for all but the AgCl-coated. For the Ag⁰-coated textile, XANES analyses indicated a change in speciation after exposure to the TCLP solution. While the speciation of the second phase could not be confirmed, this change is consistent with a change in the leaching of Ag from the fabrics. In general, the fabrics from the TCLP test, despite containing less Ag, were more antibacterial than those exposed to 500 mM NaCl. Carboxylate formation constants with Ag, with log K values typically less than 2, are lower than for chloride, which have a log K of 3,⁴⁸ leaving slightly more Ag on the fabrics and the higher levels of bactericidal activity intact post-TCLP exposures compared to untreated fabric or to NaCl (500 mM) exposures (**Table E.3, Figure E.3**).

To assess the minimal threshold level of Ag necessary in the different textiles for antibacterial activity, a plot of remaining Ag content after use-phase exposures vs. the bacterial reduction percentage and the log reduction value was created (**Figure E.4 B**). This plot does not include the acidic sweat test results due to incompatibility with the test microorganism as discussed above. These data suggest that (1) the exposure solutions did not remove enough total Ag from the Ag⁰-coated fabric to decrease its potency as an antibacterial, even when the Ag has transformed completely to a low solubility form of Ag₂S; and (2) the Electrostatic-AgNP textile did not have enough attached Ag to be considered bactericidal.

E.4 ENVIRONMENTAL IMPLICATIONS

Although the primary objective of this study was to investigate how transformations of the different forms of silver across the lifecycle influenced antimicrobial performance and silver release, it provides insight into the impact: benefit ratio¹⁸ and informs design of new materials. All of the fabrics, except for the Electrostatic-AgNP, were effective as an antimicrobial under the tested use-phase conditions. The potential environmental impact of Ag release from the textiles will depend on the ratio of the longevity of the antibacterial properties (benefit) to amount of Ag added to that textile (risks and impacts) since the benefit primarily comes from a reduction in the times that the garment requires washing.^{18,49} Thus, any Ag remaining in the fabric at the end of its life represents potential risk and environmental impacts without the associated benefit. Based on the released mass of Ag from each textile (**Figures E.1-E.2**), the mass of Ag remaining in all of the textiles will be limited, except for the Ag⁰-coated textile.⁸ Even though this textile may remain antibacterial for longer periods of time, the total mass of Ag released from this fabric after each use suggests that its overall benefit to risk ratio will be lower than for the Tethered-AgNP and AgCl-coated textiles given that all three provided similar antibacterial efficiency under normal use conditions.

From a consumer perspective, the benefits of an Ag-enabled textile will typically depend upon how the usage scenarios of sweat and washing will affect the overall anti-odor functional performance. Of the four Ag containing textiles studied here, the Ag⁰-coated fabric clearly has the highest capacity for long-term performance due to the significantly higher loadings of Ag and its resulting resilience against exposure to chlorides and sulfides. As for the AgCl-coated and Tethered-AgNP textiles, which contain ~25x less Ag than the Ag⁰-coated textile, the antibacterial performance would decline more quickly considering the higher percentage of Ag release in

artificial sweat solutions (**Figure E.1 B**; **Figure E.3 B**). In practical scenarios, these releases would be more variable due to differences in users' sweat composition and output levels.⁵⁰ The Electrostatic-AgNP textile did not contain enough Ag to have consistent antibacterial activity. This study provides further support for the idea that product development could be tailored to contain the amounts and species of Ag that will leach out of the textile at a rate high enough to eliminate bacteria in sweat conditions and to fully exhaust the textile by the expected time of disposal.⁹ These results suggest that ~10 µg Ag/g of fabric may be sufficient to provide the desired antimicrobial action.

E.5 REFERENCES FOR APPENDIX E

- (1) Dastjerdi, R.; Montazer, M. A Review on the Application of Inorganic Nano-Structured Materials in the Modification of Textiles: Focus on Anti-Microbial Properties. *Colloids Surfaces B Biointerfaces* **2010**, *79* (1), 5–18.
- (2) Rivero, P. J.; Urrutia, A.; Goicoechea, J.; Arregui, F. J. Nanomaterials for Functional Textiles and Fibers. *Nanoscale Res. Lett.* **2015**, *10* (1), 501.
- (3) Perelshtein, I.; Applerot, G.; Perkas, N.; Guibert, G.; Mikhailov, S.; Gedanken, A. Sonochemical Coating of Silver Nanoparticles on Textile Fabrics (Nylon, Polyester and Cotton) and Their Antibacterial Activity. *Nanotechnology* **2008**, *19* (24), 245705.
- (4) Ki, H. Y.; Kim, J. H.; Kwon, S. C.; Jeong, S. H. A Study on Multifunctional Wool Textiles Treated with Nano-Sized Silver. *J. Mater. Sci.* **2007**, *42* (19), 8020–8024.
- (5) Becheri, A.; Durr, M.; Lo Nostro, P.; Baglioni, P. Synthesis and Characterization of Zinc Oxide Nanoparticles: Application to Textiles as UV-Absorbers. *J. Nanoparticle Res.* **2008**, *10* (4), 679–689.
- (6) Avila, A. G.; Hinstroza, J. P. Smart Textiles: Tough Cotton. *Nat. Nanotechnol.* **2008**, *3* (8), 458–459.
- (7) Liu, Y.; Tang, J.; Wang, R.; Lu, H.; Li, L.; Kong, Y.; Qi, K.; Xin, J. H. Artificial Lotus Leaf Structures from Assembling Carbon Nanotubes and Their Applications in Hydrophobic Textiles. *J. Mater. Chem.* **2007**, *17* (11), 1071–1078.
- (8) Gilbertson, L. M.; Wender, B. A.; Zimmerman, J. B.; Eckelman, M. J. Coordinating Modeling and Experimental Research of Engineered Nanomaterials to Improve Life Cycle Assessment Studies. *Environ. Sci. Nano* **2015**, *2* (6), 669–682.
- (9) Reed, R. B.; Zaikova, T.; Barber, A.; Simonich, M.; Lankone, R.; Marco, M.; Hristovski,

- K.; Herckes, P.; Passantino, L.; Fairbrother, D. H.; et al. Potential Environmental Impacts and Antimicrobial Efficacy of Silver- and Nanosilver-Containing Textiles. *Environ. Sci. Technol.* **2016**, *50* (7), 4018–4026.
- (10) Lombi, E.; Donner, E.; Scheckel, K. G.; Sekine, R.; Lorenz, C.; Von Goetz, N.; Nowack, B. Silver Speciation and Release in Commercial Antimicrobial Textiles as Influenced by Washing. *Chemosphere* **2014**, *111*, 352–358.
- (11) Von Goetz, N.; Lorenz, C.; Windler, L.; Nowack, B.; Heuberger, M.; Hungerbühler, K. Migration of Ag- and TiO₂-(Nano)Particles from Textiles into Artificial Sweat under Physical Stress: Experiments and Exposure Modeling. *Environ. Sci. Technol.* **2013**, *47* (17), 9979–9987.
- (12) Mitrano, D. M.; Motellier, S.; Clavaguera, S.; Nowack, B. Review of Nanomaterial Aging and Transformations through the Life Cycle of Nano-Enhanced Products. *Environ. Int.* **2015**, *77*, 132–147.
- (13) Mitrano, D. M.; Limpiteprakan, P.; Babel, S.; Nowack, B. Durability of Nano-Enhanced Textiles through the Life Cycle: Releases from Landfilling after Washing. *Environ. Sci. Nano* **2016**, *3* (2), 375–387.
- (14) Lorenz, C.; Windler, L.; Von Goetz, N.; Lehmann, R. P.; Schuppler, M.; Hungerbühler, K.; Heuberger, M.; Nowack, B. Characterization of Silver Release from Commercially Available Functional (Nano)Textiles. *Chemosphere* **2012**, *89* (7), 817–824.
- (15) Mitrano, D. M.; Rimmel, E.; Wichser, A.; Erni, R.; Height, M.; Nowack, B. Presence of Nanoparticles in Wash Water from Conventional Silver and Nano-Silver Textiles. *ACS Nano* **2014**, *8* (7), 7208–7219.
- (16) Hedberg, J.; Skoglund, S.; Karlsson, M. E.; Wold, S.; Odnevall Wallinder, I.; Hedberg, Y. Sequential Studies of Silver Released from Silver Nanoparticles in Aqueous Media Simulating Sweat, Laundry Detergent Solutions and Surface Water. *Environ. Sci. Technol.* **2014**, *48* (13), 7314–7322.
- (17) Levard, C.; Hotze, E. M.; Colman, B. P.; Dale, A. L.; Truong, L.; Yang, X. Y.; Bone, A. J.; Brown, G. E.; Tanguay, R. L.; Di Giulio, R. T.; et al. Sulfidation of Silver Nanoparticles: Natural Antidote to Their Toxicity. *Environ. Sci. Technol.* **2013**, *47* (23), 13440–13448.
- (18) Hicks, A. L.; Gilbertson, L. M.; Yamani, J. S.; Theis, T. L.; Zimmerman, J. B. Life Cycle Payback Estimates of Nanosilver Enabled Textiles under Different Silver Loading, Release, and Laundering Scenarios Informed by Literature Review. *Environ. Sci. Technol.* **2015**, *49* (13), 7529–7542.
- (19) Ding, D.; Chen, L.; Dong, S.; Cai, H.; Chen, J.; Jiang, C.; Cai, T. Natural Ageing Process Accelerates the Release of Ag from Functional Textile in Various Exposure Scenarios. *Sci. Rep.* **2016**, *6* (1), 37314.
- (20) Geranio, L.; Heuberger, M.; Nowack, B. The Behavior of Silver Nanotextiles during Washing. *Environ. Sci. Technol.* **2009**, *43* (21), 8113–8118.
- (21) Impellitteri, C. A.; Tolaymat, T. M.; Scheckel, K. G. The Speciation of Silver Nanoparticles in Antimicrobial Fabric Before and After Exposure to a Hypochlorite/Detergent Solution.

- J. Environ. Qual.* **2009**, 38 (4), 1528–1530.
- (22) Kulthong, K.; Srisung, S.; Boonpavanitchakul, K.; Kangwansupamonkon, W.; Maniratanachote, R. Determination of Silver Nanoparticle Release from Antibacterial Fabrics into Artificial Sweat. *Part. Fibre Toxicol.* **2010**, 7 (1), 8.
- (23) Stefaniak, A. B.; Duling, M. G.; Lawrence, R. B.; Thomas, T. A.; LeBouf, R. F.; Wade, E. E.; Abbas Virji, M. Dermal Exposure Potential from Textiles That Contain Silver Nanoparticles. *Int. J. Occup. Environ. Health* **2014**, 20 (3), 220–234.
- (24) Balakumaran, M. D.; Ramachandran, R.; Jagadeeswari, S.; Kalaichelvan, P. T. In Vitro Biological Properties and Characterization of Nanosilver Coated Cotton Fabrics - An Application for Antimicrobial Textile Finishing. *Int. Biodeterior. Biodegrad.* **2016**, 107, 48–55.
- (25) Wagener, S.; Dommershausen, N.; Jungnickel, H.; Laux, P.; Mitrano, D. M.; Nowack, B.; Schneider, G.; Luch, A. Textile Functionalization and Its Effects on the Release of Silver Nanoparticles into Artificial Sweat. *Environ. Sci. Technol.* **2016**, 50 (11), 5927–5934.
- (26) Bianco, C.; Adami, G.; Crosera, M.; Larese, F.; Casarin, S.; Castagnoli, C.; Stella, M.; Maina, G. Silver Percutaneous Absorption after Exposure to Silver Nanoparticles: A Comparison Study of Three Human Skin Graft Samples Used for Clinical Applications. *Burns* **2014**, 40 (7), 1390–1396.
- (27) EPA. Method 1311 Toxicity Characteristic Leaching Procedure. *SW-846 Test Methods Eval. Solid Waste, Phys. Methods* **1992**, 1–35.
- (28) Bolyard, S. C.; Reinhart, D. R.; Santra, S. Behavior of Engineered Nanoparticles in Landfill Leachate. *Environ. Sci. Technol.* **2013**, 47 (15), 8114–8122.
- (29) Yang, Y.; Gajaraj, S.; Wall, J. D.; Hu, Z. A Comparison of Nanosilver and Silver Ion Effects on Bioreactor Landfill Operations and Methanogenic Population Dynamics. *Water Res.* **2013**, 47 (10), 3422–3430.
- (30) Gitipour, A.; Badawy, A. El; Arambewela, M.; Miller, B.; Scheckel, K. G.; Elk, M.; Ryu, H.; Gomez-Alvarez, V.; Domingo, J. S.; Thiel, S.; et al. The Impact of Silver Nanoparticles on the Composting of Municipal Solid Waste. *Environ. Sci. Technol.* **2013**, 47 (24), 14385–14393.
- (31) Spielman-Sun, E.; Zaikova, T.; Dankovich, T. A.; Yun, J.; Ryan, M.; Hutchison, J. E.; Lowry, G. V. Effect of Silver Concentration and Chemical Transformations on Release and Antibacterial Efficacy in Silver-Containing Textiles. *NanoImpact* **2018**, 11 (November 2017), 51–57.
- (32) AATCC. Method 15: Colorfastness to Perspiration. **2013**.
- (33) Starnes, D. L.; Unrine, J. M.; Starnes, C. P.; Collin, B. E.; Oostveen, E. K.; Ma, R.; Lowry, G. V.; Bertsch, P. M.; Tsyusko, O. V. Impact of Sulfidation on the Bioavailability and Toxicity of Silver Nanoparticles to *Caenorhabditis elegans*. *Environ. Pollut.* **2015**, 196, 239–246.
- (34) United States Environmental Protection Agency. Method 3050B - Acid Digestion of

Sediments, Sludges, and Soils. *Method 3050B* **1996**.

- (35) Webb, S. M. SIXPack a Graphical User Interface for XAS Analysis Using IFEFFIT. *Phys. Scr.* **2005**, *T115* (0001), 1011–1014.
- (36) AATCC. Method 100: Antibacterial Finishes on Textile Materials. **2004**.
- (37) Herigstad, B.; Hamilton, M.; Heersink, J. How to Optimize the Drop Plate Method for Enumerating Bacteria. *J. Microbiol. Methods* **2001**, *44* (2), 121–129.
- (38) Peretyazhko, T. S.; Zhang, Q.; Colvin, V. L. Size-Controlled Dissolution of Silver Nanoparticles at Neutral and Acidic pH Conditions: Kinetics and Size Changes. *Environ. Sci. Technol.* **2014**, *48* (20), 11954–11961.
- (39) Axson, J. L.; Stark, D. I.; Bondy, A. L.; Capracotta, S. S.; Maynard, A. D.; Philbert, M. A.; Bergin, I. L.; Ault, A. P. Rapid Kinetics of Size and pH-Dependent Dissolution and Aggregation of Silver Nanoparticles in Simulated Gastric Fluid. *J. Phys. Chem. C* **2015**, *119* (35), 20632–20641.
- (40) Misra, S. K.; Dybowska, A.; Berhanu, D.; Luoma, S. N.; Valsami-Jones, E. The Complexity of Nanoparticle Dissolution and Its Importance in Nanotoxicological Studies. *Sci. Total Environ.* **2012**, *438*, 225–232.
- (41) Rowe, R. K. Leachate Characteristics for MSW Landfills. *Proceedings Sardinia 95*. London, Canada 1995, pp 327–344.
- (42) Levard, C.; Mitra, S.; Yang, T.; Jew, A. D.; Badireddy, A. R.; Lowry, G. V.; Brown, G. E. Effect of Chloride on the Dissolution Rate of Silver Nanoparticles and Toxicity to *E. coli*. *Environ. Sci. Technol.* **2013**, *47* (11), 5738–5745.
- (43) Presser, K. A.; Ratkowsky, D. A.; Ross, T. Modelling the Growth Rate of Escherichia Coli as a Function of pH and Lactic Acid Concentration. *Appl. Environ. Microbiol.* **1997**, *63* (6), 2355–2360.
- (44) Walter, N.; H. McQueen, R.; Keelan, M. In Vivo Assessment of Antimicrobial-Treated Textiles on Skin Microflora. *Int. J. Cloth. Sci. Technol.* **2014**, *26* (4), 330–342.
- (45) Grice, E. A.; Segre, J. A. The Skin Microbiome. *Nat. Rev. Microbiol.* **2011**, *9*, 244–253.
- (46) Reinsch, B. C.; Levard, C.; Li, Z.; Ma, R.; Wise, A.; Gregory, K. B.; Brown, G. E.; Lowry, G. V. Sulfidation of Silver Nanoparticles Decreases *Escherichia coli* Growth Inhibition. *Environ. Sci. Technol.* **2012**, *46* (13), 6992–7000.
- (47) Levard, C.; Reinsch, B. C.; Michel, F. M.; Oumahi, C.; Lowry, G. V.; Brown, G. E. Sulfidation Processes of PVP-Coated Silver Nanoparticles in Aqueous Solution: Impact on Dissolution Rate. *Environ. Sci. Technol.* **2011**, *45* (12), 5260–5266.
- (48) Kramer, J. R.; Benoit, G.; Bowles, K. C. *Silver in the Environment: Transport, Fate, and Effects*; Society of Environmental Toxicology and Chemistry (SETAC), 2002.
- (49) Wigger, H.; Hackmann, S.; Zimmermann, T.; Köser, J.; Thöming, J.; von Gleich, A. Influences of Use Activities and Waste Management on Environmental Releases of Engineered Nanomaterials. *Sci. Total Environ.* **2015**, *535*, 160–171.

- (50) Callewaert, C.; De Maeseneire, E.; Kerckhof, F. M.; Verliefde, A.; Van de Wiele, T.; Boon, N. Microbial Odor Profile of Polyester and Cotton Clothes after a Fitness Session. *Appl. Environ. Microbiol.* **2014**, *80* (21), 6611–6619.